Università degli Studi di Padova

PHYSICS AND ASTRONOMY DEPARTMENT "GALILEO GALILEI"
PhD course in Astronomy

PhD thesis

The extreme blazar phenomenon in a multi-messenger context

Ph.D. student:
Luca Foffano

Supervisor:
Prof. Alberto Franceschini

Co-Supervisor:
Dr. Elisa Prandini

Coordinator:
Prof. Giampaolo Piotto

Dalla meta mai non toglier gli occhi.
Alessandro Manzoni

Contents

Abstract

This Thesis illustrates the activities and the results that I have obtained during my three-year PhD course at the University of Padova.

My work was mainly based on the study of the *extreme blazars*, or better "extreme high-energy peaked BL Lac objects" (generally referred to as EHBLs). EHBLs are an emerging class of blazars with exceptional spectral properties, presenting a spectral energy distribution peaking with the synchrotron emission in hard X-rays and a high-energy emission in TeV gamma rays. The hard-TeV spectrum of EHBLs is important also for the implications on the indirect estimations of the extragalactic background light and of the intergalactic magnetic fields.

The emission processes producing such extremely-high photon energies are currently not completely understood, and may represent a challenge for the standard modelling of these sources. In fact, the standard models are generally able to fit the experimental spectral data, but the parameters they assume are unusual compared to the standard blazar modelling currently available in literature. More complex models, assuming – for example – multiple emission zones or hadronic contributions, may provide more relaxed parameter spaces. In particular, the presence of hadronic processes in the blazar emission might make the EHBLs producers of extragalactic high-energy neutrinos.

The number of EHBL objects is currently very limited. Thanks to recent observations, new sources have been classified as candidate EHBLs. Their spectral properties reveal new features that enrich the properties of this class of objects.

In this framework, my research work started with the search for new EHBL candidates on the basis of all-sky surveys in hard X-rays. This new method allowed me to select the most promising extreme blazars relying on their X-ray to high-energy gamma-ray flux ratio. The analysis of the spectral properties of this new sample revealed interesting spectral features and systematic differences that are emerging in the EHBL class, especially in TeV gamma rays. This suggests the possible emergence of a sub-classification, and a new population of EHBLs may be unveiled.

One specific aspect of my analysis was to predict the feasibility of observations of these objects with the current and next generation of Cherenkov telescopes. In the MAGIC Collaboration, I had the opportunity to propose a list of EHBL candidates for observations. Among them, a source named PGC 2402248 was observed and finally detected in TeV gamma rays, and several others are now being observed with the MAGIC telescopes. These results have been published together with a detailed discussion on the comparison between several theoretical models proposing different interpretations of the spectral properties of these sources.

During my PhD, I had the opportunity to contribute to several other projects that complemented my preparation in this field. In the MAGIC Collaboration, I was involved in projects related to the detection of new EHBLs in TeV gamma rays and in the study of

interesting blazars like PG 1553+113. I was also involved in two analyses on the relation between extreme blazars and extragalactic background light, and on the selection of extreme blazar candidates from a sample of faint sources in the high-energy gamma-ray band.

Finally, an important part of my PhD activity within the MAGIC Collaboration was devoted to a contribution to the discovery of the first association between a high-energy neutrino, the so-called *IceCube EHE-170922A* event, and the blazar TXS 0506+056. During the analysis of this event, registered on September 2017, I was main analyser of the MAGIC data. Considering the importance of the discovery – with implications about the origin of the very-high-energy cosmic rays – and the intense multi-collaboration work, it was really a unique opportunity for me to gain new experience in this field and to further motivate my interest in the multi-messenger astrophysics.

Outline

This Thesis is composed of six chapters. In Chapter 1, I present an introduction to the wide topic regarding the multi-messenger astrophysics. I will introduce the non-thermal Universe, focusing into the main mechanisms that govern the production and the emission of the neutral cosmic-rays mainly discussed in this Thesis, gamma rays and neutrinos.

In Chapter 2, I present the instruments and the telescopes I made use during this PhD. I will order the discussion by the increasing energy bands studied by the observatories: after a presentation of the Medicina radio telescope, *Swift*, and *Fermi* observatories, I will focus on the software and hardware of the MAGIC telescopes. Then, I will summarize the status of the CTA project, and mention the main features of the IceCube observatory.

In Chapter 3, a discussion about the main structure and properties of active galactic nuclei is presented. I will then introduce a particular sub-class of these objects, the *blazars*, discussing their spectral properties and the main emission models that I encountered during this Thesis activity.

This introduces the main topic of the Thesis, that is the study of *extreme blazars*, discussed in Chapter 4 and Chapter 5. In the former, I will report about the study of the spectral properties of a new sample of extreme blazars, introducing the reader to a new selection method based on the hard X-ray properties of these sources and reporting the main spectral differences that suggest the possible emergence of a population in this class. I will also report several publications to which I contributed concerning the connection of extreme blazars with the study of the extragalactic background light and their possible detectability by the current and next generation of gamma-ray observatories.

In Chapter 5, I will present my phenomenological studies dedicated to obtain a new sample of sources in the EHBL class. I will introduce the discovery in TeV gamma rays of a new extreme blazar – named PGC 2402248 – that I had the opportunity to propose and that was eventually detected with the MAGIC telescopes. I will report about my contribution to the analysis and discussion of a new set of sources that have been discovered by MAGIC in this energy band, and some other sources that have been proposed as new candidates to be observed from the southern hemisphere.

Finally, in Chapter 6 I focus the attention on the opening of the multi-messenger era of astrophysics. I will present my activities and contributions in the MAGIC Collaboration concerning the detection of the high-energy neutrino IceCube EHE-170922A in coincidence with the flaring blazar TXS 0506+056 in 2017.

Chapter 1

Multi-messenger astrophysics

This Chapter is devoted to an introduction of the multi-messenger astrophysical era, definitively opened by a recent result concerning the first coincidence between the high-energy neutrino IceCube EHE-170922A and the flaring blazar TXS 0506+056.

This new page of astrophysics is related to the development of a connection between the different astrophysical messengers: electromagnetic light, neutrinos, cosmic rays, and gravitational waves. This Chapter will introduce the last three messengers and their relation with the electromagnetic radiation, especially gamma rays. A particular focus will be given to the nature of cosmic rays, that represents one of the most studied fields in astrophysics, but with several questions remaining open about their origin.

From the second to the fifth Section of this Chapter, I will report the main properties of the high-energy radiation that covers a major part of this Thesis work, the gamma rays. I will describe the main processes about production of gamma rays, their interactions with the environments, and the most important emitters of gamma rays in the Universe. I will report on the main methods currently used to detect gamma rays, focusing on the imaging atmospheric Cherenkov technique.

Finally, I will summarize two main approaches to astrophysics: its multi-wavelength and its multi-messenger face. I will mention the major facilities that are now being involved in the detection of gravitational waves and neutrinos, and that led to the recent discoveries in this field.

1.1 Introduction to cosmic-ray astrophysics

Figure 1.1: *An illustration of cosmic rays striking the upper atmosphere.*

The discovery of cosmic rays represented a fundamental boost for the Physics of 20$^{\text{th}}$ century. This benchmark in the history of Astrophysics can be set in the year 1912, when the physicist Victor Hess discovered what was the first type of high-energy radiation that changed our conception of the Universe. By using the first balloon flights, Victor Hess measured the density of ionized particles in the atmosphere and discovered that this number was increasing with altitude (Hess, 1912). Later on, Robert Millikan named this radiation as *Cosmic Rays* (CRs, Millikan & Cameron 1926), a term that refers now to all radiation and particles coming from outside the Earth's atmosphere.

The composition of CRs is currently well known: they are mainly composed by protons (99%) and helium nuclei, and in minor part by heavier nuclei, electrons, positrons, and neutrinos. Their spectrum, reported in **Figure** 1.2, is of non-thermal origin and is probably produced by the most extreme phenomena in the Universe. However, up to now, the acceleration mechanisms that should be able to produce such high energies in the Universe are largely unknown. Observing their spectrum, it is clear that the CRs represent the particles with the highest energies observed so far, reaching values of about 10^{21} eV.

One of the most interesting features of CRs is that they are composed both by charged and neutral particles. The electric charge of particles is important: they are deflected by the magnetic fields they cross in their travel to Earth, and for this reason their origin remains unknown. Only particles with energies above some 10^{20} eV can travel several megaparsec with negligible deviation due to the magnetic fields. Consequently, the distribution of CRs with energies below EeV cannot give any information about their origin, but only on their spectrum and composition. The only way to get direct information on the origin of CRs is to study the neutral particles, like neutrinos and gamma rays, that can travel along the Universe without being deflected by the magnetic fields.

1.1.1 Energy spectrum

The spectrum of the measured CRs extends from about 10^8 to 10^{21} eV and represents one of the most interesting examples of non-thermal distribution, with a power-law spectrum of the form:

$$\frac{dN}{dE} \propto E^{-\gamma} \, .$$

A particularly interesting feature of CRs is that their spectrum is apparently universal, meaning they their spectral index γ is generally confined in the range between 2 and 3 for

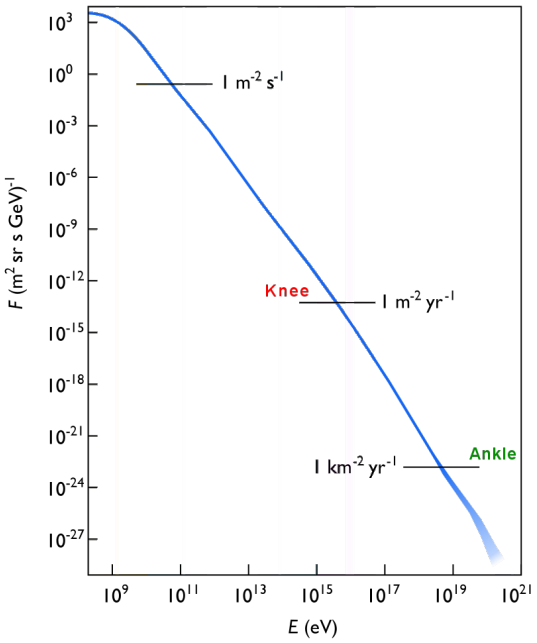

Figure 1.2: *A representation of the energy spectrum of primary cosmic rays Adapted from Swordy (2001).*

a huge range of energies. However, as reported in **Figure** 1.2, it can be divided in several energy ranges where the different slopes are related to the different origin of the processes that are producing such emission.

In fact, particles with energy below 1 GeV are supposed to be produced by our Sun, because the solar wind blocks particles at those energies arriving from outside our solar system. The rest of the spectrum follows the power-law distribution with several different (but rather constant) spectral indices. The different slopes in the spectrum are thought to be related to different acceleration mechanisms that produce the CRs. The first part, from about 100 MeV up to about 5 PeV, presents a photon index of $\gamma \sim 2.7$. At that point, the spectrum presents a bend known as the *knee*. Since the knee is electric charge dependent, particles with higher charge can bring up the knee to higher energies. After the knee, there is again a constant region with $\gamma \sim 3$ up to about 3 EeV. This part of the spectrum ends with a new hardening that is known as the *ankle*. Finally, beyond the last part of the ankle at about 3 EeV, the spectrum hardens again with $\gamma \sim 2.6$ up to about 30 EeV (Longair, 2002).

The origin of the processes producing such spectrum is still partially unknown. A robust interpretation is that particles with energies up to the knee are produced inside our Galaxy, whilst particles above the ankle seem to have extragalactic origin. In between the ankle and the knee, the origin of cosmic rays is not clear and is currently under debate. One of the crucial points is to explain the steepening of the spectrum at the knee. Some works suggested changes in the acceleration mechanism: for example a different acceleration in the supernova remnants with one at the front shock and a new re-acceleration in the inner pulsar-driven remnant (Bell, 1992), leakage of CRs out of the Galaxy by diffusion (Ptuskin et al., 1993), or even a cut-off of light elements (Antoni et al., 2005).

The study of CRs above the ankle is particularly difficult. Due to the extremely low flux of roughly one particle per square kilometre per century at 10^{20} eV, the measurement

Name	Abbreviation	Energy range
Low energy	LE	1 MeV - 30 MeV
High energy	HE	30 MeV - 50 GeV
Very-high energy	VHE	50 GeV - 100 TeV
Ultra-high energy	UHE	100 TeV - 100 PeV
Extremely-high energy	EHE	$>$ 100 PeV

Table 1.1: *Energy domains of gamma-ray astrophysics.*

of the CR spectrum beyond the ankle requires experiments of higher sensitivity at these energies. Even the most powerful accelerator on Earth, the Large Hadron Collider (LHC), produces particles of energies only up to about 10^{14} eV, more than seven orders of magnitude lower that what would be needed to study the highest energies of CRs. For this reason, it seems unbelievable to design experiments with such extended collection area on Earth, and astrophysics will probably be the natural laboratory for such experiments for a long time.

The GZK effect

An important feature that affects the CR spectrum is the so-called Greisen-Zatsepin-Kuzmin (GZK) cut-off. This effect is produced by the interaction of the ultra-high energy cosmic rays (UHECRs) with energies of 10^{20} eV with the Cosmic Microwave Background (CMB) through reactions like

$$p + \gamma_{\rm CMB} \rightarrow \Delta^{+} \rightarrow n + \pi^{+} \tag{1.1}$$

$$p + \gamma_{\rm CMB} \rightarrow \Delta^{+} \rightarrow p + \pi_{0}\ . \tag{1.2}$$

In particular, the interaction of UHE protons with the low-energy background photons forms a Δ^{+} resonance. The Δ is a family of barions with masses close to 1232 MeV. When an energetic-enough photon collides with a proton or a neutron, it quickly decays via the strong force into a nucleon (proton or neutron) and a pion of appropriate charge. While in the first process of Eq. 1.1 the proton gets absorbed, in the second reaction the proton is still a result of the equation. However, in the latter process, the proton transfers part of its energy to the pion, and the resulting GZK cut-off is even lower, reaching a few 10^{19} eV.

This interaction with the CMB photons produces also an absorption effect that limits to about 50 Mpc the maximum distance that the CRs with energies greater than 10^{20} eV can travel. This means that we do not expect to detect cosmic rays from deep space having energies greater than roughly 10^{20} eV. The absorption of CRs above about 10^{20} eV would inevitably confirm the presence of the long-sought GZK effect, and thus it would confirm the effect of cosmic-ray propagation through the Universe, or present an indication of the limit to which high-energy particles can be accelerated.

One of the most interesting problems is how to clearly confirm the presence of the GZK effect at such extremely high energies. The point is that those energies are above the capabilities of the particle physics detectors like the LHC (that cannot even reach the *ankle* of the spectrum), and the rate of incoming CRs from the space is about few events per century per squared kilometre.

Up to now, the most energetic event ever recorded is the *Fly's Eye* event (Bird et al., 1995). It has been registered with an energy of 3.2×10^{20} eV by the High Resolution Fly's

Eye Cosmic Ray Detector (HiRes) experiment[1], an ultra-high-energy cosmic-ray observatory that operated in Utah from May 1997 to April 2006.

1.1.2 Acceleration mechanisms

In order to accelerate particles, static electric and magnetic fields are not good candidates, because the former would be quickly neutralized and the latter by themselves cannot accelerate particles. Conversely, variable magnetic fields can induce variable electric fields and thus accelerate particles. When this process is involved in many cycles, particles are supposed to be accelerated to the highest energies we measure for CRs.

There are mainly two different ways to accelerate charged CRs. The first process is through variable magnetic and electric fields. The second type of processes, the ones that are supposed to contribute at most, are the diffuse shock acceleration mechanisms. These processes can be split into two main mechanisms, proposed by Enrico Fermi (Fermi, 1949): they are called respectively the first order and the second order Fermi acceleration processes.

First order Fermi acceleration process

The acceleration is supposed to take place in a plasma in which shock waves and magnetic field inhomogeneities are produced. When the charged particle travels through the shock wave, it can be reflected back by the magnetic field and increase its velocity. If this process occurs upstream, the particle can gain energy. If multiple scattering occurs, the particle can get accelerated every time it crosses the shock wave, gaining energy at each reflection proportionally to the relative velocity between the shock and the particle,

$$\frac{\Delta E}{E} \propto v_{\mathrm{rel}}/c \,.$$

The resulting energy spectrum of many particles undergoing this process (assuming that they do not influence the structure of the shock) follows a power-law distribution of the form

$$\frac{dN}{dE} \propto E^{-\gamma} \,.$$

In this process, the larger is the relative velocity, the larger is the energy gain. The number of multiple scattering through the shock wave is directly proportional to the magnetic field strength. This mechanism turns out to be very efficient and is supposed to be responsible for the acceleration of particles up to PeV ranges.

Second order Fermi acceleration process

The second order Fermi acceleration occurs when a charged particle moves in the presence of randomly moving "magnetic mirrors", and in practice when moving within magnetized clouds.

The main difference with respect to the first order Fermi acceleration mechanism is that here I assume that the directions for the shock wave are randomly distributed, and not strongly correlated in the limit of a "plane wave". So, if the magnetic field front is moving towards the particle, the particle will end up with increased energy after the reflection. The

[1] http://www.cosmic-ray.org/

energy gained by the particles in each reflection is proportional to the square of the speed of the moving cloud,

$$\frac{\Delta E}{E} \propto (v_{\rm cloud}/c)^2 \ .$$

The resulting energy spectrum, however, is not universal as in the case of first order Fermi acceleration.
When particles escape from the acceleration region (e.g. it exits the interstellar magnetized cloud), the process stops because there are no more interactions with the magnetic field. Thus, the maximum energy $E_{\rm max}$ that the accelerated CRs can reach is determined by the radius of the circular motion they describe under the presence of an uniform magnetic field, the so-called Larmor radius or gyroradius, and obeys the following relation:

$$E = q \frac{R}{kpc} \frac{B}{\mu G} \ 10^{18} \ {\rm eV} \ ,$$

where q is the charge of the particle, R is the radius, and B the magnetic field of the acceleration region. This geometrical constraint is known as *Hillas criterion*.

In **Figure** 1.3 I report the so-called Hillas plot, that shows the relation between the magnetic field strength and the radius of the acceleration region. The diagonal lines define the allowed region for particles acceleration at different energies. Objects below each line cannot accelerate those particles up to the indicated energies.

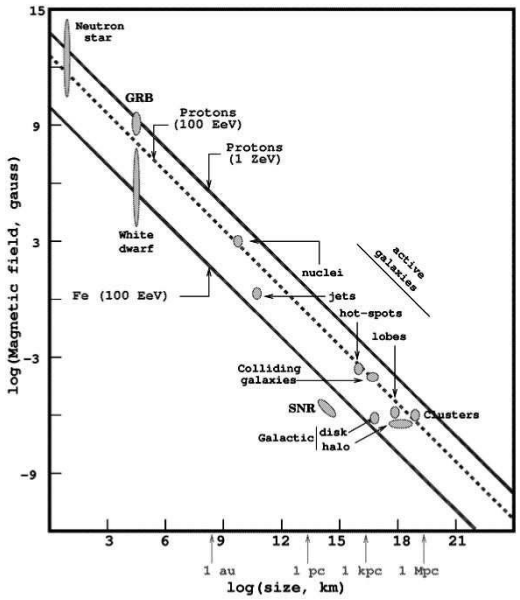

Figure 1.3: *Here I show the so-called Hillas plot (Hillas, 1984), that represents the possible CR sources as a function of their magnetic field strength and size. Objects below each line cannot accelerate those particles up to the indicated energies. Figure from Gelmini (2009).*

1.1.3 Composition

Primary cosmic rays, the particles coming from the deep Universe, are composed by all elements of the periodic table, but the largest fraction consists of protons (90%) and helium nuclei (9%). A small fraction of less than 1% is composed of neutrons or nuclei of heavier elements, such as C, O, Fe and other nuclei produced during stellar nucleo-synthesis. The remaining 0.1% is composed by electrons and photons. The number of neutrinos is estimated to be comparable to that of high-energy photons, but its major part is composed by secondary products of interaction of CRs and by low-energy neutrinos probably produced by the Solar nuclear reactions.

Primary cosmic rays generally produce secondary particles by hitting the upper part of the atmosphere. Such particles travel through the atmosphere producing multiplicative showers, and some of them reach the ground. Such particles, travelling at relativistic speed, produce the so-called *Cherenkov light*, presented in Section 1.5.1.

1.1.3.1 Neutral component

The CRs are composed only for a minimal part of neutral particles, such as gamma rays, neutrons, and neutrinos. Some authors, when referring to CRs, do not even include such neutral particles. Neutrons have a short lifetime of the order of hundreds of seconds, and for this reason they typically decay before reaching the Earth. On the other hand, gamma rays and neutrinos represent valuable messengers of astrophysical information. Thanks to their neutral charge, they are not deviated by the interstellar magnetic fields and trace perfectly to their origin place: for this reason they are considered very important messengers for the CR study. Additionally, they are detectable from Earth in both direct or indirect ways, and in both the cases we can reconstruct their incoming direction in the sky (with different accuracy, of course). Neutrinos are for sure very difficult to be detected. Several experiments have been built in order to study these elusive particles, and as a representative example I present in Section 2.6 the IceCube experiment operating at the south Pole.

Conversely, VHE gamma rays are not detectable from Earth due to the absorption by the atmosphere, and their detection from outside the atmosphere would request spacecrafts with too large collecting areas for the current facilities. Fortunately, the atmospheric Cherenkov technique allows us to detect VHE gamma rays in an indirect way from Earth, and I will present this topic in Section 1.5.1.

1.1.4 Open questions and main experimental efforts

Enormous progress has been made in the last years thanks to several experiments involved in the study of CRs. However, despite the revolutionary progress, some long-standing questions in this field remain partially or completely unanswered, especially in the high-energy part of the spectrum at UHE.
Some of these crucial aspects of UHECRs are, for example:

- What is the origin of UHECRs? Are there anisotropies in the arrival direction of the UHECRs? What are the sources producing the UHECRs? Numerous efforts are now being carried on to identify single sources of UHECRs.
- What is the precise mass composition of UHECRs at the highest energies?
- What is the acceleration mechanism able to produce so high energies? An accurate description on how particle are accelerated in astrophysical sources could contribute to understanding the transition from Galactic to extragalactic origin of cosmic rays.

- What is the flux of secondary messengers such as neutrinos and gamma rays? What information can we extract from them, when they are associated with UHECRs?

The current and next generations of ultra-high energy facilities will have the opportunity to answer definitively some of these questions.

The current generation of CR detectors to study such extreme energies is mainly represented by the Pierre Auger experiment[2], located in Argentina. It is considered a "hybrid detector" extended for more than 3000 km^2 and provided with two independent methods to detect and study high-energy CRs: a large-size surface array of water-Cherenkov tanks and an air fluorescence detector. While the first technique detects high-energy particles through their interaction with water placed in surface detector tanks, the latter tracks the development of air showers by observing UV light emitted high in the Earth's atmosphere.

The Pierre Auger experiment will undergo an important upgrade (Pierre Auger Collaboration et al., 2016) that will improve the surface detector by adding on the top of each tank a solid-state scintillator plate. This additional instrument will improve the sensitivity to the CR mass composition by simultaneous measurements of electrons and muons passing through both detectors.

Considering that the spectrum of CRs rapidly falls at few 10^{19} eV where the GZK cut-off may occur, event statistics plays an important role. In order to increase the statistics, the observatories have to increase as much as possible their integrated exposure. For example, the Telescope Array[3] (TA) – located in the high desert in Millard County, Utah (USA) – has reached $0.8 \cdot 10^4$ km^2 sr yr, while the Pierre Auger dominates with $9 \cdot 10^4$ km^2 sr yr.

Some of these recently approved upgrades go into the direction of extending the collective area of the instruments. For example, the TA has recently announced an upgrade called $TA{\times}4$ (Kido, 2018) that will extend the surface detectors for more than three times with respect to TA, bringing it to cover an area of about 3 000 km^2.

Other instruments, like the GRAND observatory (Alvarez-Muniz et al., 2020), the most ambitious ground-based experiment proposed so far, will cover also the study of ultra-high energy cosmic rays. Thanks to antennas tuned for the detection of very inclined events, the observatory will be able to extend its exposure to unprecedented values and to reach a collective area of about 200 000 km^2.

A detailed review of the current status and perspectives of the research in this field is reported in Alves Batista et al. (2019).

[2] https://www.auger.org/
[3] http://www.telescopearray.org/

1.2 Gamma-ray production and acceleration

Gamma rays are produced by several non-thermal processes. In this Section, I present the main features of the processes that will be reported throughout this Thesis. For a detailed review of this topic, the interested reader can refer to Aharonian et al. (2004).

Gamma-ray production mechanisms can be contributed by both radiative and collisional processes. In the following discussion, I present first the leptonic processes that produce gamma rays. In the second part, I introduce some hadronic processes that can lead, as secondary products, to gamma rays.

1.2.1 Leptonic gamma-ray production processes

1.2.1.1 Bremsstrahlung

When a charged particle (like an electron, that represents the case when the mechanism is more efficient) travels through a material, it interacts with the electric field of its nuclei. The interaction produces deviations of the trajectory of the particle, and this radial acceleration produces emission of electromagnetic waves in the form of gamma rays. This phenomenon is called *bremsstrahlung*, and becomes dominant against the ionization above the so-called critical energy, defined as energy at which the energy loss by both mechanisms is equal. The bremsstrahlung effect produces an energy loss as a function of the distance travelled by the electron in the medium, and can be calculated on average by:

$$-\frac{dE}{dx} = \frac{1}{\chi_0} E \ .$$

Here χ_0 is called radiation length, and represents the average distance over which the particle loses all but $\frac{1}{e}$ of its energy due to bremsstrahlung.

The radiation length depends on the material: higher the density of the material, lower will be the distance at which the particle can penetrate, and smaller will be radiation length. Since the energy loss is directly proportional to the energy of the charged particle, the bremsstrahlung effect produces a gamma-ray spectrum that follows the same distribution of the charged particle.

Bremsstrahlung represents an important mechanism to produce MeV photons, while gamma rays at VHE can be produced through bremsstrahlung of UHE charged particles.

1.2.1.2 Electron-positron annihilation

The production of gamma rays is possible also through the channel

$$e^- + e^+ \rightarrow \gamma + \gamma \ .$$

Considering the electron and position masses, this interaction produces a spectral line peak at 511 keV (that is however broadened by the kinetic energy of the particles).

One of the main problems of this process in astrophysics is the difficulty in reconstructing the birth-place of the incoming particles. This interaction would request a HE electron and a positron, but the origin of such positrons is not clear yet. Probably, the simplest way to produce them for such interaction is the decay of positive pions. Another possibility would be the creation of electron-positrons pairs through photon-photon annihilation or thanks to the decay of long-lived radioactive isotopes produced for example in the supernovae nucleo-synthesis.

1.2.1.3 Synchrotron radiation

Any charged particle which moves in a curved path emits electromagnetic radiation. In the astrophysical case, charged particles move inside a magnetic field and continuously accelerate due to the Lorentz force

$$F = \frac{d(\gamma m v)}{dt} = \frac{q}{c} v \times b + qE \ ,$$

where

$$\gamma = \frac{1}{\sqrt{1 - \frac{v^2}{c^2}}} \ .$$

This acceleration implies emission of electromagnetic radiation from microwave to hard X-rays. This radiation is called *cyclotron radiation* when the particle motion is non-relativistic. When the motion of the particle becomes relativistic, the emission is then named *synchrotron radiation*. This kind of radiation is the case mainly discussed in this Thesis. The radiation frequency is given by the gyration $\frac{qB}{mc}$ – where q is the electric charge of the particle and m is its mass – and implies a line emission in the spectrum (neglecting other broadening effects).

The total emitted power by the particle can be easily studied in the instantaneous reference frame of the electron (where the particle can be considered non-relativistic during this time interval) using the *Larmor* formula for the emitted power. This implies that the total emitted power is

$$P = \frac{4}{3} \sigma_T c \beta^2 \gamma^2 U_B \ ,$$

with the magnetic energy $U_B = \frac{B^2}{8\pi}$.

Since in the lab reference system the electron is moving with relativistic velocity, the emission suffers relativistic effects. This implies, in particular, that the emission is strongly enhanced (beamed) in the forward direction and the radiation field seen by the observer is concentrated inside a narrow cone of width $1/\gamma$.

Synchrotron polarization of the light

When the particle is moving at relativistic velocities, another relativistic effect appears: the polarization of the synchrotron light.

In the case of synchrotron emission, the flux is elliptically polarized. Considering **Figure 1.4**, inside the emission cone in the inner and outer shaded region with respect to the trace of the velocity vector, the polarization is elliptical, in one sense and in the opposite, respectively. But, when looking in the direction of maximal emission and considering a roughly uniform distribution of electrons, the two elliptical polarization components cancel out, and only the linear polarization survives. If the line-of-sight is instead outside the direction of maximal emission, in general the emission is elliptically polarized. When the line-of-sight is outside the emission cone of the particle, the emission is essentially null.

An important quantity in this topic is the degree of polarization of the light. In order to quantify it, we can refer to the two different components of the electric field: the component parallel to the projection of the B field on the celestial sphere, and the one orthogonal to it. The corresponding radiation powers are $P_\parallel$ and $P_\perp$. The degree of polarization can then be immediately obtained from

$$\Pi = \frac{P_\perp - P_\parallel}{P_\perp + P_\parallel} \ .$$

Notice that the polarization turns out to be almost frequency independent. Integrating over all frequencies, an average (linear) polarization fraction results about 75%, that is a quite high value (Franceschini lecture notes, 2016).

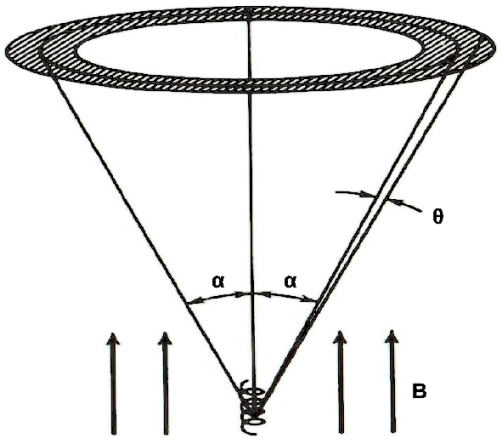

Figure 1.4: *Representation of the synchrotron light emission and its polarization. I report the direction of the magnetic filed B, the direction of the particle motion, the path made on the sky by the velocity vector, and the trace of the emission cone (in shaded grey). Taken from Franceschini lecture notes (2016).*

Additionally, there is a strong assumption that has been considered: the fact that we considered an ordered magnetic field B. In the real case we expect fluctuations and instabilities in the magnetic fields of the astrophysical objects. For this reason, often the polarization is used the other way around: measuring the polarization, one can reconstruct the distribution of the magnetic field at the source.

The polarization of the light is often used to study synchrotron emission from astrophysical objects. However, one should keep in mind that the presence of polarized light is not always evidence for ongoing non-thermal processes: other phenomena can originate it, e.g. scattering and reflections, or even anisotropic absorption by polarized orientation of dust particles.

Synchrotron self-absorption and spectral cut-offs

The discussion of the synchrotron radiation is however limited by the two following points. First, the quantum mechanical limit

$$h\nu \ll \gamma mc^2$$

has to be considered in our discussion. This implies that, since the frequency ν can also be expressed as

$$\nu = \gamma^2 eB/2\pi mc \,, \tag{1.3}$$

the following relation yields:

$$\gamma B < 5 \cdot 10^{13} \text{ Gauss} \,.$$

This relations is the limit under which the quantum corrections are negligible.

Another important limit is when the radiation losses are so high that they affect sensibly the helical orbit of the emitting particle. This implies that also the spectrum is modified. This condition implies that

$$\gamma^2 B \ll 5 \cdot 10^{16} \text{ Gauss} \,.$$

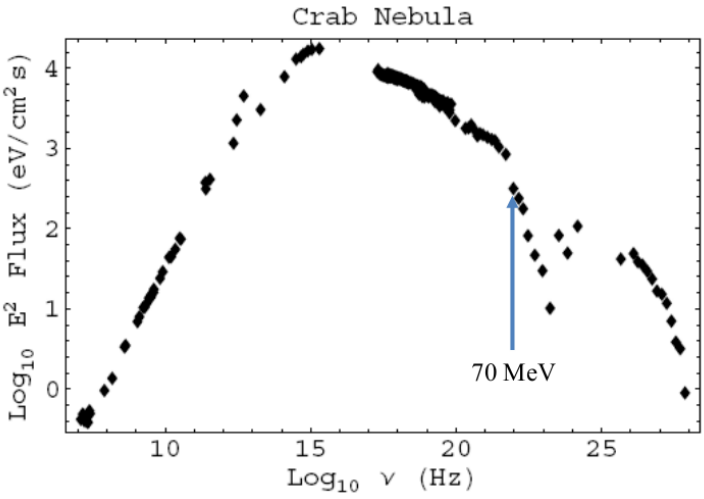

Figure 1.5: *Spectrum of the Crab Nebula showing the transition between the synchrotron and the Inverse Compton peaks. The spectral break at about 70 MeV represents the transition to the regime where the quantum effects become relevant. Taken from Franceschini lecture notes (2016).*

Such equation, considering Eq. 1.3, yields to a relation that depends on the energy at which the particle is emitting

$$h\nu \ll 70 \text{ MeV} .$$

This result means that the maximum energy below which the radiation losses are not enough strong to sensibly modify the orbit of the particle during one orbit is about 70 MeV. This result is particularly important, for example, in studying objects like the Crab Nebula spectrum reported in **Figure** 1.5. In such spectrum, one can see the transition between the main hump on the left hand side due to synchrotron radiation, and the second minor hump due to Inverse Compton processes. The spectral break at about 70 MeV represents the transition to the regime where the quantum effects become relevant.

Energy losses and synchrotron spectral evolution

Another important point is that the synchrotron radiation implies an evolution of the spectrum of the emitted light with the increasing energy of the particles.

The relation between the kinetic energy of the particle and the emitted photons can be expressed through:

$$\frac{dE}{dt} = -\sigma_T c U_B \gamma^2 .$$

Expressing E as function of γ, one obtains

$$\frac{d\gamma}{dt} = -\frac{\sigma_T}{mc^2} c U_B \gamma^2 .$$

By integrating such equation, one can extract the solutions that describe how the electron energy changes with time. In an approximate form, it yields to

$$\gamma(t) = \frac{5 \cdot 10^8 \ s}{B\, t} ,$$

or equivalently,

$$t = \frac{5 \cdot 10^8 \ s}{B\gamma} \ .$$

This result means that particles with higher energy loose energy faster than the others. The energy losses produce a progressive bending of the emitted spectrum.

1.2.1.4 Inverse Compton radiation

The inverse Compton (IC) process is an interaction between an electron and a photon. When interacting, the electron looses part of its energy and transfers it to the photon, that is re-emitted at higher energy. This seems to be the most effective mechanism for production of VHE gamma rays.
According to the energy of the electrons and the photons, two regimes can be distinguished.

Thomson regime

The *Thompson regime* is considered a sort of non-relativistic description of the phenomenon, and happens when $E_\gamma E_e \ll m_e^2 c^4$. In this limit, the process has a constant cross-section of

$$\sigma_T = \frac{8}{3}\pi r_e^2 \ ,$$

where r_e is the electron radius.

Assuming a power-law distribution for the electrons with photon index γ_e, the up-scattered gamma-ray spectrum follows a power-law function as well with index $\gamma = \gamma_e + 1/2$ (Ginzburg & Syrovatskii, 1964). In this regime, the energy losses can be calculated as proportional to E_e^2.

Klein-Nishina regime

When the electrons energy becomes considerable high and reaches a relativistic velocity with $E_\gamma E_e \simeq m_e^2 c^4$, the process is considered taking place in the so-called *Klein-Nishina regime*. In this case, the cross-section $\sigma_{\rm KN}$ results:

$$\sigma_{\rm KN} = 2\pi r_e^2 \left[\frac{1+\epsilon}{\epsilon} \left[\frac{2(1+\epsilon)}{(1+2\epsilon)} - \frac{\ln(1+2\epsilon)}{\epsilon} \right] + \frac{\ln(1+2\epsilon)}{2\epsilon} - \frac{1+3\epsilon}{(1+3\epsilon)^2} \right] .$$

Conversely, when the relation is much above the previous limit with $E_\gamma E_e \gg m_e^2 c^4$, one can apply the Klein-Nishina approximation where

$$\sigma_{\rm KN} = \frac{\pi r_e^2}{\epsilon} \left[\ln(2\epsilon) + \frac{1}{2} \right] .$$

Assuming a power-law distribution for the electrons with photon index Γ_e, in the Klein-Nishina regime the resulting gamma-ray spectrum turns out to be considerably steeper with a photon index of $\gamma = \gamma_e + 1$. In this regime, the energy losses are independent from the electron energy and proportional to the density of photons.

Synchrotron Self-Compton process

In the study of blazars modelling, a very important role is played by an application of the inverse Compton scattering in the so-called *Synchrotron Self Compton* (SSC) process. This process takes place when the seed photons on the Inverse Compton scattering are synchrotron gamma rays emitted by the very same electron population. This mechanism allows the synchrotron radiation to reach the VHE regime and to explain the multi-wavelength SED of most of the blazars. More information is reported in Section 3.2.4.

1.2.2 Hadronic gamma-ray production processes

The production of gamma rays can involve also hadronic processes. When talking about hadronic processes, we usually refer to two channels: the interaction of a proton with a nucleon, or a proton against a photon (De Angelis, A. and Pimenta, M., 2018). Finally, I mention also the gamma-ray channel production related to the synchrotron light emitted by accelerated hadrons.

1.2.2.1 Proton-nucleon collisions and pion decay

When a proton collides with another ambient nucleon at sufficiently high energies (larger than the pion mass), the final state of the reaction is in generally mainly composed by pions, with the same probability between both neutral pions π^0 and charged pions $\pi^{\pm}$ (due to isospin symmetry).

Pion is a very common particle in astrophysics. It is the lightest particle in the hadrons family, and its decay is probably the dominant hadronic mechanism for gamma-ray production.

Such particles are unstable: while charged pions have a mean lifetime of about 26 ns, neutral pions have a much shorter mean lifetime of about $8.4\ 10^{-17}$ s. The reactions that summarize the decays are the following:

$$\pi^+ \rightarrow \mu^+ + \nu_\mu \ \text{ and } \ \mu^+ \rightarrow e^+ + \bar{\nu_\mu} + \nu_e \ ,$$

$$\pi^- \rightarrow \mu^- + \bar{\nu_\mu} \ \text{ and } \ \mu^- \rightarrow e^- + \nu_\mu + \bar{\nu_e} \ ,$$

$$\pi^0 \rightarrow \gamma + \gamma \ .$$

These reactions show that neutral pions decay directly into two gamma rays. Conversely, charged pions decay into muons and neutrinos. In the latter reaction the gamma rays are then produced due to the synchrotron emission related to muons and their consequent decay-produced electrons. Thus, in these reactions the products are three neutrinos for each charged pion and three neutrinos for every gamma ray.

1.2.2.2 Photo-production

The other reaction that can involve protons is the collision with an ambient photon. This process has a much lower cross-section of the proton-proton interaction (about by two orders of magnitude). For this reason, it is important in processes taking place in environments where the target photon density is much higher than the matter density, for example in active galactic nuclei (AGNs).

When protons are accelerated to relativistic velocities, they can reach the threshold for the $p\gamma$ reactions (e.g. Boettcher, 2010):

$$p + \gamma \rightarrow \pi^+ \ .$$

In this case, synchrotron-supported pair cascades (produced secondary pions, muons and electrons/positrons at ultra-high gamma-ray energies) will develop.

This acceleration process up to more than $E_p > 10^{19}$ eV requires high magnetic fields energies: for example, in order to keep the emission region size (constrained by the Larmor radius) smaller than the typical value used in the case of blazars of $R = 10^{16}$ cm (see Section 3.2.3.1), requires magnetic fields of the order of several tens of Gauss.

1.2.2.3 Synchrotron-produced gamma rays

Gamma rays can be produced also by simple synchrotron processes of protons and muons, additionally to the electron synchrotron process. Of course, the main problem is that such particles are much heavier than the electrons, and thus much more intense magnetic fields have to be present in order to accelerate them.

In particular, in the case of spectral energy distribution of blazars (see Section 3.2), the high-energy hump is probably mainly produced by direct proton and $\mu^{\pm}$ synchrotron radiation. Conversely, the low-energy hump is always dominated by synchrotron radiation from the primary electrons.

More information about hadronic blazar models is reported in Section 3.2.5.1.

1.3 Gamma-ray interactions

Even if photons are neutral particles and are not affected by the interstellar magnetic fields through their travel time from a certain source in the Universe, they suffer of absorption effects due to several different processes. Such processes mainly occur at certain energies, and for this reason photons are absorbed through one or the other process depending on their energy.

Here I summarize the main processes through which photons may interact.

1.3.1 Photoelectric absorption

The photoelectric effect is the emission of electrons (called photo-electrons) when light falls on a material. This effect is interpreted as the energy transfer from the light to an electron, that breaks its relation with the material atom nucleus and implies the electron ejection from the atom itself. This process dominates at photon energies below about 100 keV, and requires the presence of matter. An example of such bound–free absorption is observed in most of the spectra of X-ray sources at energies below 1 keV, and represents a source of opacity in the stellar interiors (e.g. Longair, 2002).

1.3.2 Dust extinction

When travelling through long distances in the Universe, light can also pass through dense region of interstellar medium. This implies that it collides with material (dust), and it can be partially absorbed. This process of interaction between light and dust depends on the wavelength of the former and the size of the latter. The complete extinction process is in general related to the optical radiation. Then, the absorption rapidly decreases in the infra-red band, and then becomes negligible (e.g. Longair, 2002).

Close to optical wavelengths of the light, the grain size of the dust plays an important role. When the typical grain size is relatively small (a < 0.1 μm), absorption dominates the extinction and the incident light energy is transformed into ambient thermal energy. Conversely, when the grain size becomes larger a > 0.1 μm, the scattering dominates over the extinction. This process implies no more complete extinction of the light, but scattering. In particular, the scattering of light near the X-ray wavelengths becomes important (e.g. Lv et al., 2011; Covino et al., 2013), and produces X-ray halos (as first discovered by Overbeck 1965).

1.3.3 Compton scattering

High-energy photons, when not photoelectrically absorbed, may interact with a low-energy electron via Compton scattering. This process causes an energy transfer to the electron and reduces the energy of the photon through a shift of its wavelength.

Compton scattering occurs above all in the energy range from about 0.1 MeV to few MeV, and this implies that X-rays are mainly affected by such process (but also gamma rays are affected).

1.3.4 Pair production

Another important interaction that plays a crucial role in high-energy astrophysics is the pair production process (that is the inverse process of the pair annihilation of Section 1.2.1.2).

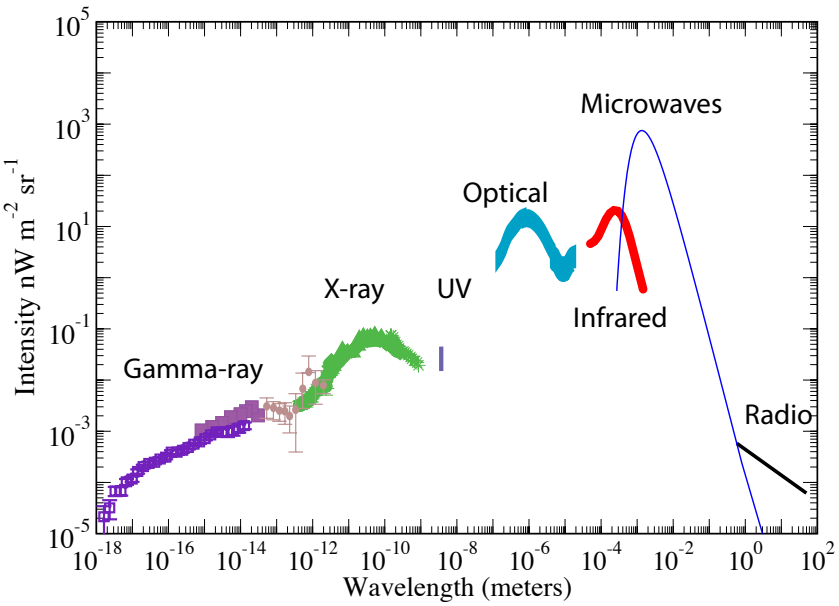

Figure 1.6: *Intensity of the extragalactic background light (νI_ν in units of $nW\ m^{-2}\ sr^{-1}$) as a function of the wavelength in meters, taken from Cooray (2016). In this figure, they combine the existing measurements from the literature to highlight the best determined estimates for the background from gamma-ray to radio.*

The interaction between a couple of photons results in the production of an electron and a positron, and produces an absorption of the intrinsic light emitted by the source of interest that is detectable from Earth.

This effect is stronger when photons with E > 100 GeV interact with lower energy photons, as it can be seen by the following relation that expresses the peak of the cross-section of the pair production:

$$E_{\gamma_1} E_{\gamma_2} (1 - \cos\theta) \sim 2\,(m_e c^2)^2 \ ,$$

where E_{γ_1} and E_{γ_2} are the energy of the seed photons that are colliding with an angle θ, and $m_e = 0.511$ MeV is the electron mass.

This implies that the highest cross-section (and hence the highest probability of absorption) for a gamma ray of about 100 GeV takes place with a photon around the Infrared (IR) and Ultraviolet (UV) bands. Such photons may be coming for example from diffuse extragalactic photon fields like the Extragalactic Background Light (EBL), that is the extragalactic diffuse photon emission from optical to infrared that is associated with star light emission and its reprocess by dust filling the cosmos respectively (Hauser & Dwek, 2001). The absorption effects follow the interaction

$$\gamma_{\rm VHE} + \gamma_{\rm EBL} \rightarrow e^+ + e^- \ ,$$

and result in the reduction of the flux that depends on the energy and on the distance of the source.

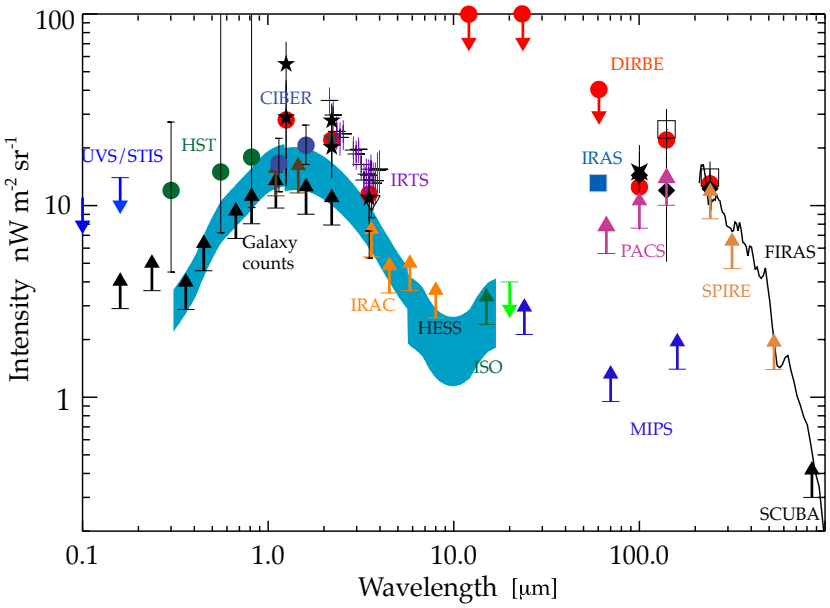

Figure 1.7: *A collection of the most updated measurements of the cosmic optical and infrared background light from 0.1 to 1000 μm, taken from Cooray (2016). A new focus in the 0.1-10 μm range has been published in Fermi-LAT Collaboration et al. (2018).*

EBL at different wavelengths

The EBL has been measured with different accuracy in the different spectral energy regions, reported in **Figure** 1.6 in Cooray (2016). Different direct and indirect approaches are needed in order to investigate it in the whole energy band. The only spectral region where a direct measurement of the EBL was possible is at the longest wavelengths λ of the sub-millimetre band (between $200 < \lambda < 900$ μm). This is possible because in this band the local foreground emissions are minimal.

Conversely, at all shorter wavelengths, the direct measurement of EBL is prevented by the overwhelming dominance of local emitters within our Solar system. Their emission is so intense that their subtraction to obtain the net effect of EBL is almost impossible, and huge uncertainties cannot be avoided.

The indirect measurement of EBL in this region is performed by studying the results of its interaction with the HE and VHE photons emitted by active galactic nuclei (AGNs). This study has been performed especially in the blazar population (see Chapter 3 for more information), with main contributions given by the *Fermi*-LAT telescope (see Section 2.3) and the Cherenkov telescopes (the last contribution from the MAGIC Collaboration is Acciari et al. 2019).

The $e^+ - e^-$ pair-production process taking place between the EBL and the gamma-ray photons produced by blazars produce a typical cut-off on the observed spectrum of these objects. This cut-off depends on the energy of the photons and on the distance of the source: higher the photon energy and the redshift of the source, higher is the absorption effect. By studying this spectral cut-off on a sample of sources at different distances, constraints on the EBL intensity can be inferred (depending on the assumed spectrum of the EBL radiation) and it is possible to map the time evolution of the cosmic photon number density, hence

constraining the history itself of the EBL photon production. Thanks to the ten years of observations performed by the *Fermi* satellite and its wide sky and spectral coverage, the evaluation of the EBL intensity and time evolution was performed in the UV-optical (range $0.1 < \lambda < 3$ μm). I report in **Figure** 1.7 one of the most recent plots representing the EBL spectrum at infrared wavelengths and the different measurements or upper-limits set by the different instruments (for more details, see Cooray 2016).

The remaining wide region between 3 and 300 μm is not accessible to the previous direct measurements through the study of high-energy photons. In this region, the dominance of the Interplanetary Dust emission (dusty particles illuminated by the Sun and thermally emitting at about 200 K) and the infrared foreground from the Galactic dust precludes the measurement of EBL. The huge background produced by these processes preclude the infrared telescopes to detect extended emissions, and so far only very luminous and numerous sources at high redshift have been detected and identified.

Thus, in order to measure the total infrared EBL between 3 and 300 μm, only indirect ways can be used. One of the most interesting indirect measurement of the EBL at IR wavelengths is through the study of its effect on the VHE gamma rays of blazars. This process can be investigated by the Cherenkov telescopes, and constitute an interesting study above all when the sources present high redshift and are well detected spectra up to several hundreds of GeV. An example of this approach is reported in Acciari et al. (2019).

In this branch of indirect EBL measurements, blazars with extremely hard spectra like the EHBLs play a particular important role and might help in disclosing the nature of EBL. One of these unexplored methods is reported in Section 4.4.1.

1.4 Gamma-ray emitters

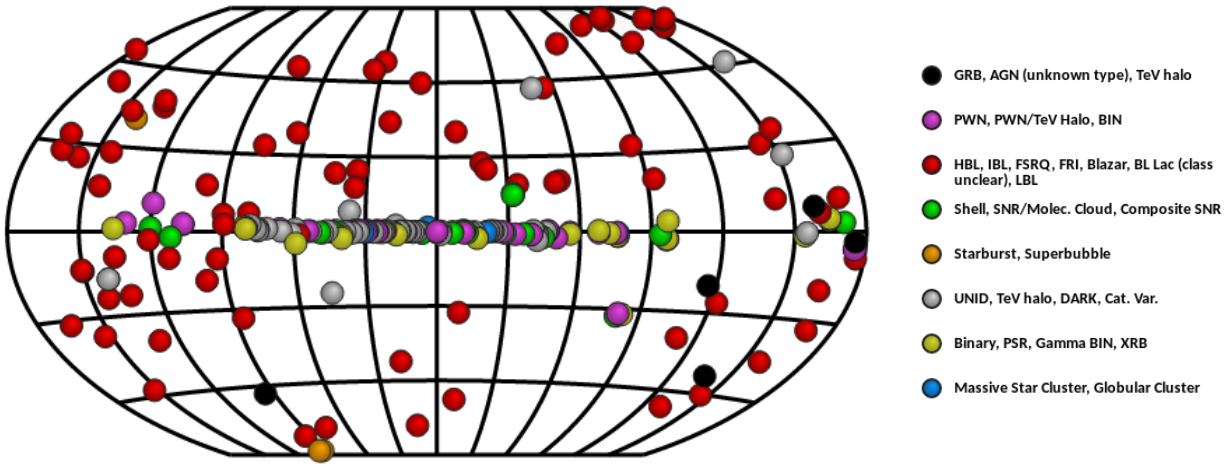

Figure 1.8: *Map of the 234 gamma-ray emitters of photons above 100 GeV in the Universe detected up to September 2019. The sources are indicated as circles, with colors representing different types of emitters. Adapted from* http://tevcat2.uchicago.edu/.

Up to September 2019, the sky in TeV gamma rays – reported in **Figure** 1.8 – counts about 234 sources. The known gamma-ray emitters can be subdivided in two main groups, according to their galactic or extragalactic nature.

1.4.1 Galactic emitters

Here I report some of the main galactic emitters of gamma rays.

Supernovae remnants
The supernovae remnants are the residuals after the explosion of supernovae. The emitted CRs are accelerated in the shock waves through first order Fermi acceleration mechanism, and then are supposed to interact with the nuclei in the interstellar medium, producing gamma rays.

Gamma-ray binaries
They are binary systems composed by a star and a compact object, like a black hole or a neutron star. The radiation produced by such systems extends up to the gamma-ray regime. Their emission can be explained by two models: microquasars and pulsar wind scenarios. In the microquasar scenario, material from the companion falls towards the compact object producing, depending on the accretion rate, relativistic jets where particles are accelerated and emitting gamma rays in the IC interaction with the stellar wind. In the pulsar wind scenario, the VHE emission arises from the interaction of the compact object wind with the stellar wind. Up to now, only few gamma-ray binaries have been detected, and all of them have been interpreted with the pulsar wind scenario. Nevertheless, gamma rays from X-ray binaries such as Cygnus X-1 and Cygnus X-3 ranked as microquasars have been detected.

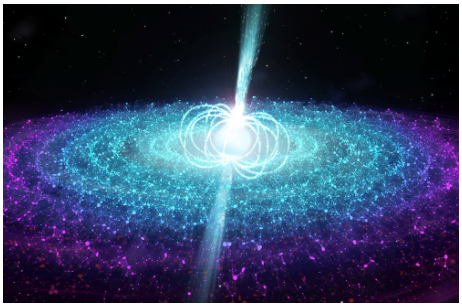

(a) Representation of a pulsar and its relativistic jets.

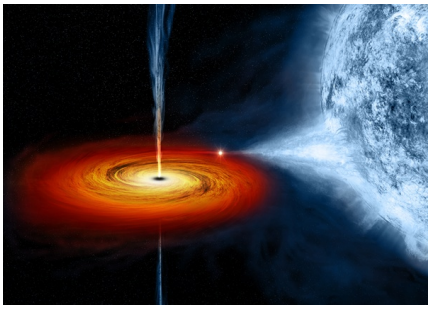

(b) Representation of an example of binary system.

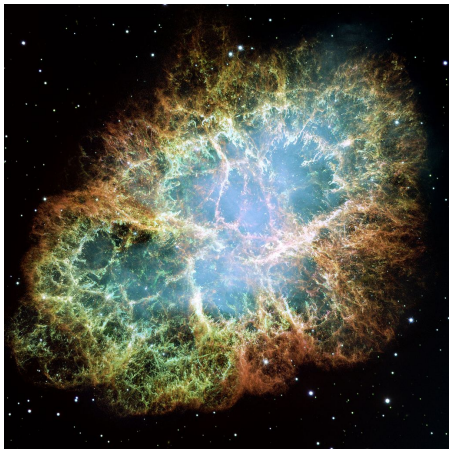

(c) The Crab Nebula as an example of supernovae remnant.

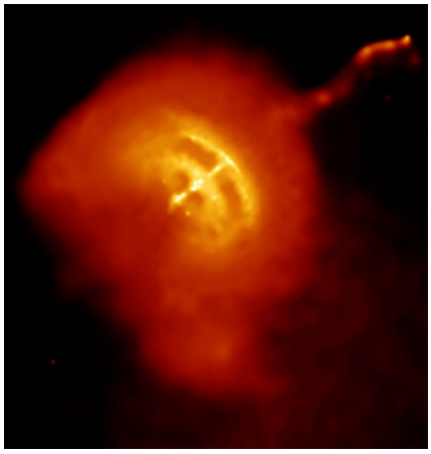

(d) The Vela Pulsar and its surrounding pulsar wind nebula.

Figure 1.9: *Some publicly-available pictographic representations and images of galactic gamma-ray emitters.*

Pulsars

They are defined as highly magnetized rotating neutron stars. The magnetic fields around the pulsars increase in density around the poles (that are not necessarily directed along the rotation axis), and there particles can be accelerated and produce very narrow gamma-ray beams. Since at the collapse of the supernova the star dramatically reduces its radius, it acquires high rotational speed in order to maintain the angular momentum. This fast rotation with not-aligned rotational axis and magnetic fields lines produces a pulsation when the beam emission is crossing our line-of-sight. The probably most famous pulsar is the Crab pulsar, first detected by MAGIC (Aliu et al., 2008) and recently detected up to TeV energies (Ansoldi et al., 2016). Besides Crab, only Vela pulsar has been detected in gamma rays (e.g. a more updated information in H.E.S.S. Collaboration et al. 2018).

Pulsar wind nebulae

When the pulsar winds interact with the interstellar medium, magnetized clouds of relativistic particles are produced and gamma rays are possibly produced through IC scattering of ambient photons by accelerated electrons.

1.4.2 Extragalactic emitters

Here I report some of the main extragalactic emitters of gamma rays.

Active galactic nuclei
They are galaxies that present electromagnetic activities coming from their nuclear regions. Such activity is supposed to be produced by hot matter rotating around a super-massive black hole located in their center. Part of the matter is probably re-emitted and accelerated through relativistic jets perpendicular to the accretion disk formed by collimated magnetic fields. More information is reported in Chapter 3.

Starburst galaxies
Starburst galaxies are galaxies with a high star formation rate, and thus with a large supernova explosion rate. Supernova explosion is supposed to produce high quantities of CRs, due to its interaction with the surrounding medium and the high energies involved in the explosion process.

Gamma-ray bursts
Gamma-ray bursts (GRBs) are extremely luminous transient events that occur at cosmological distances and are able to release an incredibly large amount of radiation energy in a very short time.

There are mainly two kinds of GRBs, depending on their duration

1) short GRBs: lasting less than 2 s;

2) long GRBs: those lasting from more 2 s up to several hundreds of seconds.

The difference duration of the GRBs is though to be related to their different origin: short GRBs are probably originated from the mergers of compact objects, while some long GRBs are probably due to supernovae collapses. The variability over time of their energetic flux emission is supposed to be related to the contribution of very compact objects like black holes and neutron stars to the processes.

The extreme energy released during the event, their short duration, and their origin, make the GRBs the most violent explosive events in the Universe. They happen suddenly and unpredictably with no repetition from random directions in the sky as flashes at different wavelengths.

At least two different phases in the GRBs are present: the first non-thermal emission is at hard X-ray energies and it is called prompt phase, and the subsequent phase is called afterglow, a much fainter and fading emission ranging in different energy bands from radio up to gamma rays. This phase can be detected in the different wavelengths from hours up to several weeks after the prompt event, and in some cases can lead to the identification of the host galaxies of the GRB, that can allow the astronomers to estimate the redshift at which the event took place.

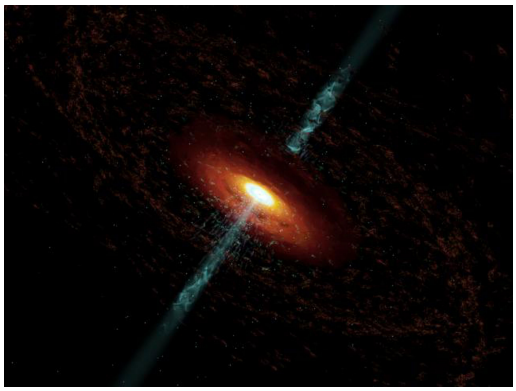

(a) Active galactic nucleus.

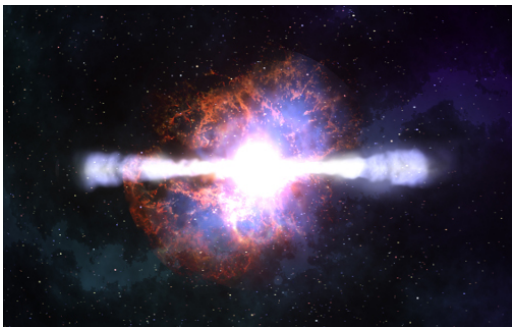

(b) Gamma-ray burst.

(c) The Antennae Galaxies are an example of a starburst galaxy. Credits: NASA/ESA.

(d) NGC 5264, and example of dwarf galaxy.

Figure 1.10: *Some publicly-available pictographic representations and images of extragalactic gamma-ray emitters.*

1.4.2.1 First detection of a GRB at TeV energies

The MAGIC telescopes (more information on the instruments mentioned in this Section is reported in Chapter 2) are designed with low-energy threshold and fast repointing capabilities in order to observe transient events like GRBs as a primary objective.

After fifteen years of operations, on January 14$^{\text{th}}$ 2019, the MAGIC telescopes detected the GRB 190114C event, probably the most important transient event ever detected at TeV energies. It was first identified as a long GRB by the *Swift*-BAT instrument and the *Fermi*-GBM instrument at 20:57:03 Universal Time (hereafter T_0). The afterglow following the prompt emission was detected at all wavelengths from radio up to gamma rays, and there was a fast estimation of the redshift that was reported as being $z = 0.4245 \pm 0.0005$[a].

Triggered by the *Swift*-BAT alert, the MAGIC telescopes – thanks to the automatic repointing of the telescope specifically allowed by the light weight of their structure – observed the GRB 190114C event from $T_0 + 57$ seconds until $T_0 + 15912$ seconds. At the moment in which the telescopes started observations, the camera was flooded by signal and an off-line analysis reported the detection of gamma rays above 300 GeV. The total significance of the event was reported in more than 50 σ, marking this event as the first detection of a GRB at energies exceeding 100 GeV (Mirzoyan, 2019b).

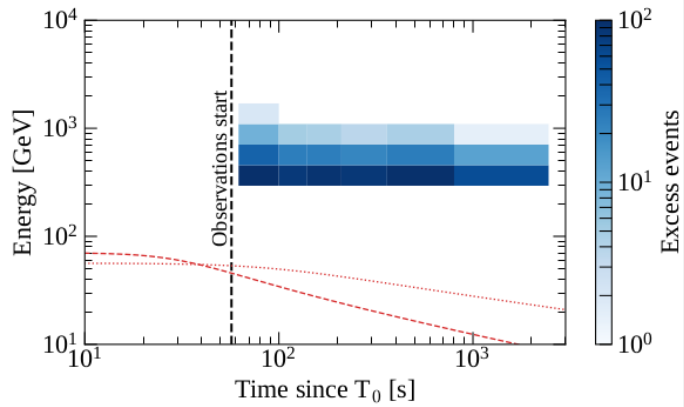

Figure 1.11: *Distribution of TeV gamma rays in energy versus time for GRB 190114C. The number of photons detected by MAGIC in each bin of energy and time are color-coded. Figure taken from MAGIC Collaboration (2019c).*

[a] https://gcn.gsfc.nasa.gov/gcn3/23695.gcn3

Light curve

The GRB event followed by MAGIC is reported in the light curve in **Figure** 1.12 taken from MAGIC Collaboration (2019c), where the EBL-corrected intrinsic flux in the energy range 0.3 - 1 TeV has been reported. An interesting feature is that it can be fitted with a simple power-law function

$$F(t) \propto t^{\beta} \quad \text{with} \quad \beta = -1.60 \pm 0.07 \,,$$

with no clear evidence of cut-off. Considering that also the light curves in the keV and GeV bands show similar slopes and that the prompt phase implies in general an irregular variability, this feature may indicate that most of the observed emission is associated with the afterglow phase.

Additionally, the flux initially observed reports an equivalent isotropic luminosity of $L \sim 3 \times 10^{49}$ erg s^{-1} in the range 0.3 - 1 TeV, and makes this event the most luminous source known above 0.3 TeV.

Finally, the MAGIC Collaboration reported in **Figure** 1.11 the distribution of the events depending on their energy and the time they were observed.

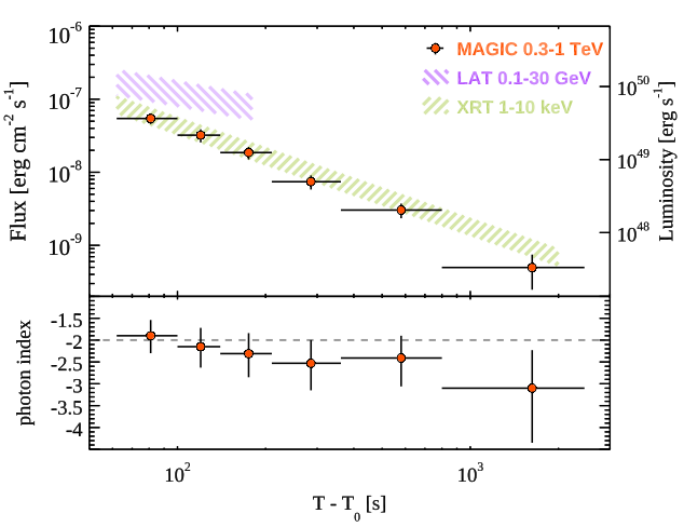

Figure 1.12: ***Top panel:*** *Light curves in units of energy flux (left axis) or apparent luminosity (right axis), for MAGIC at 0.3 - 1 TeV (red symbols),* Fermi-*LAT at 0.1 - 30 GeV (purple band) and* Swift-*XRT at 1 - 10 keV (green band). For MAGIC, the intrinsic flux is shown, corrected for EBL attenuation from the observed flux.* ***Bottom panel:*** *Temporal evolution of the power-law photon index determined from time-resolved intrinsic spectra at 0.3 - 1 TeV. Figure taken from MAGIC Collaboration (2019c).*

Spectral energy distribution

The MAGIC Collaboration reported in **Figure** 1.13 the spectral energy distribution of the event. In the energy range 0.2 - 1 TeV, it can be fitted with a simple power-law with photon index

$$\alpha_{\rm obs} = -5.43 \pm 0.22 \ ,$$

that represents one of the steepest spectra ever observed for a gamma-ray source. By considering the intense EBL absorption (by a factor ~ 300) that should lower the flux of the GRB event at about 1 TeV, in this energy range there were a lot of photons detected. Once EBL-deabsorbed, the intrinsic spectrum results with a power-law index of

$$\alpha_{\rm int} = -2.22^{+0.23}_{-0.25} \ .$$

The EBL-deabsorbed spectrum confirms the absence of spectral cut-off, and the equal distribution of energetic events over the energy range 0.2- 1 TeV. This implies that this event may be attributed to the afterglow phase.

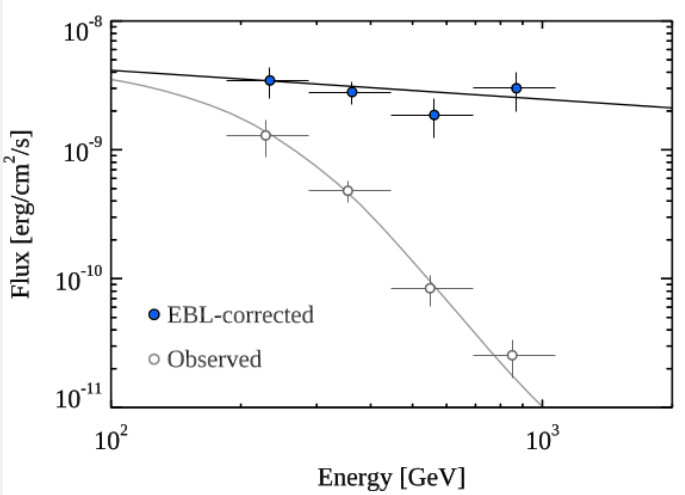

Figure 1.13: *MAGIC spectrum above 0.2 TeV averaged over the period between T_0 + 62s and T_0 +2454s for GRB 190114C. The observed spectrum is reported in grey open circles, and the intrinsic spectrum corrected for EBL attenuation in blue filled circles. Figure taken from MAGIC Collaboration (2019c).*

1.4.3 Exotic gamma-ray emitters

A third category of gamma-ray emitters may be attributed to sources that at the moment are unknown. One of the most important examples is the dark matter (DM). In fact, some dark matter models foresees gamma-ray emission extending up to the VHE range. This gamma-ray radiation might be produced by annihilation of two particles of dark matter or its decay, and this radiation might be detected by the current Cherenkov telescopes.

Such signals might be coming from cosmic places where dark matter is supposed to be particularly concentrated, like the galactic center, dwarf spheroidal satellite galaxies, intermediate mass black holes, and cluster of galaxies.

During the last fifteen years, big efforts have been carried our to catch the signature of DM annihilation with the current generation of IACTs (see e.g. Doro, 2014). So far, no VHE gamma-ray emission has been detected yet from any potential DM source, and constraining upper limits have been put for example on the WIMP annihilation cross-section and on their mass. As DM candidates are assumed to be WIMPs (weakly interacting massive particles), they could produce very low flux of gamma rays, and the highly improved sensitivity of the next generation of IACTs represented by the forthcoming CTA will improve the possibility to detect it.

1.5 Gamma-ray detection techniques

The detection of gamma rays is a relatively recent field of astronomy. The main problem is that they are absorbed by the atmosphere, and this does not allow for a direct detection from ground based observatories. Additionally, their density rapidly decreases with energy, and this implies that several techniques are needed in order to detect them through their entire spectrum covering several orders of magnitude in energy.

Up to now, there are mainly three methods to detect gamma rays:

Satellites: they are the first natural solution to the direct detection of gamma rays considering the fact that they do not reach the ground on Earth. At the moment, the most important gamma-ray satellite is *Fermi* in **Figure** 1.14a, with its two instruments LAT and GBM (see details in Section 2.3). The dominant mechanism for the detection of gamma rays above about 30 MeV is pair production. These detectors present a wide field of view (FoV) that observe during almost 100% of their duty cycle. Due to the reduced collection area that detectors on-board satellites have (about 1 m^2), this technique provides information from MeV to a few hundred GeV. In order to go at higher energies, we would need more extended collective areas (of orders of some hundreds of squared meters), but the current technologies do not allow for launching such big satellites.

Water Cherenkov arrays: this technique is based on the fact that secondary particles produced by the incoming VHE gamma rays (at energies greater than about 100 GeV) can reach the ground. Such particles produce Cherenkov light when they cross the water tanks (as reported in **Figure** 1.14b), and their incoming direction and energy can be estimated through the study of the development of the shower through several hundreds of water tanks spread above some squared kilometers on the ground. They are characterized by full duty cycles (since also day-time observations are possible) and large FoV.

Imaging Atmospheric Cherenkov telescopes (IACTs): this technique was applied on telescopes in the late 80's in order to overtake the impossibility to detect gamma rays above some hundreds of GeV from the spacecrafts. It is based on the detection of Cherenkov light produced in the electromagnetic cascades originated by the interaction of a primary gamma ray with the nuclei of our atmosphere. Such Cherenkov telescopes use the atmosphere as indirect detector of gamma rays: this increases the collection area up to several squared kilometers, and therefore the reachable energy range considerably increases. In turn, these telescopes cannot be operated during daytime, and only few of them can be operated during moderate moon time (e.g. MAGIC in as reported in **Figure** 1.14c, see Section 2.4).

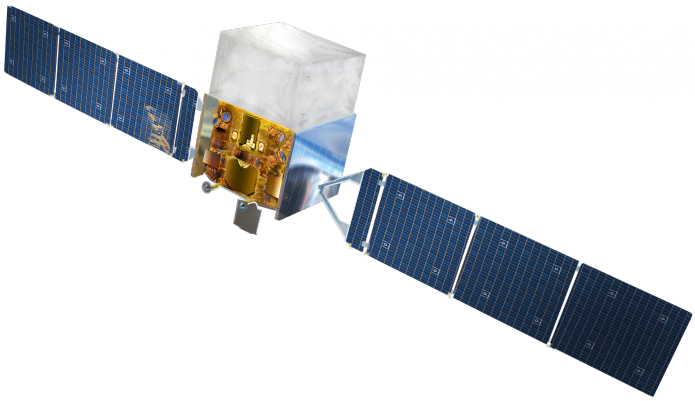

(a) The *Fermi* satellite.

(b) The HAWK telescope.

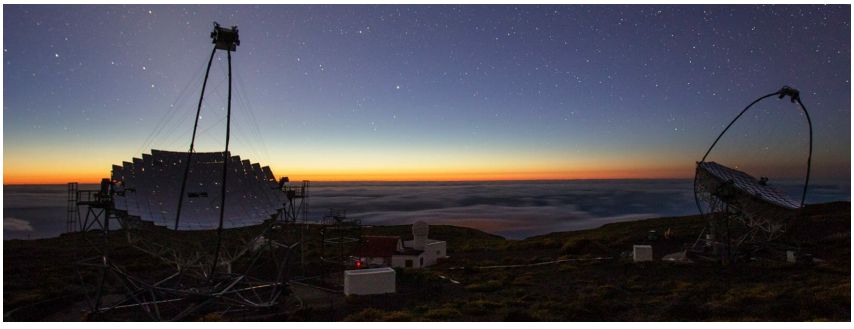

(c) The MAGIC telescopes.

Figure 1.14: *Some examples of both gamma-ray direct and indirect detectors.*

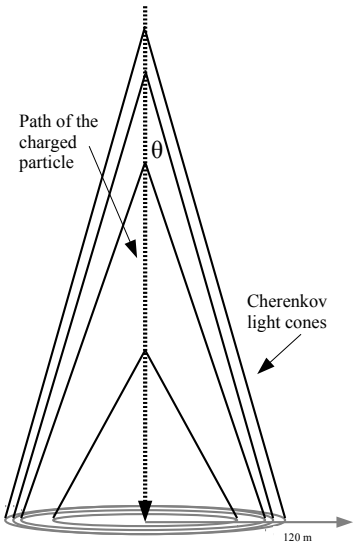

Figure 1.15: *The superposition of the Cherenkov light rings produces a circle on the ground, the so-called Cherenkov light pool.*

1.5.1 Gamma rays and the Cherenkov technique

Gamma rays are the most energetic radiation of the electromagnetic spectrum. As human beings, the interaction between our bodies and such energetic radiation would be fatal. Fortunately, the Earth's atmosphere protects us by making such radiation interact with the molecules of the air. On the other side, this means that we cannot study such gamma rays directly from Earth. The first solution would be to use detectors on-board of satellites, like the *Fermi* telescope. Nevertheless, due to weight and volume limitations, they can only support detectors with small collection area. Therefore, they cannot provide results for energies above some hundreds of GeV.

The solution in order to study gamma rays with energies higher than about 50 GeV is the indirect measurements by means of Cherenkov telescopes. Such telescopes use the Cherenkov light of secondary particles produced by the interaction of gamma rays with the atmosphere, that will be presented in the first part of this Section.

1.5.1.1 Cherenkov light

The interaction between a VHE gamma ray and the molecules of the air of the atmosphere can be imagined as a crush: the gamma ray produces cascades of highly energetic particles, called Extensive Air Showers (EAS). Such cascades are composed by charged and neutral particles, and travel faster than the speed of light in the atmosphere. This implies that they produce Cherenkov light through their path to the ground. The existence of this type of light was proposed by the Soviet physicist Pavel Alekseyevich Cherenkov (Cherenkov, 1934) who, along with Ilya Frank and Igor Tamm, received the Nobel prize in 1958 for the discovery and interpretation of the Cherenkov effect.

Such light, whose wavelength ranges between 300 and 500 nm and typically peaks at about 320 nm (i.e. in the UV band), evolves in light cones with an angular aperture θ. The angle θ

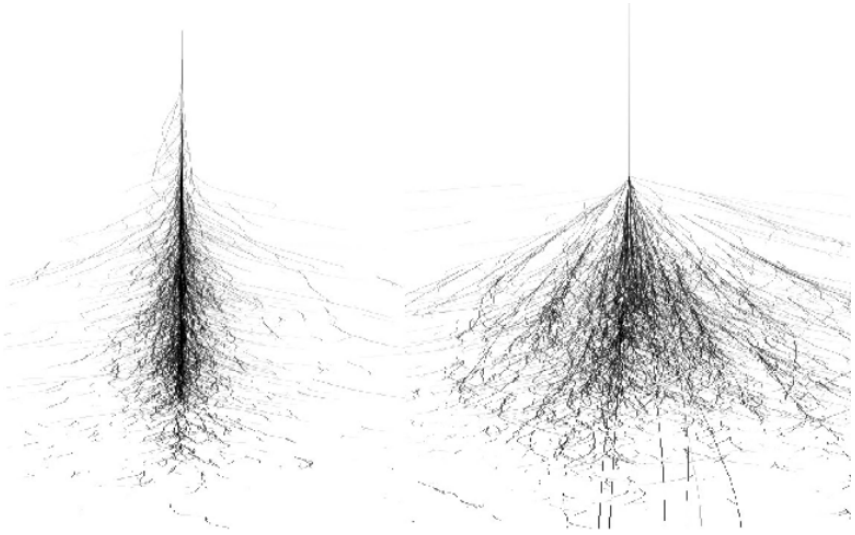

Figure 1.16: *Left: MC simulation of an EM cascade initiated by gamma rays. Right: MC simulation of a hadronic cascade initiated by protons. Figure taken from Völk & Bernlöhr (2009).*

- so-called *Cherenkov angle* - follows the relation

$$\cos\theta = \frac{c'}{v} = \frac{c}{vn(\lambda)} \ ,$$

where $c' = c/n$ is the speed of light in the material and $n(\lambda)$ is its refractive index, whose value varies with the wavelength λ of the Cherenkov light. In the air, the average value of the Cherenkov angle results to be about 1 degree. The superposition of the Cherenkov light rings of several narrow light-cones produces a full circle of light at the ground (the so-called Cherenkov light pool) with a radius up to about 120 m from the core of the cascade. light of the Cherenkov pool can be collected and studied with the Cherenkov telescopes.

However, the Cherenkov light collected at the ground is affected both by the zenith angle at which it interacts with the atmosphere and by the transmission losses in the atmosphere. This effects imply that the emitted and the observed radiation spectra turn out to be different. The dependency on the zenith angle - meaning that the higher the angle, the higher the attenuation - is obviously affecting the cascade because the fraction of atmosphere that it has to go through is much thicker, and consequently the interaction rate is higher. The main consequence is that only the particles with the higher energies can be detected by the Cherenkov telescopes at high zenith angle observations, and the peak of the Cherenkov radiation spectrum shifts to larger wavelengths.

1.5.2 Extensive air showers

The Cherenkov light can be produced by cascades initiated both by gamma rays and by hadrons (mainly protons). Since they are deeply different in their development through the atmosphere, we study their structure in this Section.

Electromagnetic showers

When a cascade is initiated by a gamma ray, the main process that converts the highly energetic gamma ray into the cascade itself is the bremsstrahlung effect (see Section 1.2.1.1). If the energy of the gamma ray entering the atmosphere is $E > 20$ MeV, it can interact with the air nuclei and be converted in a $e^+ - e^-$ pair. Such $e^+ - e^-$ particles suffer bremsstrahlung effect above a critical energy that in air is $E_c = 86$ MeV, which is the energy for which the energy losses by bremsstrahlung and ionization are equal. The energy losses are converted into photons that are still very energetic, and such photons can undergo further pair production. Such recursive process produces the so-called electromagnetic shower (reported in the left panel of **Figure** 1.16).

The energy losses dE for an electron due to bremsstrahlung are expressed by

$$\frac{dE}{dx} = \frac{-E}{X_{0,e}} \, ,$$

where $X_{0,e} = 37.2$ g cm^{-2} is the radiation length for an e^+ or e^- in the air and then mean free path (average distance travelled between collisions) of gamma rays due to pair creation is $X_{0,\gamma} = 7/9 X_{0,e}$.

Consequently, the particles in an EM shower are not particularly affected by scattering effects, and turn out to produce quite symmetric cascades (see left plots on **Figure** 1.16). Additionally, since the cross-section for interaction between gamma rays and atmospheric nuclei is weakly dependent on the gamma ray energy, all the showers starts forming at about 20-30 km above the sea level. At each step of the recursive process of conversion between photons into pairs, the number of particles is doubled and their energy is the half of the energy of the previous particle producing the interaction. When the energy of the $e^+ - e^-$ pairs reach again E_c, the cascade stops, the shower is disrupted and the number of particles reaches its maximum. Such height above the sea level is known as height of the shower maximum ($H_{\max}$), and it is inversely proportional to the logarithm of the energy $H_{\max} \propto 1/ln(E)$ of the primary gamma ray.

Hadronic showers

In this section we study the case of an EAS initiated by an hadron as primary particle. Such first interaction with an atmospheric nuclei is governed by the strong force, and the main products of hadronic processes are pions (about 90%, in roughly equal proportions between π^0 and $\pi^\pm$), kaons (10%), and few light baryons (like protons and neutrons, and corresponding antiparticles).

When hadrons are again produced, they can undergo further collisions, making the shower grow until the energy per nucleon reaches the minimum energy required for pion production decay (about 1 GeV).

Additionally, pions can decay into photons and muons through the following relations:

$$\pi^0 \rightarrow \gamma + \gamma \, ,$$

$$\pi^+ \rightarrow \mu^+ + \nu_\mu \;\text{ and }\; \pi^- \rightarrow \mu^- + \bar{\nu_\mu} \, ,$$

generating secondary electromagnetic showers and muon-initiated showers. Also muons can decay through the following relations:

$$\mu^+ \rightarrow e^+ + \nu_e + \bar{\nu_\mu} \quad \text{and} \quad \mu^- \rightarrow e^- + \bar{\nu_e} + \nu_\mu \ .$$

The increased number of involved processes and the possibility of producing secondary cascades imply that the hadronic cascades are much more scattered with respect to the electromagnetic ones, as illustrated in the right panel of **Figure** 1.16.

Additionally, the strong interaction involved in such processes implies that the transverse momentum of secondary hadrons is larger than that of leptons in electromagnetic showers. This fact implies that the hadronic showers are much wider with respect to the electromagnetic ones with respect to their vertical development.

Another important point in order to differentiate between electromagnetic and hadronic cascades is the timing of the showers. While gamma-ray initiated showers develop in less than 3 ns for impact parameters smaller than the hump (the region where the Cherenkov photon density is highest), the hadron-initiated ones take more than 10 ns to develop.

1.5.3 Imaging atmospheric Cherenkov technique

The imaging atmospheric Cherenkov technique is the method we use to indirectly detect gamma rays not detectable from the space. This technique collects the Cherenkov light emitted by the electromagnetic cascades initiated by the gamma rays when hitting the atmosphere. Such indirect method of detection combines the spatial and the temporal information of the measured light to produce images of the showers and differentiate between hadron and gamma-initiated showers. The main point in this process is to build Cherenkov telescopes with large collective area and able to differentiate high-resolution time differences.

The light from the cascades is collected and sent to the pixelized cameras equipped with very fast response pixels. The trigger system in this process plays an important role due to the high level of noise: the events are rapidly selected (the shorter the time, the less Night Sky Background that is integrated) and recorded.

The main problem of using high area collectors is that they affect the high-precision time measurements that have to be performed. In fact, the arrival timing difference to the camera plane of light reflected by different segments of the mirror becomes important. The use of parabolic reflectors is important because they are isochronous (although they have large coma aberration for off-axis angles), and reduce the difficulties in collecting rapid signals.

Finally, another important feature of the Cherenkov telescopes is that they are usually built as system of telescopes. When there are more than one telescope, the reconstruction of the direction of the primary gamma ray is much simpler and less affected by errors. The use of such telescopes in stereoscopic mode allow also for a better discrimination about the signals, recording only the events triggered by more than two telescopes in a given time window.

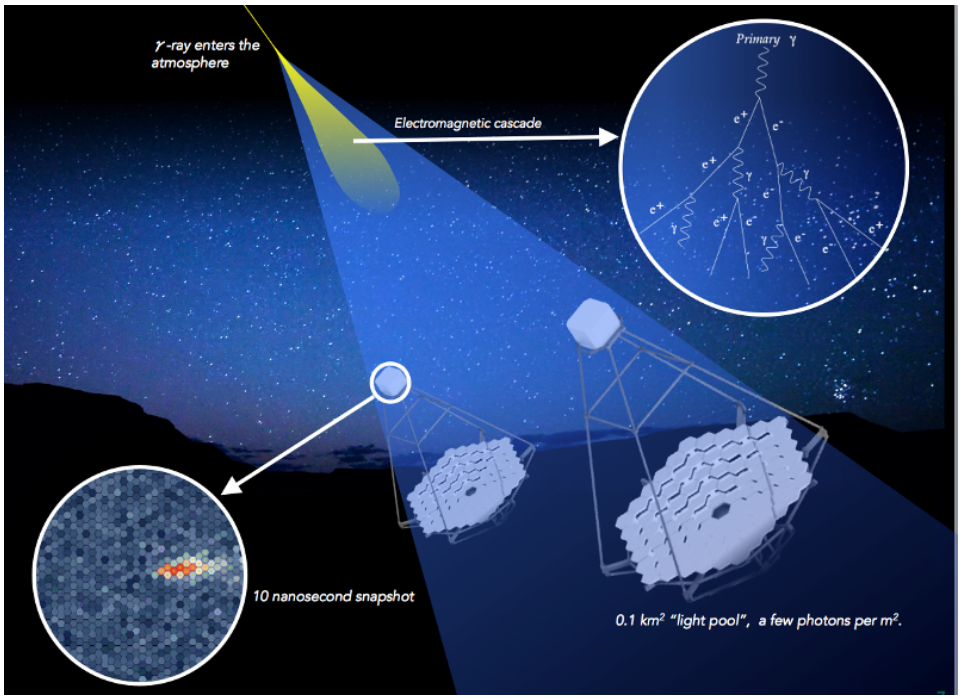

Figure 1.17: *Sketch of the imaging atmospheric Cherenkov technique. The Cherenkov light from the cascade is reflected by the mirrors and collected in the camera. Modified image from* www.cta-observatory.org.

1.6 Multi-wavelength and multi-messenger astrophysics

1.6.1 Multi-wavelength astrophysics

During the last decades, the scientific community has put major efforts on the development of experiments able to cover all the electromagnetic wavelengths. Nowadays, we are experiencing an era in which we are eventually able to observe a single astrophysical source with different observatories at the same time, gathering the information coming from each of them.

Several astrophysical objects are known multi-wavelength emitters. The most famous ones are the AGNs, to which a major part of this Thesis is devoted. The light emitted by these objects, thanks to the contribution of different emission processes, covers the whole electromagnetic spectrum from radio up to gamma rays. The correlation between the different energy bands at which the light is emitted implies the necessity to study such objects with a complete dataset containing all the information coming from each wavelength. A typical example, that will be studied in Chapter 3, is the spectral energy distribution of blazars. An example is reported in **Figure** 1.18, where a wide multi-wavelength observational campaign allowed to constrain the emission of the blazar Mrk 421 through almost the whole electromagnetic spectrum.

The study of extreme blazars, the main subject of this Thesis (reported in Chapters 4 and 5), is another good example of the importance of a multi-wavelength approach. As I will present in Chapter 4, the spectral energy distribution of the objects in this class is similar through all the wavelengths except for the TeV gamma-ray band, where they show crucial spectral differences. Only the multi-wavelength approach allows us to detect such differences,

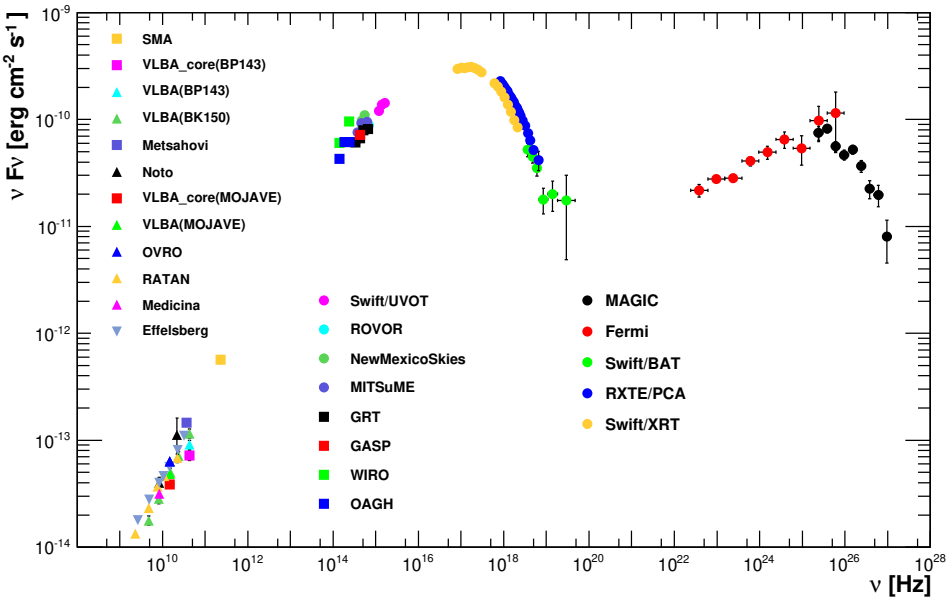

Figure 1.18: *The typical blazar SED of Mrk 421 during a multi-wavelength campaign reported in Abdo et al. (2011b).*

and then to use them to infer the physical mechanisms behind different sources.

However, the multi-wavelength approach presents also several difficulties. For example, when dealing with different instruments and observatories, we have to manage their different properties:

- the covered energy band, that has to match the one we need;
- the sensitivity as a function of the energy and of the different source;
- the data distribution in the case of telescopes (survey or pointing mode);
- their availability for observations (observational proposals or target of opportunity request);
- the data policy;

among many others.
This implies that, in order to complete the broad-band SED of a source we are studying, we cannot always use the best instruments in a determined energy range. For example, in the case of extreme blazars it is particularly useful to constrain their peak emission in the hard X-ray band. The current best instrument to cover that energy band is the *NuSTAR* satellite (Harrison et al., 2013), but it is very difficult to obtain simultaneous observations with it. For this reason, we can usually constrain that emission in hard X-rays by using the *Swift* observatory (BAT instrument) that, though with lower sensitivity with respect to *NuSTAR*, it can easily provide simultaneous observations via target of opportunity request (generally approved). For more information about these instruments, see Chapter 2.

1.6.2 Multi-messenger astrophysics

During the last few years, we have witnessed the creation of experiments able to detect physical phenomena that up to few decades ago were considered the most long-standing dreams of astronomers and astrophysicists: gravitational waves and neutrinos.

In 2017, we experienced a step further in astrophysics. The discovery of the first identified counterparts of a gravitational wave transient (GW 170817A) and a high-energy neutrino (IceCube-170922A) has concretely opened the new era of the multi-messenger astrophysics.

In both cases, a crucial contribution to the physical information concerning the origin of the events came from the study of the gamma rays. This highly energetic radiation is usually related to the most extreme processes in the Universe, and the correlation with neutrinos and gravitational waves implies a strong connection between these messengers and the phenomena producing them.

The improvement of the experiments and of the facilities in these fields able to combine the information coming from these astrophysical messengers will give us new opportunities to understand the most extreme astrophysical processes.

In order to investigate the status of this emerging branch of Science, I present here some of the most important fields of research and experiments.

1.6.3 Gravitational wave detection

The extraordinary development of the gravitational wave detection facilities led us to the opportunity to catch this new type of information from high-energy events in the Universe. Events like the merging of compact objects and supernovae explosions play an important role in this field, and produce at the same time strong gravitational waves and electromagnetic light. The coexistence of these two astrophysical messengers is particularly important because leads the scientific community to understand the connection between the two and the processes that produce them. In particular, for example, the follow-up observation of gravitational wave events together with gamma ray bursts was successful in the study of the GW 170817A event. Gamma rays are probably produced in the high-energy processes that take place in these merging events or explosions. For this reason, the strong multi-messenger connection between these two disciplines will be crucial for the next years.

1.6.3.1 Gravitational waves

The theory of general relativity proposed by Albert Einstein in 1915 (Einstein, 1915) considers the whole Universe as held together by a uniform structure called space-time. In this framework, space and time are permanently connected: the presence of mass affects the shape of the space-time itself, by causing curvature and perturbations when solicited.

Thus, all processes that relate with modifications of the mass of astrophysical objects or the position of the mass itself inevitably imply perturbations of the space-time. For example, the formation of black holes (BHs) through supernovae explosions produce perturbations in the space-time, and such "vibrations" are called gravitational waves. Such processes, thanks to the connection between gravity (and thus, the presence of mass) and acceleration of objects, are produced also by violent processes like the merging of black holes and neutron stars. Gravitational waves move at the speed of light, and the effect of their passage is the distortion of the space-time itself: the distances between different objects increase and decrease rhythmically at the frequency of the wave.

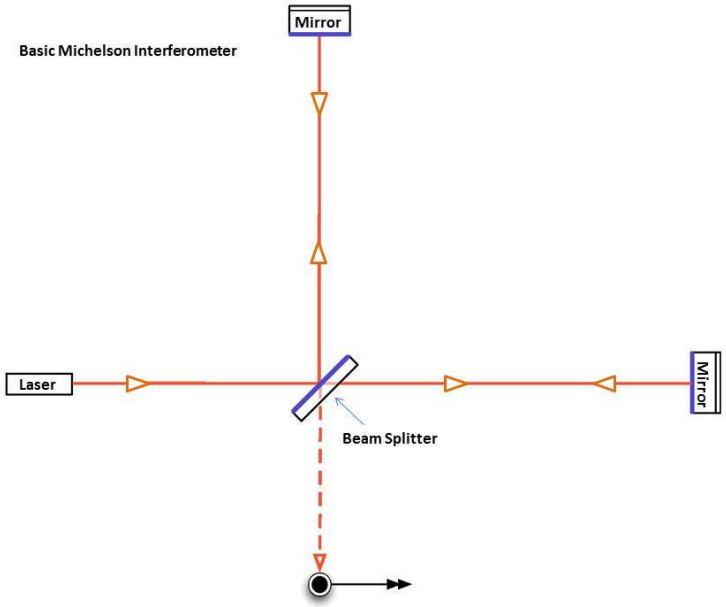

Figure 1.19: *Sketch of the Michelson experiment, now adopted in the gravitational wave detectors like LIGO and VIRGO. Figure taken from* https://www.ligo.caltech.edu.

The detection of gravitational waves has been one of the most interesting discovered in the XXI century. Their detection allows to get information about the cataclysmic events that originated them and that are incredibly difficult to be studied in astrophysics, and about the nature of gravity itself that can be extrapolated by their phenomenology.

The astrophysical events that are most interesting when producing gravitational waves are among the most violent and energetic ones: the collision of black holes, the collapse of stellar cores (supernovae), the coalescence of neutron stars or white dwarf stars, the slightly wobbly rotation of neutron stars that are not perfect spheres. Some scientists think that, in the near future, also the remnants of gravitational radiation created by the birth of the Universe will be a possible target for the human detectors. However, the problem in detecting such gravitational waves is the extremely lower amplitude they have with respect to the ones produced – for example – in BH-BH collisions. At the moment, they represent an incredibly challenging task for the current generation of GW detectors.

One of the humanity's greatest scientific achievements was obtained in September 14^{th}, 2015, when the LIGO observatory directly detected the physical distortion of space-time caused by passing GWs generated by two colliding black holes nearly 1.3 billion light years away from the Earth.

1.6.3.2 Current detectors

Lucky for us here on Earth, the extremely violent processes that generate gravitational waves loose their energy in the space-time by the time the waves reach the Earth, due to the huge astronomical distances to these sources. In fact, by the time the gravitational waves passes through Earth, the disturbances produced in the nearby space-time are incredibly small. For this reason, the detection of such GW is extremely difficult and only instruments like interferometers have turn out to be successful in detection such low signals.

Figure 1.20: *Picture of the VIRGO experiment in Italy. Figure taken from* http://www.virgo-gw.eu.

Interferometers are tools to measure incredibly small variations in the length of objects. In GW astrophysics, the interferometers had to be build of enormous size. They work by measuring the interference pattern between two sources of light, and they are able to detect lengths variations up to several orders of magnitude below the atom radius. In fact, the current GW detectors are designed to measure a distance $1/10000^{\text{th}}$ the width of a proton.

Widely used today, interferometers were actually invented in the late 19^{th} century by Albert Michelson, and first used in 1887 in the "Michelson-Morley Experiment". In a Michelson interferometer, a laser beam is splitted thanks to a "beam splitter" that divides the original single beam into two separate beams: one half is allowed to pass through the splitter, the other half of the signal is reflected by 90-degrees from the first. Each beam then travels down an arm of the interferometer, and gets reflected by the mirror at the end of it. The two beams, when coming back from the arms and recombined into a single beam, interfere with each other. Such interference can be detected by the interferometer by measuring such shift in the wavelengths, and allows for the determination of incredibly small length differences. Such length variations might be produced in the length of the arms: when a GW is passing through the detector, the space-time is slightly deformed and, depending on the direction, one of the two arms would be deformed more than the other one, and this would be reflected in a interference of the two waves. LIGO's interferometers are set up so that, as long as no GW is detected and the arms do not change length, the recombined light waves cancel each other out (destructively interference) and no light reaches the photodetector. Thus, in the case of GW detection, some light would be detected and the shape of the interference pattern emerging from the interferometer over a period of time can be used to calculate precisely how much change in length occurred over that period.

The Laser Interferometer Gravitational Observatory (LIGO) observatory[4] is the largest GW detector ever built on Earth. It is a system of two interferometers with arms about 4 km long and working in unison as a single "observatory": one in south-eastern Washington

[4] https://www.ligo.caltech.edu

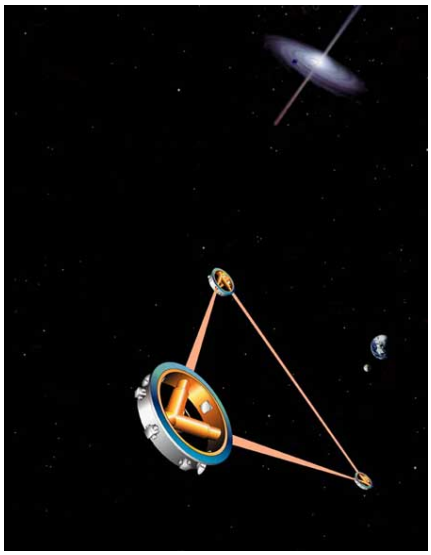

Figure 1.21: *Representation of the forthcoming LISA telescope. Figure taken from https://it.wikipedia.org/wiki/LISA.*

State and the other in the rural Livingston, Louisiana. Such instruments are able to measure distances variations of the order of 10^{-19} m, that is about four orders of magnitude lower than an atom nucleus radius. One of the major difficulties in building such precise instruments to measure GWs is that they have to be designed in such a way to greatly reduce the noise coming from the natural and artificial activities, and this is achieved with refined and innovative technology pushing all the employed technologies to the limit.

However, the two antennas of the LIGO observatory are not enough in order to catch the incoming direction of the GWs with a good enough accuracy. Such problem was solved thanks to the collaboration with the Virgo detector in Cascina (Italy). The Virgo detector[5] started observing the sky from 2007 together with the two interferometers of LIGO. At present, the two collaborations are able to detect GWs from the sky and provide a detailed incoming direction for such events.

1.6.3.3 The future

The next generation of interferometers for the detection of GWs will probably be built outside the Earth's atmosphere.

The length between our detectors on Earth constrains the objects that can be studied at stars with masses a few 10× that of the Sun. Other much more massive sources, particularly interesting like massive black holes at the centres of galaxies, when merging produce signals at much lower frequencies, undetectable from Earth. For this reason, scientists are now planning to launch new experiments into the space.

One of the most interesting proposals currently under development by ESA is the Laser Interferometer Space Antenna (LISA)[6].

LISA will be composed by three spacecraft, arranged in an equilateral triangle with sides of about 2.5 million km long, flying along an Earth-like heliocentric orbit. The distance

[5] http://www.virgo-gw.eu
[6] https://lisa.nasa.gov

between the satellites will be precisely monitored to detect a passing gravitational wave.

Thanks to these much longer arms, LISA will enable us to study some of the most intriguing and inaccessible objects and events of the Universe, such as the massive black holes and the Big Bang.

LISA will be able to join the current multi-wavelength community based on the electromagnetic spectrum and the neutrino astronomy. It will operate over a broad band of frequencies between 0.1 mHz to 100 mHz, enabling us to measure the gravitational effects in a window where we suppose that the Universe is richly populated by strong sources of gravitational waves.

1.6.4 Neutrino detection

Thanks to the multi-messenger approach of this new era of astrophysics, the mystery of the origin of CRs can now concretely handled. Besides the electromagnetic radiation, also neutrinos can travel through the space without being affected in their path by the intergalactic magnetic fields. For this reason, they play an important role in the investigation about the origin of CRs. However, our theoretical models that describe how they are produced suggest that there should be a strong relation between the neutrinos and gamma rays: the same processes are probably able to generate both of them. This means that these two branches of research can help each other: gamma rays at lower energies could also help to identify neutrino sources and, thus, cosmic-ray sources. This is the main reason for which, in the last decades, strong efforts have been put on the collaboration between different observatories – and especially the gamma-ray facilities – in order to build a network of telescopes able to perform follow-up observations in different wavelength and messengers.

In July 2018, I have been participating to the discovery of an extremely-high-energy neutrino in coincidence with a flaring blazars called TXS 0506+056, located 3.7 billion light-years away in the direction of the constellation of Orion. This is the first time that a neutrino detector has been used to locate an extragalactic object in space and that a source of cosmic rays has been identified.

In this Section I present some information that led to the new era of neutrino astronomy, and in Section 6.1 I will present the analysis of that event as detected with the MAGIC telescopes and the consequent data analysis of the event.

1.6.4.1 Neutrino astronomy

Neutrinos are weakly interacting particles that have always been particularly interesting since their discovery. On one side, their scarce interaction makes them very difficult to be studied and detected, while on the other side it makes them particularly interesting because they can reach us passing through places where for example light cannot pass because of absorption effects. Additionally, their neutral charge makes them interesting candidates as tracers of the cosmic rays, and this lead the interest for the birth of *neutrino astronomy*. For example, the application of neutrinos to study the Sun is particularly interesting: while the light cannot give much information expect for the surface of the star, the neutrinos might pass through several shields of the star and reach us giving information about its interior parts.

On the other side, the Sun itself severely affects our chances to observe extrasolar neutrinos. The enormous rate of astrophysical nuclear reactions in the Sun produces an enormous rate of neutrinos that hit the Earth, and this turns out to be a noise source when looking for neutrinos of extrasolar origin.

Thus, the neutrino turns out to be very interesting. In order to face with its controversial properties, the neutrino detectors have to be conceived with particular characteristics. For example, the highly improbable interaction implies that the detectors have to be very big and with a large mass, along with a sensitive amplification system. Additionally, the very weak signal implies that we have to reduce as much as possible the sources of background noise. The detectors must be shielded by a large shield mass, and for this reason the main places where they can be build are deep underground, or underwater, or even within the ice.

1.6.4.2 Astrophysical neutrinos

While the first neutrinos were observed in 1956 by Clyde Cowan and Frederick Reines in an experiment employing a nuclear reactor as a neutrino source (leading to the Nobel Prize for

physics in 1995), the first neutrinos of atmospheric origin were detected in 1965 and those of solar origin were discovered only in 1968. During those experiments, the scientists used gold mines in order to detect the neutrinos and to reduce the background noise.

The first generation of undersea neutrino telescope projects began with the proposal by Moisey Markov in 1960, in which we can read that he wanted to "... install detectors deep in a lake or a sea and to determine the location of charged particles with the help of Cherenkov radiation" (Markov, 1960).

The first underwater neutrino telescope began in 1976 as the DUMAND[7] (Deep Underwater Muon and Neutrino Detector) project. Although it was cancelled in 1995, DUMAND acted as a precursor of many of the following neutrino telescopes.

In 1996, the AMANDA project[8] (Antarctic Muon And Neutrino Detector Array) was built in a 3 km thick ice layer at the South Pole, located at some hundred meters from the Amundsen-Scott station. Holes were created in the ice with pressurized hot water in order to deploy the optical detectors able to catch the Cherenkov radiation produced by the interaction between the neutrinos and the surrounding ice of the South Pole.

The AMANDA array was subsequently upgraded until January 2000, and then it became the predecessor of IceCube in 2005. The IceCube detector, completed in December 2010, represents now the second generation of neutrino telescopes. This Thesis has used several information regarding this telescope, and a detailed discussion about it is reported in Section 2.6.

After the decline of DUMAND, there were different new projects in order to support the research about the neutrino astronomy within the sea. The ANTARES project is an experiment composed of 12 strings of optical detectors deployed up to a maximum depth of 2475 m anchored to the sea floor in the region off Toulon at the French Mediterranean coast.

The NEMO[9] (NEutrino Mediterranean Observatory) represents an Italian project conceived to investigate the feasibility of a cubic-kilometer scale deep-sea detector, and it is located in the South-Eastern coast of Sicily. It has been operating from 2007, and in its second phase it will contribute to the KM3NeT framework.

Finally, the NESTOR Project (Rapidis & NESTOR Coll., 2009) was installed in 2004 to a depth of 3800 meters some 30 kilometres off the coast of Greece. This project operated for some time and then, after some technical problems but several scientific results, it is now being part of the KM3Net framework.

All these projects are now being implemented in the KM3Net framework[10], that will represent the second generation of neutrino detectors together with the IceCube detector. The difference will be that the KM3Net project will be acting in the Mediterranean sea, and it is planned to cover several cubic-kilometers but at a much higher energy threshold with respect to the IceCube experiment.

[7] https://www.phys.hawaii.edu/~dumand/
[8] http://amanda.uci.edu/
[9] http://www.roma1.infn.it/km3/NEMO.html
[10] https://www.km3net.org/

Chapter 2

Relevant instrumentation

One of the main features of modern astrophysics is the crucial role played by the interpretation of natural phenomena through all the frequencies of the light. In fact, most of the astrophysical processes take place by producing radiation at different wavelengths, and the only way to access the deep physical mechanism behind them is to collect data over all the wavelengths of the emitted light. This is the so-called *multi-wavelength* approach to astrophysics.

In order to follow this approach, I have been working with the data from several telescopes operating at different energy bands. In this Chapter, I describe the main instruments I made use during this Thesis. I order the discussion by increasing wavelengths analysed by the observatories: after a presentation of the Medicina radio telescope, *Swift*, and *Fermi* observatories, I will focus on the software and hardware of the MAGIC telescopes and summarize the status of the CTA project. When relevant, I also present briefly the main steps of the data analysis for each telescope.

Finally, I will introduce the main features of the IceCube observatory. Thanks to this experiment located at the South Pole, we have now improved our detection of neutrinos of possible extragalactic origin. This experiment led us to enter the *multi-messenger* era of astrophysics, discussed also the in next Chapters of this Thesis.

2.1 The Medicina radiotelescope

Figure 2.1: *The Medicina radiotelescope.*

The Medicina radiotelescope is a 32 m single-dish parabolic telescope located 35 km south-east of Bologna, Italy. Its first light dates back to 1983, and it is currently managed by the Istituto di Radioastronomia (IRA), which is part of the Istituto Nazionale di Astrofisica (INAF). In this Thesis, this telescope was used to provide a monitoring of the blazar PG 1553+113 in a multi-wavelength monitoring program to which I am contributing.

This Section describes the main features of this telescope and of its data analysis, focusing specifically on the description of the devices used for the data taking and the data analysis during this Thesis. The main techniques have been learnt during an informal school held in Bologna in October 2016, to which I participated.

2.1.1 The telescope

The Medicina antenna is composed by a big antenna of 32 m of diameter with parabolic shape, and it is installed on an altazimuthal mount. The telescope is provided with two different foci: a primary focus and a secondary (or "Cassegrain") focus. The focus with Cassegrain optical configuration, schematically represented in **Figure** 2.3, uses a parabolic reflector as primary mirror, while the secondary mirror is hyperbolic.

The two foci can be selected in the so-called "frequency agility" mode: the user can remotely command a sub-reflector (located near the primary focus) to slide to a retracted position in such a way to switch between the (only) primary or the secondary focus, and vice versa. This procedure can be performed with valuable velocity, and it takes less than four minutes for both the switching and preparation of the setup configuration. This procedure allows the telescope to use different receivers, and thus to study different wavelengths (bands).

The two foci host the `frontends` of the telescope, whose devices can be represented as in **Figure** 2.4, composed by the receivers. The receivers are sensible to the radio waves, and transform it in electric signal representing the properties of the incoming wave (e.g. the intensity). Such signal is sent to the `backend`, like the spectrometers and the total-power devices. They analyse the electric signal corresponding to the incoming radio waves, and

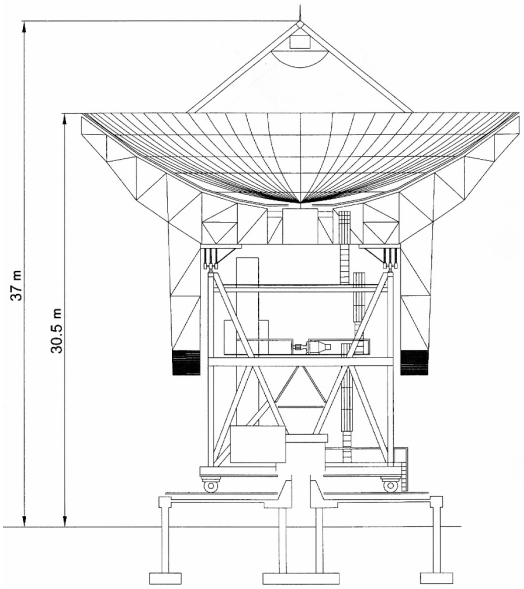

Figure 2.2: *Schematic representation of the structure of the antenna.*

write the data into files.

The telescope is provided with five different receivers, that are able to cover five different frequency bands:

- 1.6 GHz, called L-band, that works in the range 1.595-1.715 GHz;
- 5 GHz, called C-band, that works in the range 4.3-5.8 GHz;
- 6.7 GHz, called high-C-band, that works in the range 5.6-7.3 GHz;
- 8.4 GHz, called X-band, that works in the range 8.18-8.98 GHz;
- 18-26 GHz, called K-band, that works in the range 18-26.5 GHz.

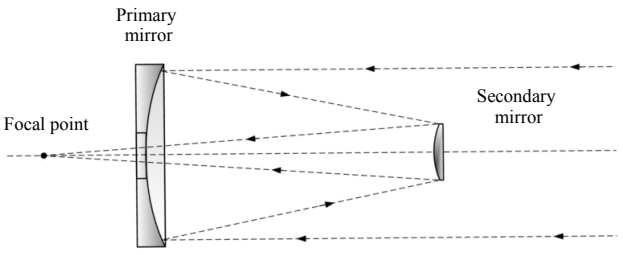

Figure 2.3: *The Cassegrain focus.*

More information on the technical details of the receivers is reported the webpage of Medicina[1].

The different frequency bands have different behaviours when considering the observing conditions under which they are used. In fact, we can find the following correlations:

- **Low frequency bands:** they present heavy radio frequency interference, and also poor angular resolution (in particular, blazars are unresolved at all frequencies); they are scarcely influenced by the weather.
- **High frequency bands:** in this case the weather is relevant, sources are usually fainter, and the smaller beam size implies greater challenges in granting a proper pointing accuracy.

Three bands were considered relevant for this work, namely: the C, the X, and the K band. This choice was based on the following considerations:

5 GHz (C-band): located in the secondary focus. This frequency band presents a low level of noise and it behaves well under different atmospheric conditions. Conversely, it presents severe radio frequency interference and the total flux density is partly contaminated by steep spectrum emission;

8 GHz (X-band): installed in the primary focus. This frequency band shows a low level of noise, it behaves well under different atmospheric conditions and the radio frequency interference are under control;

18-26 GHz (K-band): located in the secondary focus. It is provided with a dual feed (one on the source, one on the sky) and presents a moderate level of system noise. It is very sensitive to weather conditions.

The `backend` instruments allow to exploit three different observing modes:

- **Spectroscopy:** narrow band signals, at specific frequencies (lines);
- **Continuum:** measurement of the integrated signal over wide bands;
- **Polarimetry:** analysis of the polarized signal (both continuum or lines).

The most important observing mode for the planned observations was the *continuum* observing mode. In this mode, the collected signal can be observed up to flux density of the order of 10^{-27} W Hz^{-1} m^{-2}.
The sensitivity S of the instrument can be expressed with the following formula

$$S = \frac{T_{sys}}{G} \frac{1}{\sqrt{t\,\Delta\nu}}\,, \tag{2.1}$$

where T_{sys} is the system temperature, G is a dimensionless parameter proportional to the antenna gain, t is the integration time, and $\Delta\nu$ is the frequency bandwidth.

[1] https://www.radiotelescopes.inaf.it/summary.html

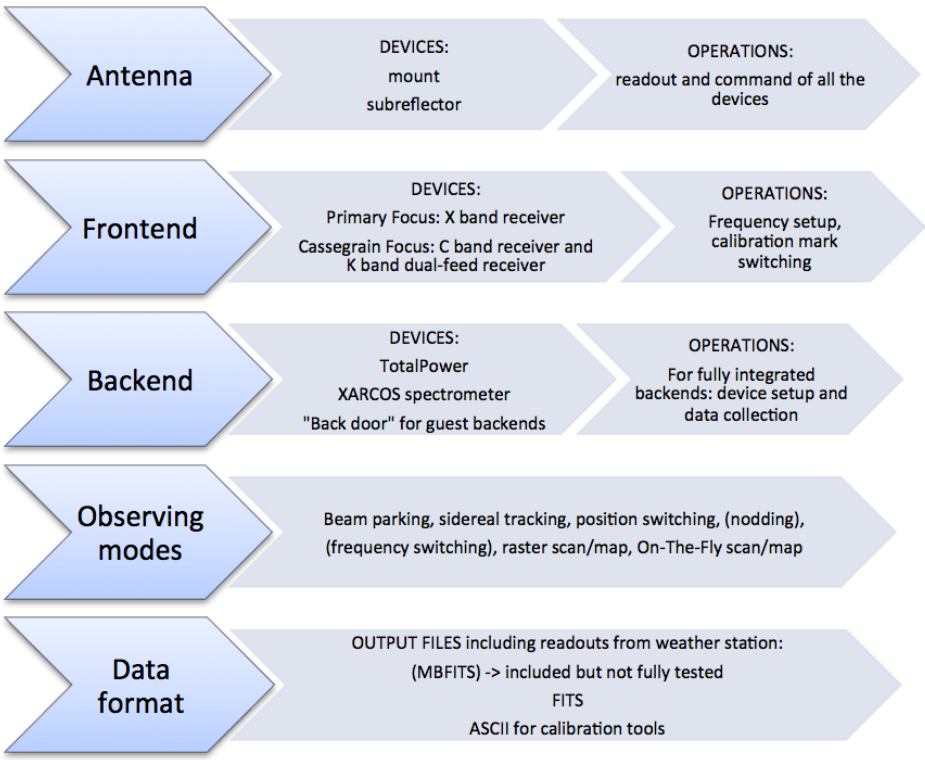

Figure 2.4: *A sketch of the devices and modes operated by the ESCS system. Figure taken from* https://discos.readthedocs.io/en/latest/user/medicina/index.html.

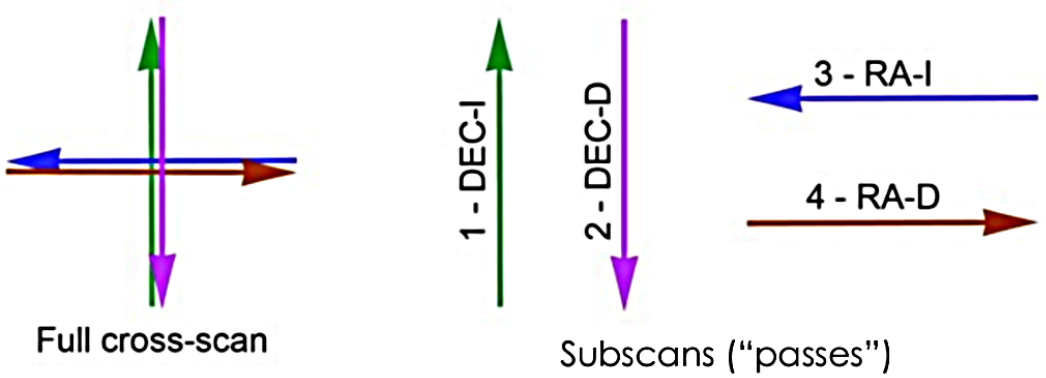

Figure 2.5: *An example on how the Medicina radiotelescope takes data when observing a point source. The telescope performs a series of scans with a typical cross-like shape. Every scan is composed by four sub-scans, each of them is a 15 s acquisition run in which the telescopes takes data passing over the position of the target. Courtesy of Simona Righini.*

2.1.1.1 The remote data taking

The data-taking operations with the Medicina radiotelescope are performed by remotely controlling the telescope. Such remote control is performed thanks to the `ESCS` (Enhanced Single-dish Control System) software, that is a flavour of the software `DISCOS`, produced for the three italian radio telescopes (Medicina, Noto, and Sardinia telescopes). This system is based on ACS (ALMA Common Software), and allows the user to command all the devices of the telescope and to perform single-dish observations in the most common modes. The software is based on a code composed by more than 550000 active lines, and is partially used also to perform very-long-baseline interferometry (VLBI, or guest-backend) observations.

VLBI observations

The Medicina antenna contributes to the European VLBI Network[a] (EVN) since 1984. The EVN is a network of radiotelescopes composed by antennas located in Europe, Asia, South Africa, and Puerto Rico, and is nowadays the most sensitive VLBI array in the world.

[a] https://www.evlbi.org/

Data taking procedure

An online guide of such software is provided at the following link[2]. In **Figure** 2.4, I present a list of the most important devices and operations which the ESCS deals with during the observations.

During the observations, the standard procedure proceeds as follows.
When opening an `ESCS` observing session, the antenna has to be unstowed and prepared with a standard setup that configures the mount in tracking mode.

[2] https://discos.readthedocs.io/en/latest/user/medicina/index.html

After setting up the telescope, the user runs an observing schedule. Using a schedule, all the information about the sources and their programmed observations are followed automatically by the telescope. During the observations, the user monitors the possible presence of errors or problems.The dedicated schedule for PG 1553+113 observations has been prepared after a commissioning phase in order to speed up the data-taking chain, that usually takes place remotely during the night. Basically, the schedule contains the following procedures:

calibration phase: for each source, a calibration acquisition, aimed at assessing the atmospheric conditions during observations is performed. In this phase, the telescope performs the so-called `skydip`, that is a four-minutes long observation of the sky at fixed azimuth while varying elevation between 85 and 15 degrees. This allows to estimate the atmospheric opacity.

calibrators runs: during this phase, a source with known stable flux density, possibly close to the direction of the source of interest is observed for some minutes in order to calibrate the flux density estimation. Such flux calibration over the known sources is performed during the off-line analysis.

standard observations: the schedule is then composed of the predefined step of observations of the source of interest.

2.1.2 Analysis and results

The telescope, when operated in single-dish mode, performs high-speed On-The-Fly acquisitions of the source of interest. This means that the telescope performs a series of `scans` with a typical cross-like shape, and every cross is composed by four `sub-scans` in the different orthogonal directions (as reported in **Figure** 2.5). Each subscan is a about 15 s acquisition run in which the telescopes takes data passing over the position of the target. During each subscan, the signal obtained from the target is superimposed to the background. More details about the speed of the telescope during the subscans in the different frequencies is reported in **Table** 2.1.

Frequency band	Speed	Span
5 GHz	4°/min	1.0°
8 GHz	2.4°/min	0.6°
22 GHz	0.8°/min	0.2°

Table 2.1: *Typical speed of the telescope when taking data during a subscan in On-The-Fly mode.*

Considering a typical configuration of the observation, a source with an integrated flux signal S can present the following practical detectability:

- S>1 Jy: detection in a single “pass” (subscan);
- 0.1<S<1 Jy: detection in a few (about 10-30) passes;
- S<1 mJy: extremely difficult to be detected.

Most of the extragalactic sources in the monitoring program of the telescope provide a signal S of the order 0.1<S<1 Jy, and thus can be detected in some tens of minutes of observation.

An example of the resulting raw counts data of some real events from the blazar PG 1553+113 is shown in **Figure** 2.6.

A detailed report on the preliminary results concerning the observations of PG 1553+113 are reported in Section 3.2.6.4.

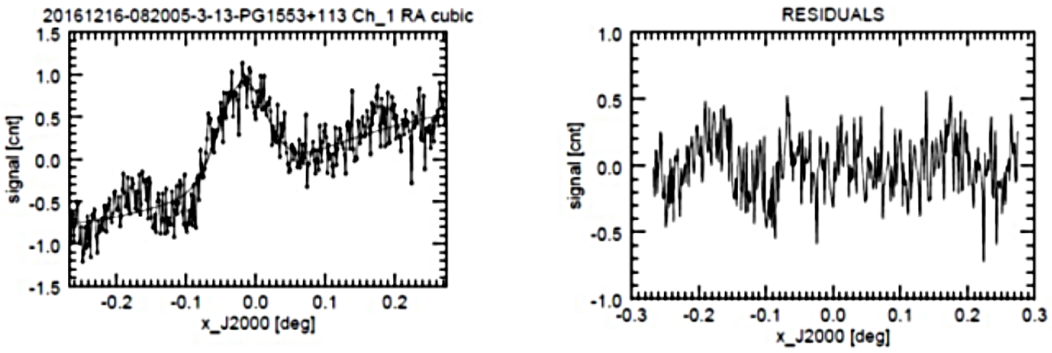

Figure 2.6: *An example of the first analysis of some acquisitions on the blazar PG 1553+113. During each subscan, the signal obtained from the target is superimposed to the background, that will be estimated and removed in the following off-line analysis.*

2.1.2.1 Flux density calibration

In order to get physical results from the observations, a flux density calibration procedure has to be performed before all the data taking of each source. Such calibration is achieved by means of cross-scans on a set of point-like flux density calibrators.

The aim is to measure their amplitude in raw counts and, comparing it to their pre-computed flux densities, to achieve a counts-to-Jy conversion factor.
Such factor must be rescaled taking into account:

- pointing offset;
- gain vs elevation curve;
- atmospheric opacity.

2.2 The Neil Gehrels *Swift* Observatory

Figure 2.7: *The Neil Gehrels* Swift *Observatory.*

The Neil Gehrels *Swift* Observatory (Gehrels, 2004), launched into a low orbit around Earth on November 20$^{\text{th}}$, 2004, is a multi-wavelength observatory focused on the study of gamma-ray bursts (GRB) science. It is composed of three co-aligned instruments, namely

- the Ultraviolet/Optical Telescope, named UVOT;
- the X-Ray Telescope, named XRT;
- the Burst Alert Telescope, named BAT.

These instruments work together to observe GRBs and afterglows in the optical-UV, soft X-rays, and hard X-rays, respectively.

The idea behind this observatory is the following. The BAT, the largest instrument on-board *Swift*, with its wide field of view of approximately a sixth of the entire sky, can detect approximately 100 or more gamma-ray bursts per year. After few seconds having detected a burst, the spacecraft can automatically repoint by itself in order to perform deep observations with the other two instruments - the XRT and the UVOT. These two instruments together can determine with high precision the position of the burst both in X-rays and in optical. Immediately, the information about the detection can be distributed in near real-time to the world-wide scientific community via the internet by sending an alert to the GRB Coordinate Network (GCN) of telescopes that can observe such events. The combination of these two instruments can also study the spectrum and the light curve of the incoming radiation in these energy bands. In most of the cases, the *Swift* satellite can also determine the redshift of the bursts that it detects.

However, besides the main usage of the *Swift* satellite for the search for GRBs, the telescope can also be used for pointed observations of selected targets. The *Swift* Collaboration provides a procedure to submit proposals for observation and Target of Opportunity (see next Sections) requests: this allowed me to perform observations of several sources of interest for this Thesis, some of them simultaneous to the observation slots of several other facilities, such as the MAGIC telescopes.

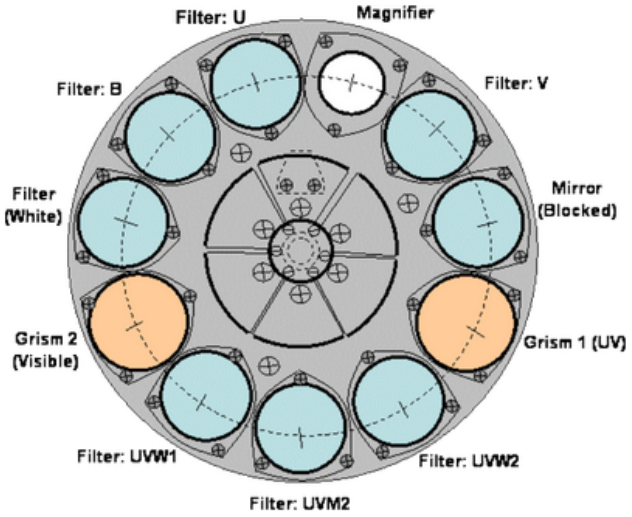

Figure 2.8: *The filter-wheel of the* Swift*-UVOT instrument. Figure taken from* https://www.mssl.ucl.ac.uk/www_astro/uvot/uvot_instrument/filterwheel/filterwheel.html.

2.2.1 BAT instrument

The BAT (Barthelmy et al., 2005) is the largest instrument on-board of the *Swift* telescope. It operates in the 14-195 keV energy range, and it is provided with a wide field of view of about 60×100 degrees that enables it to detect GRB events and compute their coordinates in the sky. The position accuracy that can be provided for each event is between 1 and 4 arcminutes within 15 seconds of observation. This first estimation of the position is immediately sent to the ground-network and used to repoint the telescope for a deep study of the event with the other two instruments XRT and UVOT.

In this Thesis, the BAT instrument was particularly useful thanks to its capability of providing all-sky surveys: the latest survey in this energy band resulted in a catalog of the brightest sources after 105 months of observation (Oh et al., 2018). This is – up to now – the most sensitive and uniform hard X-ray all-sky survey, reaching a sensitivity of $8.40 \cdot 10^{-12}$ erg cm^{-2} s^{-1} over 50% of the sky and $7.24 \cdot 10^{-12}$ erg cm^{-2} s^{-1} over 90% of the sky.

As presented in Chapter 4, the extreme blazars – the most important part of this Thesis – emit their highest synchrotron flux in the hard X-ray band, and they are the only category of BL Lac objects able to cover that band. For this reason, the selection of sources in the latest available hard X-ray survey provided by the BAT instrument allowed me to prepare a list of good EHBL candidates. For more information, see Section 4.3.

2.2.2 UVOT instrument

The UVOT instrument is able to detect an optical afterglow related to a GRB with a sub-arcsecond position accuracy. An additional use of the UVOT instrument is also to provide long-term light-curves of GRB afterglows and observations of selected sources, as used in the case of blazars in this Thesis.

As shown in **Figure** 2.8, the instrument is provided with several different filters and grisms: the filters are used to obtain optical and ultraviolet images, while the grisms take

Date	Source	Number of visits	Total exposure time	UVOT	Status
03/19/2019	1RXS J081201.8+023735	2	2 ks	all filters	Approved
03/07/2019	1RXS J081201.8+023735	1	2 ks	all filters	Approved
02/22/2019	1RXS J081201.8+023735	1	2 ks	all filters	Approved
01/30/2019	1RXS J081201.8+023735	2	2 ks	all filters	Approved
12/26/2018	1RXS J081201.8+023735	2	4 ks	all filters	Approved
10/02/2018	1RXS J055717.0-061705	2	5 ks	all filters	Approved

Table 2.2: *List of the last* Swift *ToO requests approved for observing sources presented in this Thesis.*

optical and ultraviolet spectroscopic measurements. They can be selected in such a way to provide optical/UV photometry and low-resolution spectra in the 170-650 nm range.

2.2.3 XRT instrument

The XRT instrument is able to provide both imaging and spectral data of a GRB afterglow. This X-ray instrument provides more precise location of the GRB with a typical error circle of approximately 2 arcseconds radius. As UVOT, also the XRT instrument can be used to perform long-term monitoring of the GRB afterglows producing low-resolution light curves up to weeks after the event. The XRT is a Wolter Type I X-ray telescope, provided of twelve nested mirrors and focused onto a single MOS charge-coupled device. The on-board software is completely automated, and provides observations selecting the appropriate observing mode for each object, based on its measured count rate.

Considering that the telescope operates in the energy range of 0.2-10 keV, it was particularly useful during this Thesis work. In fact, as reported in Chapter 3, the BL Lac objects on which this Thesis is focused (mainly HBLs and EHBLs) have the synchrotron emission peaked in this energy range. Thus, the detailed estimation of such emission by means of the XRT instrument allowed to improve the studies on these sources.

Additionally, there is a webpage[3] where an automatic analysis of the XRT data can be performed. This instrument is particularly useful for a quick overview of the results of the observations.

2.2.4 *Swift* ToO system

The *Swift* telescope allows the scientists to ask for *Target of Opportunity* (ToO) observations with a dedicated webpage[4] where the user provides all the information related to the source he wants to observe. Once the PI of the project on duty has analysed and approved the request, the source might be observed between hours and weeks from the requests, depending on the time criticality of the event.

In this Thesis, I made use of this ToO system having approved all the requested observations. Since most of them were requested for the monitoring of extreme blazars, the data have been requested on monthly based observations, accordingly to the simultaneous

[3] https://www.swift.ac.uk/user_objects/
[4] https://www.swift.psu.edu/secure/toop/too.php

observations performed with other instruments like the MAGIC telescopes. A list of all the recent ToO requests is presented in **Table** 2.2.

2.3 The *Fermi* gamma-ray space telescope

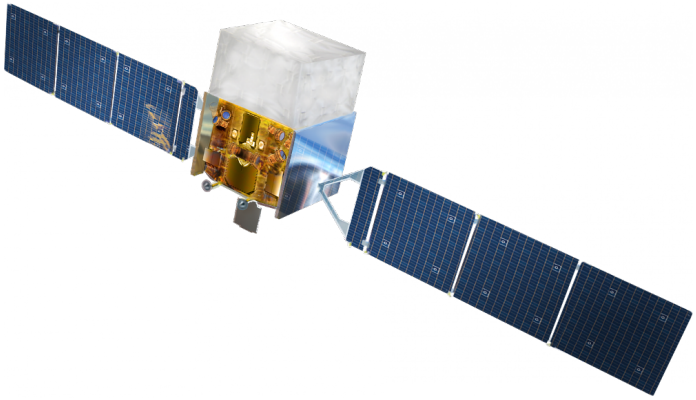

Figure 2.9: *The* Fermi *telescope.*

In this Thesis, I made use of data of the pair-conversion Large Area Telescope instrument on board the *Fermi* satellite, an all-sky survey instrument that covers the energy range from 20 MeV to more than 300 GeV (Atwood et al., 2009), and more than 2 TeV with dedicated analyses.

2.3.1 The telescope

The *Fermi* gamma-ray space telescope – represented in **Figure** 2.9 – was originally named Gamma-ray Large Area Telescope (GLAST), and then changed name in honour of the physicist Enrico Fermi. It was launched on June 11$^{\text{th}}$, 2008, and consists of two main instruments:

- the Gamma-ray Burst Monitor (GBM);
- the Large Area Telescope (LAT).

The GBM works on the low-energy band between 8 keV and 40 MeV. It composed of two main set of detectors: the first set are twelve sodium iodide scintillators that cover the energy range between 8 keV and 1 MeV, and the second set is composed by two cylindrical bismuth germanate scintillators that allow to detect energies between 0.2 and 40 MeV.

The GBM can reveal bursts coming from any direction of the sky, and it works by comparing the incoming direction in the different detectors located around the telescope. GBM triggers about 200 GRBs per year with an uncertainty on their position of several degrees. It acts as a huge field-of-view detector of GRBs to which the LAT instrument can point at and consequently perform high sensitivity exposures in the HE gamma-ray band.

Similarly to its precursors EGRET and AGILE, the LAT instrument is a pair production telescope sensitive in high-energy gamma rays between 20 MeV and 300 GeV (and more than 2 TeV with dedicated analyses). Its field of view is about 20% of the sky, and has a good angular resolution that improves at higher energies between 0.15 at 10 GeV. The LAT consists of a 4×4 matrix of identical towers modules. Each tower is composed of a silicon tracker-converter – in which the detection planes are alternated with thin tungsten sheets –

Parameter	Value
Energy range	20 MeV – 300 GeV (up to 2 TeV)
Effective area	up to > 9000 cm^2
Field of view	2.4 sr
Timing accuracy	300 ns

Table 2.3: *Some of the main performances of the* Fermi-*LAT telescope.*

and a Cesium Iodide crystal electromagnetic calorimeter. Gamma rays that collide with the detector are then converted into electron-positron pairs. The couples are in turn tracked by the detectors of silicon, which allows to trace event by event to the direction of the photon accident, and then absorbed into the calorimeter which allows to measure its energy. The tracker is surrounded by an anti-coincidence (ACD) screen for the rejection of the bottom of charged particles, which in a low orbit are much more numerous of the gamma rays that the LAT is designed to reveal.

2.3.2 Data analysis

In this Section, I cover the main steps of the data analysis of *Fermi*-LAT data that are usually performed with the dedicated software *Fermi*-LAT Science Tools (ST). A detailed information about the data-analysis chain is reported in the *Fermi* GSFC webpage[5].

2.3.2.1 Data retrieve

The *Fermi* Collaboration publicly provides the reconstructed photons on the *Fermi* Science Support Center.

The photon list is provided with information about the energy of the event, its arrival time, and its direction. An event class is assigned to each photon, and response functions are provided for each event class, parametrizing the performance of the instrument and of the event analysis.

Besides the photon lists, the analysis tools need information about the spacecraft. Such information is not related to the events, but to the observing conditions at the moment of the data-taking pointing, and it is provided through an additional file called "spacecraft file" in `fits` format.

2.3.2.2 Event selection and reconstruction

The selection of the events can be operated using the `gtselect` macro. This first step allows the user to filter the overall events by (for example) event class, event type, coordinates (and aperture radius), energy range, and maximum zenith distance (such selection is useful in particular to remove noise coming from Earth limb).

After the event selection, the macro `gtmktime` allows to compute the Good Time Intervals (GTIs). Such time intervals, defined as time ranges for which the data are considered valid, are produced by considering the spacecraft file and consider when the LAT instrument was properly working and collecting data (e.g. not in calibration mode).

Once the events have been selected and the GTIs have been computed, the macro `gtbin` allows to generate the count map of the so-called region of interest (ROI).

[5] https://fermi.gsfc.nasa.gov/ssc/data/analysis/

2.3.2.3 Binned and unbinned analysis

The *Fermi* analysis allows the user to choose between two different types of analysis: the `binned` and the `unbinned` analysis. While in binned mode a multidimensional count histogram is first built as a function of energy and sky coordinates, in the unbinned analysis each event is treated individually.

The point is that, since the LAT IRFs depend on the angle between the pointing direction and the source position, the photon count (the flux) measured from a given source changes as the source moves across the field of view.

This implies that, while the unbinned analysis is generally more sensitive, the amount of computing time and memory required is also significantly larger. Thus, in general the binned analysis is used when studying large data samples.

Unbinned analysis
The first step in the unbinned analysis is to compute the livetime cubes with the `gtltcube` macro. The livetime cubes are an estimation of the accumulated time during which the instrument was collecting data in a three dimensional grid (2 dimensions for the sky position and one for the inclination angle). Then, a similar step is performed by using the `gtexpmap` macro, that computes the exposure maps as the predicted number of photons within a given ROI for the diffuse components in the source model. At this step, a source model XML file has to be defined. The source model contains all the sources that are expected to be in the ROI (including the source of interest) and their spectral and spatial information (which may depend on some free parameters as the normalization flux and the spectral indices).

Finally, the `gtdiffrsp` performs a calculation of the integral over solid angle of a diffuse source model convolved with the IRFs for each of the photons in the events file and the likelihood of the model can be evaluated.

Binned analysis
In the case of a binned analysis, the procedure requires to compute a three-dimensional version of the counts map (two spatial dimensions and the third one for the energy). This step is performed by means of the `ccube` option of the `gtbin` program. After the production of a source model XML file defined as done for the unbinned analysis, the calculation of livetimes and exposure is performed through the `gtltcube` and `gtexpcube2`, and results in a set of exposure maps computed at different energies.

Finally, the program called `gtsrcmaps` produces a model of the count maps with the sources from the XML file, convolving it with the exposure and the PSF to be computed for use in the maximum likelihood.

2.3.2.4 *Enrico* software

In this Thesis, the *Fermi*-LAT analysis has been carried on by using the so-called `enrico` software (Sanchez & Deil, 2013). Such software has been produced to simplify the analysis of the *Fermi*-LAT data and to provide easily readable output plots. It is easily usable by the user for the analysis of *Fermi*-LAT data simply by providing a configuration file in which all the information about the analysis are included. Then, the user can run the `enrico-sed` command in order to run all the *Fermi* Science Tools (ST) routines up to the production of a SED. Finally, several other routines allow the user to produce - for example - light-curves and sky maps.

The `enrico` software is particularly useful in the case of quite standard and repetitive analyses. Considering that most of the analysis of blazars have been using standard parameters

and configurations of the analysis tools, I implemented this software in the INFN-PD MAGIC cloud-based computing system, making it easily available for all the users of the group (more information is reported in Appendix A). Additionally, the implementation of this software in the cloud system was performed in such a way to parallelize a significant part of the *Fermi* analysis.

2.4 The MAGIC telescopes

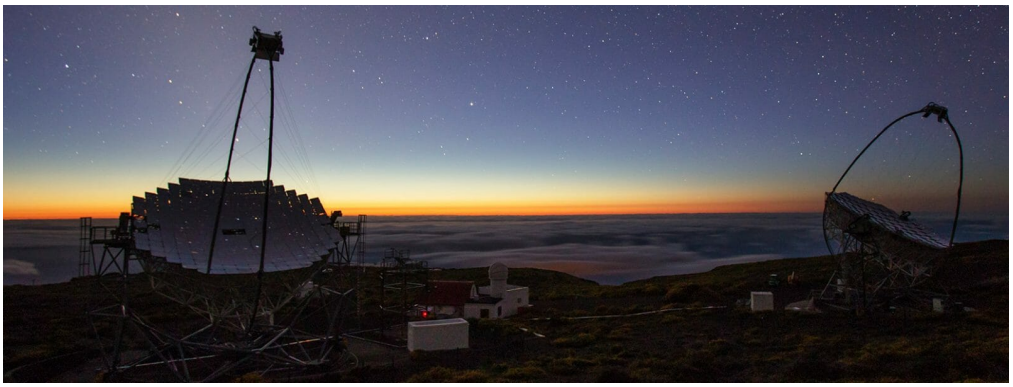

Figure 2.10: *The MAGIC telescopes.*

MAGIC (Aleksić et al., 2016a) is a stereoscopic system consisting of two 17 m diameter imaging atmospheric Cherenkov telescopes (IACTs) located in the Canary island of La Palma, Spain (28° 45' N, 17° 53' W). The MAGIC site is part of the astrophysical observatory of the island, the so-called ORM (Observatorio del Roque de Los Muchachos), provided with more than 18 telescopes and several projects under construction looking at different wavelengths.

The site is located at about 2225 m above sea level, almost on top of the Roque de Los Muchachos mountain (2423 m). This particular place is located in such a position that during almost the whole year the clouds lay below the site at few hundreds meters over the sea, and they do not disturb the observations. Additionally, the sky results relatively unaffected by the light coming from the towns on the island.

The MAGIC telescopes represent one of the three major facilities of the current generation of IACTs. Initially, MAGIC was designed as a stand-alone telescope (now called MAGIC I). Such mono configuration was able to achieve an integral flux sensitivity around 1.6% of the Crab Nebula flux in 50 hours of observation (Aliu et al., 2009). However, the performances were greatly improved when, in autumn 2009, the second telescope called MAGIC II started to operate. Such improvements of the facility allowed to reach in stereo mode an energy threshold up to 50 GeV at low zenith angles (Aleksić et al., 2012a), and with a sensitivity improved to 0.76 ± 0.03% of the Crab Nebula flux for energies greater than 290 GeV in 50 hours of observations.

The improvements of the telescopes continued between summer 2011 and 2012, when both the telescopes underwent a major upgrade that involved the digital trigger, the readout systems and the MAGIC I camera (Aleksić et al., 2016a). Such developments of the hardware allowed to reach the current performances, with an integral sensitivity of 0.66 ± 0.03% of the Crab Nebula flux in 50 hours above 220 GeV (Aleksić et al., 2016b).

For more information, the performances of the instrument are fully described in Aleksić et al. (2016b).

In the following Sections, I will report a summary of the main structural and hardware components of MAGIC. At the end, I introduce the reader to an overview of how MAGIC works, and how the observations are carried on. Finally, the last section will describe the details regarding the data analysis.

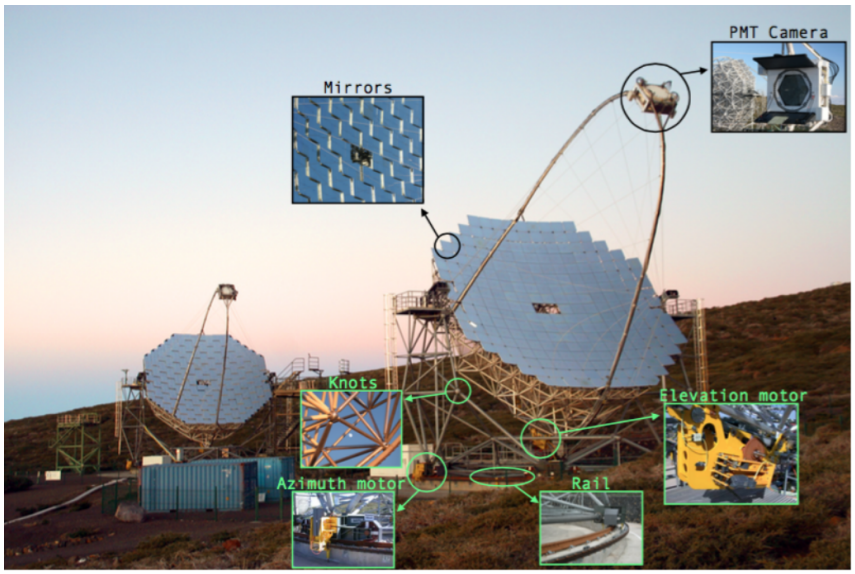

Figure 2.11: *The MAGIC telescopes (MAGIC I behind, MAGIC II on the front) with some of their hardware subsystems highlighted. Image taken from* https://magic.mpp.mpg.de/.

2.4.1 Hardware

MAGIC is a system of two telescopes composed by similar structures and devices. They are provided with parabolic reflective surfaces of 17 m of diameter. Such surfaces are covered by mirrors that reflect the light coming from the space into the camera, held at 17 m from the center of the dish on the focal plan by a parabolic steel arc. The analog signal is received by a set of thousands of photomultiplier, converted into digital signal, and sent to the counting house. There it is analysed by the electronic room, and scientific data are extracted.

In this Section, a detailed presentation of the most important parts of the hardware chain of the MAGIC telescopes is presented.

2.4.1.1 Structure and drive system

The MAGIC telescopes drive system is fully described in Bretz et al. (2009), and in this Section I describe some of its main features.

One of the main goals of MAGIC is the detection of fast transient events, for example the follow-up observations of GRB, GW, and neutrino alerts. This task is addressed by designing the MAGIC telescopes in such a way to be light enough to be fast when repositioning. In fact, the structure of the two telescopes is made of light carbon fibre-epoxy tubes which are hold together by aluminium knots. Only the camera box is held by an aluminium circular tube secured to the main structure by 20 steel cables. Such light materials make possible to lower the weight of the whole structure to only about 20 tons and to permit a fast repointing of the telescope. The movement of the telescopes during repositioning is performed at the angular speed of 4 deg/s, but in the so called fast movement mode (or *GRB mode*), the speed is increased to 7 deg/s. This allows to reposition the telescopes in less than 30 s.

The telescopes can move both on azimuth (Az) and zenith (Zd) thanks to an alt-azimuthal mount. In Az, the telescopes can cover the range -90 to 318 degrees, while in the Zd they cover the range between -70 and 105 degrees. While the Az movements are carried out by

two 11 kW motors, the Zd ones are provided by one motor of the same power located behind the dish structure.

The distribution of the total weight of about 70 t of the telescope is as follows: the camera is about 0.9 t, the camera bow and counterweights are about 3.4 t, the carbon fibre dish is about 8 t, the mirror system is about 9 t, the towers to access some parts of the telescopes (about 20.2 t), and the six carriages (about 25 t).

Even with this light and robust structure, there can be imperfections and deformations of the mechanical structure. Such deformation of the structure is generally lower than 3.5 mm at any direction, and small corrections to such deformation can be applied by using a *pointing model* which parametrizes the deviations from an "ideal" telescope thanks to the Active Mirror Control (AMC, see Section 2.4.1.2). The pointing model is produced using the *TPoint package* by analysing the image provided during the observations by a Starguider camera. The Starguider camera is a charge-coupled device (CCD) camera located in the middle of the dish (as in **Figure** 2.12). It points continuously to the same direction of the telescopes, and analyses the stars in the FoV. This FoV is compared with a catalog of 150 stars (the so-called *bending model*) to find any possible mispointing (undesirable shift between the camera center and the real coordinates of the source). Such mispointings are potentially reported in a list of "mispointings" (the so-called *TPoints*) that are recorded on each occasion the telescope readout. Thus, making use of this model and the shaft encoders, a pointing precision of 0.01 deg is achieved.

The software analyses misalignments and flexures of the structure of the telescopes, that are recorded in the drive and starguider bending models (multi-parameter calibration functions). The information coming from the former is applied directly in the software controlling the drive system (called `Cosy`), while the starguider bending models are applied by the data-analysis software (usually at `star` level, see Section 2.4.3.3).

2.4.1.2 Mirrors and reflector

The MAGIC telescopes have got parabolic reflectors with diameters of 17 m. The large size of these detectors would imply a large arrival timing difference of the reflected light from different parts of the different part of the dish. However, the parabolic shape of the detectors makes the incoming light isochronous, reducing the noise coming from this broadening of the signal at about 1-2 ns and allowing to apply a smaller integration signal window. In the MAGIC telescopes, also the focal length of the reflector (distance at which the camera is placed with respect to the center of the dish) is 17 m long.

The mirrors mounted on the MAGIC telescopes are different between MAGIC-1 and MAGIC-2. MAGIC-1 has mainly aluminium-honeycomb sandwich 50×50 cm mirrors built by the INFN of Padova (some also by MPI – Munich), and some other cold-slumped 1×1 m mirrors by INAF.

Due to the atmospheric conditions, the mirrors get naturally damaged after some years and have to be replaced. Some of the most common issues are:

- inelastic modification of the mirrors structure due to temperature cycles;
- humidity absorbed in the mirrors and turned into water and eventually ice modifying the mirrors surface;
- bad micro roughness of the surface due to the diamond-milling technique causing high scattered light.

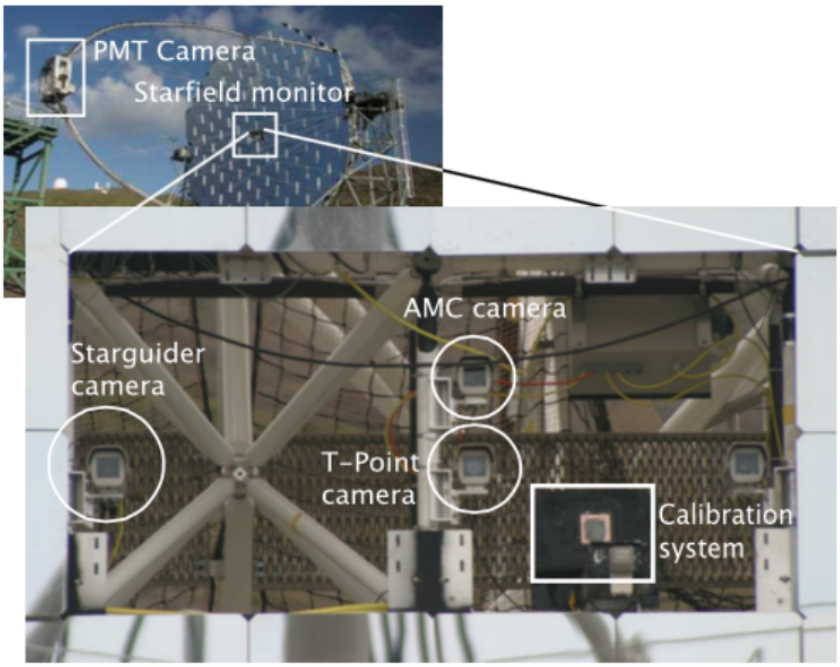

Figure 2.12: *CCD in the middle of the reflector dish. Credits: Wagner (2006), Mazin et al. (2007).*

The quality and the status of each mirror can be evaluated through the definition of the Point Spread Function (PSF). For each individual mirror, the PSF is defined as the diameter at which 39% of the light from a point-like source is contained. In general, this value is about 10 mm at the on-axis of the camera.

Additionally, the PSF can be evaluated also for the whole telescope, and it turns out to be a key parameter to estimate the performances of the telescope. Its value is made up by the contribution of all the mirrors, but the contribution is different considering the direction of light. At the beginning of the night, some images of bright starts (at different Zd and Az). The evaluation of the bright stars images can spot any structure deformation, and small corrections can be applied with the AMC system (see Section 2.4.1.2) that focus each mirror until the PSF of the whole telescope is the best achievable.

The AMC is a system composed by two actuators installed on the back of each mirror that move the mirrors around a third fixed point with a precision of less than 20 μm. The adjustment of the mirrors is performed through Look-Up Tables (LUTs) binned in Az and Zd, i.e. tables that keep memory of the defects and mispointing of each mirror and bring it in the best configuration in such a way to provide the best PSF (the best "ideal" telescope). During the observations – for each repositioning of the telescopes – the proper values of the actuator positions are read from the LUTs according to the zenith and azimuth of the observation, and the software make the mirrors always focused.

The PSF of the MAGIC telescopes is measured every night before the observations with the so-called SBIG camera. The SBIG camera is a CCD camera placed at the center of the dish and designed for measuring the optical PSF of the telescope by looking at the reflection of a star in the camera. It can measure the PSF both for individual mirrors or for the complete reflector (as usually used). It is provided of three different filters: for the PSF measurement during normal operations, the blue filter is used. In the case of Very Large

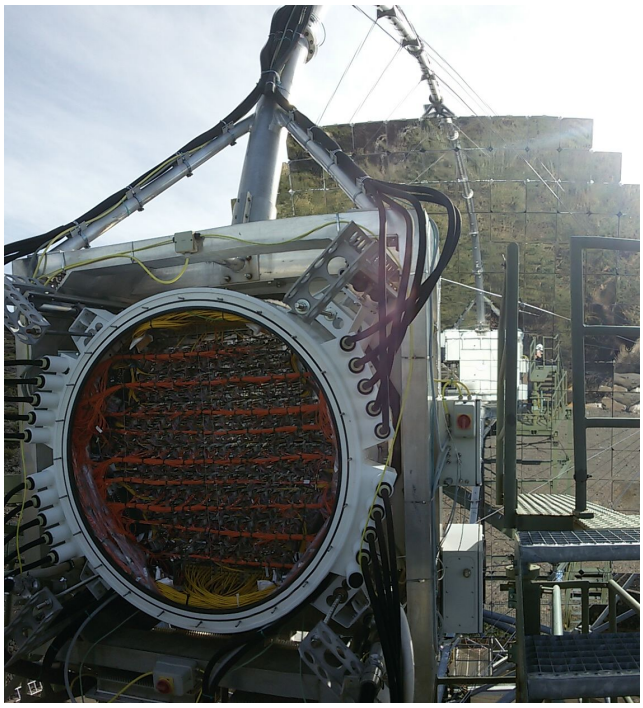

Figure 2.13: *Picture of the MAGIC camera inside, taken during a technical check we did during my shift in La Palma.*

Zenith Angle observations (VLZA, Mirzoyan et al. 2019), since the LIDAR cannot work at such high zenith angle, the SBIG camera with all the filters is used.

2.4.1.3 Camera

When the mirrors reflect the light to the camera, then a set of photomultipliers (PMTs) converts it to photoelectrons and creates an electrical signal that is processed by the readout and trigger systems (see Sections 2.4.1.5).

The two cameras are composed each by 1039 PMTs with a diameter of one inch and a field of view of 0.1 degree, for a total of 3.5 degree of the whole camera. The PMTs are designated for catching Cherenkov light, and their peak quantum efficiency is 34% for light with 350 nm of wavelength. Each PMT has a light-guide on top of it in order to focus the light on the PMT sensor and prevent NSB light coming from large angles to enter the PMTs. The PMTs work with a power unit for the bias voltages with a peak voltage of 1250 V.

The PMTs generate an electrical signal converting and amplifying the signal of the photocathode. Such signal is afterwards converted (by Vertical Cavity Surface Emitting Lasers – VCSELs) into an analog optical signal that allows it to travel through long distances reducing dispersion of the signal and crosstalk effects.
Additionally, each camera is composed by following components:

- two cooling aluminum plates that keep stable the pixel temperature;
- several sensors to monitor the humidity and the temperature in the camera;
- two low voltage power supplies, one for each half of the camera;

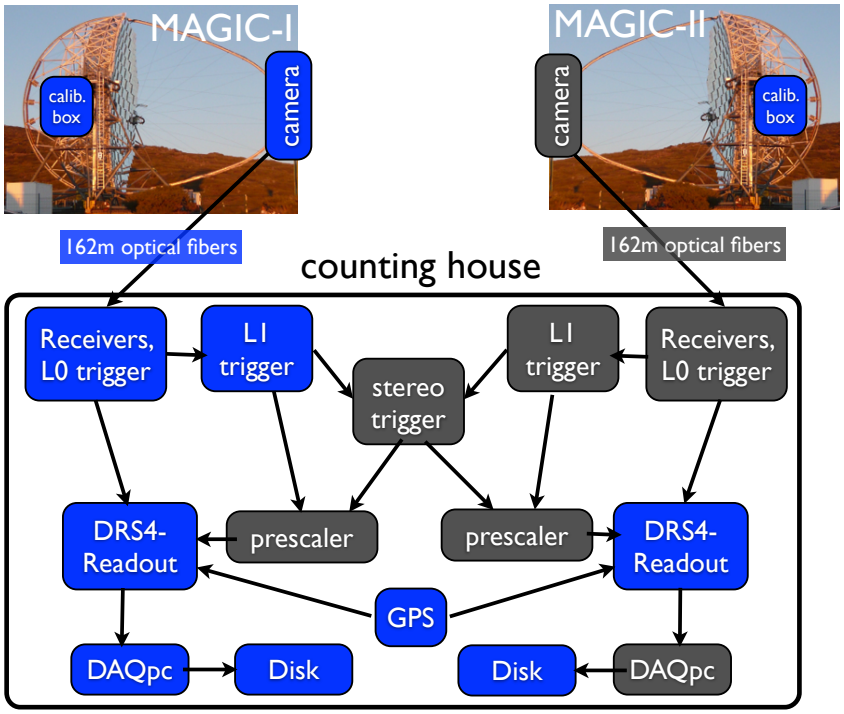

Figure 2.14: *Overview of the MAGIC electronic chain, from Aleksić et al. (2016a).*

- a drying unit to lower the humidity level;
- the camera lids, controlled by the lid drive box on the camera side. They are used to protect PMTs during day and during bad weather conditions (high wind or humidity, rain);
- starguider LEDs, used by the starguider camera to find the camera center.

During data taking operations, the shifters can monitor the status of the cameras through the LabView based programs `CaCo1` and `CaCo2` (CaCo stands for "Camera Control"). More details about the cameras are reported in Aleksić et al. (2016a).

2.4.1.4 MAGIC readout system

Here I report a brief overview of the MAGIC readout system, represented in **Figure** 2.14.

The PMTs in the camera provide an electric signal that is converted into an analog optical signal by the VCSELs. Some 162 m long optical fibers bring the signal from the PMTs base to the counting house (CH) in 19 bundles (72 fibers each) per telescope. The total time delay due to the propagation in the bundles is 138 ps, and is automatically corrected for by the trigger.

In the CH, the signal is then elaborated by the MAGIC Optical Nano-Second Trigger and Event Receiver (MONSTER or receiver boards, from now on I will simply refer to them as "receivers"). The receivers convert back the signal to an electric analog signal and split it into two branches:

- a digitization branch, where a DRS4 (Domino Ring Sampler version 4) based readout stores the signal waiting for the trigger decision (see Sections 2.4.1.5);
- a trigger branch, with two sub-branches: a digital one (L0 trigger, for trigger type details see Section 2.4.1.5) which is sent to the L1 trigger and a copy of the starting analog signal that can be sent to the Sum-Trigger (SUMT). After the first trigger decision (L1 or SUMT, one per telescope), the signal is digitalized and is sent through the L3 trigger (stereoscopic). If the L3 trigger is positive, the signals stored in the DRS4 buffers (one per telescope) are sent to the Data Acquisition System (DAQ) after being digitized by a standard Analog-to-Digital Converter (ADC). Eventually, the events are stored on disk.

The sampling of the events is provided by a system of two electronic boards: a motherboard or PULSAR board (developed at University of Chicago) and a DRS4 mezzanine designed at INFN/Pisa laboratory. The DRS4 acts as an ultra-fast analog memory composed of a ring buffer built out of 1024 switching capacitors that are read in the event of a trigger using a conventional 14-bit analog to digital converter Discriminator Threshold at low speed (32 MHz). The sampling frequency of the DRS4 chip is tunable and currently set at about 1.6 Gsamples/s. The mezzanine noise is dominated by the noise from the DRS4 chip. In total, the digitization electronics contributes to about 50% of the total noise.

The DRS4 chip requires a calibration with three corrections: the mean cell offset, the readout time lapse, and the signal arrival time. The first two are applied by the DAQ software (see Section 2.4.1.7), while the last is applied offline.

The calibration of the mean cell offset is performed through the pedestal calibration run, that is taken at the beginning of the night (and then subtracted from readout values) and allows to measure the average baseline of each capacitor (variations are up to 15% from cell to cell).

Finally, the time spreads due to the DRS4 chip (depending on the individual chip, between 1 and 4 ns) is corrected (recovering the actual arrival time) using calibration runs performed taken every night during data taking.

For more details on these electronics, see Sitarek et al. (2013).

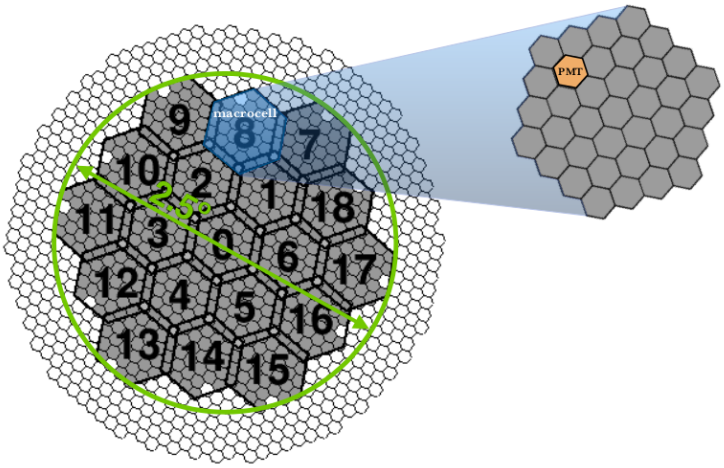

Figure 2.15: *Hexagonal L1 macrocells in the current MAGIC camera version. Adapted figure from Lopez-Coto (2016).*

2.4.1.5 Trigger

The trigger is a fundamental system allowing to discriminate the gamma-ray-induced cascades from the NSB, and thus lowering the total number of events that are registered by the readout system.

Here I report the main steps of the trigger that are valid for both old and current MAGIC cameras working in stereoscopic mode.

Level 0 (L0) trigger. This trigger is located in the receiver boards, and emits a squared signal every time the analog signal from an individual PMT overpasses a certain amplitude threshold, the so-called Discriminator Threshold (DT). The DT level can be different depending on the level of the moonlight: lower during dark observations and higher during the moonlight (or similar conditions of higher NSB of the sky). Since during observations the light conditions of the sky might change, the rate o each individual pixel is monitored online and the DT values are automatically continuously modified to keep a stable rate during variable light conditions.

Level 1 (L1) trigger. The L1 trigger works on the signal inputs given by the L0 trigger from each pixel, over 19 overlapping hexagonal cells that cover the entire camera, the so-called macrocells. Each macrocell is composed by 37 PMTs, and one of them is blind (see **Figure** 2.15). The main function of the L1 trigger is to find spatial and timing coincidence between closer pixels: when a number n of neighbouring pixels (called Next Neighbour, NN) in any macrocell, provides a signal above the DT, the L1 trigger sends a signal. The possible combinations of neighbouring pixels are for n=2, 3, 4 and 5. During standard stereoscopic observations, the trigger uses the 3NN configuration. Therefore, in stereo observations the L1 trigger is positive only when 3 closeby PMTs show a L0 signal. During mono observations, the L1 trigger uses a 4NN configuration, an the L1 signal from each macrocell is processed by a Trigger Processing Unit (TPU).

Level 3 (L3) trigger. During stereo observations, the signal from the two telescopes has to be analysed and compared: this is the function of the L3 trigger. The L3 receives

the output of the TPU, and if both the telescopes registered an event, the L3 trigger is positive. The signals are artificially stretched to 100 ns (to avoid misalignments of the telescopes) and delayed one with respect to the other accounting by the Az and Zd and the consequent different arrival times of the cascade in each telescope. If L1 signals from MAGIC I and MAGIC II are closer than 180 ns, then the event is accepted and the readout starts.

2.4.1.6 Sum-Trigger

The analog Sum-Trigger is a new type of trigger that has been invented and developed on the MAGIC telescopes. It was designed to lower the trigger threshold down to 25 GeV and observe many interesting objects such as some galactic sources (e.g. pulsars), high-redshift AGNs, and transient events (e.g. GRBs).

The main idea of this technique is to add up the signals from a group of neighbouring pixels (the so-called *macrocell*) and then apply a threshold to the summed signal. At this scope, the trigger region has been subdivided into three overlapping layers of hexagonal macrocells, as reported in **Figure** 2.16.

In this framework, all pixels within a macrocell contribute to the trigger decision, making non negligible also small photon signals that generally are below the sensitivity of the standard trigger. For this reason, the Sum-Trigger improves the signal to noise ratio (shower signal to NSB), and allows MAGIC to study the energy region at few tens of GeV.

For a complete presentation of the Sum-Trigger on the MAGIC telescopes, see García et al. (2014).

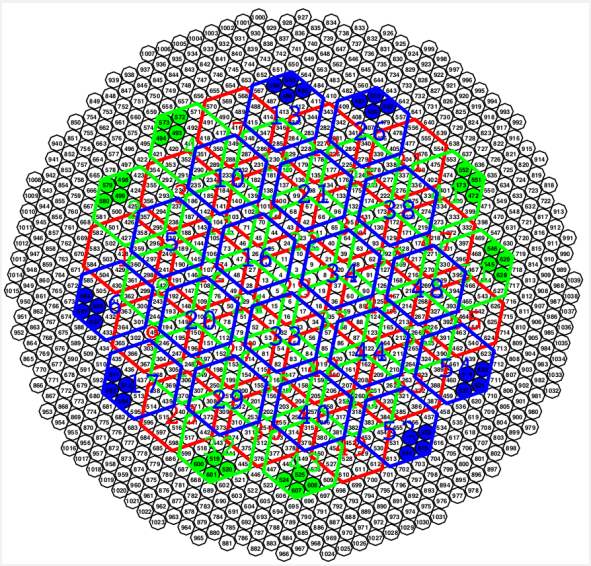

Figure 2.16: *Layout of the trigger region of Sum-Trigger. Each color represents one of the three different layers. Adapted figure from García et al. (2014).*

2.4.1.7 Data acquisition system

If a trigger is issued, the data stored in the DRS4 chips are sent to the data acquisition system (DAQ). The DAQ computers run a program called `Domino4Readout` that performs the following operations:

- reads the data packets from the DRS4 boards and builds the complete event;
- applies corrections and calibration of the DRS4 chips response, as described in the previous Section;
- stores the data on disk;
- sends charge and arrival time information for each event to the MOLA program, see Section 2.4.2.3.

For more details, see Tescaro et al. (2013).

2.4.1.8 Operational safety and weather limits

The MAGIC telescopes operations have to be monitored against natural dangers that could damage the telescopes. For this reason, some safety limits must be respected at all times: if any of them is not fulfilled, the telescopes cannot be started up, or the observations have to be interrupted and the telescope brought in a secure state. The safe position of the telescopes under bad weather is generally fulfilled by putting them in park position and secured with a sufficient number of bolts, which are manually removed by the shifters before switching on the motor power and taking data.

Some of the main limits on the local weather conditions are

- mean wind speed below 50 km/h;
- wind gusts speed below 40 km/h (a lower value with regards to maximum mean wind speed in order to avoid impulsive forces acting on the camera);
- humidity must be $< 90\%$, with an absolute limit of 98% to operate hardware at high voltage;
- no rain, snow, and ice.

Additionally, there are some safety reasons that have to be followed. For example, the drive system is automatically stopped to avoid the movement if the fence around the telescopes is open (i.e. somebody is inside the telescopes area).

When these safety conditions related to the operations and to the weather are fulfilled, the telescope can start observations. During observations, there are other guidelines that avoid the damage of the telescopes, and they are reported in Section 2.4.1.9.

Some instruments let the shifters to control the online developments of the weather conditions. I report some of the main instruments in the next Section.

2.4.1.9 Other weather-related subsystems

During observations, the shifters have to monitor the weather in order to and keep safe conditions for the people and for the telescopes. In order to let them evaluate continuously the conditions, here I report some of the main subsystems that help the shifters during

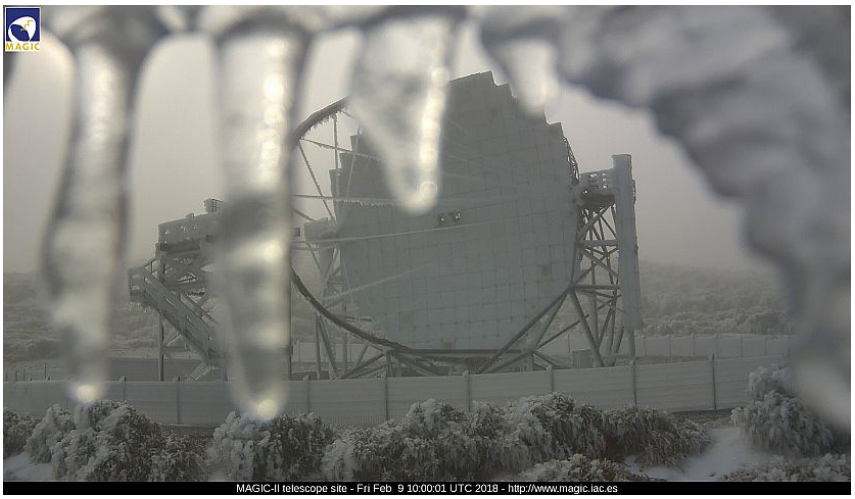

Figure 2.17: *Webcam picture representing MAGIC after a bad weather night.*

observations. They allow to evaluate if observations can be performed, and if the data must to be processed in the post-analysis reduction in order to correct them.

These main subsystems are: the weather station, the pyrometer, the LIDAR (LIght Detection And Ranging), and the AllSky camera.

Weather station
The weather station on the roof of the counting house measures the atmospheric state variables every two seconds. The current weather information as the weather website are monitored through an online system called ATCAguard.

Some of the main information reported in the corresponding screens are:

- Time and summary of current data in a scroll on the bottom,
- Alerts and warnings in a special report box,
- Temperature and dew point,
- Relative humidity,
- Wind speed,
- Cloud satellite,
- Most recent LIDAR data,
- Most recent AllSky Camera image,
- Wind rose,
- Wind direction,
- Dust concentration of the TNG,

Figure 2.18: *The LIDAR mounted on the roof of the MAGIC counting house.*

- Transmission from the LIDAR,
- Transmission from the SBIG images,
- Cloudiness from the pyrometer,
- Cloud base height from the pyrometer,
- Weather at other ORM telescopes in a secondary window.

MAGIC telescopes can operate only if the safety conditions are fulfilled.

Pyrometer
The pyrometer is installed on the dish of the M1 telescope and points to the same direction of the telescope. Measuring the temperature of the sky, it provides an estimation of the atmospheric transparency and the cloudiness parameter. The latter parameter is provided by measuring the IR radiation (in the 8-14 μm band) fitted with a black-body spectrum, obtaining this way the temperature of the sky. The measured temperature increases if the sky is cloudy, because it reflects radiation from the ground. Thus, an estimation of the cloudiness (higher cloudiness implies lower transparency) is given by:

$$\frac{T_{\rm low} - T_{\rm m}}{T_{\rm low} - T_{\rm up}} \ , \tag{2.2}$$

where $T_{\rm low}$ and $T_{\rm up}$ correspond to the temperature of the sky at its worst and best conditions, respectively, which are set to $T_{\rm low} = 250$ K and $T_{\rm up} = 200$ K. T m is the measured temperature by the pyrometer.

LIDAR
The LIDAR system, located in a dome on the roof of the counting house, is able to measure the transparency of the atmosphere and provide a ratio between cloud/aerosol scattering and molecular scattering. The pulsed light from the laser is backscattered by the clouds

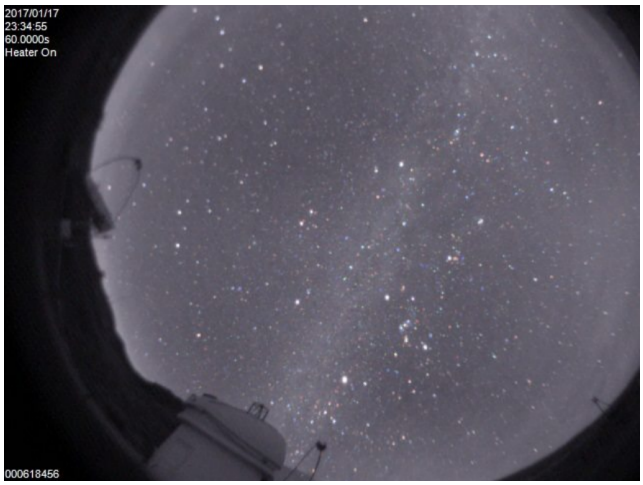

Figure 2.19: *An example of image taken with the AllSky camera mounted on the roof of the MAGIC counting house.*

and aerosols in the sky. The transparency is measured as a function of the arrival time distribution of the backscattered photons. The LIDAR can provide transmission estimation at different altitudes of 3, 6, 9, and 12 km (Fruck et al., 2014), but the most interesting one for the analysis of MAGIC data is the one at 9 km, that is where most of the Cherenkov showers form.

The LIDAR is a single-wavelength elastic Rayleigh LIDAR that operates at 532 nm wavelength, a value that is close to the Cherenkov spectrum peak at about 330 nm. However, the slightly different wavelength - in addition to the fact that LIDAR shoots the laser at a position shifted by 4 deg from the observing source - is in order not to interfere with the MAGIC telescope observations.

Its laser pulses with an energy of 5μJ and a repetition rate is 1 kHz. It fires 25000 laser shots with a frequency of 500 Hz and hence, each data run takes around 2 min and another 30 sec to analyse the data. A new run is performed every 4 min, and the telescope takes data continuously during the night.

The backscattered light is collected by a 60 cm diameter mirror with 150 cm focal length and focused on the detector module. The data are analysed and recorder in the very same files where MAGIC data are recorded.

All-Sky Camera

The AllSky Camera is mounted on the roof of the counting house, close to the weather station and the LIDAR tower. It points to the Zd and takes a long-exposure picture (60 s) of the sky every 2 min. It has complete FoV of 360 deg in Az and almost 90 deg in Zd. These images are monitored online during observations.

2.4.2 Introduction to data taking

2.4.2.1 The data taking shift and roles of the shifters

Since 2004, the MAGIC telescopes have been operating with more than 200 periods of data taking collected in 14 yearly cycles of observations. Such periods are almost 28-days long, based on the lunar cycle.

During each period, a shift crew of 4 people (5 in some periods during winter) executes the observations. Such people are chosen belonging to the MAGIC Collaboration in such a way that each of the members of the Collaboration respect this duty once per year, with exceptions for people with other organizational duties. The source schedule is prepared in advance by the MAGIC scheduling group, and the shifters have to monitor the weather and telescopes conditions in such a way to perform the required observations.

The shift crew is subdivided in different roles, considering the experience of the people. Two Operators (two per shift) are usually non-experienced scientists, often at the site for the first time, and they have to learn all the procedures regarding the safety and the data taking. They are supervised by two Deputy Shift Leaders (DSLs), who has been on the island at least once and have demonstrated good comprehension of the procedures. In the shift crew, the main responsibilities (safety, decision taking, teaching to the other shifters) are attributed to the Shift Leader (SL), the more experienced person among the shifters. The roles – in general – are progressive, and usually after one shift everyone is judged by a specific committee in the MAGIC Collaboration and in case upgraded to the next role. During my PhD course, I had the opportunity to be directly upgraded by Operator (first year, 2016) to Shift leader of the MAGIC shift (2017 and 2018).

In order to keep a good maintenance of the telescopes during the long-term period, on the island there are two senior postdocs. They are people in charge of the maintenance of the telescopes, and they are on call during the night if some particular problem occurs. The two postdocs help the technicians that work on the telescopes and have a good knowledge of all the subsystems and instruct the shifters about the safety rules at the beginning of the shift.

During a yearly cycle of observations, MAGIC can observe both during dark time and during moon time (with some limits). The average efficiency of the MAGIC observations, meaning the fraction of dark time actually observed, is usually around 60%. Thanks to advanced techniques of image cleaning, the MAGIC telescopes can operate also during moonlight and twilight time. The analysis in this case is non-standard: it allows the telescopes to increase up to 40% the duty cycle of the telescopes at the price of an higher energy threshold.

More information about the analysis of such data is reported in Section 2.4.3.12.

2.4.2.2 Pointing modes

The data taking of the MAGIC telescopes can be operated with two different pointing modes: the ON mode and the wobble mode.

ON mode In this mode, the telescopes are pointing directly to the position of the source in the sky, and the target lies always in the center of the camera. The background estimation is obtained by performing a second observation called OFF observation: a patch of the sky without (known) gamma-ray sources with the same zenith and azimuth distribution (or as close as possible) is observed for the same time as the ON observation. The crucial point of such observations is that the background in the ON observation is the same as the one in the OFF observation. Such criterion might be not fulfilled due to possibly different data-taking conditions (also during the same night)

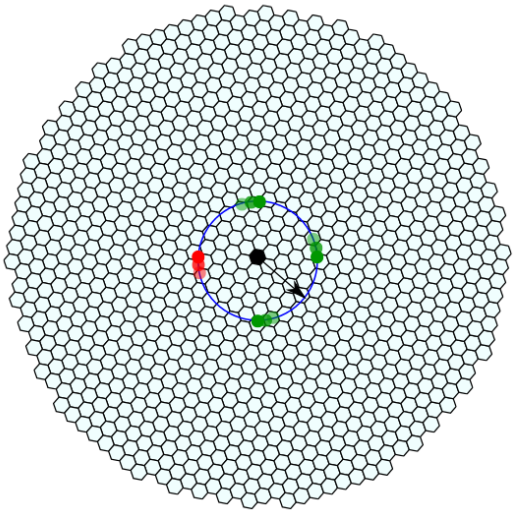

Figure 2.20: *The wobble pointing mode as seen in the camera plane for one wobble. The blue circle has a radius of 0.4 degree, the standard value of the used offset. In this case, 3 OFF regions are used. Credits: MAGIC Collaboration.*

between the ON and the OFF pointing positions. The OFF observations can also be affected when performed on different portions of the sky with different backgrounds (like extragalactic and galactic fields). Apart from the difficulty of obtaining a reliable OFF dataset, one of the main cons of such method is that every source need twice the time that is allocated for it (one for ON observations, one for OFF observations).

Wobble mode In this mode, the telescopes are not pointing directly to the position of the source in the sky, and the target lies always with a predefined offset with respect to the center of the camera. This offset is optimized using MC simulations: for point-like sources, MAGIC uses a standard offset of 0.4 degree, but it can be increased in the case of observations of extended sources. In order to account for the inhomogeneous response of the camera and to have an unbiased estimation of the background, the wobble observations are performed for equal times at opposite offset positions with respect the center of the camera. Such opposite positions are called wobble positions and in standard observations are at 0 and 90 degrees for W1 and W2 wobbles respectively, and at 180 and 270 degrees for W3 and W4 wobbles respectively. So the observation of the target usually starts with W1, then switches to W2, then W3, and finally W4. After that, the cycle repeats up to cover the entire observation slot of the source.
The advantage of wobble observations is that the signal and the background from the source are collected at the same time under the same conditions. The cons is that the efficiency of the camera can be slightly lower in registering signals in a not centred position of the camera. With regards to the MC events that are used to analyse such wobble data, they are called ring wobble MCs: this because during the observation, the tracked source follows in the camera an arc of circle of radius equal to the used offset.

2.4.2.3 Online information subsystems

GRB alert subsystem

As detailed in Chapter 1, there is a number of transient events that MAGIC is able to follow only if fast enough in the repositioning to the incoming direction of the transient event. In MAGIC, there is a program named `GSPOT` (Gamma Sources POinting Trigger, Galante 2006) that runs continuously during standard observations and allows the evaluation of the possible follow-up of the transient event and, in case of positive conditions, it can automatically repoint the telescopes to that direction. This program was though for GRB alerts, but it is now adapted also to the follow-up observations of astrophysical events related to the emission of gravitational waves and neutrinos emission.

The detection of VHE gamma-ray emission from transient events is one of the Key Observational Program (KOP) of the MAGIC experiment. The observation of transient events by IACTs is intrinsically difficult due to several reasons:

- the transient events occur unpredictably in any position of the sky. Conversely, the IACTs have a limited field of view (e.g. 3.5 deg for MAGIC) compared to satellite-based instruments (which can cover almost all sky in any moment), and while they are observing a certain source they are not immediate in repointing the telescopes and changing the techinal tools in order to perform good observations in the sky position of incoming direction of the transient events. This intrinsic limit implies that IACTs need an external trigger provided by satellite instruments to know the location of potentially observable GRBs;

- GRBs can happen both during the day and during the night, or during bad weather conditions at the MAGIC site, or even in a point of the sky that is not visible by MAGIC (e.g. under the horizon, or behind the mountains). This of course limits the chance to observe an interesting transient events, and a first exam of the direction of such events is essential in order to understand if they are observable before interrupting automatically the observations and repointing the telescopes;

- some events like GRBs are probably produced by cosmological sources, with median redshift of $z \sim 2$. This implies that there is a strong absorption of the gamma-ray flux by effect of the interaction of gamma rays with the extragalactic background light, and the possibility of catching the VHE emission is reduced.

Considering the previous points, the follow-up observation of transient events is generally performed as follows. The MAGIC telescopes is part of the Gamma-ray Coordinates Network (GCN), that is a system that distributes real-time information (called notices) about the direction of an incoming GRB detected by space-based instruments (e.g. *Swift, Fermi*, INTEGRAL ecc.). The notices stimulate follow-up observations that may be performed by ground-based and space-based observatories. The GCN system also automatically receives and distributes messages, called circulars, that inform about the performed follow-up observations. A dedicated web page[6], usually called the Burst Monitor, is available for the MAGIC operators to check the connection status to the GCN and the info about the last GCN packet received. When a GCN-notice is received by MAGIC, the software `GSPOT` evaluates if the events is observable from the MAGIC site and if the observation conditions are good enough to observe it. The latter condition is related to observational criteria (the so-called GRB strategy) such as the zenith distribution of the event, its time of observation, constraints on the physical properties producing them, etc. If the criteria are met, `GSPOT` will interact

[6] http://www.magic.iac.es/site/grbm/index.html

with the telescopes software in order to automatically repoint the telescopes to the transient event position and start the follow-up.

MOLA

The analysis of MAGIC data requests several step that have to be performed in a dedicated off-line analysis. However, the operators that are performing the data taking with the MAGIC telescopes are interested in having a first rough evaluation of the signal that the telescopes are registering from a certain source. For example, in the case the current source is flaring (i.e., the flux gets higher and more variable in a very short time during the observations), the observation might be extended in order to get the maximum signal and perform variability studies. A preliminary real time analysis is also particularly interesting for the whole community of the observatories: if the MAGIC telescopes register an enhanced activity from a certain source that might be interesting, preliminary results might be used to issue alerts to other observatories which could perform follow-up observations of the source. In MAGIC, the real-time analysis is performed by MOLA (MAGIC On-Line Analysis, Tescaro et al. 2013). MOLA is a multi-threaded C++ program which evaluates the charge and arrival time for each pixel of the camera evaluated from the two DAQ systems independently. MOLA performs the first steps of the standard MAGIC analysis through the calibration and the image parameters calculation. Its so-called "analysis thread" performs the stereo analysis and the gamma/hadron separation, and finally provides the high-level analysis results like the θ^2 plots, the sky maps and the light curves.

This first analysis is performed in two energy ranges: the Low Energy (LE) band when the image size is greater than 40 phe, and the High Energy (HE) band when image size is greater than 125 phe. These two energy bands correspond roughly to threshold like 110 GeV (for the LE band) and 350 GeV (for the HE band) that are normally obtained during Crab Nebula observations at low zenith. The sensitivity that MOLA can register is about 1% of the Crab Nebula flux in 50 h.

On-Site Analysis

The raw data that are collected with the MAGIC telescopes when observing are temporarly stored in La Palma, and then sent the following morning to the permanent data storage at the Port d'Informaci'o Cientifica (PIC) in Barcelona. However, since the size of the data is considerable, the transferring process takes a lot of time (several hours).

In order to overcome to this problem, a dedicated software called `On-Site Analysis (OSA)` software has been installed in La Palma. The OSA sofware is always running in some machines called `ana`, and reduces the data size by performing the standard MAGIC analysis as soon as raw data and metadata from the DAQ or reports from SuperArehucas are available. The OSA analysis is managed through several jobs that are executed in parallel with a proper distribution of CPU resources. At the moment, the OSA reduces the data up to the superstar level for the usage of all the general analyses. In the case the analysers need to work on data taken under dark conditions, they can start directly downloading the already ready superstar data. Conversely, if they need to analyse data taken during moon light, they will download the calibrated files: in this step the OSA helps greatly for example because the conversion and calibration of the raw files is done on site and the analyzers do not have to download several gigabytes of data.

The following steps of the analysis require RFs for the reconstruction of the energy and the direction of events. However, this is a problem for example in the case of transient events or flaring sources follow-up observations performed during the night: the real-time analysis performed by MOLA is indeed very preliminary, and available only for very standard dark

observations.

For this reason, the OSA software provides also the following steps of the analysis, that are performed only for a first glance at the resulting data. These first results are available at the very beginning of the following mornings in the form of high-level results i.e. θ^2 plots, sky maps, light curves, and spectra, and this helps a lot in a first evaluation of the signal obtained during the night. In case of interesting observations or follow-up, during the days some analyser will perform a detailed off-line analysis in order to obtain robust estimations of the signal with proper RFs and tools.

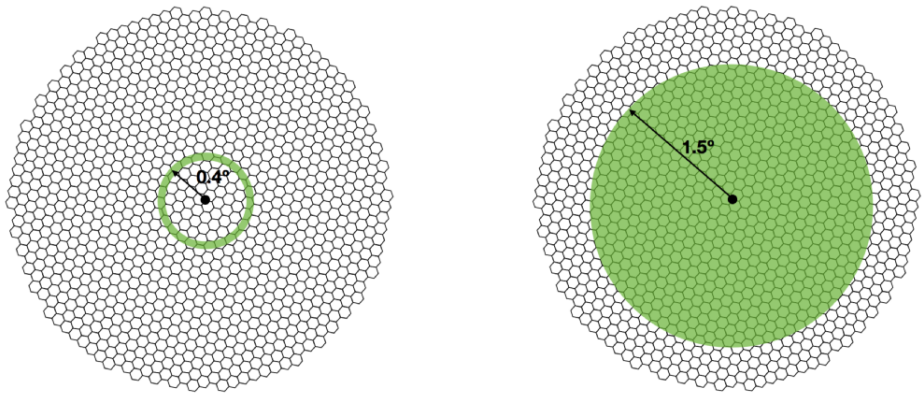

Figure 2.21: *The MC modes: ringwobble MC mode on the left, and diffuse MC mode on the right. Credits: MAGIC Collaboration.*

2.4.3 Data analysis chain

The MAGIC Collaboration has developed a dedicated software able to analyse the data obtained by observing with the MAGIC telescopes. Such software is called MARS (MAGIC Analysis Reconstruction Software, see Zanin 2013), an it is written in an object-oriented ROOT framework, whose main language is the C++. The MARS software has always been updated and developed, keeping the compatibility with the previous version of the software (for example one can still analyse data taken in mono mode with the current version of the software). At the current version (V2-19-3), MARS has reached about 40 executables that use more than 900 classes, for a total of more than 700000 lines of code.

In this Section, I will summarize how the reconstruction of the events is performed in the MAGIC software. It can be mainly subdivided in three levels:

- **Low level:** at this stage, the raw data from each telescope are calibrated and cleaned. The Hillas parameter are also estimated.
- **Intermediate level:** in this phase, the data from the two telescopes are merged and the stereoscopic information estimated. For each event, the energy and arrival direction is associated. direction of the events;
- **High level:** represents here the highest level of the analysis, that is the production of sky maps, signal search, spectrum, and light curve calculation.

The intermediate and high-level analyses are commonly performed in the standard off-line analysis chain, while the low level is generally performed by the On-Site Analysis chain (OSA, see Section 2.4.1.9), and it has to be performed by the analyser only during non-standard analyses like when dealing with moon data.

2.4.3.1 Monte Carlo data

The analysis of real data taken with the IACTs is based on the production of appropriate Monte Carlo (MC) simulations. The MAGIC Collaboration uses a modified version of CORSIKA (COsmic Ray SImulations for KAscade, Heck et al. 1998) called `mmcs`, to produce

Name	Period
ST.03.03	from 2013-07-27 to 2014-06-18
	and from 2014-07-05 to 2014-08-05
ST.03.04	from 2014-06-19 to 2014-07-04
ST.03.05	from 2014-08-31 to 2014-11-22
ST.03.06	from 2014-11-24 to 2016-04-28
ST.03.07	from 2016-04-29 to 2017.08.02
ST.03.08	from 2017.08.02 to 2017.11.02
ST.03.09	same as ST.03.07
	from 2017.11.02 to 2018.06.29
ST.03.10	after 2018.06.30

Table 2.4: *List of the main MC periods used in this Thesis and corresponding time intervals.*

the MC simulations of the Cherenkov photons produced in a electromagnetic shower in order to reconstruct the energy of the primary gamma ray and its arrival direction, as described in Majumdar et al. (2005).

In MAGIC, the MC gamma rays are simulated by means of two main methods:

- **ringwobble MCs:** they simulate a ring of 0.4° radius (with a width of 0.1°) from the center of the camera, accounting for the 0.4° offset used in the standard wobble mode. This set of MC is mainly used for the analysis of point-like sources;
- **diffuse MCs:** they are generally used to study extended sources or sources shifted from the nominal position. In this case, diffuse gamma rays are simulated covering a circle of 1.5° radius.

In **Figure** 2.21 I show a simplified view of both types of MCs.

I provide separated MC data for the following different Zd ranges:

- low Zd range (5° - 35°);
- medium Zd range (35°- 50°);
- high Zd range (50° - 62°);
- and very-high Zd range (62° - 70°).

The initial spectrum of the gamma rays is a power law with spectral index equal to $\gamma = -1.6$.

Once the MC Cherenkov photons are produced by the CORSIKA simulation, their propagation and absorption in the atmosphere is computed with the `reflector` program. Such program processes the MC photons by considering also the reflectivity of the mirrors, and it records the position and time of the incoming photons when arriving at the camera. After that, another program called `camera` reconstructs the response of the PMTs and of the whole electronic chain, taking into account also the noise from NSB and electronics. At the

Program	Task
Sorcerer	Calibration signal-extraction (current program)
Star	Image-cleaning Hillas-parameters
SuperStar	Stereo-reconstruction
Melibea	Direction and energy reconstruction, hadroness estimation
Flute	Flux, spectrum and lightcurve estimation
Fold	Spectrum fitting using forward-folding Poissonian Likelihood maximization
Odie	θ^2 plot production
Caspar	2D skymap production
CombUnfold.C	Unfolding of energy spectra
Coach	Random Forest training

Table 2.5: *List of the main routines of the MAGIC MARS software.*

end of the whole simulation chain, the events are saved in ROOT files and can be analysed like real data with MARS.

Since the MC simulations consider all the hardware chain, when the telescopes need particular maintenance or updates in their hardware, the MC simulations have to be upgraded. In the history of MAGIC, several different MC productions have been processed depending on the telescope and hardware status.

In MAGIC, the different MC productions for different analysis periods are tagged as ST.XX.YY, where ST means "stereo" , XX defines major hardware changes (it is equal to 03 for data after the 2012-2013 upgrade) and YY is the analysis period corresponding to minor changes in the hardware. In this Thesis, I made use of several MC productions in order to analyse long-term observations of some sources reported in Chapters 5 and 6, and they are summarized in **Table** 2.4.

2.4.3.2 Calibration

The MAGIC raw files contain the information coming from the FADC or ADC (counts as a function of time), that is the waveforms of the signal for each event and for each pixel. To be able to analyze the raw files, one needs to convert them into ROOT format. This conversion is made by a program called `merpp` (MERging and Prepoccesing Program), which also attaches other subsystems reports to the ROOT files.

The first step in the analysis chain is represented by the signal extraction: in fact, the signal has to be interpreted in such a way to compute the charge in photoelectrons that actually hits the PMT and the arrival time of the signals. The waveform in the FADCs is converted into 50 time bins of 0.5 ns each, and is composed by the signal and the baseline of the waveform. In order to extract the signal only, the baseline can be estimated using the so-called pedestal events, i.e. events with random triggers and so without any pulse taken during a technical run at the beginning of each source observation and during data taking. To estimate the baseline, the signal from each time slice is binned into a single histogram and fitted with a gaussian, whose mean is taken as the baseline. When the baseline is known, the signal can be extracted. After the signal extraction, the measured charge is calibrated to obtain the conversion in photoelectrons through the *F-Factor method* (Mirzoyan, 1997). For more details, see Aliu et al. (2008).

The MARS executable taking care of the whole calibration process is `sorcerer` (Simple, Outright Raw Calibration; Easy, Reliable Extraction Routines).

2.4.3.3 Image cleaning and parametrization

Considering that generally the image of the shower in the camera covers only a small part of the total surface, the following steps of the data analysis have to clean the signal coming from pixels where only random noise from NSB, electronic noise, and light from stars, are present. This step of image cleaning, together with the image parametrization, is performed by the MARS executable `star` (STandard Analysis and image Reconstruction).

In MAGIC, several cleaning algorithms were developed across the years, depending on the hardware configurations. For stereo data taken after the major MAGIC upgrade, the default cleaning method is divided in two steps, see Aleksić et al. (2012b) for details:

sum image cleaning: with this method, the signals are first clipped (to reduce biases due to after-pulses and strong NSB fluctuations) in amplitude and possible combinations of 2, 3, or 4 (usually referred as 2NN, 3NN and 4NN respectively) compact neighboring pixels are identified. The pixels of each combination are not discarded if the sum of their charge is above a certain threshold and the difference between the time of arrival of the pixels is within a predefined time window. Given the number of neighboring pixels, the values for the charge threshold and the time difference change, becoming more relaxed for larger groups.

time-constrained absolute image cleaning: this method is applied after the sum cleaning method, and the survived pixels are tagged as core (or boundary) pixels. This procedure selects pixels with charge greater than a reference value Q_{core}, and they are tagged as `core pixels` if at least one neighbour pixel survived the previous step. Then, the program computes the mean time of arrival for the core pixels forming the main island of the image, and it is rejected if it is outside a time window of 4.5 ns. Finally, the `boundary pixels` are selected: they has to have a core pixel as a neighbour, charge above a second reference level Q_{boundary}, and time difference with respect to the core pixels within 1.5 ns.

The star program is able also to remove "hot" pixels produced in the camera by bright stars in the FoV, that produce high signal in one of more pixels.
In **Figure** 2.22, I report an example of events before and after the image cleaning.

After the image cleaning process, the images can be parametrized with the computation of the so-called image parameters. Some of these parameters were introduced by Hillas (1984) for the first time to discriminate between hadron and gamma initiated showers.

In **Table** 2.6 I report a list of the main image parameters that are reconstructed by the star program in the image parametrization.

Parameter	Description
size	total number of photoelectrons in the image.
	At zero-order approximation, it is proportional to the energy of the primary particle
length	half length of the major axis of the ellipse
width	half of the minor axis of the ellipse
alpha	angle between the major axis of the ellipse and the line
	connecting the reference point and the center of gravity
center of gravity	coordinates X and Y in the camera reference frame representing
	the center of gravity of the shower image
conc-n	given the n brightest pixels, it represents the fraction of photoelectrons
	contained in those pixels
asym	difference between the peak of the charge distribution in the image and the center of gravity
number of islands	number of different islands of the image, defining an island as a group of isolated
	pixels survived after the cleaning)
leakage	given the last 1/2 camera pixel rings, it is the fraction of signal
	distributed in them with respect to the image size
M3long	third momentum of the image along the major axis of the ellipse
dist	distance of the center of gravity from the reference point
time-gradient	angular coefficient of the linear function used to fit the arrival time distribution
	of each pixel after their coordinates have been projected on the major axis of the ellipse
time-rms	spread of the arrival time distribution of the pixels belonging to the image

Table 2.6: *List of the main parameters used by the* star *routine of the MAGIC MARS software.*

2.4.3.4 Stereo parameters reconstruction

The data analysis up to this step is performed individually for each of the telescopes. The superstar programme takes care of combining the information coming from each telescope in order to reconstruct a 3D image of the Cherenkov shower, by calculating the so-called stereo parameters.

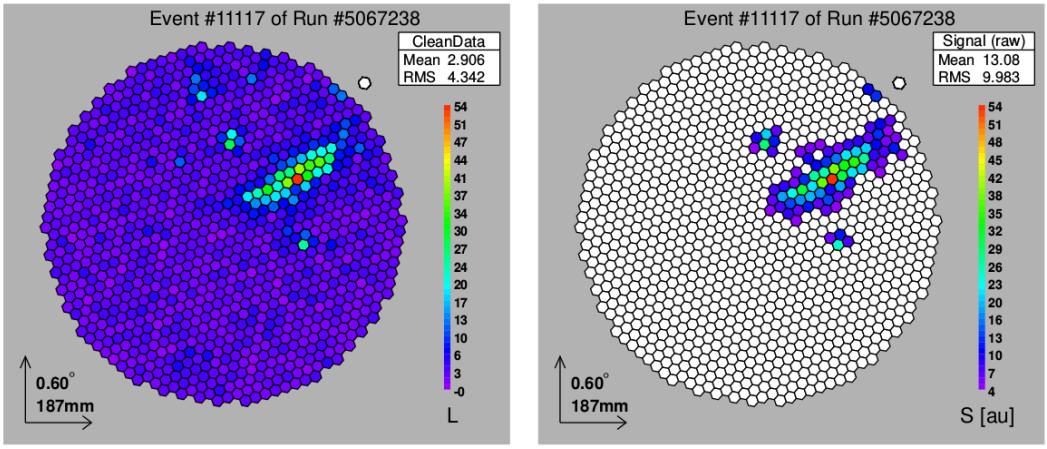

Figure 2.22: *Example of the image cleaning process: on the left the raw signal coming from the camera, and on the right the camera signal cleaned without the average background.*

Here I report some of the most relevant stereo parameters:

shower axis: from the intersection of the major axes of the two images of the shower in the camera, the direction of the incoming shower can be reconstructed. The impact point will be the projection of the direction axis on the ground (taking into account the distance between the two telescopes). The shower axis direction is particularly important in order to verify the detection of a source and the amount of signal we are detecting (please see Section 2.4.3.7);

impact parameter: it is the perpendicular distance between the shower axis and the telescope pointing axis;

shower maximum height: the estimation of the height at which the shower had its maximum;

Cherenkov radius and density: they are the radius and density of the Cherenkov light pool on the ground;

2.4.3.5 Data selection

The data selection is a particularly important step in every MAGIC analysis, and it is performed by the `quate` program.

Some of the main selections are:

atmospheric transparency: atmospheric conditions can affect the air shower development and detection. For more information on the analysis under bad weather conditions, please see Section 2.4.3.12;

observations conditions: when the observations are performed with particular filters, trigger, or under enhanced moon conditions. In this case, particular analysis has to be performed and in the standard analysis they are removed;

intrinsically bad quality data: for example when data are affected by hardware failures, or when there are cars passing at the MAGIC site (the so-called car flashes, increasing the trigger rate for few seconds).

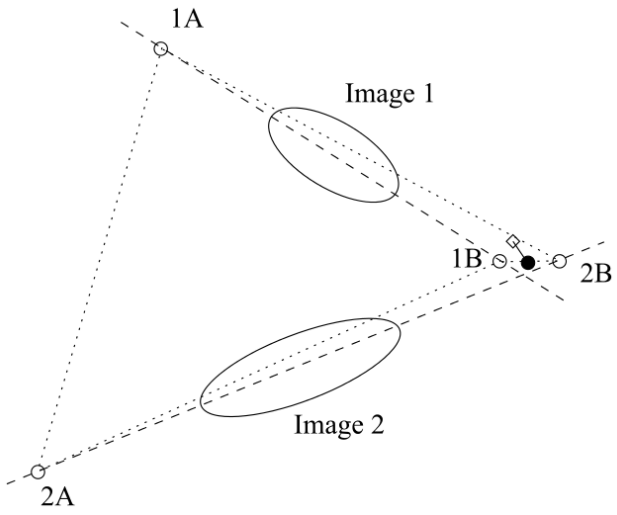

Figure 2.23: *Graphical representation of the DISP method for the reconstruction of the arrival direction of the events. Given two images for the same event, there will be four reconstructed source positions, denoted by empty circles. The angular distances between them are shown by dotted lines: the closest pair is chosen (in this example 1B-2B) and their weighted average is taken as the final reconstructed position for the source (black dot). The solid line is θ, the angular distance between the true (empty diamond) and reconstructed position of the source. From Aleksić et al. (2016b).*

2.4.3.6 Event characterization

Gamma/hadron separation

In Section 2.4.3.3, the reader was introduced to the shower image parametrization, that turns out to be a powerful tool to discriminate among the different types of events that can trigger the IACTs (accidental triggers, muons, hadrons and gamma rays). After that step, the analysis needs a robust tool in order to select the events that are likely gamma rays. In MAGIC this is done through a machine learning method based on MC information, called Random Forest method (RF, Albert et al. 2008). This method is used to compute a parameter called hadronness, that correlates with the chance probability for the event of being produced by a hadron-like cascade. This procedure is based on a statistical basis, because the number of background events is always much higher than that of gamma-ray events: even for strong gamma-ray sources, the background is dominant.

The RF training, performed by the `coach` program, needs the following information as input:

- a sample of pure gamma-rays, provided through simulation with CORSIKA (Heck et al., 1998);
- a sample of (almost) pure hadronic cascades, extracted from previously background observations (e.g. the so-called Dark Patches), where no significant gamma-ray signal is expected;
- a list of shower parameters containing the relevant separation information to grow the decision trees that allow the separation between gamma rays and hadronic showers in bins of size, zenith angle, azimuth, etc.

Energy range	$E_{\rm thr}$	θ^2	Hadronness	Size in M1	Size in M2
Low energy (LE)	100	<0.02	<0.28	>60	>60
Full range (FR)	250	<0.009	<0.16	>300	>300
High energy (HE)	1000	<0.007	<0.1	>400	>400

Table 2.7: *Standard cuts for the different energy ranges in the MAGIC analysis.*

Energy estimation

The standard method to provide the energy estimation of the events in MAGIC is represented by the Look-Up Tables (LUTs). In this method, the sample of gamma MC is binned in some image parameters, and for each bin the mean energy and RMS of the MCs is computed. A real event can be attributed to one of these bins, and consequently it acquires the related energy.

Actually this process proceeds through different approximation stages. The first assumption in this method is that the energy of the primary particle is proportional to the number of Cherenkov photons in the shower, and this zero-order approximation translates in a proportionality between the energy and the size of the images. After that, the table is filled with corrections of E/size instead of the true energy (first order). Finally, small corrections are applied based on atmospheric optical depth, geomagnetic field, and image leakage.

Finally, some additional small corrections based on the zenith angle (important at high zenith angles, where the Cherenkov light gets more absorbed), leakage and geomagnetic field are applied assuming that they do not depend on other parameters.

Arrival direction estimation

The arrival direction of the primary gamma ray with respect to the produced electromagnetic shower can be determined with the so-called DISP (from Distance between the Image centroid and the Source Position, Aleksić et al. 2016b) RF method.

In order to reconstruct, on a event-by-event basis, the angle between the direction of the shower maximum of each event and the incident direction of the gamma-ray or source position, the method uses the shape of the image as seen by an individual telescope.

Once the DISP is known, the reconstructed source position is not unequivocally determined: there are two possible solutions along the major axis of the ellipse. Though in the mono observations (originally designed for) this head-tail discrimination (or ghost busting problem) lead to about 10-20% of wrong parametrization of the shower, in its implementation the MAGIC telescopes it has been successfully solved in the stereo observations.

2.4.3.7 Signal search

Here I describe the two main routines that allow the analyser to look for excesses in the field of view and in determining their statistical significance.

Sky map

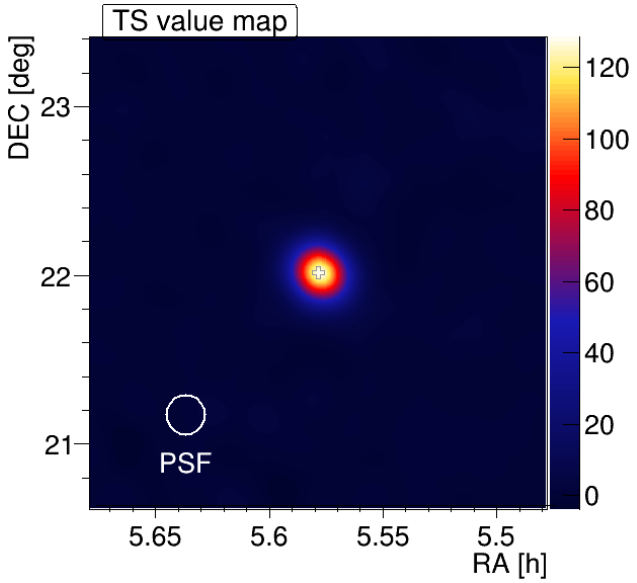

Figure 2.24: *Example of TS sky map produced on the source Crab nebula with the MARS software.*

The signal search in the field of view of the telescopes can be performed also by means of **sky maps**, that are two-dimensional representations of the incoming direction of gamma-like events. They are usually projected in the sky (either in azimuthal or equatorial coordinates) within the FoV of the instrument. They can be used also to look for other signals in the field of view, or to verify the extension of the signal (i.e. in the case of galactic sources).

The events recorded by MAGIC are selected through the standard cuts applied to the data (as those shown in **Table** 2.7), and then analysed and plotted by the program called `caspar`. An example of sky map is reported in **Figure** 2.24.

In producing a sky map, the most difficult task is to produce a reliable background estimation. In fact, the inhomogeneities in the pixel response, stars in the FoV and observations at different Zd and Az, affect the estimation of the background. In the wobble observations, the background can be extracted from the same data sample as the signal, avoiding contamination from the signal region and correcting the camera inhomogeneities

In order to compute the significance of a signal in a sky map, we use the Test Statistics (TS) significance, which is the Li&Ma significance (Li & Ma, 1983) applied on a smoothed and modelled background estimate.

Considering the signal and background sky maps, the excesses histogram is obtained by subtracting the signal sky map from the background one. Such histogram is smoothed by using the instrument PSF added in quadrature with a Gaussian kernel to smear the obtained number of excesses.

The σ_{smooth} smooth used to smear the excesses histogram is given by

$$\sigma_{\text{smooth}} = \sqrt{\sigma^2_{\text{PSF}} + \sigma^2_{\text{Kernel}}} \, ,$$

where σ_{Kernel} is usually considered equal to the PSF, and thus finally

$$\sigma_{\text{smooth}} = \sqrt{2}\, \sigma_{\text{PSF}} \, .$$

Signal significance

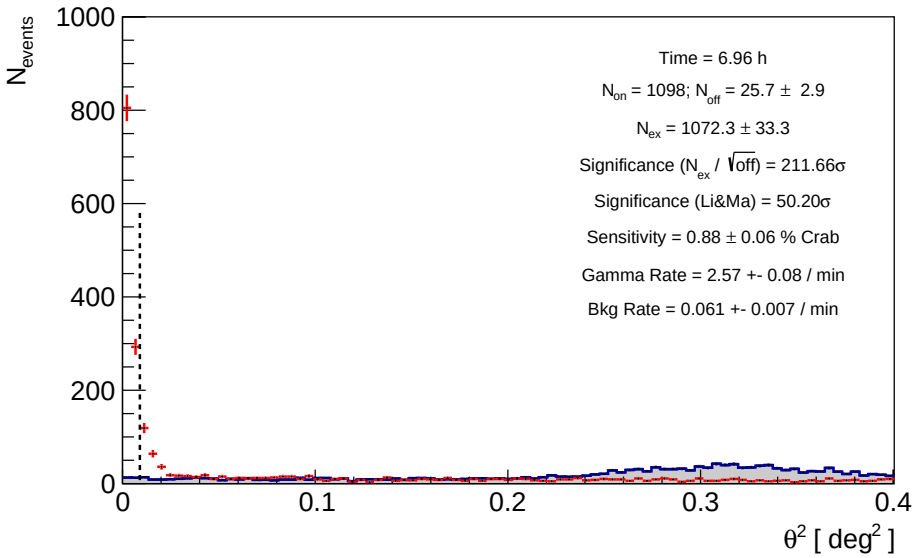

Figure 2.25: *Example of θ^2 plot of the Crab nebula, represented as distribution of the events for the MAGIC observations, signal (red) and background (shadowed grey). The vertical dashed line indicates the defined signal region to which the significance of the detection is calculated.*

After the evaluation of the parameters related to hadronness, reconstructed energy and direction of the events, the analyser can evaluate the statistical significance of the signal present in the data sample. This step is performed by using the program called `odie`, that computes the angular distance θ between the reconstructed and the expected source position. In order to visualize the result, `odie` fills an histogram called θ^2 plot.

In the data sample of the events, `odie` applies some analysis cuts such as size, hadronness, or a specified zenith. The events that survive the analysis cuts are included in the signal histogram. Although these cuts can be optimized on independent and known sources, we usually apply standard cuts for the MAGIC analysis which define specific energy ranges for the analysis, as reported in **Table** 2.7 on page 85.

Once the signal histogram has been filled with the events surviving all the cuts and the signal region has been defined, we consider these events as "events in the signal region", with number N_{on}. It is worth to note that these events are not only gamma rays coming from the source, but also gamma-like hadrons, $e^{\pm}$, and diffuse gammas.

For the estimation of how many hadron events are inside the signal region, we fill a different θ^2 histogram, the background histogram, where θ is now the distance from the reconstructed position to the "off position". The off position can differ for specific analyses,

but in general it is defined as a position situated at the same angular distance as the source from the center of the camera, but on a different region. This histogram leads to the evaluation of the number of off events N_{off}.

If we assume that the camera is homogeneous close to the center where the source position lies, the background events should be uniformly distributed over the whole histogram. Conversely, the gamma-ray events coming from the source should be peaking at small θ^2 values. An example of a typical θ^2 plot is shown in **Figure** 2.25.
Finally, the computation of the number of excesses N_{ex} is given by:

$$N_{\text{ex}} = N_{\text{on}} - \alpha N_{\text{off}}$$

where α is 1/(number of OFF regions), and the number of OFF region can be different depending on the particular analysis (in general it is equal to 3).

After the computation of the number of excesses, the analyser is particularly interested in the statistical significance of the signal. At this scope, the VHE gamma-ray astronomy relies on the Frequentist method called Likelihood Ratio Test (LRT). In this approach, two hypotheses are compared in terms of their Likelihood: the null hypothesis (H_0) that typically refers to the case of no signal, while an alternative hypothesis (H_1) refers to the case of having a signal. The ratio between the likelihoods computed on the two hypotheses relates exposure with the chance probability of the excess being due to a spurious fluctuation. In odie, this method is applied to the evaluation of the significance of the gamma-ray signal through the formula n.17 of Li & Ma (1983):

$$\sigma_{\text{LiMa}} = \sqrt{2\left(N_{\text{on}} \ln\left[\frac{1+\alpha}{\alpha}\frac{N_{\text{on}}}{N_{\text{on}}-N_{\text{off}}}\right] + N_{\text{off}} \ln\left[(1+\alpha)\frac{N_{\text{off}}}{N_{\text{on}}-N_{\text{off}}}\right]\right)}$$

that, in the Gaussian approximation, can also be given as:

$$\sigma_{N_{\text{ex}}/\sqrt{N_{\text{off}}}} = \frac{N_{\text{ex}}}{\sqrt{N_{\text{off}}}} \,.$$

Its validity holds if N_{on} and N_{off} are above about 10 counts. In MAGIC, it is common to add a sign to this significance depending on whether the excess is positive or negative.

In general, a source is considered detected in the VHE gamma-ray range, if the significance of the excess of gamma-like events over background events exceeds $5\,\sigma$.

2.4.3.8 Sensitivity

The sensitivity is a quantity that can be computed for each instrument and it is useful to compare the performance of different instruments and to compute the minimum flux that can be detected for a fixed amount of observation time.

The usual definition of sensitivity of a IACT is the minimum flux that can be detected in 50 hours with $5\,\sigma$ using the significance $\sigma_{N_{\text{ex}}/\sqrt{N_{\text{off}}}}$. This value is commonly expressed in terms of percentage of the Crab Nebula flux.

Considering an observation of the Crab Nebula and the related quantities number of excesses N_{ex} and background events N_{off} in the signal region in a time t are observed, the significance in a time $t_0 = 50$ hours can be expressed as:

$$\sigma_{N_{\text{ex}}/\sqrt{N_{\text{off}}}}(t_0) = \frac{N_{\text{ex}}}{\sqrt{N_{\text{off}}}}\sqrt{\frac{t_0}{t}} \,.$$

The sensitivity of the instrument, considering the minimum flux that can be detected in 50 hours with a significance of $5\,\sigma$, expressed in Crab units is:

$$\text{Sensitivity} = \frac{5\sigma}{\sigma_{N_{\text{ex}}/\sqrt{N_{\text{off}}}}(t_0)} \ .$$

In literature, there are two main forms by which the sensitivity of an experiment (for a set of cuts, like hadronness, size, θ^2...) can be expressed:

Integral sensitivity: this is the integrated signal above a given energy threshold that allows for the detection of the signal itself;

Differential sensitivity: this is the integrated signal in small energy bins with a given energy threshold that allows for the detection of the signal itself.

The current MAGIC integral and differential sensitivities are reported in Aleksić et al. (2016b). With respect to the other IACTs, the MAGIC telescopes have a better sensitivity at low energies. This value goes to even lower energies when using the Sum-Trigger configuration (see Section 2.4.1.5).

2.4.3.9 Instrument Response Function

The capabilities of a telescope are governed by its hardware design, the software design, and the criteria used for the quality selection of the events.

In this Section, I describe the main characteristics of the three functions describing the Instrument Response Functions (IRF) of the MAGIC telescopes: the effective collection area, the angular resolution, and the energy resolution. The former one is particularly important since it is used in the calculation of the spectra and light curves.

Effective collection area

The effective area A_{eff} is defined as the geometrical area around the telescope where a signal coming from the gamma-ray shower produces a trigger. This value is corrected by the gamma-ray efficiency of all the cuts applied in the analysis, that depends on the spatial coordinates, the gamma-ray energy, zenith angle, and azimuth angle. Considering its dependence on many parameters, the effective area is calculated in bins of energy, zenith, and azimuth angle, etc.

The effective area in MAGIC, shown in **Figure** 2.26a, is computed by applying the same cuts and analysis procedures to a sample of MC simulated gamma rays. Considering a number $N_{\gamma,\text{sim}}$ MC simulated gamma-ray events on an area $A_{\text{MC,tot}}$ (defined as πr^2_{max} , with r_{max} being the maximum shower impact simulated) and the number $N_{\gamma,\text{final}}$ of gamma-ray events surviving the analysis cuts, the effective area is defined as:

$$A_{\text{eff}} = A_{\text{MC,tot}} \frac{N_{\gamma,\text{final}}}{N_{\gamma,\text{total}}} \ . \tag{2.3}$$

It is interesting to compare the effective area of IACTs like MAGIC versus the effective area of a telescope like *Fermi*-LAT: as shown in **Figure** 2.26a, in MAGIC the order of magnitude of the effective area is about 10^5 m^2, while in *Fermi*-LAT is constrained by the size of the telescope itself at about 1 m^2.

One of the crucial aspects of the effective area is its dependency on the zenith angle, and this implies the differences we get when observing at high zenith angles. In fact, the

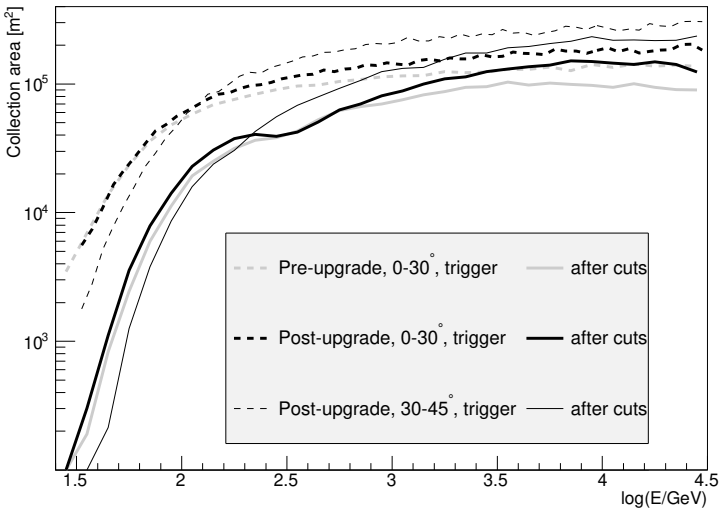

(a) Effective collection area of the MAGIC telescopes after the upgrade at the trigger level (dashed lines) and after all cuts (solid lines). Thick lines show the collection area for low zenith angle observations, while thin lines correspond to medium zenith angle. For comparison, the corresponding pre-upgrade collection areas are shown with gray lines.

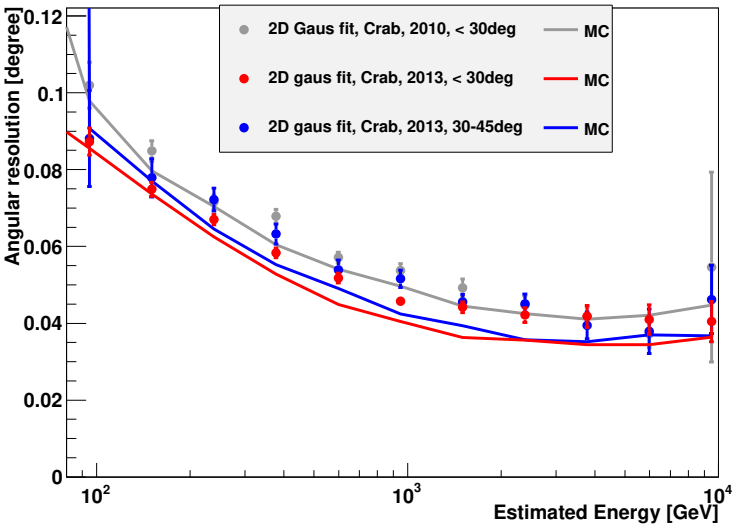

(b) Angular resolution of the MAGIC telescopes after the upgrade as a function of the estimated energy obtained with the Crab Nebula data sample (points) and MC simulations (solid lines). Left panel: 2D Gaussian fit, right panel: 68% containment radius. Red points: low zenith angle sample, blue points: medium zenith angle sample.

Figure 2.26: *Some of the most important performances of the MAGIC telescopes, from Aleksić et al. (2016b).*

showers coming from different zenith angle illuminate the ground in different ways: lower is the zenith angle, smaller is the light pool and higher the corresponding photon density. Conversely, when observing at high zenith angles, the light pool might increase notably, but the corresponding photon density decreases. Additionally, in this case the light coming from the impact point of the primary gamma ray has to travel through a much thicker range of atmosphere, and for this reason is much more affected by the atmospheric conditions (e.g. pollution and clouds), and this absorption effect generally kills the low-energy events. This results in an higher energy threshold and larger effective area at high energies (Mirzoyan et al., 2019).

Angular resolution

The ability of reconstructing the incoming direction of gamma rays is defined as angular resolution of the instrument. In MAGIC, there are two definitions that can be used:

- angular resolution θ_{gauss} defined as standard deviation of the 2-dimensional Gaussian function fitting the distribution of the reconstructed arrival direction of the gamma-ray excesses;
- angular distance θ_{68} from the source position enclosing 68% of the excess events.

The values obtained by these two methods are generally different and usually $\theta_{\text{gauss}} < \theta_{68}$.

An interesting feature of the angular resolution is that it is energy-dependent: showers corresponding to high-energy events are better reconstructed, so the angular resolution improves. For example, while the angular resolution at low energies (about 100 GeV) is about 0.1°, it improves down to 0.04° starting from TeV energies. In **Figure** 2.26b I present the angular resolution of the MAGIC telescopes.

Energy resolution

The energy resolution provides an estimation of the quality of the energy reconstruction for the main events (excluding all the outliers). It is defined as the standard deviation of a Gaussian fit to the peak of the $(E_{est} - E_{true})/E_{true}$ distribution.

The difference from zero of the peak of the $(E_{est} - E_{true})/E_{true}$ distribution is called the average *energy bias*. It depends on the energy: while for low-zenith observations it is less than 5% above few hundreds GeV, at lower energies it increases up to 20% due to threshold effects.
In **Figure** 2.27a, I present the energy resolution and energy bias of the MAGIC telescopes.

Energy threshold

In MAGIC, the energy threshold of a source observation is described by the peak energy of the energy distribution of the simulated MC gamma rays. The MC gamma rays are generally produced with a fixed power-law spectrum with spectral index γ_{MC} equal to -1.6. Considering that the observed source of interest may have a power-law spectral index of γ_{source}, the correct energy threshold is computed as difference with respect to the fixed γ_{MC} as $\gamma_{\text{correct}} = \gamma_{\text{MC}} - \gamma_{\text{source}}$.

As shown in **Figure** 2.27b, the typical energy threshold for dark good-weather and low-zenith observations is about 75/80 GeV. However, it increases when the zenith becomes higher, or when analysing moon data.

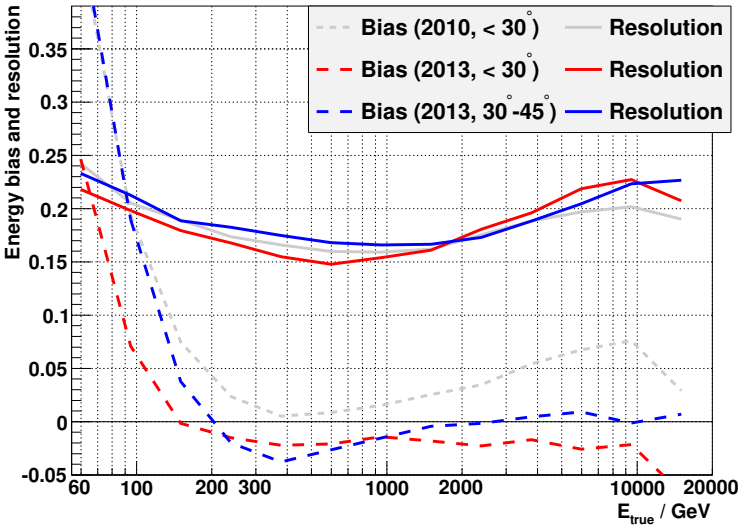

(a) Energy resolution (solid lines) and bias (dashed lines) obtained from the MC simulations of gamma rays. Events are weighted in order to represent a spectrum with a slope of -2.6. Red: low zenith angle, blue: medium zenith angle.

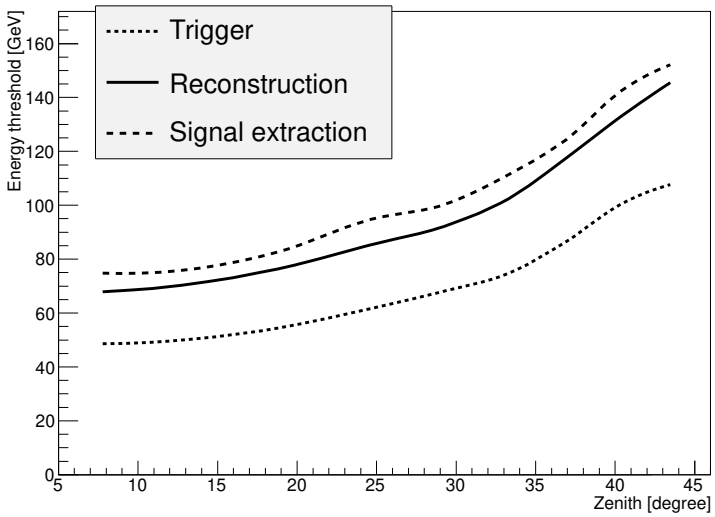

(b) Energy threshold of the MAGIC telescopes as a function of the zenith angle of the observations. The energy threshold is defined as the peak energy in the differential rate plot for a source with -2.6 spectral index. Dotted curve: threshold at the trigger level. Solid line: only events with images that survived image cleaning in each telescope with at least 50 phe. Dashed line: with additional cuts of *hadronness* < 0.5 and $\theta^2 < 0.03\text{deg}^2$ applied.

Figure 2.27: *Some of the most important performances of the MAGIC telescopes, from Aleksić et al. (2016b).*

2.4.3.10 High-level analysis

Spectrum

The high-level analysis is obtained when we switch from the signal measured in terms of instrumental units (counts) to the signal measured in terms of physical quantities. In order to estimate the flux coming from a gamma-ray source in physical units, we need to define the following observables:

Effective observation time t_{eff}. Each system that records data has a certain duty time and, once triggeder by an event, a cercaint dead time during which the data acquisition system is busy with that event and the system cannot accept any new events. In MAGIC, the dead time d per event is due to the DRS4 based readout, and it is equal to about 26 μs. The effective time is then given by the simple relation

$$t_{\text{eff}} = \frac{t_{\text{elapsed}}}{1 + \lambda\, d}\ ,$$

where λ is the rate of events.

Collection area A_{eff}: as reported in Section 2.4.3.9.

The calculation of these quantities is performed by the program `flute`.

In order to estimate the gamma-ray flux Φ from a given source, the first step is to count the number of events that survived the analysis cuts. Considering that the IRFs depend on the energy of the events, the data is divided into bins of estimated energy E_{est}. For each of these bins, the θ^2 histograms are generated and a signal region that optimizes the sensitivity and minimizes systematic effects is chosen: this allows to compute the number of ON events, OFF events, and finally the number of excess events. Usually, the number of excess events is corrected by using the efficiency of the selected cuts in a pure MC gamma-ray sample, that is the percentage of gamma rays contained in the signal region.

After that, the *spectrum* of the source can be computed. In its differential form, the gamma-ray spectrum is defined as the total number of detected photons, in unit of energy, area and time:

$$\frac{d\Phi}{dE} = \frac{dN_\gamma(E)}{dt_{\text{eff}}\, dA_{\text{eff}}(E)\, dE}$$

where N_γ is the total number of gamma rays from the source at the energy E, t_{eff} is the effective observation time, and $A_{\text{eff}}$is the effective area of the instrument.

Migration matrix

The reconstructed estimated energy E_{est} of the events is not the true energy E_{true} of the events. This is due to a so-called *spillover effect*: when computing the spectrum in bins of estimated energy, we have to use the effective area that is known in bins of true energy. This true energy of the Monte Carlo data depends on the simulated spectrum that is fixed and is in general different from the one of the source of interest. For this reason, the analyser has to re-weight the spectrum of MC simulated gamma rays to match that of the source of interest and obtain reliable effective areas.

The comparison between quantities binned in estimated energy and the ones binned in true energy, has to be corrected by using the so-called *migration matrix*. In fact, the same reconstruction artefacts due to the usage of estimated and true energies are present also in the MC gamma rays, and they can be used to correct the same effects in the real data. An example of a migration matrix is reported in **Figure** 2.28.

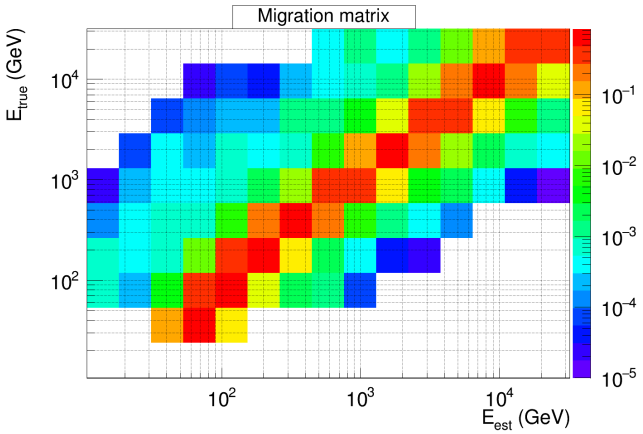

Figure 2.28: *Example of migration matrix produced with a real data analysis.*

Unfolding

The correction of the spillover effect provided by `flute` can be considered a first correction of the systematics due to the energy reconstruction.

However, when considering also other effects like those deriving from the non-perfection of the detector (limited acceptance, limited energy resolution, detection efficiency, etc.), from the statistical analysis (binning of the variables), or systematic distortion (threshold effects), an *unfolding* procedure has to be applied.

Unfolding is a way to transform the distribution of an observable (for example, the estimated energy $E_{\rm est}$) to the true distribution of a physical quantity ($E_{\rm true}$).

Some of the main features of unfolding are:

- The unfolding procedures that can be adopted are generally mathematically difficult. Their numerical application to real data, involving matrix inversions and approximations, can be unsuccessful or request very long computing time;
- There are many different unfolding algorithms with many parameters each;
- Unfolding can be ambiguous. Each of the above algorithms/parameters gives you different spectra: one of these is really wrong, but some make more sense than others to represent your data.
- Unfolded data has correlated errors. This is one reason why many ambiguous solutions of the unfolding can be "correct" at the same time.
- Unfolding noisy data with a noisy response matrix from discrete simulations leads to fluctuating solutions because of the matrix inversions. This requires to apply a smoothing called *regularization*: although there are some recipes on how much to regularize, its so-called weight is basically a free parameter.

In MAGIC, the unfolding procedure is applied to most of the analyses and consists of six different methods:

- Schmelling (minimization by Gauss-Newton method);
- Schmelling (minimization by MINUIT);

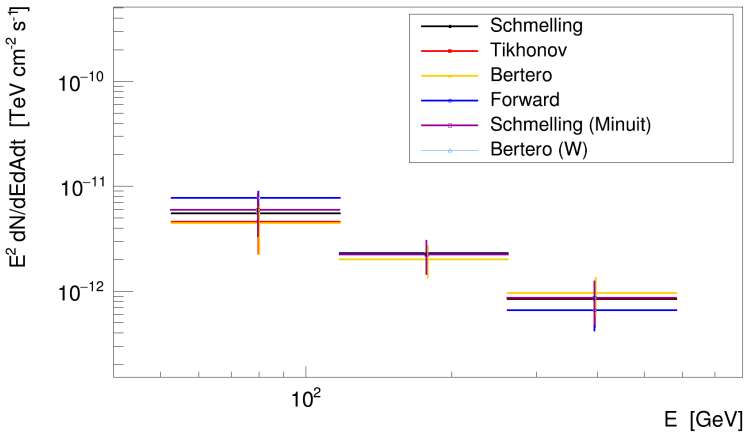

Figure 2.29: *Example of comparison plots between different unfolding methods.*

- Bertero (appropriate for under-constrained case);
- Bertero W (appropriate for over-constrained case);
- Tikhonov (minimization by MINUIT);
- Forward folding.

Some of them differ only by the application of the minimizer (such as MINUIT or Gauss-Newton), that are tools to find the minimum value of a multi-parameter function and analyse the shape of the function around the minimum.

The *forward folding* method is considered in the unfolding procedure, but it is not a real unfolding. In fact, in the forward folding the spectral shape is assumed to be an analytical function, and the result is not a series of spectral points, but the parameters of that function. Technically, that means it's just a fit. No regularization is needed, and the result is pretty robust: for this reason, the forward unfolding is considered to be the most robust of the unfolding methods.

When comparing the final data points, the six methods should give compatible results (see for example **Figure** 2.29). For a detailed review of the differences between these six methods and their application on the MAGIC data analysis, see Albert et al. (2007b).

This procedure of correction is performed by the `CombUnfold` macro. It is in general numerically difficult due to the need of involving matrix inversions and approximations. The solution can be ambiguous and sensitive to noise and fluctuations that require to use regularization methods to smooth out the data.

In the MAGIC software, there is another software called `fold` that takes care of correcting the spectrum. The approach of `fold` is different from that of `CombUnfold`, and is valid also for low-statistics bins: the latter assumes the event excesses (vs. estimated energy) as determined by `flute` have Gaussian uncertainties, which is not true in the few-events regime, i.e. at the highest energies. The results of `fold` are just the spectral parameters with their uncertainties. Nevertheless, `fold` gives in output also a spectrum and SED with individual points: they are obtained from the excess rates measured in bins of estimated energy, and converted into flux points using a collection area which contains a "spillover correction", calculated using fold's best-fit spectrum.

Light curve

By dividing the data into time bins and, in each of these bins, by estimating the integral flux above a certain threshold, the macro `flute` can generate light curves of the data sample. During this process, the computation considers a fixed spectrum to build each bin, and only the normalization of the spectrum changes. This macro allows the analyser to compute light curves with different type of time bins: night-wise, single-bin, or customized time bins.

2.4.3.11 Systematics in MAGIC data analysis

All instruments are affected by systematic uncertainties. In MAGIC, there are several factors that may contribute to the total systematics, most of them might vary during the single night or in short time periods. Some of the main ones are: the Earth's atmosphere, the hardware differences like the PMT response or gain, mirrors reflectivity and inhomogeneities, or other software differences like approximations used in the MC simulations.

Here I summarize some of the main systematics.

Instrument performances. The MAGIC telescopes operates under changing weather conditions, and for this reason the optical properties of the telescopes (reflectivity, PSF) might vary with time, for example dust accumulates on the reflecting surfaces (as happened during the data taking of TXS 0506+056, see Section 6.1). Then, the PMTs are all slightly different and their performances might be affected by their age: this might cause for example inhomogeneities in the distribution of events in the camera, and systematics in the evaluation of the background. The background subtraction can affect the estimation of the measured flux, and thus affect the evaluation of light-curves and spectra. Also the pointing position is important: in fact, at different pointing positions the weight of the telescopes affects differently the structure of the telescope itself, and this affects the accuracy of the MAGIC pointing, resulting in a systematic uncertainty 0.02°. Finally, the energy scale estimation can be affected by systematics. In fact, MAGIC-I and MAGIC-II have a slightly different light scale (amount of light generated by an event at a given energy.), with MAGIC-II having a response larger of about 11%. This effect is considered when producing the MCs, but it is based on a stable condition of the other instrument performances like reflectivity and PSF. A miscalibration in the energy/light scale of the telescopes affects especially the spectrum reconstruction at low energies and near the threshold. In this case, there is a lower collection area and a lower flux estimation, and a migration of events to lower energies: generally, this effect is visible thanks to the appearing of a pile-up effect below the energy threshold because of the fast decrease in the collection area.

Earth's atmosphere. Some night to night variations might be due to different atmospheric conditions. In fact, most of the systematics are controlled by using the LIDAR corrections, but residual systematics will continue to create a mismatch between the simulated shower development in the MC gamma-rays and the actual observations.

All the systematics have been deeply estimated by the MAGIC Collaboration. They are evaluated in less than 15% in energy scale, about 11 - 18% in flux normalization, and ± 0.15 in the slope of the energy spectrum assuming a power-law shape.

More details on this topic can be found in Aleksić et al. (2016b).

2.4.3.12 Non-standard analyses

Considering that the imaging atmospheric Cherenkov technique uses the atmosphere itself as part of the detector, it is clear that IACT performances can be severely affected by the observing weather conditions.

The IACTs have been developed to perform at their best under dark and perfect transmission conditions, but unfortunately also at the site where the La Palma observatory is located such conditions are not always realized and strictly affect the efficiency of the telescopes. For this reason, the MAGIC Collaboration has worked intensively on the implementation of several tools able to make the telescopes work also in reasonably good but not optimal weather conditions. Such developments have notably increased the duty cycle of the MAGIC observations at the price of a slightly reduced performance and longer times for the analysis, but are now applied to several science cases that can support such tools.

This allows to increase the duty cycle of the telescopes and to obtain scientific results In particular, the two main issues under which the MAGIC telescopes can operate are:

- observations under moonlight (Ahnen et al., 2017a);
- bad weather conditions.

In the following sections, I report some information on how to deal with such non-standard analyses.

Observations under moonlight

Considering that the MAGIC telescopes observe the dim Cherenkov light emitted by the showers in the atmosphere, it is clear that the observations during moonlight increase the background light and thus the detectability of the showers by the IACTs.

In a more technical view, the night sky background (NSB) level during the moonlight is in general much higher that the NSB during the good dark nights. In order to extend the duty cycle of the MAGIC telescopes and to make them able to observe during some moonlight, the hardware and the analysis techniques were adapted to cope with these more difficult conditions.

Observing with the moonlight implies higher NSB, but the relation between the $\mathrm{NSB}_{\mathrm{moon}}$ and the $\mathrm{NSB}_{\mathrm{dark}}$ is not linear: in fact, depending on the Moon zenith, phase, angular distance from the target, reflection by the clouds, distance from the Earth and its position in the sky, the NSB level can be very different.

During the data taking, the most important quantity to monitor is the DC in the camera: in fact, higher is the NSB, more is the light that the camera can collect, and higher is the current associated with that increased light. Considering a very standard observation during good dark time, the median DC might be of the order of 1.1 and 1.3 μA. But, the influence of the moon makes this value much higher, so that the median DC value can increase up to 10 μA. After that point, the shifters has to consider the safety limits during the data taking (see Section 2.4.1.8) that impose to set a lower HV and to keep the DC under the safety limits (47 μA for a single pixel and 15 μA for the median). During such moon observations before setting different HV level, the corresponding NSB can increase up to about 12×NSB dark. By reducing the HV settings in the PMTs (consequently lower the gain), the DC can be as high as that the NSB reaches about 20×NSB dark level. In order to increase even more the NSB level at which observations can be performed, some UV-pass filters can be installed in the cameras, allowing the telescopes to observe with NSB as high as 50×NSB dark (100×NSB dark) if nominal (reduced) HV are used.

Other effects that are induced by higher NSB level are for example an higher accidental L0 trigger rates, so that DTs are increased by the Individual Pixel Rate Control (IPRC) and consequently the energy threshold at trigger level will be higher.

In the analysis, higher NSB implies a different procedure at the calibration level. In fact, the distribution of pedestal events is modified: the mean value shifts towards higher values (in phe) and the RMS increases. This implies that the camera is affected by more light than during normal observations, and the images of the showers are much more difficult to be detected and analysed, in particular the smaller events.

In order to take care of this calibration effect, the first difference with respect to the standard analysis is at `star` level. The standard cleaning levels (6 phe and 3.5 phe) must be increased for moonlight analysis because the average level of the pixels are higher. Depending on the mean DC registered during the observations, the new cleaning levels are chosen so that less than 10% of the pedestal events survive the cleaning process.

When the data are cleaned at `star` level, the analysis procedure can continue as in the standard procedure with the superstar program. However, when going to the `melibea` stage, the analyser has to consider that all the data reconstruction in MAGIC analysis is based on the comparison with gamma MC data, so the higher noise due to the NSB must be taken into account in MC data. Thus, the analyser can use the star program in order to add noise to the MC data, and then better reproduce the real gamma we observed. This is performed by putting the higher mean and RMS of the pedestal distribution of real data taken under moonlight to adapt the MC data to the noise level present during observations. This process is concluded once also an appropriate choice of the OFF data sample is performed, that is by using OFF data with similar NSB level is similar to the real data.

Finally, considering that the simulations cannot reproduce the trigger and IPRC behaviour under moonlight, in the analysis a higher cut on the size parameter must be applied. The size cut depends on the NSB level and its value is chosen as the minimum one for match MC and real data.

For more information about the appropriate values of the pedestal distribution mean and RMS, cleaning levels, and size cut according to the different NSB level, are reported in Table 2 of Ahnen et al. (2017a).

In conclusion, as mentioned in the previous Sections, the main cons that have to be taken into account when performing observations under the moonlight is that it leads to a higher energy threshold. In fact, the higher cleaning levels and size cuts will remove the low energy events and will modify the distribution of the rates of gamma MC events as a function of energy, whose peak shifts towards higher energies for higher background level. An example of the degradation of the threshold is as follows: when the NSB is at about 15-30×NSB dark level with UV filters, the energy threshold for low zenith observation increases from about 70 GeV to about 300 GeV. However, for each analysis a new estimation of the threshold has to be computed.

Bad atmospheric conditions

In Section 2.4.3.5 we saw that the atmospheric conditions can affect sensibly the quality of the data. In particular, when the MAGIC telescopes can operate respecting the safety limits presented in Section 2.4.1.8, the most important feature is the transmission of the air, that can be evaluated with the LIDAR or the pyrometer (see Section 2.4.1.9).

A low atmospheric transmission implies a degradation of the shower images, and thus a worse parameters estimation. For this reason, the analysis has to operate looser cuts on hadronness and θ^2, as reported in Fruck et al. (2014). The corrections to the events are computed at `melibea` level, and then applied at `flute` level.

When the LIDAR is operating, the data are considered as taken under good quality atmospheric conditions when the transparency T_{9km} of the atmosphere calculated at 9 km (the average height where the showers develop) is $T_{9km} > 0.85$. When the data are characterized by limited transparency in the range $0.55 < T_{9km} < 0.85$, they can still be used but with a particular care by applying corrections in the following steps of the analysis (e.g. in the energy estimation). Data with $T < 0.55$ cannot be corrected and thus cannot be used.

2.5 The CTA observatory

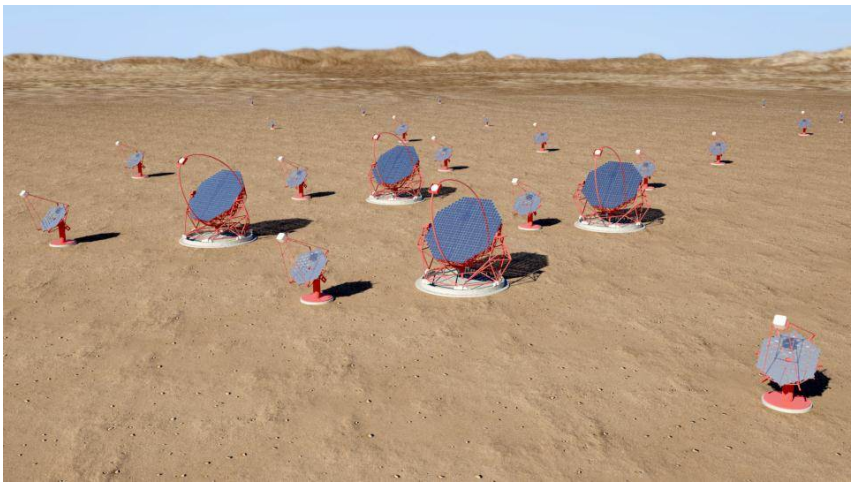

Figure 2.30: *An artistic view of some elements of the CTA telescope.*

The next generation of IACTs will be the Cherenkov Telescope Array (CTA, e.g. Actis et al., 2011), represented in **Figure** 2.30. It will be an open observatory with two main sites: in La Palma aimed at the observations of the northern sky, and in Chile for the southern sky. The two sites will consist of large arrays of IACTs of different sizes, and they will provide a full-sky coverage in gamma rays from 20 GeV to more than 300 TeV. The sensitivity of the instrument will improve up to an order of magnitude the sensitivity of the existing instruments such as H.E.S.S., MAGIC, and VERITAS. The construction of CTA is now being carried out by a consortium of scientists and institutes from all over the world.

2.5.1 The project

The CTA will be the next major observatory in the TeV gamma-ray band, with more than 100 telescopes located in the northern and southern hemispheres. It will bring forward the well-known Cherenkov technique (see Section 1.5.3) of the current generation of IACTs represented by H.E.S.S., MAGIC, and VERITAS. A representation of the improved differential sensitivity of CTA with respect to the current generation of gamma-ray detection facilities is shown in **Figure** 2.32. The technical performances will provide the scientific potential needed to address some of the most important questions in this field, such as the origin of cosmic rays, the strength of intergalactic radiation fields, and the nature of dark matter.

The project will be the first open observatory in the TeV gamma-ray band. Its design is already compatible with the new era of multi-messenger and multi-wavelength astrophysics, and it will have a crucial role in the relation with other scientific communities through all the world.

The realization of such enormous observatory through the two sites on the opposite side of the world needs a complex organization of people and institutions. CTA is though to be designed by the CTA Consortium (CTAC), a collaboration consisting of more than 1400 scientists and engineers from 32 countries around the world. The CTA Consortium has developed the science cases of CTA, and the institutes that are part of the Consortium are

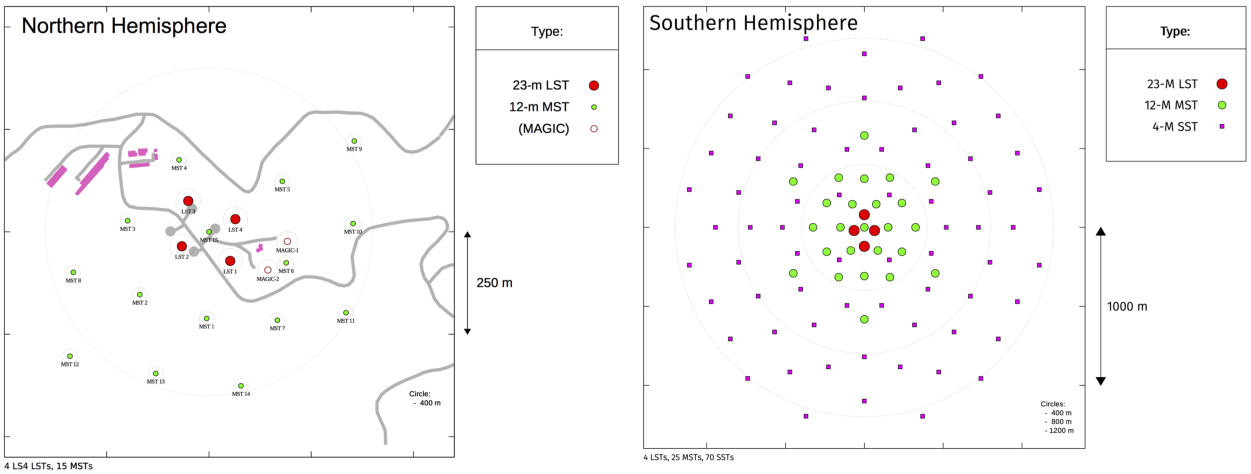

Figure 2.31: *Possible layouts for the baseline arrays for CTA North (left) and CTA South (right).*

expected to participate in building the components of the telescopes, both hardware and software.

In 2014, the council of country representatives established the CTA Observatory (CTAO), a legal entity that will control the CTA Project Office while constructing CTA and will be responsible for observatory operations and data management. The telescopes are expected to be built by the CTAC and, when matching the expected requirements, to be accepted and merged in the array of the CTAO.

The development of CTA has found increasing interest by the scientific community, and the project is proceeding quickly. The inauguration of the first Large Size Telescope (LST) in La Palma island was the first celebration of the success of this project.

2.5.2 Performances and array layout

The project of CTA will provide an open proposal-driven observatory with a full-sky coverage, and for this reason it will need two different sites for the two hemispheres. The energy band that CTA will be able to cover cannot be guaranteed by a single type of telescopes, and thus the array will need different types of telescopes. At the moment, three different sizes of telescopes will be built:

- **Large Size Telescopes (LST).** These telescopes will be the largest of the array with their 23 m diameter mirrors. They will be able to cover the lowest energies and bring the energy threshold down to 20 GeV.
- **Medium Size Telescopes (MST).** They will be telescopes with about 10-12 m diameter mirror surfaces, and they will be responsible of the core sensitivity of CTA between about 100 GeV and 10 TeV.
- **Small Size Telescopes (SST).** Telescopes with 2 - 4 m diameter mirrors that will extend the sensitivity range up to 100 TeV and will be located only in the southern hemisphere.

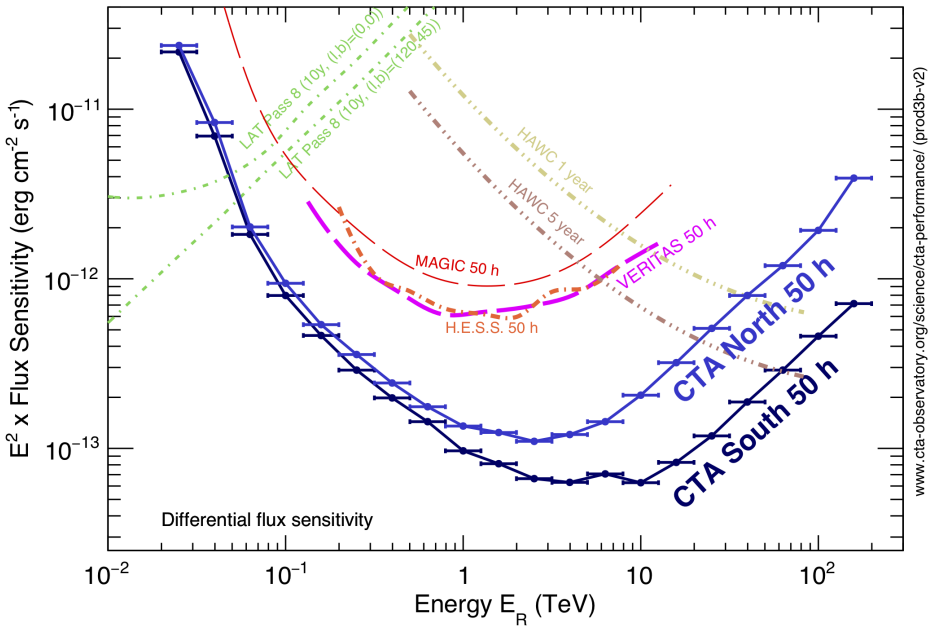

Figure 2.32: *The differential sensitivity of CTA – both northern and southern arrays – with respect to other current gamma-ray observatories. It is defined as the minimum flux needed by CTA to obtain a 5-standard-deviation detection of a point-like source, calculated in non-overlapping logarithmic energy bins (five per decade). The figure is taken from the official webpage of CTA* https://www.cta-observatory.org/science/cta-performance/.

CTA Telescope Specifications

	Large-Sized Telescope (LST)	Medium-Sized Telescope (MST)			Small-Sized Telescope (SST)		
		FlashCam	NectarCam	SCT	ASTRI	GCT	SST-1M
Required energy range	20 GeV – 3 TeV	80 GeV – 50 TeV			1 TeV – 300 TeV		
Energy range (in which subsystem provides full system sensitivity)	20 GeV – 150 GeV	150 GeV – 5 TeV			5 TeV – 300 TeV		
Number of telescopes	4 (South) 4 (North)	25 (South) 15 (North)			70 (South) 0 (North)		
Optical design	Parabolic	Modified Davies-Cotton		Schwarzschild-Couder	Schwarzschild-Couder		Davies-Cotton
Primary reflector diameter	23.0 m	11.5 m		9.7 m	4.3 m	4.0 m	4.0 m
Secondary reflector diameter	--	--		5.4 m	1.8 m	2.0 m	--
Effective mirror area (including shadowing)	370 m^2	88 m^2		41 m^2	8 m^2	8.9 m^2	7.5 m^2
Focal length	28 m	16 m		5.6 m	2.15 m	2.28 m	5.6 m
Total weight	103 t	82 t		80 t	19 t	11 t	8.6 t
Field of view	4.3 deg	7.5 deg	7.7 deg	7.6 deg	10.5 deg	8.3 deg	8.8 deg
Number of pixels in Cherenkov camera	1855	1764	1855	11328	2368	2048	1296
Pixel size (imaging)	0.1 deg	0.17 deg	0.17 deg	0.067 deg	0.19 deg	0.17 deg	0.24 deg
Photodetector type	PMT	PMT	PMT	SiPM	SiPM	SiPM	SiPM
Telescope readout event rate (before array trigger for MSTs and SSTs)	>7.0 kHz (after LST array trigger)	>6 kHz	>7.0 kHz	>3.5 kHz	>0.3 kHz	>0.4 kHz	0.6 kHz
Telescope data rates (readout of all pixels; before array trigger)	24 Gb/s	12 Gb/s			2 Gb/s		3.2 Gb/s
Positioning time to any point in the sky (>30° elevation)	30 s	90 s			60 s		
Pointing precision	<14 arcseconds	<7 arcseconds		<10 arcseconds	<7 arcseconds		
Observable sky	Any astrophysical object with elevation > 24 degrees						

(last updated: Dec 2017)

Figure 2.33: *Main performances and characteristics of the different telescopes within the CTA. The table is taken from the official webpage of CTA* https://www.cta-observatory.org/science/cta-performance/

2.5.3 Current status

The CTA project is currently in an advanced status, and several prototypes of the different telescopes are being built and commissioned in different parts of the world.

By the end of 2018, the first LST has been inaugurated. The infrastructure conceptual planning for the northern hemisphere site is mostly completed. The refinement of the design and the last permits for construction of the telescope foundations and infrastructures have been obtained, and the bulk of the site construction is foreseen to begin in 2019.

The southern site has been now decided and the first phase of construction of the site and infrastructure design has begun.

In this Section, I summarize the status of the most notable prototypes for each size of telescopes.

2.5.4 SSTs

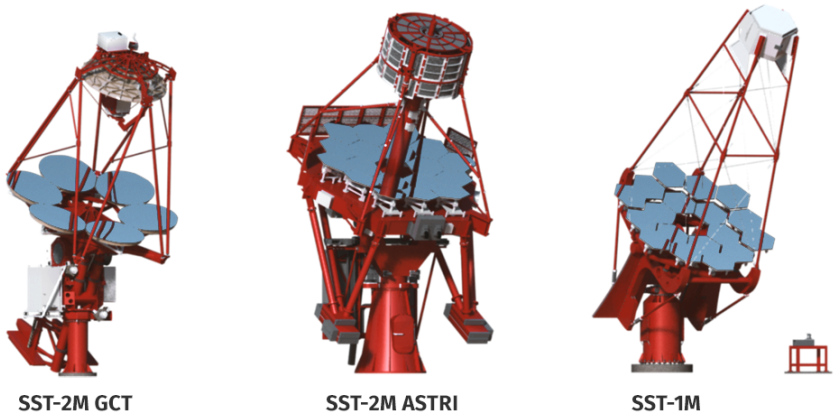

Figure 2.34: *A representation of the three designs of SSTs.*

The major number of telescopes in the array will be composed of SSTs, located only in the southern hemisphere site. About 70 telescopes are planned to be spread out over an area of several square kilometers. The reason for such high number of small telescopes spread out over a big area is that the very high-energy gamma-ray showers that they will detect (between a few TeV and 300 TeV) generally produce large Cherenkov pools on the ground. The size of the telescopes is smaller because the light they collect is generally sufficient, but their number is high in order to cover the widest area on the ground. For this reason, they will cover the highest energy part of the sensitivity of the full array of CTA.

There are three different SST implementations being prototyped and tested, as reported in **Figure** 2.34:

- one single-mirror design (SST-1M)
- two dual-mirror designs (SST-2M ASTRI and SST-2M GCT)

In order to simplify the management of the full array, in may 2018 was decided that the observatory will adopt a single design for the SST. For this reason, the project manager is now working to combine the three teams and projects in such a way to get the best performances for the future SST of CTA.

The main characteristics of the SST will be a 4 m diameter mirror surface and a large field of view of about 8-10 degrees. In the sections below, I present the main features of the three different prototypes.

2.5.4.1 SST-1M

The single-mirror telescope of the SST is a Davies-Cotton prototype, a sort of small version of the corresponding Davies-Cotton MST mount. It is provided with a 4 m diameter mirrors, composed of hexagonal mirror facets. The camera is based on silicon photomultipliers (SiPMs) that, unlike photomultipliers, can operate during high levels of moonlight.

2.5.4.2 SST-2M ASTRI

One of the two dual-mirror configurations of the SST will be a Schwarzschild-Couder design called ASTRI[7]. The telescope is provided with a camera based on SiPMs, and uses a rigid alt-azimuth mount. The mirror surfaces are a 4.3 m diameter for the primary one (segmented into hexagonal facets), and 1.8 m for the secondary mirror (monolithic).

2.5.4.3 SST-2M GCT

The SST-2M GCT is composed by optics similar to those of the SST-2M ASTRI, but its concept focuses on the low-mass design of the alt-azimuthal mount. The optics is composed by a 4 m diameter primary mirror and a 2 m secondary one, each one divided into six petal-shaped segments.

[7] http://www.brera.inaf.it/~astri/wordpress/

2.5.5 MSTs

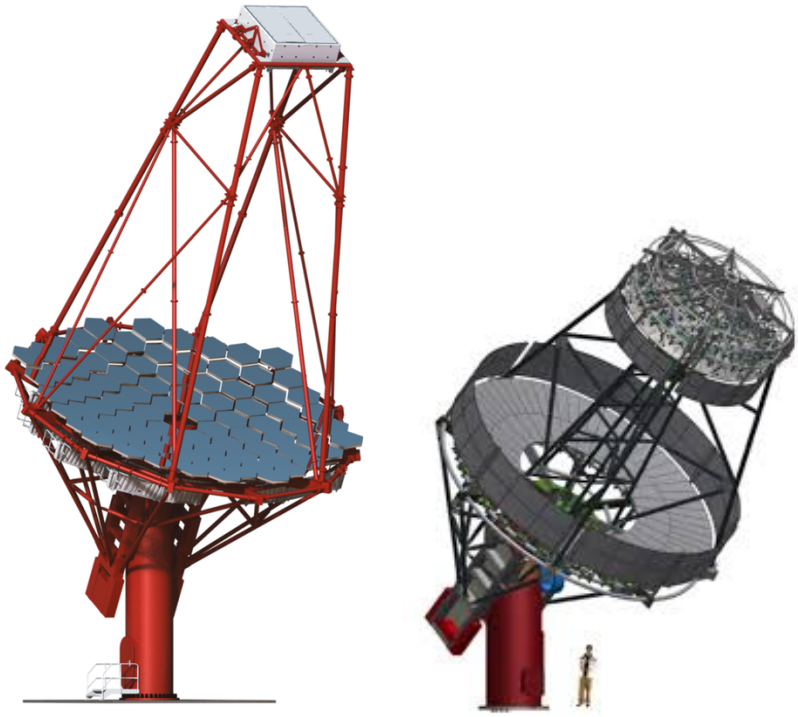

(a) Davies-Cotton telescope **(b)** Schwarzschild-Couder Telescope

Figure 2.35: *A representation of the three designs of MSTs.*

The MST telescopes will play an important role because they will cover the most part of the sensitivity at medium energies from about 150 GeV to 5 TeV. The plan foresees a total of 40 MSTs: 25 located in the southern hemisphere and 15 in the northern hemisphere.

The main characteristic of the MST telescopes will be a diameter of the reflective surface of about 12 meters and camera designed with photomultiplier tubes (PMTs). The large field of view of about 8 degrees will make the MSTs fast in surveying the full gamma-ray sky.

The MST telescopes are now subdivided in two main designs: the Davies-Cotton design and the Schwarzschild-Couder one.

2.5.5.1 Davies-Cotton telescope

This single-mirror telescope is provided with a design similar to the Davies-Cotton MST one. The mirror surface of 12 m diameter will be covered by hexagonal mirrors aligned by an active mirror control.

2.5.5.2 Schwarzschild-Couder telescope

This dual-mirror telescope of the MST array, often called Schwarzschild-Couder Telescope (SCT), follows the Schwarzschild-Couder design to achieve a better focus the light, with improvements in the imaging detail and detection of faint sources (smaller point spread function). The optics is composed by a 9.7 m diameter primary mirror and a 5.4 m secondary one, both provided with hexagonal mirrors and aligned by an active mirror control. The camera is based on silicon photo-multipliers (SiPMs) and has a field of view of about 8 degrees.
It was inaugurated in January 2019 in Arizona, when it reached its first light.

2.5.6 LSTs

Figure 2.36: *The current status (beginning 2019) of realization of the first LST telescope of the northern site in La Palma, Canary Island.*

The LSTs, with their wide reflective surface, will collect light coming from the lowest part of the sensitivity of CTA between 20 and 150 GeV. The design plan consists of four LSTs arranged at the centre of both the northern and the southern sites.

The telescope, planned with a unique design, is provided with an alt-azimuthal mount and a 23 m diameter parabolic reflective surface of 400 m^2. The camera is composed of photomultiplier tubes. Although the big size of LST and the weigh around 100 tonnes, the light design will be able to re-position the telescope within 20 seconds, in such a way to contribute to the follow-up observations of transient events.

One of the most important phases of this project – not only from a mediatic point of view – was the inauguration of the LST prototype in La Palma in October 2018. Additionally, during the night between 14-15 December 2018, the LST prototype recorded its first Cherenkov light. An example of such event is reported in **Figure** 2.37.

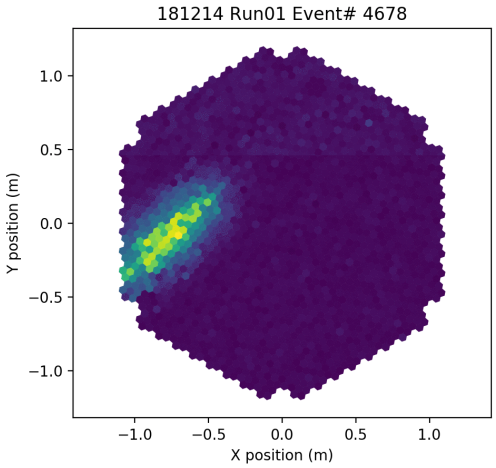

Figure 2.37: *One of the first-light events registered by the LST.*

2.6 The IceCube observatory

Figure 2.38: *The control room of the IceCube telescope at South pole.*

IceCube (Aartsen et al., 2017) is the current most innovative observatory of astrophysical neutrinos. The main aim of IceCube is the detection of cosmic neutrinos, the neutrinos from the most violent astrophysical sources in our universe. The neutrinos, being almost massless neutral particles, travel from the deep Universe almost unaffected by interposed matter (galaxies, for example) and intergalactic magnetic fields. Therefore, the cosmic rays (which consist mainly of protons) might be studied thanks to these particles that are able to trace their production site.

Neutrinos are not observed directly. When they are travelling towards the Earth, there is a small but not negligible probability of interaction with the ice around the detector. Such interaction produce showers of highly energetic secondary particles that emit Cherenkov light because of their high velocity. Such light can be detected by the PMTs of the IceCube detector. This information, collected from the whole telescope, is analysed by the computers in the IceCube Lab on the surface (**Figure** 2.38), reconstructing the direction and energy of muons and neutrinos.

However, the up-to-now faint signal that has been detected from cosmic neutrinos is particularly prevented due to the existence of strong backgrounds by atmospheric muons and neutrinos, particles produced when the CR interact with the Earth's atmosphere.

2.6.1 Structure

IceCube is a cubic-kilometer particle detector literally made of Antartic ice, buried in the deep ice beneath the South Pole. The whole observatory is actually composed of several sub-detectors.

Main in-ice array

The main in-ice component consists of 5160 digital optical modules (DOMs). As represented in **Figure** 2.39, each DOM has a spherical shape and is composed of a photomultiplier tube and the associated electronics. The DOMs are attached to vertical "strings", frozen into 86 boreholes, and arrayed over a cubic kilometer with depth between 1450 and almost 2500 m. Besides IceCube, an additional surface array called IceTop and a denser inner subdetector called DeepCore, significantly enhance the capabilities of the observatory, allowing it to study different targets. For example, the IceTop is particularly useful to measure CRs in the energy range from 300 TeV to 1 EeV. The DeepCore, on the other side, lowers the neutrino energy threshold to about 10 GeV, allowing the community to study neutrino oscillations.

Figure 2.39: *The digital optical modules of the IceCube detector.*

IceTop

IceTop consists of an array of 81 Cherenkov detectors located on the surface of the glacier. Each station has two tanks, situatee approximately above each IceCube string. The main use of IceTop is to act as veto (if a muon is observed going through IceTop, it cannot be from a neutrino interacting in the ice) and calibration detector for IceCube. Additionally, it can detect air showers from primary cosmic rays in the 300 TeV to 1 EeV energy range, measuring the cosmic-ray arrival directions as well as the flux and composition of cosmic rays.

Deep Core Low-Energy Extension

Eight strings located at the center of the main in-ice detector were deployed with a more compact design, with a horizontal separation of about 70 meters and a vertical DOM spacing of 7 meters. This configuration forms the so-called Deep Core Low-Energy Extension, which extends the observable energies below 100 GeV and up to about 10 GeV, crucial to study neutrino oscillations.

AMANDA

The Antarctic Muon And Neutrino Detector Array (AMANDA, as reported in Section 1.6.4) was the first part built, conceived as a prototype for IceCube. AMANDA was turned off in May 2009.

Precision IceCube Next Generation Upgrade

The Precision IceCube Next Generation Upgrade (PINGU) is an hypothetical infill extension under proposal review that would allow to detect low-energy neutrinos at GeV energy scale. Such low-energy neutrinos will help in studying the neutrino mass hierarchy, the precision measurement of atmospheric neutrino oscillation, and the search for dark matter.

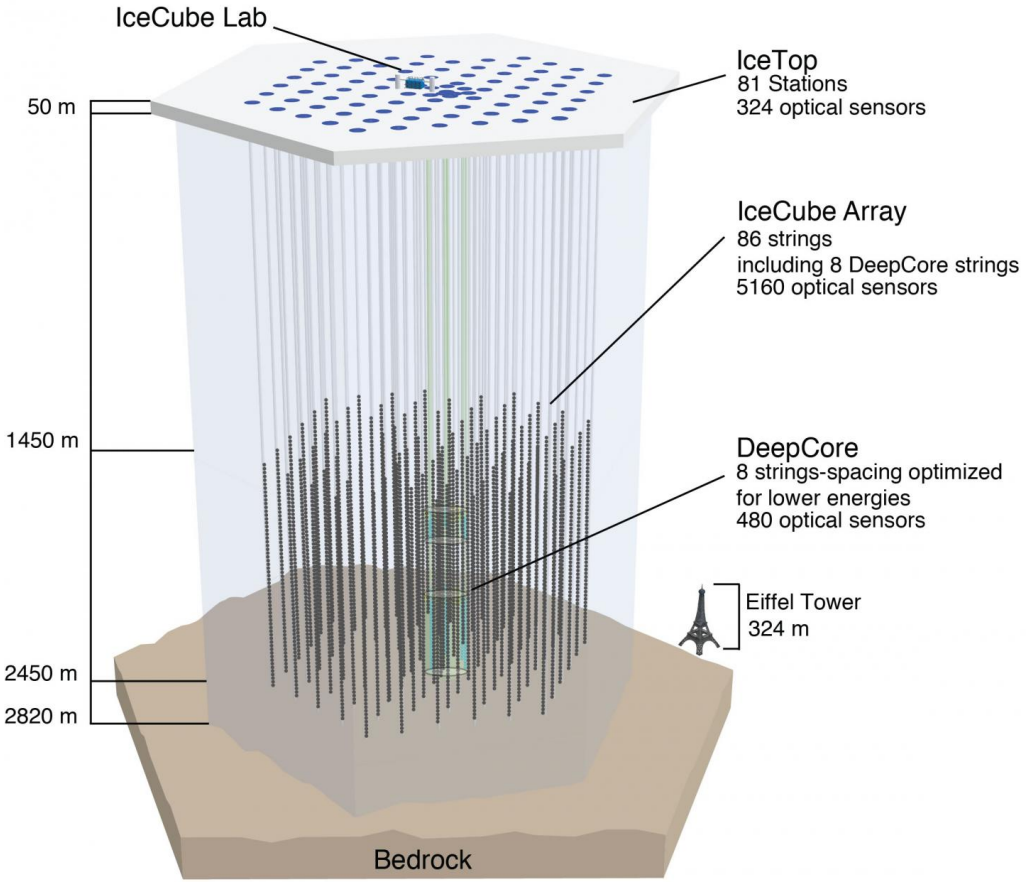

Figure 2.40: *The main structure of the IceCube detector. Figure credits: IceCube Collaboration - National Science Fundation.*

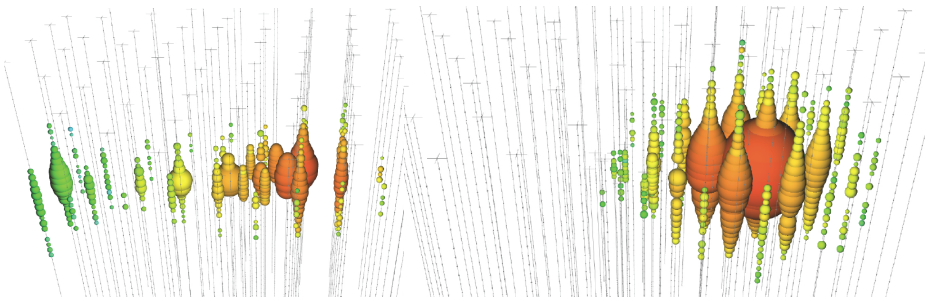

(a) Track event. **(b)** Cascade event.

Figure 2.41: *A representation of the most interesting IceCube events.*

2.6.2 Neutrino events

The IceCube detector does not observe directly neutrinos, but it observes their resulting interactions with the matter (ice) around the detector. In particular, some of these interactions produce secondary charged particles, that in turn emit Cherenkov light in the ice, that is then detected by the DOMs. In practice, the main problem regarding the analysis of IceCube data can be referred to its ability to recognize the events detected by the DOMs, and relate them to the physical process that produced them, and finally to estimate the particles arrival time, energy, and direction.

There can be several types of events within the IceCube detector. I present in **Figure** 2.41 the main features registered by the DOMs.

2.6.2.1 Muon track events

In the left panel of **Figure** 2.41, a muon-track event is presented. It describes the signature left by a muon which was produced by a charged current muon-neutrino interaction of the type

$$\nu_\mu + N \rightarrow \mu + X$$

or an air shower.
The property that characterizes this type of events is the fact that the muon can travel large distances in the detector (potentially the whole detector) before decaying or losing all their energy. This implies that the direction can be well inferred, but it is difficult to estimate how much energy the muon left into the detector and thus the energy of the incoming neutrino.
These events are also called extremely-high energy neutrinos (EHE) events.

2.6.2.2 Cascade events

In the right panel of **Figure** 2.41, a cascade event is presented.
This event occurs in the case of

- charged current electron-neutrino interaction

  $$\nu_e + N \rightarrow e + X \ ,$$

  that produces an electron that, in turn, begins a shower of gamma rays, positron, and electron production via bremsstrahlung and pair production respectively.

- or any neutral current neutrino interaction

  $$\nu_X + N \rightarrow \nu_X + X \ ,$$

  that produces the breakup of a nucleus that can produce charged products (which can re-interact in the medium) and neutral pions (that often decay to two gamma rays).

The electromagnetic shower dies out within some tens of meters, and its signature can be approximated as a spherical emission with a slight asymmetry in the direction of motion.

When these events are most predominantly contained within the detector, the energy reconstruction is very good (because the whole event looses its energy inside the detector), but the directional reconstruction is difficult.
These events are also called high-energy starting events neutrinos (HESE) events.

2.6.2.3 Direction reconstruction

The direction reconstruction of the events is mainly due to the arrival time of the photons detected by the DOMs. This task is made difficult by the scattering due to the imperfect ice within the detector.

However, simulations and tests concerning how photons propagate in the ice allow reconstructions to achieve angular resolutions of about 0.3 degrees (in the case of track events).

2.6.2.4 Energy reconstruction

The energy reconstruction is correlated with the energy dissipated by the event in the detector. When the particle is fully contained in the detector, almost all of its energy is converted into light, and its original energy can be estimated. This calorimetry cannot be performed properly when the interaction happens partially outside the detector.

The resolution can be improved if particles location and direction are known: this happens because additional information about the emission profile of the light and local ice properties can provide good estimates of how much light should have been collected.

2.6.3 IceCube-genII

The main solution in order to improve the sensitivity of a neutrino detector similar to IceCube observatory is to extend its collective volume. After several years of operations with IceCube, the scientists understood that actually the sensitivity of the instrument can be improved also by using less dense arrays of DOMs. In fact, the new generation of IceCube, called *IceCube-genII*, will achieve a tenfold increase in volume to about 10 cubic kilometers, but using a spacing between the DOMS of about 250 m instead of the 125 m now adopted by IceCube. This huge extension will be made economically affordable by using only the double of the instrumentation already deployed, but gaining an order of magnitude increase in neutrino detection rates.

The main reason to build such extension of the observatory is increase the statistics of very energetic astrophysical neutrinos, in the PeV to EeV range, and neutrinos of all flavours at energies above 100 TeV. Such higher statistics will help significantly in the point source detections, new spectral studies, and new discoveries.

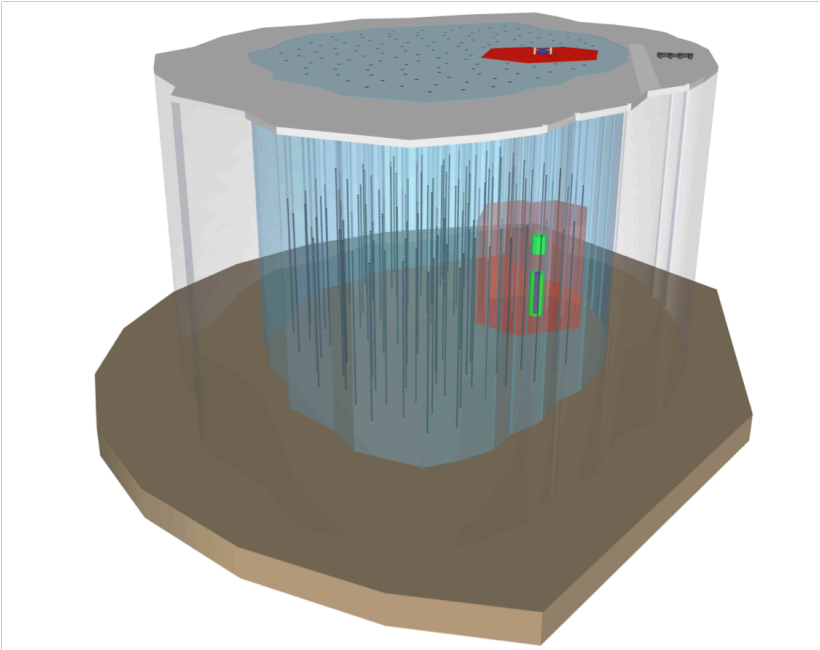

Figure 2.42: *The IceCube generation II detector. IceCube, in red, and the infill subdetector DeepCore, in green, show the current configuration. The blue volume shows the full instrumented next-generation detector, with PINGU displayed in grey as a denser infill extension within DeepCore. Figure obtained from* https://IceCube.wisc.edu/.

Chapter 3

Active galactic nuclei

Active galactic nuclei constitute one of the most studied objects in astrophysics, and they populate the sky with an enormous variety of phenomenologies. They are the most powerful persistent accelerators in the Universe, and represent natural laboratories where we can study extreme processes that are not reproducible on Earth.

The first part of this Chapter is dedicated to the presentation of an historical overview of active galactic nuclei, their classification and unification models.

After that, I describe the spectral properties of a particular subclass of active galactic nuclei named *blazars*, that are distinguished by their jet orientation at small angles with respect to the line-of-sight of the observer. The most extreme objects of this class, named *extreme blazars*, constitute an important part of my Thesis work, and will be presented in Chapter 4 and Chapter 5. For this reason, I will introduce the main theoretical models that interpret the blazars emission, focusing on their application on extreme blazars in the next Chapters.

Finally, I will describe the main properties of a famous blazar, PG 1553+113, to which analysis I contributed in the MAGIC Collaboration. This blazar is particularly important because, besides its high luminosity through the entire electromagnetic spectrum that makes it well detectable with several instruments, it presents an interesting periodicity at different wavelengths, mostly interpreted as a probe of the presence of a system of two black holes at the center of its nucleus.

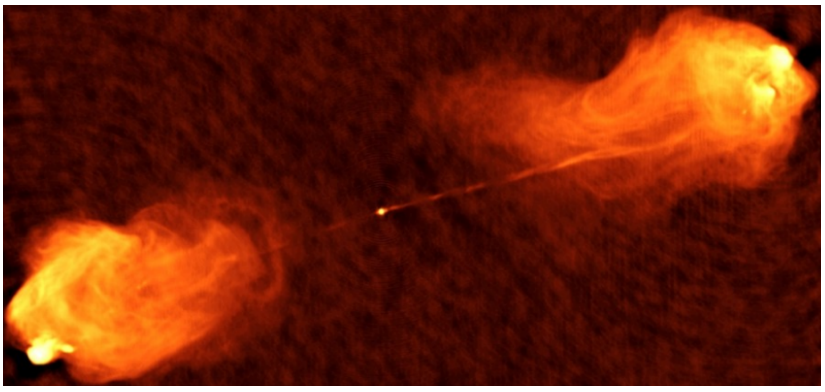

Figure 3.1: *An image of the radio-galaxy Cygnus A.*

3.1 A brief introduction

In a fraction of galaxies we register an enhanced electromagnetic activity taking place in their nuclear region: such galaxies are called *active galaxies*, and consequently their nucleus is called *active galactic nucleus* (AGN). Their population is spread over a wide range of morphologies and spectral emissions, and they constitute one of the most studied fields in astrophysics.

AGNs are particularly important in astrophysics because they harbour a large variety of phenomena, and their emission covers the full electromagnetic spectrum from radio up to gamma rays. Such radiation is distinguishable from the light produced by the host galaxy due to the fact that it is produced by non-thermal processes.

The main components of an AGN (Ghisellini, 2013; Padovani et al., 2017) are:

- a super-massive black hole (SMBH), with masses between 10^6 and some 10^9 $M_\odot$.
- An accretion disk, composed by matter rotating around the SMBH.
- A X-ray corona. It is supposed to be a see of hot electrons, sandwiching the accretion disk.
- A torus, located at several parsec from the black hole. It is supposed to be composed by dust that obscures some fraction of the radiation produced by the regions around the SMBH.
- A broad line region (BLR). This is a region composed of many small clouds at a distance of about one parsec from the SMBH, and they partially re-emit the light coming from the accretion disk.. Their rapid movement (about 3000 km s^{-1}) causes the broadness of the lines due to Doppler effect.
- A narrow line region (NLR). At larger distance (about 100 parsec) sparser clouds are moving at minor speed, and their re-emitted light is less affected by Doppler effect.
- A fraction of about 10% of AGNs is supposed to be producing also *relativistic jets* of matter, probably aligned with the rotational axis of a spinning black hole. These jets are probably formed thanks to the particular configuration of the magnetic fields produced by the fast rotation of matter around the central black hole. The idea is that in these objects part of the circum-nuclear matter rotating around the central black hole is warming up due to the friction. A fraction of this matter is re-ejected through the relativistic jets, where is then accelerated at relativistic speeds. There are several processes that might be involved in such acceleration, but their origin is still under debate.

3.1.1 First image of a black hole

Black holes are extraordinary astrophysical objects with enormous mass concentrated in few kilometres. They are the most massive single objects in the Universe, and their presence strongly modifies the local space-time. Within the so-called *event horizon*, even the light cannot escape. For this reason, up to now only indirect measurements of their gravitational interaction with other objects in the surrounding space have been performed.

The material surrounding the central black hole falls into its region of influence, and may create an accretion disk becoming hotter and hotter as it gets closer to the BH. Such hot gas emits light before falling into the BH, and this effect is detected by our telescopes as a bright region surrounding the BH. Following Einstein's general relativity, the BH is expected to create a dark region similar to a shadow. This shadow, caused by the gravitational bending of the event horizon, is particularly important to get new insightful information about the SMBHs and measure its mass.

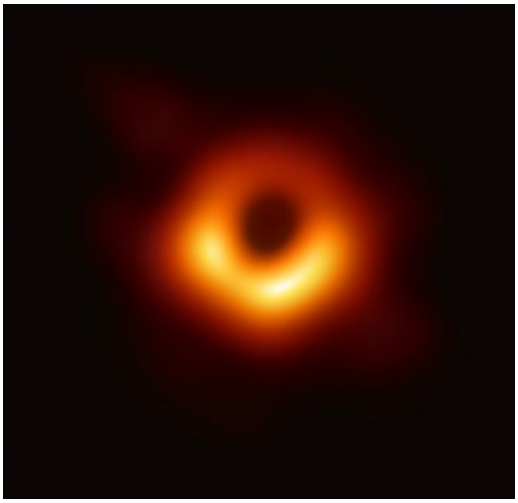

Figure 3.2: *The first image of the super-massive black hole at the center of an AGN called M87. Credits: Event Horizon Collaboration.*

At the beginning of 2019, the Event Horizon Collaboration was able to provide the first image of a black hole at the center of a gigantic elliptical galaxy called M87 (Event Horizon Telescope Collaboration et al., 2019), reported in **Figure** 3.2. M87 is a well-known radio-galaxy that emits at all wavelengths, and is known for several studies on its jets and its broad-band emission.

After more than ten years of coordinated operations, the radio very-long-baseline interferometry (VLBI) technique provided the first exciting result that confirms the existence of black holes. The experimental results on the black hole shadow are incredibly agreeing with the theoretical expectation about this phenomenon, and gives a new definitive confirmation about the theory of General Relativity. The EHT that uses this technique represents a worldwide network of eight pre-existing telescopes deployed at a variety of challenging high-altitude sites, like volcanoes and high mountains through all over the world. In **Figure** 3.3 I show a representation of the telescopes network.

The EHT telescopes are synchronized in such a way to form a huge, Earth-size telescope observing at a wavelength of 1.3 mm. VLBI observations allowed the EHT to achieve an incredible angular resolution of 20 micro-arcseconds.

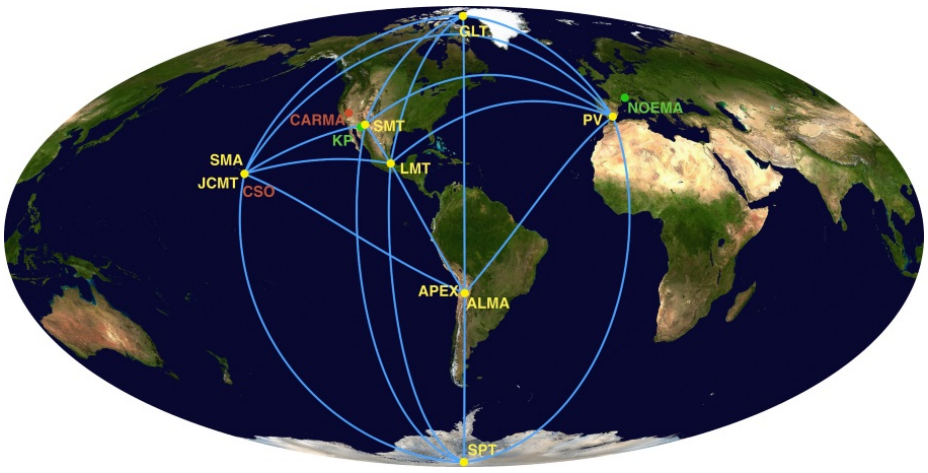

Figure 3.3: *A map of the EHT. Stations active in 2017 and 2018 are shown with connecting lines and labeled in yellow, sites in commission are labeled in green, and legacy sites are labeled in red. Credits: Event Horizon Collaboration.*

3.1.2 AGN classification

Observations suggest the presence of a zoo of different types of AGNs, each of them with different spectral properties, polarized emission, and flux variability. As in biology, a sort of taxonomy has been developed based on the observational differences that these classes present.

This topic can be presented at several levels of detail. In this Section, I will present only a quick overview of the main differences that the AGN classification presents in order to give an adequate understanding of the following topics. For a complete presentation of the AGN classification, see e.g. Padovani et al. (2017).

3.1.2.1 Luminous infrared galaxies

In the whole population of galaxies in the Universe, some of them (locally about 10%) show particularly intense activity in the infrared (IR) band, at which they emit more energy than at all other wavelengths combined. They are called *luminous infrared galaxies*, and are classified on the basis of the total luminosity L they emit with respect to the Sun. When

- $L > 10^{11}\ L_{\odot}$ they are called luminous infrared galaxies (LIRGs);
- $L > 10^{12}\ L_{\odot}$ they are called ultraluminous infrared galaxies (ULIRGs);
- $L > 10^{13}\ L_{\odot}$ they are called Hyper-LIRG;
- and finally when $L > 10^{14}\ L_{\odot}$ they are called extremely luminous infrared galaxies (ELIRGs).

Infrared galaxies are in general single gas-rich spiral galaxies whose luminosity is due to the large formation rate of stars within them. The energy emitted by LIRGs is comparable to that of AGNs, so that this extreme luminosity may also come from the presence of an AGN. Indeed, some hyper-LIRGs, due to the extremely high luminosities, are considered to be some of the most luminous persistent objects in the Universe, and most of them are known to harbour AGNs (e.g. Sanders et al., 2009).

3.1.2.2 Historical classification

AGNs can be classified on the basis of two fundamental parameters (Padovani, 1997), namely:

- radio emission properties;
- presence/absence and width of the emission lines;

as summarized in **Figure** 3.4 (a complete discussion can be found in Urry & Padovani 1995).

Radio emission properties
On the basis of the radio properties of the sources, a first distinction can be made as follows:

- **radio-quiet** AGNs;
- **radio-loud** AGNs.

Although the first discovery of AGNs in the Universe more than 30 years ago was lead by the detection of strong "radio-loud" sources, in the following years the community

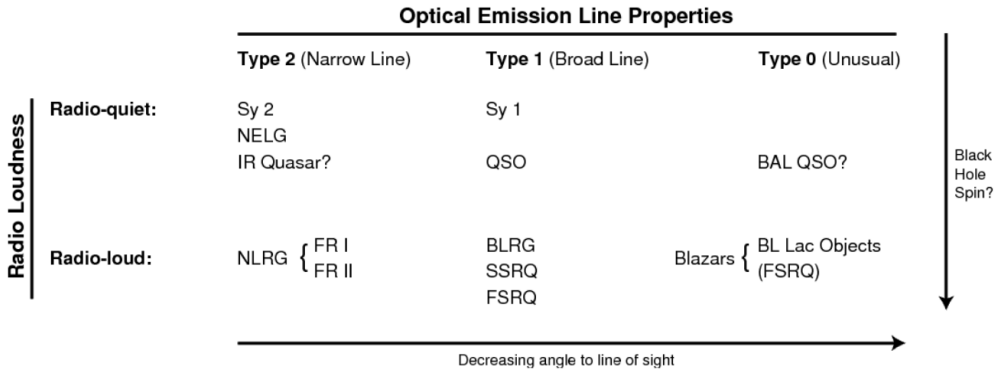

Figure 3.4: *AGN classification table. Scheme adapted from Lawrence (1987).*

understood that actually the majority of quasars are radio-quiet, and were not detected by the radio telescopes of the time due to their lower luminosity in this energy band.

The difference in the radio emission between radio "quiet" and radio "loud" is related to the ratio between the radio luminosity and the optical luminosity (Kellermann et al., 1989). When plotting this quantity one would see that there are like two populations of AGNs: at fixed optical luminosity, some AGNs emit radio flux about 3-4 orders of magnitude higher than the other sources. Technically, the ratio is computed between the radio flux at 5 GHz and the optical flux in the B-band as

$$F_{radio}/F_{optical} > 10 \ .$$

The radio-loudness of AGNs is supposed to be related to the presence of powerful and very collimated relativistic jets of material launched from central region around the nucleus. They might be related to the host galaxy type (Smith et al., 1986) or to black hole spin (Kassiola et al., 1990; Wilson & Colbert, 1995).

Optical emission lines

The other feature characterizing AGNs and used for their classification is the presence of emission/absorption lines in the optical spectra, and their width. Various elements (like H, He, C, N, Ne, Mg, Fe) in the source can produce these lines, and they are modified on the basis of the velocity of the emitting region with respect to the observer due to Doppler effect. On the basis of the presence of such emission lines, the AGNs can be subdivided in:

- **Type 1:** show broad lines;
- **Type 2:** show narrow lines.

The difference between these two categories is when the lines are narrower (Type 2) or broader (Type 1) than 1000 km/s (measured at FWHM). Some other objects show unusual emission, for example BL Lac objects, as they do not show at all emission lines (or they are not detectable).

The phenomenological classification of AGNs

The combination of the two previous classifying parameters – radio emission and optical emission lines – leads to different classifications of the AGNs. As reported in **Figure** 3.4, this implies the creation of mainly six categories of AGNs:

- radio-quiet Type 2 and Type 1 objects, that is a group composed by Seyfert 2 and Seyfert 1 galaxies. Unusual objects of Type 0 are represented by the radio-quiet quasars (called *quasi-stellar objects*, QSO);

- radio-loud Type 2 AGNs, often called Narrow-Line Radio Galaxies (NLRG), are radio galaxies, classified as Fanaroff-Riley I and II (FR I and II) according to their radio morphology;
- radio-loud Type 1 AGNs are broad-line radio galaxies (BLRG) and radio quasars;
- radio-loud Type 0 AGNs with not detectable (or absent) emission lines are known as BL Lacertae objects (BL Lacs), from the name of the class prototype.

3.1.3 AGN unification model

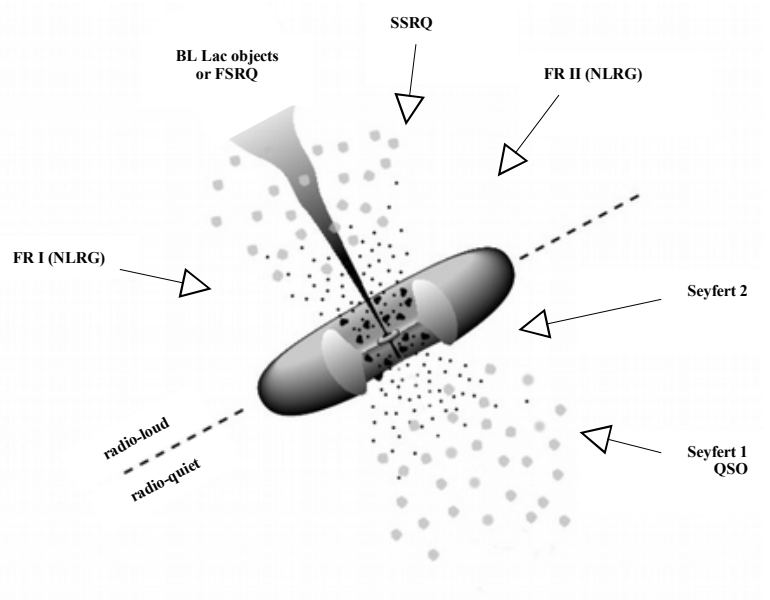

Figure 3.5: *A schematic diagram of the current paradigm for radio-loud AGNs (not to scale). Adapted from Urry & Padovani (1995).*

The complex classification of AGNs we have presented can be interpreted in a consistent and comprehensive scenario that describes the structure of the AGNs and that explains the differences between Type 1 and Type 2 objects (see Antonucci 1993 and Urry & Padovani 1995 for a detailed discussion and references therein). A schematic representation of such structure is reported in **Figure** 3.5.

The main point of this scenario is that the different classes of AGNs might be due to different views of the same object, because of a complex highly asymmetrical structure. Thus, the line-of-sight of the observer with respect to the object turns out to be particularly important, and this affects the emission properties of each class.

3.1.3.1 Radio-quiet blazar unification model

As represented in **Figure** 3.4, the radio-quiet AGNs are mainly subdivided in Seyfert I and Seyfert II galaxies. Seyfert galaxies are spiral galaxies with a bright core (but not showing presence of relativistic jets). The difference is that in Seyfert type-I galaxies the optical spectrum shows broad emission lines, and on the other side in type-II galaxies there are only narrow emission lines.

In 1985, Antonucci & Miller (1985) opened the first classification of Seyfert galaxies while studying the spectropolarimetry of NGC 1068, a bright nearby Seyfert 2 galaxy. In this galaxy, the broad emission lines were not visible in total light, while they emerged

when observing in polarized light. The conclusion was that the broad line region is present in the AGN, but it is obscured by the presence of a dusty torus at certain (large) angles of observation. Conversely, the NLR – that is located at much more distance than the BLR – is not obscured by the torus and reaches the observer located at any viewing angle.

For this reason, type-I Seyfert galaxies are supposed to be viewed at small angles with respect to the axis of the galaxy, and the observer can see both the BLR and the NLR in their spectrum. On the other side, type-II Seyfert galaxies are supposed to be pointing at large viewing angles with respect to the line-of-sight of the observer, and they do not show the light coming from the BLR that is obscured by the dusty torus.

3.1.3.2 Radio-loud blazar unification model

In the case of radio-loud sources, the model has to interpret also the relatively stronger emission at radio wavelengths.

The matter is launched into the jet at relativistic speed, and the resulting radiation is highly beamed. When the matter decreases its speed and the beaming decreases, it creates extended regions emitting light isotropically at radio wavelengths, called *hot spots* and *radio lobes*. The comparison between the extended isotropic radio emission and the beamed light produced by the jet is an indication of the viewing angle of the object.

Additionally, the spectrum of the radio emission of the jet and of the radio structures is different. The jet emits a very flat radio spectrum, but when its beaming is suppressed, only the steep-spectrum radio emission coming from the lobes is visible. For this reason, the radio emission in misaligned sources generally shows a steep radio spectrum.

In this framework, the jetted AGNs pointing at large viewing angles with respect to the line-of-sight of the observer show depressed beamed light and strong extended radio emission coming from the radio structures. When the latter structures are prominent and powerful emitters at radio wavelengths, we call this type of AGNs *Fanaroff-Riley type-II* (FR II) radio-galaxies. Conversely, when these structures are dim and not visible, they are called *Fanaroff-Riley type-I* (FR I) radio-galaxies, and are supposed to be provided with symmetric radio jets whose intensity falls away from the nucleus.

When the viewing angle decreases, the ratio between beamed light and extended radio emission increases. Moving to lower and lower viewing angles, the beamed light of the jet becomes dominant, and the radio spectrum of the source becomes flat. When the source is viewed at very low angles with respect to the line-of-sight of the observer, it is called a *blazar*. The blazar is then subdivided into two main groups of objects: the flat spectrum radio quasars (FSRQs) that show strong emission lines in their optical spectrum, and the *BL Lac objects* that show faint or absent emission lines. More information on this class of objects is reported in the next Section.

Emission in FSRQs and SSRQs

Here I report a short description of radio quasars, that have an important role in the blazar classification.

Radio quasars can be divided into steep-spectrum radio quasars (SSRQ) and flat-spectrum radio quasars (FSRQ). The difference is due to the different radio spectral index at a few GHz (0.5 being usually taken as the dividing line, see Padovani et al. 2017), that is related to the size of the radio emitting region. The radio emission of these sources is interpreted as synchrotron radiation (see Section 1.2.1.3), and it assumes different spectra whether the emitting region is extended (steep spectrum) or concentrated (flat spectrum).

In the case of FSRQs, the overall emission is thought to be the result of the superposition of various self-absorbed components, and it indicates that the nuclear emission dominates over the more extended emission of the so-called "radio-lobes". Conversely, the properties of SSRQs are intermediate between FSRQs and radio quiet quasars, and their emission coming from the external extended emission overwhelms the radio core emission (see e.g. Gu & Ai, 2011).

3.2 Blazars

The active galactic nuclei presenting a relativistic jet that is pointing within a narrow angle with the line-of-sight of the observer are called *blazars*. As we will see in this Section, blazars are particularly important because the radiation produced by the relativistic jet is basically unobscured and allows us to study the physical mechanisms that accelerate the particles up to the highest energies.

3.2.1 Spectral energy distribution

In blazars, the emitted radiation covers the entire electromagnetic spectrum from radio wavelengths up to VHE gamma rays. The spectral energy distribution (SED) of blazars is dominated by the non-thermal emission of the relativistic jet (Urry & Padovani, 1995), and is generally composed of two main humps (see **Figure** 3.6) located at low and at high energies.

In particular, the first hump is commonly attributed to synchrotron radiation produced within the relativistic jet. Such light covers all the wavelengths from radio up to the hard X-ray band, and its high level of polarization confirms the synchrotron origin of this emission.

Conversely, the emission at high energies from X-rays up to VHE gamma rays is more debated and seems to be more dependent on the particular type of blazar we are talking about. In most of the blazars, the main component is supposed to originate from inverse Compton (IC) scattering of photons. These photons are assumed to originate from the same population of electrons responsible for the synchrotron radiation, and this process is known as Synchrotron Self–Compton (SSC, see Section 3.2.4.1). For example, in the case of extreme blazars, instead, the emission mechanism might be contributed by other processes (see Chapter 4).

3.2.1.1 Environment of FSRQ and BL Lac objects

The environment of some blazars might contribute with additional scattering due to the rich external photon fields in the so-called External Compton (EC) scenario. Such photons may come from the accretion disk of the black hole at the center of the galaxy (Dermer & Schlickeiser, 1993), from the broad line regions (Sikora et al., 1994), or the dusty torus (e.g. Blazejowski et al., 2000). This phenomenon is typical of FSRQs, where the intense photon fields fill the space between the disc and the jet. In their SED, there are several emission components that can be measured, and the EC process fits well the data obtained by observing such blazars (see e.g. the case of 3C 454.3 in Vercellone, 2011). This process implies that the electrons cool rather strongly and produce a powerful inverse Compton component.

On the other hand, in BL Lac objects this scenario seems not to work and the electrons are able to produce photons up to the highest energies because of the lack of cooling processes. In some of such objects (the most energetic ones, named extreme blazars), there might be also a contribution coming from hadronic processes.

3.2.1.2 The blazar sequence

A particular role has been played by the relation between BL Lacs and FSRQs within the broad family of blazars. The differences of these objects seem to be not only related to different powers and luminosity, but probably also to different acceleration mechanisms of the particles.

Blazars are traditionally subdivided between BL Lacs and FSRQ following two main methods:

- **Emission lines:** this is the most common method, and it defines a BL Lac object when the emission lines are “narrow”, meaning that their equivalent width is < 5 Å

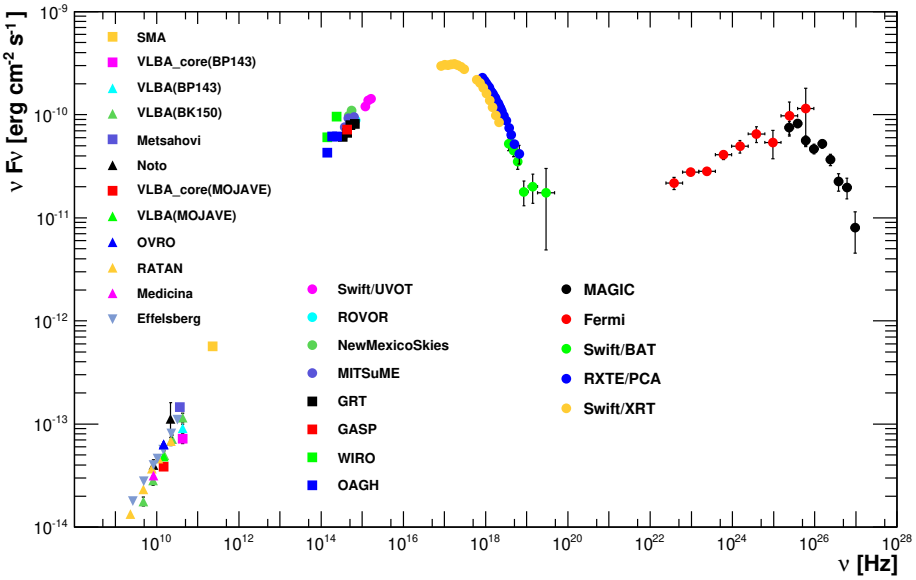

Figure 3.6: *The typical blazar SED of Mrk 421 during a multi-wavelength campaign reported in Abdo et al. (2011b).*

or not present at all (Urry & Padovani, 1995). Alternatively, the blazar is defined as a FSRQ (broader emission lines).

- **Eddington luminosity:** this is an alternative method that can be used only when the mass of the central supermassive black hole is known. A difference between FSRQs and BL Lacs can be traced when $L_{\rm BLR}/L_{\rm Edd} \geq 10^{-3}$ (FSRQs at higher ratio values, BL Lac at lower values), considering the ratio of the luminosity of the broad lines $L_{\rm BLR}$ to the Eddington luminosity $L_{\rm Edd}$ (Ghisellini et al., 2011; Sbarrato et al., 2014).

There are probably also some selection effects that affect the observability of blazars. Considering that the source detectability is constrained by the limited sensitivity of our instruments, there is always the tendency to sample the most luminous sources at higher distances. Such selection effects creates a bias (the *Malmquist bias*) that is not easy to remove. For example, in the case of BL Lacs, this traditionally motivated a supposed distinction between low-redshift BL Lacs (Type 0) and high-redshift BL Lacs (Type 1, or quasar-like), and the possible presence of evolution/transition between these two types of objects (e.g. Morris et al., 1991). However, there is no real evidence that such evolution exists for BL Lacs.

For a detailed review of all the properties of the sample in the different wavelengths see Padovani et al. (2017). If the selection effects are not the main issue of our sample of blazars and we assume that the acceleration mechanism is similar for all of them, there is an historical interpretation of these two categories as they are plausibly part of a phenomenological sequence that blazars may be following (Fossati et al., 1998). Such "blazar sequence" is based on the anti-correlation between the bolometric luminosity and the peak energy of their SED humps, and it was interpreted as due to the different radiative cooling efficiency of the emitting electrons in different sources (Ghisellini, 1999; Ghisellini & Tavecchio, 2008; Ghisellini et al., 2017).

The FSRQ are considered the "redder" blazars, i.e. the objects with the two peaks in the SED located at lower frequencies: their synchrotron peak is usually located between 10^{11} and 10^{15} Hz, while the high-energy one ranges from 10^{21} to 10^{24} Hz. They are characterized by high bolometric luminosity, and this is probably correlated to a rich environment around the jet that makes the second hump of the SED being dominated by external radiation.

Beyond FSRQs, the sequence is composed by the BL Lac objects. Actually, the BL Lac objects are not a uniform class, but are further subdivided into four different subclasses of BL Lac objects, classified depending on the frequency $\nu_{\rm peak}^{\rm sync}$ at which the synchrotron hump is peaking.
The four classes are composed by:

1. low synchrotron peaked BL Lac objects (LSPs) with $\nu_{\rm peak}^{\rm sync} < 10^{14}$ Hz;
2. intermediate synchrotron peaked BL Lac objects (ISPs) with $\nu_{\rm peak}^{\rm sync}$ between 10^{14} and 10^{15} Hz;
3. high synchrotron peaked BL Lac objects (HSPs) with $\nu_{\rm peak}^{\rm sync}$ between 10^{15} and 10^{17} Hz;
4. extremely-high synchrotron peaked BL Lac objects (EHSPs) with $\nu_{\rm peak}^{\rm sync} > 10^{17}$ Hz. These objects represent the main subject of this Thesis, and will be discussed in detail in Chapters 4 and 5. In this Thesis, I will also use the term *extremely high-peaked BL Lac objects (EHBLs)*, with reference to the EHSPs, following an historical nomenclature of low- and high-energy peaked BL Lacs (LBL/HBL) in Padovani & Giommi (1995). From now on, I will use indifferently the term EHBLs or "extreme blazars" for this class of objects.

In BL Lac objects, the environment surrounding the relativistic jets is much poorer with respect to FSRQs and the seed radiation for the IC process is supposed to be provided by the internally produced synchrotron photons. This implies lower energy losses for electrons, therefore larger typical electron energies and a smaller Compton dominance, meaning that the synchrotron peak shifts toward higher energies, justifying the fact that they are located at much higher frequencies.

Additionally, also the ratio between the luminosity of the synchrotron peak and the high-energy IC one increases. This can be evaluated through the definition of the parameter *Compton dominance* (CD, see Section 3.2.3.5), defined as the ratio between the second hump peak luminosity and the synchrotron peak luminosity νL_ν. The idea is that, the further we go into the BL Lac objects category, the lower should be the CD parameter due to poorer photon environment surrounding the AGN.

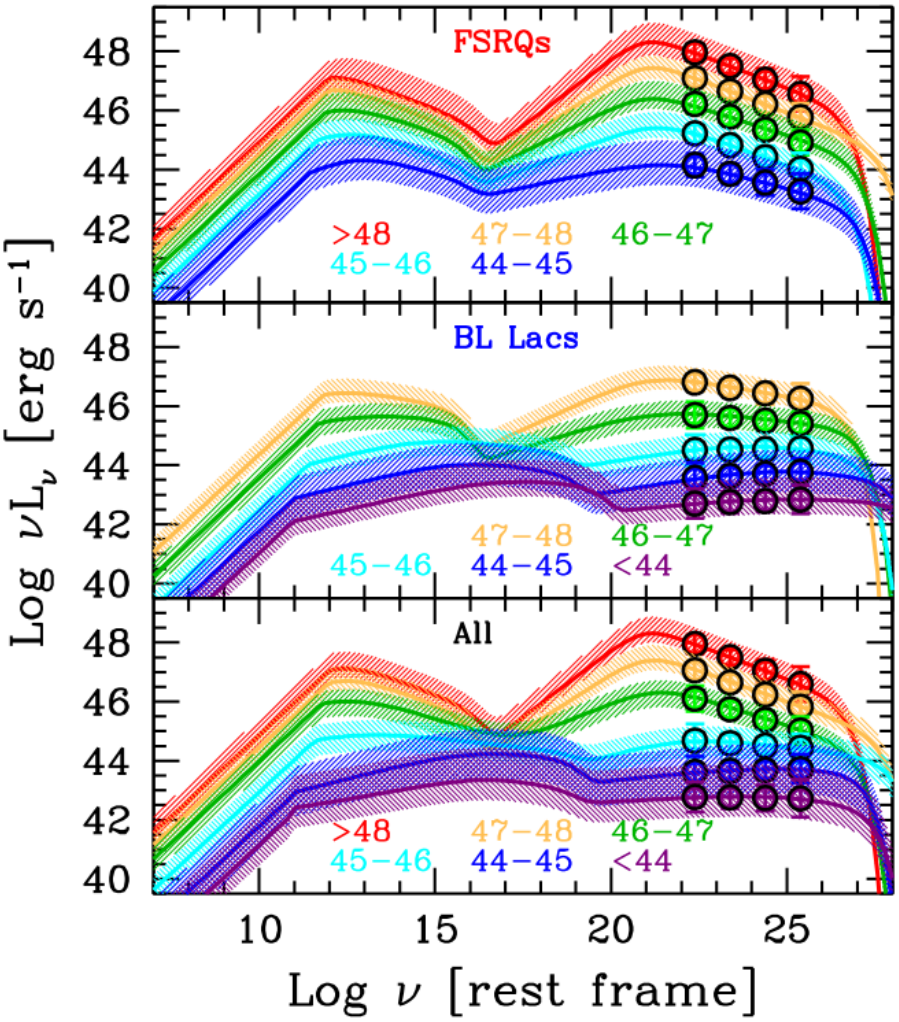

Figure 3.7: *The blazar sequence reported by Ghisellini et al. (2017). Average SEDs for sources of different gamma-ray luminosity in the blazar sequence (represented in different colors).*

3.2.2 Blazars and their observational properties

3.2.3 Beaming

The particles accelerated in the AGN jets reach relativistic velocities. This means that the special relativity has to be applied in order to interpret their motion and the consequent phenomena. In this Section, I will briefly introduce some of the main concepts related to this topic. A detailed discussion can be found in Ghisellini (2013).

Special relativity taught us that space and time are strongly correlated. Let us consider a clock and a ruler moving in the space. Let us call K' the reference system in which they are at rest and that is moving with them, an K the reference system of the laboratory that is seeing them moving at a velocity $v = \beta c$. Let's assume that the relative motion between the reference systems is only on the x axis. Then, special relativity tells us that the relation between the two reference systems is given by

$$\begin{cases} x' = \Gamma\,(x - vt) \\ y' = y \\ z' = z \\ t' = \Gamma\,(t - \beta\frac{x}{c}) \end{cases}$$

and its inverse relations. Here, the symbol $\Gamma = \frac{1}{\sqrt{1-\beta^2}}$ is called *Lorentz factor*.

In we measure the length of the ruler, it has to be measured at the same time t. This implies that, the length in the comoving reference system results $\Delta x' = \Gamma \Delta x$ and in the lab reference system is

$$\Delta x = \frac{1}{\Gamma}\,\Delta x' \ .$$

In this last equation, when the ruler is moving $\Gamma > 1$, and $\Delta x < \Delta x'$ representing a *contraction* of the length as measured in the K' reference system.

Similarly, in order to determine the time interval in the K lab system, we obtain a time *dilation* given by

$$\Delta t = \Gamma\,\Delta t' \ .$$

When measuring the motion of a ruler with photons, this process has to consider that their path from the two sides of the ruler to the observer is different (longer for the point at larger distance from the observer). For this reason, if we consider the same ruler moving at the velocity v and with an inclination angle θ with respect to the line of sight, the length of a ruler moving towards us will be affected by the limited velocity of the photons by which we measure the position of the two sides. The total length l we measure is thus given by

$$l = \frac{l'}{\Gamma(1 - \beta\cos\theta)} = \delta\ l' \ .$$

The observed length of the ruler depends on the viewing angle, and reaches a maximum when $\cos\theta = \beta$.

A similar discussion can describe the measurement of a time interval by using photons. Considering the arrival time of the photons, the time interval measured in K is related to that in K' by

$$\Delta t = \frac{\Delta t'}{\delta}$$

In this last formula, we are experiencing a *time contraction* instead of a time dilation, that is recovered only when $\theta = 90$ degrees. This is due to the presence of photons by which we measure distances.

Considering that the frequency ν is the inverse of the time, the previous relation yields to

$$\nu = \nu'\delta \ .$$

For this reason, the δ term is called *Doppler factor*. It is particularly interesting to note that the Doppler factor contains two terms:

- a first term is $\frac{1}{\Gamma}$, that corresponds to the special relativity term;
- another term $\frac{1}{(1-\beta\cos\theta)}$ that is related to the Doppler effect.

When the object is moving with $\theta = 90$ degrees with respect to the line of sight of the observer, only the special relativity term remains. When θ is close to zero, the term related to the Doppler effect becomes very large and the special relativity term becomes secondary.

This effect is at the basis of the so-called *superluminal motion* of some blobs measured in radio galaxies. The velocity of the blob as measured by the observer is

$$v_{\rm app} = \frac{d\Delta\theta}{\Delta t_A} \ ,$$

where d is the distance from the source, and $\Delta\theta$ the angular distance of the blob measured at two different moments related by the time interval Δt_A. In several cases, this velocity appears larger than the light speed c. The explanation is that the term Δt_A can be much shorter than the emission time Δt_e. Due to the different path of the photons by which we measure the time interval, the displacement projected in the plane of the sky can be expressed by

$$d\Delta\theta = \beta c \Delta t_e \sin\theta \ .$$

Dividing by the time interval $\Delta t_a = \Delta t_e(1-\beta\cos\theta)$, we get again $v_{\rm app}$ as

$$v_{\rm app} = \frac{\beta c \Delta t_e \sin\theta}{\Delta t_a} \ ,$$

or similarly

$$\beta_{\rm app} = \frac{\beta\sin\theta}{1-\beta\cos\theta} \ .$$

This implies that, when $\theta \to 0$ or to infinity, then $\beta_{\rm app} \to 0$. On the other side, when θ is small, then $\beta_{\rm app}$ becomes larger than unity and we get the apparent superluminal motion.

Thanks to the previous formulae, one can also calculate how the monochromatic intensity transforms

$$I(\nu) = \delta^3 I(\nu' = \nu/\delta) \ ,$$

and when integrating to obtain the bolometric intensity

$$I = \delta^4 I' \ .$$

It is interesting to note that the fourth power of the δ term can be interpreted as related to three different contributions: one δ term comes from the transformation of the time, one from the frequencies, and two from the solid angle.

A similar treatment comes for the transformation of the luminosity. In fact, it is proportional to the flux, that in turn is proportional to the integral of the flux over the solid angle. This solid angle, however, is the same in both the K and K' reference systems. In conclusion, in the case of a single spherical blob the luminosity transforms as

$$L = \delta^4 L' \ .$$

3.2.3.1 Variability time-scale

In the last decades, the observations of blazars at various wavelengths have reported a notable amount of information regarding their flux variability. However, this is still a major open question in this field for several reasons. In fact, the flux variability in blazars covers a huge range of time scales: while some blazars have been showing minute-basis

time variability (e.g. the famous case of PKS 2155-304 reported in **Figure** 3.8, see Aharonian, 2007), some others show longer periods of hours and weeks. Additionally, there is now an increasing interest for some objects that show variability on months to year time-scale: for example, the most interesting blazar showing periodicity of about two years is PG 1553+113, that I will present in Section 3.2.6.

However, this important difference in the flux variability does not mean that we are dealing with the same phenomenon. While a flux variability of minutes to days is registered in the case of flaring episodes of blazars, the long-term variability of months to years is supposed to be correlated with phenomena more connected with the structure itself of the AGN, for example the presence of oscillation in the accretion disk or the presence of a system of BH at the center of the AGN.

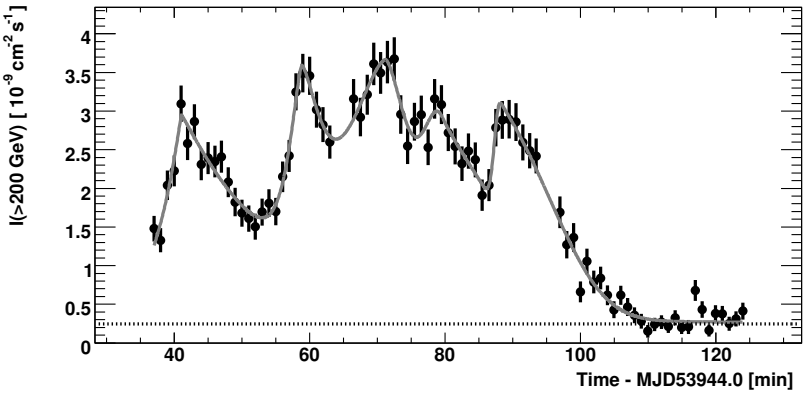

Figure 3.8: *The famous case of PKS 2155-304 with the fastest minute-variability ever observed in blazars. Reported by Aharonian (2007).*

3.2.3.2 Size of the emission region

The emission region size of blazars is a particularly interesting aspect to consider, since all the theoretical models need it in order to guess the physical parameters that are producing the particle acceleration within the jet.

Considering the light curves of blazar objects in the gamma-ray band, constraints on the size and location of the emission region of the blazar can be inferred by considering the flux variability time-scales of the jet during the flaring events (e.g. Longair, 2002). The flux variability time-scale provides information on the maximum size of the emission region, since the light has to connect within a certain light-time the whole region. Given the emitting region size R, the variability time-scale t evaluated on the light curves, the redshift z of the source, and the Doppler factor δ, the following relation holds:

$$R \leq c\, t\, \frac{\delta}{1+z}\ .$$

For example, in the case of M87 that has shown several flaring episodes with variability of approximately one day, the 2010 TeV flare led to an upper limit on the emission region size of $R \leq 5 \times 10^{15}\ \delta$ cm (Abramowski et al., 2012).

Probably the most interesting case in this topic was the case of PKS 2155-304 (reported in **Figure** 3.8, see Aharonian, 2007). Thanks to the minute-based time variability, a region size of less than $R\,\delta^{-1} < 4.65 \cdot 10^{12}$ cm was evaluated. Such low value of $R\,\delta^{-1}$ brought the authors to think that there could be only two interpretations of this result: one has to assume either that there are very large Doppler factors present in AGN jets, or that the observed variability is not connected to the central black hole.

Studies about the minimal variability time-scale of blazars with respect the gamma-ray emission has been performed by several authors. For example, Vovk & Neronov (2013) verified the observed minimal variability time scales for several sources with the *Fermi*-LAT

data, finding them to be very close to the light-crossing times of their SMBHs and guessing a strong correlation between the SMBH and the gamma-ray emission zone. However, their study was limited by the sensitivity of the *Fermi*-LAT instrument, which presents a collective area of about 1 m^2 that allows the detection of flux variability on the light-crossing time scales only for the brightest sources.

Conversely, ground-based gamma-ray telescopes like the IACTs present much bigger collective areas of the order of $10^4 - 10^5$ m^2. This implies that they are able to detect flux variations of sources much dimmer with respect the *Fermi*-LAT capabilities, and play an important role in this field (Vovk & Babić, 2015).

3.2.3.3 Blazars spectra in gamma rays and EBL absorption

In Section 1.3.4 I have reported general information about the presence of interaction between light at different wavelengths, and in particular the one between gamma rays and IR light coming from the EBL. This interaction strongly affects the study of blazars, and especially in the gamma-ray band. In fact, the interaction of their emitted light with the EBL implies a strong absorption at HE and VHE gamma rays.
This effect can be modelled by an exponential absorption of the type:

$$F_{\rm obs}(\tau) = F_{\rm int} \cdot e^{-\tau(z,E)} \ ,$$

where we indicate with $F_{\rm obs}$ and $F_{\rm int}$ the observed and intrinsic flux of the source respectively, and with $\tau(z, E)$ the absorption due to interaction with EBL of gamma rays with energy E and coming from a source with redshift z.

As shown in the formula, the dependence of τ on the distance of the source and the energy of the radiation implies that distant sources will be difficult to be detected in VHE gamma rays: the higher the distance and the higher the energy of the spectrum I am interested into, the lower the flux I actually receive.

This effect is particularly important in the study of EHBLs, reported in Chapters 4 and 5, where we are interested in the last part of the spectrum at high energies above about the TeV gamma-ray band.

Thanks to several efforts in modelling the EBL spectrum, we are now able to apply their corrections to the measured data. In this Thesis, I will use mainly three models by Franceschini et al. (2008a), its updated model in Franceschini & Rodighiero (2017), and in the MAGIC Collaboration also the model by Dominguez et al. (2011).

3.2.3.4 Relation between different wavelengths

One of the most important features of blazars is that they emit non-thermal light through the entire electromagnetic spectrum from radio up to gamma rays. For this reason, the MWL approach for blazars is crucial. In particular in the case of blazars, this approach allows the scientists to investigate possible correlations between the different energy bands and test the hypothesis of a common emission mechanism.

The emission of blazars is generally well represented by the two-hump structured SED, as in **Figure** 3.6 on page 124. The synchrotron hump goes from radio to X-ray wavelengths with a pretty coherent shape, except for few features. For example, at low radio frequencies the auto-absorption is responsible for a lower flux with respect to that expected in the case of pure synchrotron frequencies. For this reason, generally the radio component of blazars is not considered when testing the theoretical models to the experimental data. Additionally, the synchrotron hump is affected by the thermal radiation of the galaxy at optical wavelengths.

The host galaxy in blazars SED

The presence of the radiation coming from the host galaxy in the blazars SED depends on several features, for example:

redshift of the source: the higher the redshift, the lower is the average flux of the host galaxy. In practice, the host galaxy can be observed in the SED of blazars up to redshift of about 0.5 in the most optimal cases;

relative luminosity of the host galaxy and of the blazar jet light: obviously, if the blazar jet is too strong with respect the host galaxy light, it will be dominating the SED in that energy range. For example, the case of the blazar PG 1553+113 in Section 3.2.6 where the redshift estimation is particularly difficult because the bright blazar jet light is overhelming the host galaxy light, and this does not allow for a precise determination of the redshift;

frequency at which the synchrotron hump is peaking: the previous effect is even more enhanced when the blazar is peaking with its SED where the flux of the host galaxy should be detected, i.e. in the optical range. For example, the LBL/IBL objects are typically peaking in that energy range, and it is typically more difficult to determine their redshift by this approach.

The synchrotron hump is then generally composed by freshly injected electrons that are peaking in the optical to X-ray bands: considering that this region is produced by the most energetic electrons in the jet and it is highly sensible to variations in their density, the flux registered in these energy bands is generally particularly variable.

The high-energy hump in the SED of blazars is generally supposed to be mainly contributed by the reprocessed photons emitted in the synchrotron processes. For this reason, there seems to be a relation between the emission in the first (synchrotron) hump and in the second hump. For example, the optical-UV radiation is supposed to correspond to the HE gamma-ray band, while the X-ray radiation of freshly injected electrons is probably related to the VHE gamma-ray regime (a very similar variability in the X-ray region is often detected in VHE gamma rays).

3.2.3.5 Compton dominance

The Compton dominance (CD) is a parameter commonly used in blazar physics as additional information with regards the different classes of blazars in the *blazar sequence*. It is defined as the ratio between the second hump peak luminosity and the synchrotron peak luminosity νL_ν, that is the ratio between the power injected in the form of electrons and the power in the external photon component.

The environments of FSRQs are supposed to be rich of external photon fields. The latter interact with the jet by cooling the relativistic matter, and producing higher powers in the IC peaks, and for this reason high values of the CD are reported in this class of objects. Conversely, poorer environments are supposed to be present in the BL Lac objects, and for this reason the CD parameter is generally lower. When in general the CD value becomes lower when the frequency of the synchrotron peak increases, and in EHBLs it turns to be of the order of about $0.1 - 0.2$.

3.2.4 Models of blazar emission

The modelling of blazar emission is a particularly hot topic because it is the key to access the hidden physical mechanisms able to accelerate particles in the blazar jets.

Historically, the most important model of the blazar emission is the leptonic Synchrotron Self-Compton model. Besides this model, several other leptonic models have been proposed, characterized by different characteristics of the emitting regions or of the involved processes.

In the last years, the particle acceleration mechanism within the blazars jet has received an increasing interest, especially trying to overcome the current difficulties by making more complex scenario or adding more complex hadronic processes. In fact, the hadronic contribution to the main leptonic processes is the only way to explain the possible production of neutrinos, as recently revealed by the discovery of the neutrino emitted by the flaring blazar TXS 0506+056 (see Section 6.1).

In this Section, I report some of the most interesting models that I encountered during my PhD activities.

Leptonic models

3.2.4.1 Synchrotron Self-Compton model

The synchrotron self-Compton (SSC) model is the historical standard one-zone leptonic model that has been extremely successful in modelling the broad-band SED of BL Lac type objects (e.g. Maraschi et al., 1992; Tavecchio et al., 1998).

In this scenario, the emission is provided by isotropic relativistic leptons (electrons or pairs) with energy distribution $N(\gamma)$ given by a double power-law distribution with a smooth connection

$$N(\gamma) = K\,\gamma^{-p_1}\left(1+\frac{\gamma}{\gamma_b}\right)^{p_1-p_2} ,$$

where K is the normalization factor, p_1 and p_2 are the spectral indices respectively before and after the spectral break, at which the Lorentz factor of the electrons is γ_b. This particular form for the distribution function is commonly assumed on a purely phenomenological basis in order to describe the typical SED of blazars.

The emitting region is supposed to be contained in a spherical region ("blob") of radius R and tangled by a uniform magnetic field B. It is moving with a bulk Lorentz factor Γ along the axis of a relativistic jet, which forms an angle θ with respect to the observer line-of-sight.

The relativistic effects are taken into account by introducing the relativistic Doppler factor

$$\delta = \frac{1}{\Gamma(1-\beta\cos\theta)} .$$

In this model, the electrons are supposed to be accelerated within the jet by some acceleration mechanism. The curved path they describe implies that they are accelerating, and then they produce synchrotron radiation.

The photon fields produced by the synchrotron mechanism are then supposed to be processed again by the very same population of electrons via IC scattering, and they are accelerated up to the higher energies and produce the high-energy SSC component.

This simple model is fully constrained if a good sampling of the SED (especially around the peaks) and an estimate of the variability time-scale are provided (Tavecchio et al., 1998). A good dataset covering all the broad-band spectrum is essential for the test of this model and allows to get strong constraints on the physical parameters of the jet.

3.2.4.2 1D conical jet model

Within the single-zone leptonic models, I mention here the numerical code by Asano et al. (2014) (see also Asano & Hayashida, 2015, 2018) called 1D conical jet model. This model

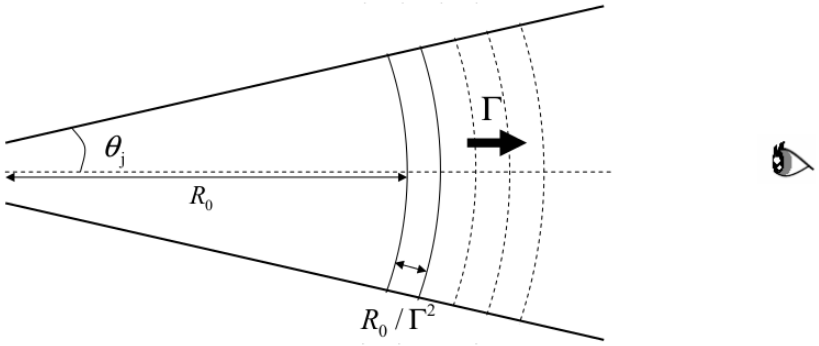

Figure 3.9: *Schematic picture of the model by Asano et al. (2014).*

.

makes use of the SSC process, but with a different evolution of the emission zones within the blazar jet.

In this model, represented in **Figure** 3.9, the emission from the non-thermal electrons is supposed to be produced in a conical jet. The evolution of the electron and the photon energy distributions are computed as a function of time along their motion within the jet. This framework is similar to the `BLAZAR` code by Moderski et al. (2003), which has been frequently adopted to reproduce blazar spectra (see e.g. Kataoka et al., 2008; Hayashida et al., 2012).

The conical expansion of the jet naturally implies an adiabatic cooling of the electrons. This effect resembles the electron escape in one-zone steady models, that thus is neglected in this 1D code.

A continuous injection of non-thermal electrons from the initial radius $R = R_0$ up to the radius R is computed during the dynamical time-scale $R_0/c\Gamma$ in the plasma rest frame, during which time-scale the injection rate into a given volume V (which is expanding as $V \propto R^2$) is assumed to be constant.

The energy distribution of the electrons at injection is assumed to be a broken power-law with exponential cut-off

$$N(\gamma) = K\,\gamma^{-p_1}\left(1+\frac{\gamma}{\gamma_b r}\right)^{p_1-p_2}\cdot\exp\left(-\frac{\gamma}{\gamma_{\max}}\right),$$

where p_1 and p_2 are the two indices of the power-law, $\gamma_{\rm br}$ is the break energy (Lorentz factor), and $\gamma_{\max}$ is the cut-off energy. The minimum Lorentz factor $\gamma_{\min}$ is fixed to 20. The electron energy distribution and the photon emission are computed even after electron injection ends as far as R reaches $R = 10\ R_0$.

The main feature of this model is the adoption of a Fermi second-order process for the acceleration of particles and to produce hard spectra at gamma ray energies. This process, characterized by a slow acceleration of the electrons, can naturally explain the lower maximum energy of electrons. This parameter is a characteristic feature of the study of EHBLs (see Chapter 4), and for example the Fermi second-order process was used in Lefa et al. (2011) to fit the archetypal EHBL called 1ES 0229+200, with a detailed discussion focused on the balance between the acceleration and cooling.

In the plasma frame, the magnetic field B evolves as

$$B = B_0\,\frac{R_0}{R}\ .$$

During the numerical computation, several effects are taken into account: for example, the synchrotron and inverse Compton scattering with the Klein-Nishina effect, the γ-γ-absorption, the secondary pair injection, the synchrotron self-absorption, and the adiabatic cooling.

The code considers an on-axis observer with viewing angle θ_v equal to zero, and jet opening angle assumed to be $1/\Gamma$, where Γ is the bulk Lorentz factor of the jet. The

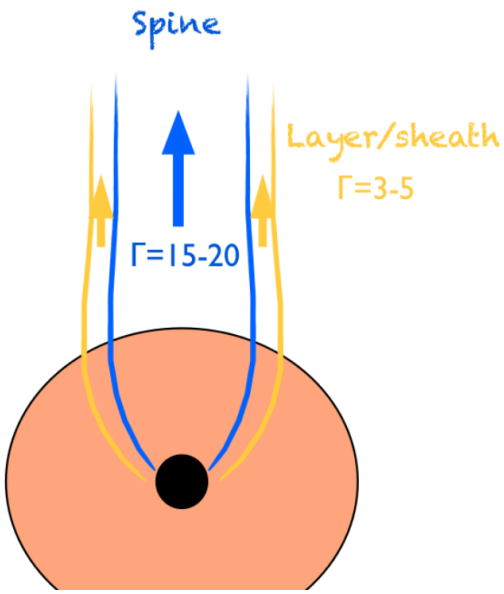

Figure 3.10: *Schematic picture of the spine-layer model. Taken from a presentation at TeVPA2018 conference (https://tevpa2018.desy.de) by Fabrizio Tavecchio.*

.

photon flux is obtained by integrating the emission over the entire jet, taking into account the Doppler boosting by the conically outflowing emission region.

Considering the steady emission scenario, this model assumes a total number of eight parameters: the initial radius R_0, the bulk Lorentz factor Γ, the initial magnetic field B_0, the electron Luminosity L_e, p_1, p_2, γ_{br}, and γ_{max}.

3.2.4.3 Spine-layer model

The one-zone leptonic models have been successful in describing the majority of the blazar SEDs. However, as in the case of EHBLs described in Chapter 4, there are several difficulties that make them not easily adoptable in some limit case of the blazar family.

Some of such extreme parameters needed in the one-zone models can be avoided by assuming leptonic processes taking place in a more complex structured jet, for example the so-called spine-layer model introduced by Ghisellini et al. (2005). In this framework, represented in **Figure** 3.10, the relativistic jet is supposed to be structured and consisting of two components: a central fast spine and a slower layer around it. The former moves with Lorentz factor $\Gamma_{spine} = 10 - 20$ in the inner part of the cylindrical jet, while the external layer has $\Gamma_{layer} = 2 - 5$ (Chhotray et al., 2017). This structure has been suggested by several theoretical and observational hints, for example the deep study of radio emission in the radio galaxy M87 (e.g. Tavecchio & Ghisellini (2015) for more details).

In this model, the relative motion between the layer and the spine acts as an amplifier of the radiation energy density in the frame of the spine. In these conditions, the IC emission of the spine is mainly due to the scattering of the soft photons of the layer, and the SSC component plays a minor role. Due to the larger Lorentz factor, the spine emissions dominates over that of the layer in the case of emission observed ad small angles, that is in the case of blazars.

For more information about the application of the spine-layer model in the case of EHBLs, see Chapter 4.

3.2.5 Hadronic models

In this Section, I report a fully hadronic model that I used in the description of the SED of PGC 2402248 (see Section 5.1). In hadronic models for blazars the high-energy hump of the SED is supposed to be produced by the protons in the jet or by secondary leptons produced in p-γ interactions. Such models have been widely studied as an alternative to leptonic models, for example in Mannheim (1993); Aharonian (2000); Mucke & Protheroe (2001); Boettcher et al. (2013).

One of the main problems of this scenario is that in general it requires high proton powers, well above the Eddington luminosity of the black hole powering the blazar. However, these models can be successfully applied in the case of EHBLs, and constitute a viable alternative to leptonic models. For more information about that, see Chapter 4.

In hadronic scenarios, at least an additional proton population has to be considered, which implies six more free parameters with respect to the standard SSC scenario: the three Lorentz factors $\gamma_{\mathrm{p;min}}$, $\gamma_{\mathrm{p;break}}$, and $\gamma_{\mathrm{p;max}}$, the indices of the proton power-law distribution, and the normalization factor of the proton distribution. These parameters have to be constrained, and generally this procedure differs in the different models.

3.2.5.1 Proton-synchrotron model

Here I present the main hadronic model that I used during this Thesis, the numerical code developed by Matteo Cerruti in Cerruti et al. (2015), that has been studied in a particular way for the application to EHBLs. In this model, there is a coexistence of different leptonic and hadronic processes.

The leptonic processes are an evolution of Katarzynski, K. et al. (2001). The emitting region is considered of spherical shape with radius R, filled with a tangled and homogeneous magnetic field B, and moving with a Doppler factor δ. The primary electron distribution is supposed to be stationary and described by a broken power-law function, with a break due to the cooling of the particles emitting via synchrotron processes and IC scattering (see e.g. Inoue & Takahara 1996).

In Cerruti et al. (2015), the previous model has been modified by applying the following points:

- the broken power-law function is provided with an additional exponential cut-off;
- there is a more detailed computation of the synchrotron emission with less approximations, crucial to extend this model with hadronic processes;
- the synchrotron emission is computed by using the standard formulae for the emissivity and self-absorption, and contains a more precise computation of the absorption of high-energy photons interacting with low-energy ones via $\gamma + \gamma \rightarrow \mathrm{e}^+ + \mathrm{e}^-$;
- the secondary population of leptons coming from γ-γ pair production is computed;
- The EBL absorption with the model by Franceschini et al. (2008a) is included in the computation.

The hadronic processes are included in the model by assuming a stationary population of relativistic protons, in addition to the electrons. The protons share the same acceleration process as the electrons with a distribution described by a broken power-law function and an additional cut-off.
The synchrotron emission produced by the protons is evaluated in the same way as for the electrons by replacing the electron mass with the proton mass. In this model, the only target photons are considered to be the synchrotron emission from the primary electron population in the jet, that represent by far the dominant component at low energies in

EHBLs.

The protons in the emitting region interact with the low energy photons through photo-meson processes

$$p + \gamma = p' + n^0\pi^0 + n^+\pi^+ + n^-\pi^- + \dots \quad \text{and} \quad p + \gamma = n + n^0\pi^0 + n^+\pi^+ + n^-\pi^- + \dots$$

computed by using the publicly available Monte-Carlo code SOPHIA (Mucke & Protheroe, 2001), and through electron-positron pair production (Bethe-Heitler process):

$$p + \gamma = p' + \mathrm{e}^+ + \mathrm{e}^- \ ,$$

that is not included in the SOPHIA package and that are computed using the analytical formulae by Kelner & Aharonian (2008).
Thus, the hadronic component in this code is contributed by seven different processes: the synchrotron emission from protons and muons and their associated synchrotron emission from γ-γ secondary pairs, the synchrotron emission from the cascades triggered by photons produced via the π_0 decay, by $e^{\pm}$ produced via the $\pi^{\pm}$ decay, and by $e^{\pm}$ produced via the Bethe-Heitler process.

With this scenario in mind, the code considers the following assumptions in order to reduce the number of free parameters:

- since electrons and protons share the same acceleration process, the index α of the injected energy distribution is identical;
- the maximum proton Lorentz factor $\gamma_{p,max}$ is constrained by the equality of cooling and acceleration time-scales;
- at equilibrium, the electron energy distribution is computed considering that electrons are cooled primarily by synchrotron radiation;
- the emitting region size R is limited by the variability time constrains the size R of the emitting region;
- the Doppler factor δ of the emitting region is fixed to 30.

Under these assumptions, the standard procedure is to produce a certain number of hadronic models scanning the parameter space. A χ^2 test is usually used to select the solutions which correspond to a $1\,\sigma$ confidence interval.

Cerruti and collaborators, before applying it to a set of EHBLs, successfully applied the model to the SED of Mrk 421 of Abdo et al. (2011a).

Finally, they apply the numerical code to the study of five different EHBLs: 1ES 0229+200, 1ES 0347-121, RGB J0710+591, 1ES 1101-232, and 1ES 1218+304. A summary of the results on this study is reported in Section 4.1.5.2.

3.2.6 The blazar PG 1553+113

One of the most interesting examples of blazars is the source PG 1553+113 that I will present in this Section.

The source PG 1553+113 is a powerful blazar with enhanced emission at several wavelengths. It shows a synchrotron emission peaked above the optical regime $> 10^{15}$ Hz, and thus it represents the high-frequency peaked BL Lac (HBL) class. The MWL SED of this blazar is well sampled: an example taken from archival data is represented in **Figure** 3.11.

The synchrotron emission shows moderate variability from the IR to the X-ray bands. The enhanced emission in the optical band makes difficult to distinguish the optical thermal radiation coming from the host galaxy. For this reason, the redshift of PG 1553+113 is currently unknown, and only indirect estimations have been tried.

The high-energy hump is mainly related to IC emission, and shows variability in both the HE and VHE gamma-ray bands.

In this Section, I will present some information of this blazar that has been observed through the entire electromagnetic spectrum, and present some interesting special features, such as:

- the still unknown redshift;
- the strong periodicity in HE gamma rays, interpreted as possibility of having a system of two black holes in the nuclear region.

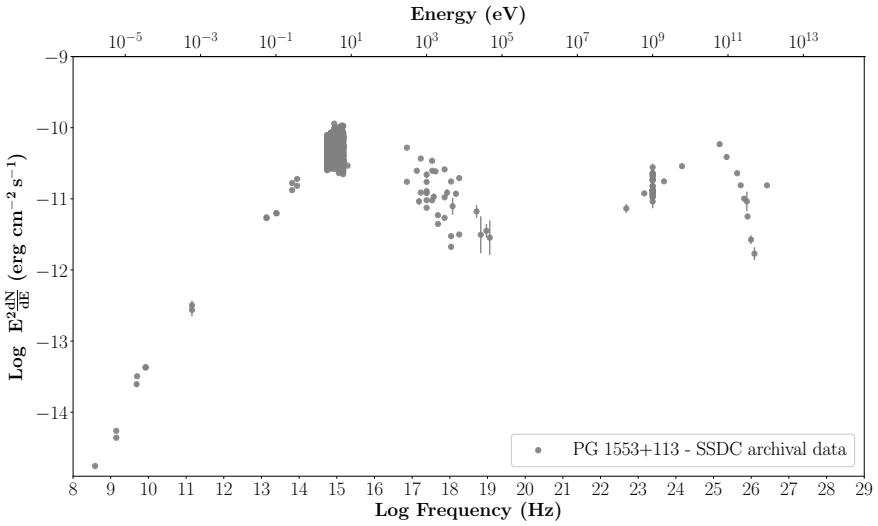

Figure 3.11: *Archival data (from SSDC) of the observed SED of PG 1553+113.*

3.2.6.1 Redshift and interaction with the EBL

The estimation of the redshift of PG 1553+113 is particularly important due to the fact that this source is a strong emitter in HE and VHE gamma rays, and the information we get from these energy bands in the observed flux can be extracted only with a good knowledge of the distance of the source in order to correct the flux for the EBL absorption. Having a strong emission in these gamma-ray bands and a possibly high absorption due to the interaction of such photons with EBL (see Section 1.3.4), this source results to be an interesting candidate to study this topic.

The fact that its redshift is basically unknown is due to the strong non-thermal emission of the relativistic jet that is overhelming the light from the host galaxy. There

are only rough estimations of the redshift that put it in the range $z \sim 0.4 - 0.6$ (Danforth, 2010), but with several contradictory estimations that have not been solved yet (e.g. Sbarufatti et al., 2005).

Several other tentative estimations of the redshift have been tried by using indirect methods. For example, the measurement of the absorbed flux at TeV gamma-ray energies can be used also to infer the possible maximum value of the redshift of the source. In the method by Prandini et al. (2011), by assuming a power-law spectrum of the source and an absence of pile-up (never observed in blazars at gamma-ray energies), one can deabsorb the spectrum until it starts to take over the power-law spectrum. When this happens (on a statistical basis), the corresponding value of redshift can be considered a good upper-limit on the true redshift. An example of the application of this method has been performed on PG 1553+113 in Prandini et al. (2009), of which I report in **Figure** 3.12 the main figure.

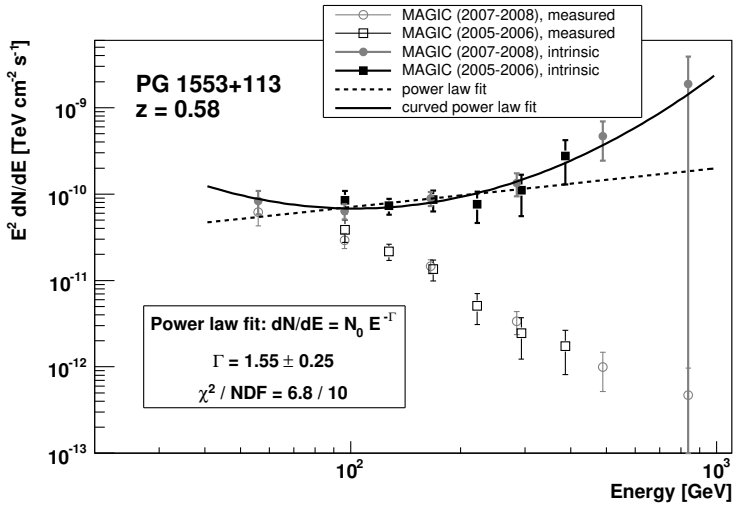

Figure 3.12: *Estimation of the redshift of PG 1553+113 by using indirect methods based on the effects of EBL absorption in Prandini et al. (2009). The assumed redshift is changed gradually. When the continuous black line fitted to the assumed intrinsic spectrum disagrees statistically with the hypothesis of absence of pile-up in the VHE gamma-ray spectrum of the blazar, an upper-limit on the redshift is set.*

3.2.6.2 Periodic variability

The blazar PG 1553+113 has been detected so far in the optical, X-ray, GeV and TeV gamma-ray bands. In particular, a first detailed study was performed by the *Fermi*-LAT Collaboration in Abdo et al. (2010b), and in 2015 it turned out to be particularly interesting due to the discovery of an hint of periodicity in this energy band published in Ackermann et al. (2015).

Such periodicity is clearly visible in the HE gamma-ray emission of the object. The continuous observations of this object over about seven years from 2008 August 4^{th} to 2015 July 19^{th} report a quasi-periodic trend with main peaks of gamma-ray emission occurring over a period of about 2.18 years (corresponding to the observer frame, and in the source frame to P/(1 + z) 1.5 yr) at a confidence level greater than 99%.

A MWL monitoring of this source is available covering the last years, and a similar periodicity has been found also in other wavelengths. Such periodicity, however, turns out to be different depending on the energy at which it is observed.

For example, a similar modulation was found in optical (Tuorla) and in radio (Owens Valley Radio Observatory OVRO, 15 GHz) light curves, with prolonged enhancements and emission minima in qualitative agreement with the gamma-ray overall trend.

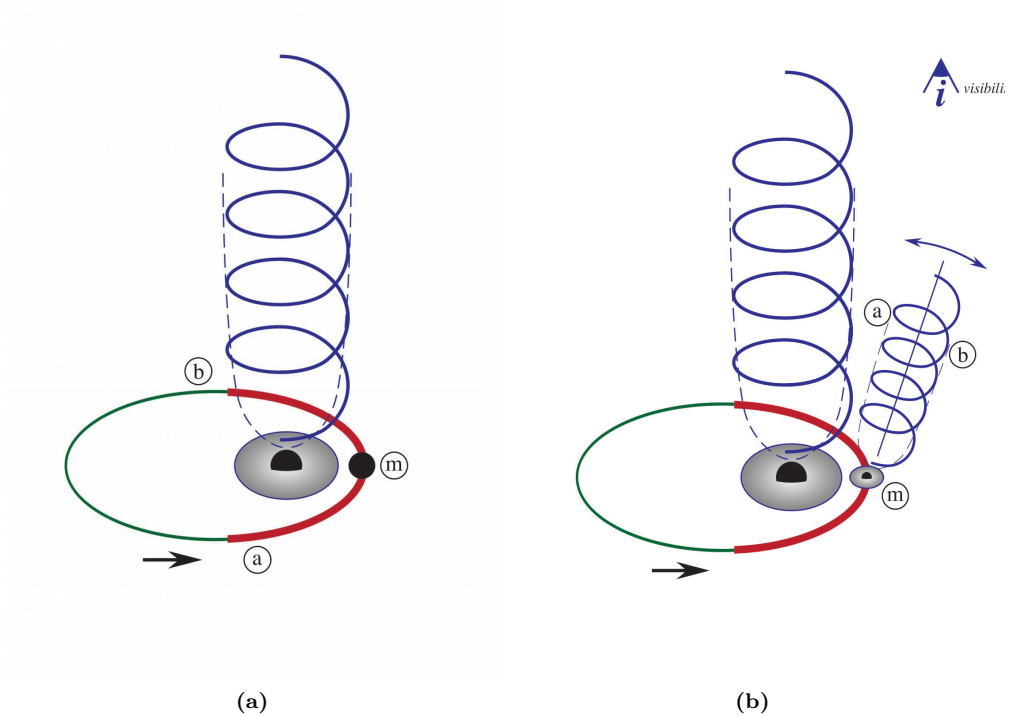

(a) **(b)**

Figure 3.13: *Schematic representation of the binary system of SMBHs in PG 1553+113 (Tavani et al., 2018). While the main periodicity is supposed to be related to the presence of a minor SMBH that interferes with the jet emission of the main SMBH, the secondary periodicity may be related to the presence of a second jet from the minor SMBH.*

Additionally, sparse X-ray monitoring of the source indicates the existence of a less statistically significant periodic behavior of X-ray flaring not always correlated with the gamma-ray flares.

The hint of periodicity of this blazar is particularly important because it is the first time such a significant periodicity has been found in a gamma-ray blazar. Among the possible interpretations, the periodicity might be due to the interaction of two SMBHs. This binary system of two SMBH would be located at the center of the AGN (in place of a typical individual SMBH) at a distance of few milli-pc and with a rotation in order to avoid the gravitational collapse. The flux periodicity that we observe might be due to the jet precession or to the intrinsically rotating flow or feeding the jet (see, e.g. Caproni et al., 2017; Tavani et al., 2018).

In the case of disk instabilities, there could be variations of the matter flux within the jet, and this might cause outflow variations observable from Earth. In the case of a second BH, all the models provide an interpretation based on two BHs of different mass, with mass difference of about an order of magnitude. This could justify the prevalence of the jet of the main BH, and the perturbation of this jet due to the passing minor BH every about two years. However, all the geometrical models (see e.g. Camenzind, 1992; Romero, 2000) agree with the production of a quasi-periodic variation of the beaming factor due to the change of the viewing angle (Rieger, 2004). This seems to imply that almost achromatic variability is expected at all wavelengths, and such variability should be correlated among different wavelengths. A recent geometrical model proposed by Sobacchi et al. (2017) provides a coherent description of both the light curve and SED variability through the variation of the observation angle of a structured jet.

Additionally, in Tavani et al. (2018) the authors provide an hint of detection for a periodical structure of twin peaks in flux at equal time distance just before and after the main peaks. This twin peaks might confirm the binary structure of the central engine,

and might suggest perturbation of the main jets due to the presence of the second BH near the periastron (see also Lehto & Valtonen, 1996) or the perturbation of the total flux due to the contribution of the jet of this second BH.

3.2.6.3 Fast variability time scale

Thanks to the flaring phases registered for the blazar PG 1553+113, there as been several studies about the fast variability time scale of its flux over the time. Such parameter is particularly important for the study of the emission region size and provides an important input for the modelling of the intrinsic emission from the source, and was used as a probe of possible Lorentz invariance violation and of the extragalactic background light.

The occurrence of several flaring activities in the blazar PG 1553+113 during the last years made possible estimations of its flux variability time scale of the order of some weeks (Aleksić et al., 2015; Aliu et al., 2015).

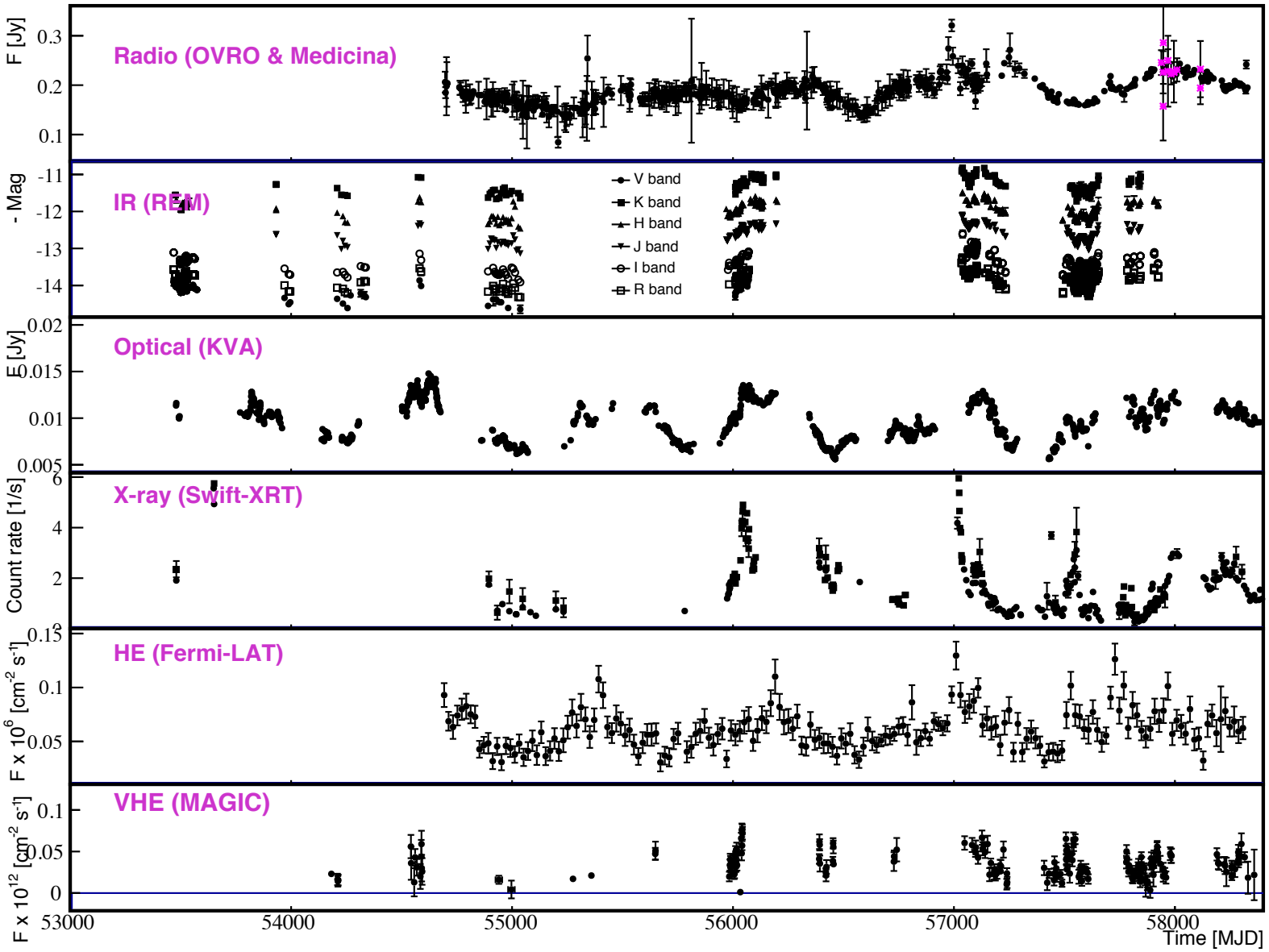

Figure 3.14: *MWL light curve of the periodic blazar PG 1553+113. Here we present recent results collected by the MAGIC Collaboration with simultaneous observations performed in radio (OVRO, and recent data with Medicina in purple), IR (REM), optical (Tuorla, KVA), X-ray (Swift-XRT), and HE gamma-rays (*Fermi*-LAT).*

3.2.6.4 Monitoring program with the Medicina radiotelescope

Since the radio band has been revealed as a precursor of the periodic phase of enhanced emission in the gamma-ray band, a monitor of this low-energy band could foresees a high-state activity of the source to be followed by the IACTs in gamma rays. In order to monitor the radio light curve of PG 1553+113 on the long term and to alert the IACTs (that operate only in pointing mode) in case of enhanced flux, we performed a dense monitoring with the Medicina radio-telescope (see Section 2.1) within a rich observational programme of monitoring of blazars.

Scientific methods and results

The monitoring program was performed as part of an extensive multi-wavelength campaign, from radio to gamma rays, started during December 2015. The campaign, led by the MAGIC Collaboration, aims at constraining the processes driving the almost 2-year modulation recently reported by the *Fermi*-LAT Collaboration in high-energy gamma rays and in the optical band (Ackermann et al., 2015).

The goal of this simultaneous monitoring of radio and gamma-ray fluxes is the study of the evolution of the MWL SED of PG 1553+113 on time scales from days to years and to provide a clear view of the spectral behaviour of the source in different states of its variability, pinpointing the nature of the mechanisms generating the observed modulation.

This can be accomplished through:

- the characterization of both light curve and spectrum in radio frequencies over an extended period;
- the inspection of daily and weekly variability during the active phases;
- the simultaneous MWL coverage, including the VHE gamma-ray band, in a variety of flux states and variability time scales, with similar cadence proposed for Medicina.

An intriguing interpretation of the periodicity may lie in the presence of a milli-parsec supermassive black-hole binary system located at the nucleus of PG 1553+113. Different possibilities can be envisaged, such as jet precession, accretion flow instabilities, or quasi-periodic perturbations of the accretion disk. More information has been reported in a dedicated discussion in Section 3.2.6.

Our use of the Medicina radio telescope was to perform a radio monitoring at different frequencies, which are pivotal to address these interpretations, through the study of flux and spectral variability, and the detection of time lags with respect to other bands.

Observations

Observations were carried out during the period between 2016 to 2019 with a monitoring composed of about 2-3 observations per month. Each observation takes about two hours and it is performed usually during the night. During each observation, the user remotely controls the telescope, performs the preliminary procedures to prepare and calibrate the telescope, and finally starts the schedule. During the observations, the user monitors the stability of the parameters and the quality of the data. Finally, when observations finish, the user stows the antenna and closes the remote control session.

The off-line data-analysis of the results is now being carried out every few weeks when enough data have been collected. It consists of a selection of all good events by the user, a calibration of the source with the signal obtained by the known sources (called *calibrators*), and finally an estimation of the overall integrated signal during each observation.

At the moment, the observations are ongoing and only some preliminary results have been produced in the off-line analysis. An example of some preliminary results are presented in **Figure** 3.15, where we computed the resulting flux of the blazar PG 1553+113 obtained in our monitoring program compared to the OVRO results publicly available. Our results are well compatible with the monitoring offered by the OVRO observations.

The larger error bars in some cases are due to relatively bad weather conditions, but are still well usable in order to detect the low state of the source and its periodic high state when it can be observed at VHE for example with the MAGIC telescopes. More information on this point is reported in Section 3.2.6.

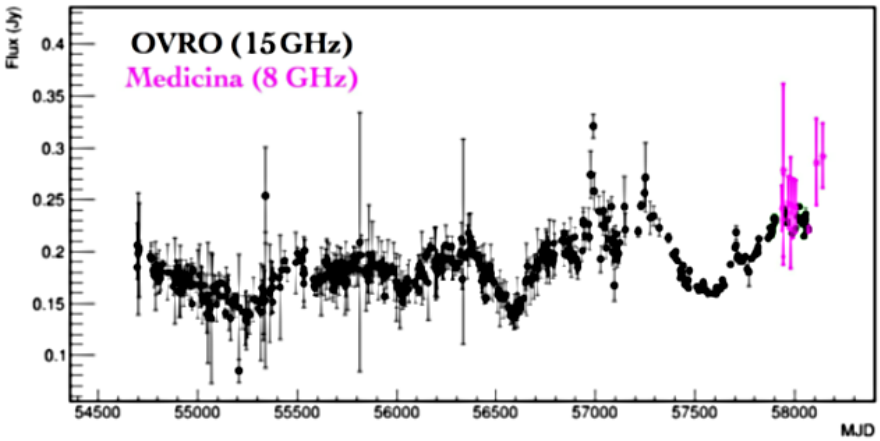

Figure 3.15: *An example of the resulting preliminary flux of the blazar PG 1553+113 measured with Medicina, compared to some simultaneous OVRO results.*

3.2.6.5 Monitoring program with the MAGIC telescopes

Observations

The source PG 1553+113 is one of the most interesting blazars that MAGIC has been observing since the beginning of its operations. Due to the periodic nature of its emission in the gamma-ray band, a dense monitoring of the source on the long-term was performed between 2005 and 2018, reporting a total exposure time of several hundreds of hours.

During my PhD activities, I had the opportunity to get involved also in the analysis of PG 1553+113 during the observations carried on from 2015 to 2017. During such a long time, the MAGIC telescopes were upgraded both in the hardware and in the software. For this reason, the analysis of this source was particularly complex under a technical point of view due to the huge quantity of data and different analysis period (and thus different RFs) that have been used.

In such analysis, the data have been collected in three different Monte Carlo (MC) periods:

- year 2015: ST.03.06 MCs with about 20.8 h of good quality data;
- year 2016: ST.03.07 MCs with about 12.7 h of good quality data;
- year 2017: ST.03.07 MCs with about 26.0 h of good quality data;

The data in this analysis were selected only as good quality dark time (no moon observations).

Signal search

The blazar PG 1553+113 is a high-flux source in VHE gamma rays. During this analysis, the source was always clearly detected in the selected time slots.

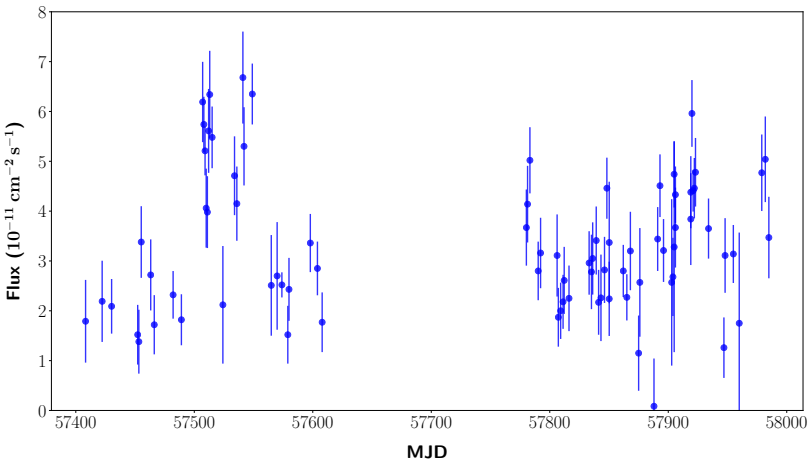

Figure 3.16: *MAGIC light curve of PG 1553+113 between 2016 and 2017.*

Flux

Since the observations of PG 1553+113 are particularly interesting for the variability and the periodicity of its flux, it has been pointed regularly during the MAGIC observation cycle. The regular monitoring of the source, with special interest during the expected high-state of the source, can be shown in the MWL light curve represented in **Figure** 3.14. The VHE gamma-ray band is particularly interesting to understand what type of physical phenomena are taking place in this blazar.

During my Analysis, I produced a long-term light curve of PG 1553+113 with data taken from 2015 and 2017. In particular, these data were presented at the *Texas symposium* during 2018, and the dataset was chosen between 2016 and 2017. The light curve presented in **Figure** 3.16 was produced with a night-wise time binning of all the good-quality observations. The threshold for these observations was chosen to be a mean integrated flux above 200 GeV.

Spectrum

The spectrum of PG 1553+113 observed by the MAGIC telescopes is at the moment under analysis and publication, and for this reason it cannot be shown in this Thesis. The main idea of the project is to analyse the spectrum of the source during the different low-state and high-state activities, and to verify the correlation between the spectral slope and the periodicity of the signal.

Chapter 4

Extreme blazars and their spectral properties

Extreme blazars are the main topic of this Thesis. In the first Section, I present the definition of extreme blazars and some problems concerning its application to the experimental data.

Then, after presenting some of the most important selection methods that have been proposed in the literature, I will describe my selection method based on the study of the hard X-ray properties of a sample of extreme blazars. In that Section, I will analyse the broad-band spectral properties of the sources, reporting the main spectral differences that suggest the possible emergence of a population of these objects.

In the third and forth Sections, I will discuss the results reported in two publications to which I contributed. The former is related to the connection between extreme blazars and the extragalactic background light, by studying the role of the next facilities in the TeV gamma-ray band.

In the last section, I will report the study of a sample of faint sources in the HE gamma-ray band. Among these sources, it is possible to find extreme blazars with spectral properties favourable to their detection also in the VHE gamma-ray band, and that might be detected by the current or next generation of gamma-ray observatories.

4.1 Extreme blazars

4.1.1 The last part of the blazar sequence

In Section 3.2.1.2 I presented the so-called *blazar sequence*, a phenomenological sequence that correlates the different sub-categories of blazars. This sequence is based on the anti-correlation between the bolometric luminosity and the peak energy of the blazar SED humps, and it is interpreted as due to the different radiative cooling efficiency of the emitting electrons in different sources (Ghisellini & Tavecchio, 2008; Ghisellini et al., 2017).

In particular, the BL Lac objects populate the medium to high energy part of the sequence. They are classified on the basis of the maximum frequency of their synchrotron hump $\nu_{\rm peak}^{\rm sync}$ of their spectral energy distribution. They are subdivided in

- low synchrotron peaked BL Lac objects (LSPs, with $\nu_{\rm peak}^{\rm sync} < 10^{14}$ Hz);
- intermediate synchrotron peaked BL Lac objects (ISPs, with $\nu_{\rm peak}^{\rm sync}$ between 10^{14} and 10^{15} Hz);
- high synchrotron peaked BL Lac objects (HSPs, $\nu_{\rm peak}^{\rm sync}$ between 10^{15} and 10^{17} Hz).

In 2001, Costamante et al. (2001) presented sources with synchrotron peak frequency higher than $\nu_{\rm peak}^{\rm sync} > 1$ keV ($\simeq 2.4\ 10^{17}$ Hz), and this led to the definition of an additional class of objects, the so-called

- extremely-high synchrotron peaked BL Lac objects (EHSPs, with $\nu_{\rm peak}^{\rm sync} > 10^{17}$ Hz).

In this Thesis, I will use the term *extremely high-peaked BL Lac objects (EHBLs)*, with reference to the EHSPs, following an historical nomenclature of low- and high-energy peaked BL Lacs (LBL/HBL) in Padovani & Giommi (1995). From now on, I will use indifferently the term EHBL or "extreme blazars" for this class of objects.

Up to now the number of known EHBLs is very limited, and only recent observations have started to populate this class. Thanks to their synchrotron and high-energy hump shifted to the highest energies, these sources are representing an extension of the blazar sequence. Most of these sources show extreme spectral properties that present challenging interpretation. For example, thanks to their extremely hard-TeV spectra, they are interesting for the implications on the indirect measurements of the intergalactic magnetic fields (IGMF) and the extragalactic background light (EBL).

In this Section, I will introduce the spectral features characterizing this class of blazars.

4.1.2 A controversial definition

The EHBLs form an emerging class of BL Lac objects. Their extreme spectral properties represent a challenge for the theory of this field, and are interesting for their applications to correlated topics. However, the recent discovery of new sources in this category have revealed some difficulties in the definition of this class and in the classification of these sources.

One of the main reasons is probably due to the fact that the most important EHBL ever classified (and that is now the archetypal of this class) – namely 1ES 0229+200 – is also among the most energetic sources ever seen. In fact, the spectral emission of 1ES 0229+200 – shown in **Figure** 4.1 – is extreme both in its synchrotron and in its high-energy peak. However, it should be underlined that not all EHBLs have a so energetic emission in both the peaks. The increasing number of EHBLs suggests a more gradual classification of these sources, and for this reason a precise definition of what an extreme blazar is turns out to be very important in order to avoid mis-classifications and errors.

The definition of this class of objects is based on the peak frequency of their synchrotron emission, that is located at exceptionally high energies in the medium and hard X-ray band. The original definition of this class was given by Costamante et al. (2001), that

defined EHBLs the sources with a $\nu_{\rm peak}^{\rm sync} > 1$ keV ($\simeq 2.4\ 10^{17}$ Hz). However, this definition can be slightly changed to a more frequency-based one in order to reconcile it with the definition of the different sub-classes of blazars in LSP/ISP/HSP proposed by Abdo et al. (2010c) on the basis of the *Fermi*-LAT survey. For this reason, hereafter we adopt the definition of EHBLs as sources having their synchrotron peak frequency $\nu_{\rm peak}^{\rm sync}$ exceeding 10^{17} Hz. This definition includes in the classification also all the sources considered as EHBLs by Costamante et al. (2001).

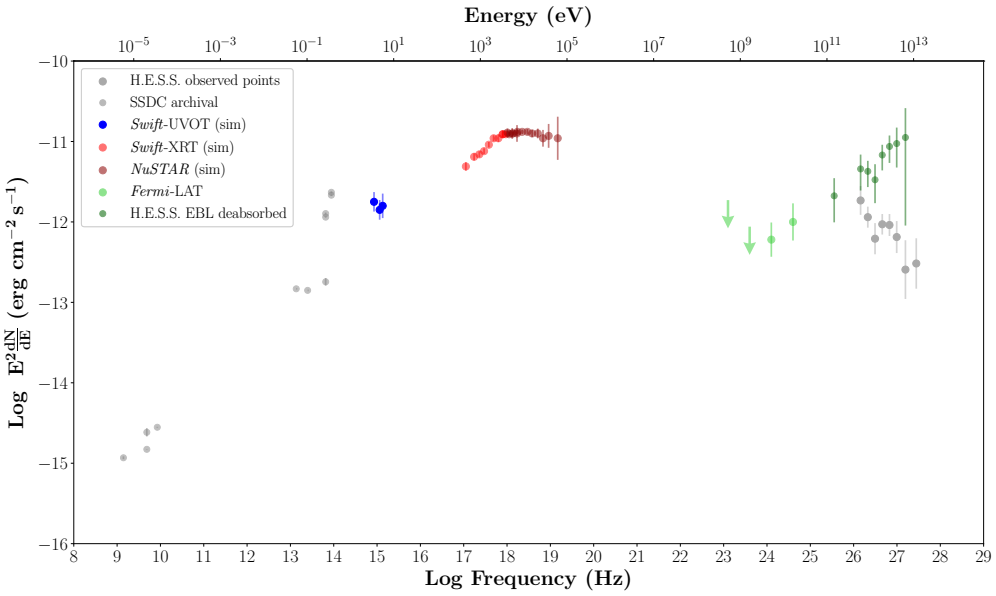

Figure 4.1: *Multi-wavelength SED of the archetypal EHBL called 1ES 0229+200. Here we report in grey archival data from SSDC website*[1]*, and from Costamante et al. (2018) we show in light red the data points from* Swift-*XRT, in dark red the data points from* NuSTAR *(Harrison et al., 2013), in light green the updated analysis of* Fermi-*LAT data. Finally in dark green are reported the VHE data from Aharonian et al. (2007d). The data of the high-energy peak are plotted both as they are observed and in their intrinsic form already corrected for EBL absorption with the model by Franceschini & Rodighiero (2017).*

This definition turns out to be - in some cases - particularly difficult to be applied to the phenomenological data. In fact, it is generally quite difficult to constrain the synchrotron peak frequency with a reasonable errorbars in such a way to classify the blazars within the HBL or the EHBL class. An example is reported in **Figure** 4.2a, where the source 1ES 1028+511 shows a broad synchrotron peak just above the limit of 10^{17} Hz that defines the EHBLs. In this case the peak estimation is robust thanks to the low flux errorbars, but in sources where the peak is shifted slightly towards lower frequencies the classification remains uncertain.

Additionally, in most of the cases there are not simultaneous sets of data that can constrain the emission in the X-ray band, and for this reason such datasets are not sufficient to classify the source with high confidence level. In other cases, the synchrotron peak itself shows moderate variability: this effect is related to the fact that the last part of the synchrotron emission represents the tail of the emission of the freshly injected electrons in the blazar jet. For this reason, some variability is expected due to the instabilities that might be present in the jet itself. Considering that in the EHBLs this flux variability concerns mostly the synchrotron peak located in the X-ray band, also the determination of the peak itself turns out to be – in some cases – challenging. An example is reported in the interpolation of the synchrotron peak of the source 1ES 0347-121 in **Figure** 4.2b.

Finally, the performances of the instrument are particularly important. The different sensitivity and accuracy that determine the flux estimation of the datapoints affect

sensibly the fit results. In the case of this Thesis, I was able to study the X-ray band mainly with the *Swift* observatory, and precisely with the XRT and BAT instruments. Since the *Swift*-BAT instrument has a worse sensitivity in hard X-rays than *Swift*-XRT, it is common to obtain larger errorbars in the hard X-ray band rather than in the lower X-ray band covered by XRT. An example is reported in the interpolation of the source RBS 259 in **Figure** 4.2c.

4.1.3 1ES 0229+200 and hard-TeV EHBLs

The archetypal EHBL that represents this class of objects is 1ES 0229+200. This source is up-to-now among the most energetic blazars ever observed both in the synchrotron peak and in the high-energy peak. Its archival SED has been enriched by several multi-wavelength (MWL) observational campaigns during the last years, and shows the most common features of this class of objects. I showed in **Figure** 4.1 an example of SED where the main energy bands have been reported with the most recent measurements.

As typical for EHBLs, the synchrotron hump is shifted towards high energies with respect to conventional HBL blazars, making the thermal optical radiation of the host galaxy visible for low-redshift objects (as it appears between about 10^{14} and 10^{15} Hz). The most precise determination of the peak of the synchrotron emission of this source has been estimated by Costamante et al. (2018) with a detailed simultaneous sampling of the full X-ray band with *Swift*-XRT and *NuSTAR* observations, and results in 9.1 ± 0.7 keV.

The synchrotron peak located in the medium to hard X-ray band is followed by a second SED peak located in the VHE regime. For this reason, EHBLs are generally faint in HE gamma rays in order to have their high-energy hump peaking in VHE gamma rays (Tavecchio et al., 2010). Once corrected for EBL absorption, the 1ES 0229+200 spectrum at VHE is among the hardest ones ever measured (e.g. Aliu et al., 2014) and shows low flux variability on time scale of several years (Cologna et al., 2016).

Such hard TeV spectrum has been detected also in other sources that resemble the SED of 1ES 0229+200. This sample of sources, where the second hump goes beyond several TeV with very hard TeV spectrum, have been named "hard-TeV" blazars by Costamante et al. (2018), and is composed for example by 1ES 0347-121 (Aharonian et al., 2007b), RGB J0710+591 (Acciari et al., 2010), and 1ES 1101-232 (Aharonian et al., 2007a). Such objects are particularly interesting for this Thesis, and represent the hard core of the EHBL class.

4.1.4 Hard-TeV EHBLs and their challenging spectral properties

The challenging spectral properties of EHBLs have been historically discovered by studying the SEDs of hard-TeV EHBLs like 1ES 0229+200. For this reason, in this first part of the Chapter I follow a sort of historical approach presenting the properties of the hard-TeV EHBLs. Later on, I will present several phenomenological reasons for which the EHBL class should be extended also to sources non necessarily with a so hard TeV spectrum, underlining that hard-TeV EHBLs seem to be only a part of the whole EHBL class.

The hard-TeV EHBLs, with their synchrotron peak located at about 1 to 10 keV and their hard spectrum in the VHE gamma-ray band, represent a challenge for the standard modelling of blazar emission, the so-called SSC model (see Section 3.2.4.1). In fact, the synchrotron peak located in the X-ray band is followed by a second hump close to the VHE gamma-ray band. Recent observations revealed that in some objects the second peak is actually shifted at even higher energies in the full TeV gamma-ray region at more that 10 TeV (i.e. the same 1ES 0229+200). In the SSC scenario, such hard TeV spectra are very difficult to explain. The high energies reached by the synchrotron hump imply interactions that enter the Klein-Nishina regime (see Section 1.2.1.4). In this regime, the decreasing scattering cross section with energy inevitably leads to rather soft SSC spectra at TeV energies, and this goes against the observations (Tavecchio et al., 2009).

[1] https://tools.ssdc.asi.it/index.jsp

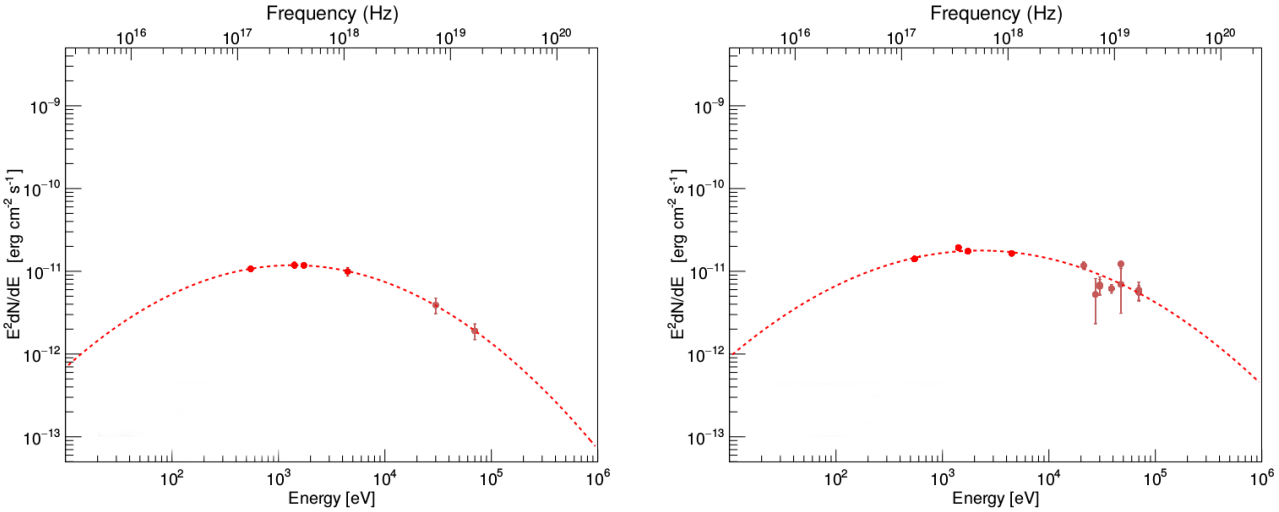

(a) 1ES 1028+511.

(b) 1ES 0347-121.

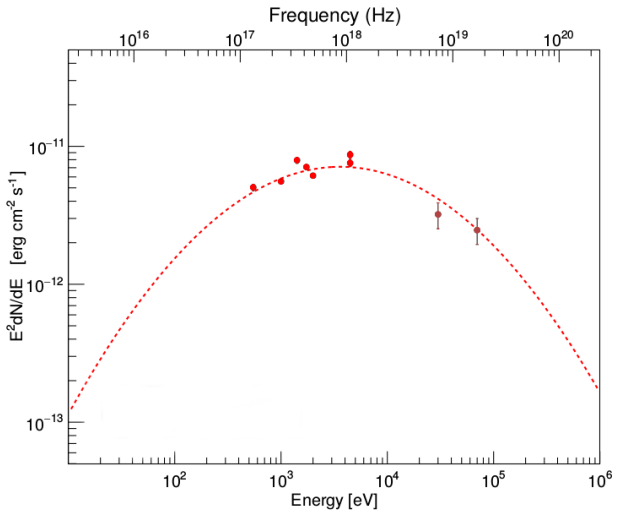

(c) RBS 259.

Figure 4.2: *Three examples of log-parabolic fits on the* Swift-*XRT X-ray (red) and* Swift-*BAT hard X-ray data (dark red). While in (a) the first source shows a broad synchrotron peak around the limit of* 10^{17} *Hz that defines the EHBLs, the second one in (b) is clearly an EHBL but shows moderate variability in hard X-rays. In the case of RBS 259 in (c) the different sensitivity of the instruments affects the errorbars of the collected data. However, the hard X-ray point are crucial to constrain the peak emission.*

This result does not mean that the SSC model cannot be used at all to model the hard-TeV EHBLs, but means that we are probably stretching the model and the resulting parameters invoke a different explanation for such emission mechanism. The SSC model can accommodate the observed SED of these objects at the price of using particularly extreme model parameters (a collection of some of the most updated results on EHBL modeling can be found e.g. in Cerruti et al. 2015, reported in the next Sections). In particular, the most common parameters that turn out to be "unusual" for the conventional modelling of blazars (Tavecchio et al., 2009) are:

- high values of the minimum Lorentz factor $\gamma_{\rm min}$ of the electron distribution;
- unrealistically large Doppler factors δ;
- extremely low values of the magnetic field B;
- energetics far from equipartition.

In particular, high values of $\gamma_{\rm min}$ might occur in very specific conditions: for example, when electrons are injected with a narrow energy distribution into the emission region and their subsequent cooling is inefficient, or in the case of stochastic turbulence that may be responsible for the electron acceleration in blazar jets (see e.g. Asano et al. 2014). On the other hand, the request for large Doppler factors δ would imply a fast flow of the plasma or an extremely small viewing angle, and generally this goes against radio observations of the movement of knots inside the jets or against the statistics of observed blazars (see e.g. Lister et al. 2013).

Additionally, also more complex models such as the two-zone spine-layer model (see Section 3.2.4.3) provide some extreme parameters when applied to the data of hard-TeV EHBLs. For example, in Costamante et al. (2018), almost all the sources with hard TeV spectrum up to the deep VHE regime still provide energetics far from equipartition for several orders of magnitude.

Many different alternative scenarios within the leptonic model have been proposed. Some works, for example, interpret the high values of $\gamma_{\rm min}$ in a time-dependent one-zone model with extremely hard Maxwellian particle distributions (Saugé & Henri, 2004; Lefa et al., 2011) or with a low-energy cut-off of the electron distribution at VHE (Katarzynski et al., 2006). Other works suggest that such very hard VHE gamma-ray spectra might be reproduced by models including external Compton up-scattering of ambient photon fields (Lefa et al., 2011). However, the latter are commonly thought to dominate in powerful FSRQs rather than in HBLs, where no strong emission from the accretion disk or the environment has been detected yet. Finally, in the case of 1ES 0229+200, that is one of the most studied TeV gamma-ray detected EHBLs, the hard TeV spectrum was successfully interpreted also in the intergalactic cascades scenario (Murase et al. 2012, but for more details see Section 3.2.5.1).

4.1.5 Extreme blazars as possible neutrino counterparts?

4.1.5.1 Possible hadronic component

One of the most common features of hard-TeV EHBLs (and especially of the archetypal 1ES 0229+200) is the lack of high and rapid flux variability, as other blazars like HBLs show. For example, the low variability of 1ES 0229+200 on the long-term light curve in VHE gamma rays has been reported by Cologna et al. (2016), where the flux varies of only few times (3×) with respect to the huge flux variations in the flaring events of HBLs. Considering that this flux variability is very low with respect to the standard flaring episodes of HBLs, as a matter of fact, no hard-TeV EHBLs has ever been seen *flaring* in the X-ray or gamma-ray bands. This effect may be related to the low flux of these sources in some wavelengths (especially at TeV energies), and thus to the current limited sensitivity of our instruments.

Assuming the stability of the flux, leptonic models are disfavoured to describe the physical emission mechanism of the blazars. In fact, leptonic models would predict large flux variations on short time-scales that have never been observed in hard-TeV EHBLs.

On the other side, the hard VHE gamma-ray spectra and the absence of rapid flux variability make hard-TeV EHBLs interesting candidates for hadronic and lepto-hadronic emission models, that can well reproduce their observed SED (e.g. Cerruti et al. 2015). This solution is able to interpret the SED of some hard-TeV EHBLs without using extreme physical parameters, whose can be found considering an hadronic origin for the gamma-ray component. In the blazar hadronic models, the gamma-ray component is ascribed to emission by protons in the jet, or by secondary leptons produced in p-γ interactions, (e.g. Mannheim, 1993; Aharonian, 2000; Mucke & Protheroe, 2001; Boettcher et al., 2013) and may represent an alternative to the leptonic models. The main issue of this hadronic scenario, when adopted to describe FSRQs or other BL Lacs, is that it often requires a high proton power, well above the Eddington luminosity (i.e. the maximum luminosity a body can achieve when there is balance between the radiation pressure acting outward and the gravitational force acting inward) of the black hole powering the blazar.

However, the case of EHBLs is particularly favourable to hadronic models because they are intrinsically relatively less luminous compared to other blazar subclasses, and a successful hadronic modelling can be achieved with an acceptable energy budget (see Cerruti et al., 2015). In addition, the absence of fast flares from hard-TeV EHBLs (in contrast with the gamma-ray variability seen in more common HBLs) is also consistent with the cooling time-scales of protons in the jet.

4.1.5.2 Hard-TeV EHBLs and lepto-hadronic models

An application of some hadronic and lepto-hadronic models to EHBLs is reported in Cerruti et al. 2015 (reported also in Section 3.2.5.1). In that work, the authors analyse five hard-TeV EHBLs: 1ES 0229+200, 1ES 0347-121, RGB J0710+591, 1ES 1101-232, and 1ES 1218+304. They proposed two distinct analyses with a proton-synchrotron scenario and a lepto-hadronic scenario. In both the models, the low-energy component is dominated by the electron-synchrotron radiation. Conversely, while the high-energy contribution of the first model is supposed to be dominated by emission of proton-synchrotron light, in the latter case the high-energy contribution is a combination of SSC and pion-induced cascade emission, and justifies the "lepto-hadronic" classification. In this case, the proton-synchrotron component is strongly suppressed and shifted to intermediate energies.

An important point to underline is that in the application of this model there is an underestimation of the MeV-GeV emission. This mismatch is attributed to the integration on the long term of the gamma-ray spectra of the hard-TeV EHBLs, and might be related to long- or medium-term variability of the source spectra.

4.1.5.3 Correlation with neutrinos

Within the blazar sequence context, EHBLs are the less luminous blazars but with the most energetic emission of the whole class. This fact suggests that the cooling of the particles is less effective, and thus particles can be accelerated up to the highest energies. This fact might imply high-energy acceleration of particles heavier than electrons, such as the protons.

Invoking a hadronic contribution when modelling the SED of EHBLs may represent an alternative way not to require too extreme spectral parameters generally needed by the leptonic models. However, also the application of hadronic models can provide unusual parameter values: for example, since they require high magnetization in the emission region, the magnetic field is usually so high that the energetics remains several order of magnitude out of equipartition. The hadronic processes might allow them to produce UHECRs, and this might imply EHBLs as neutrino counterparts. This topic has received enhanced focus by the scientific community thanks to the first correlation recently found between a neutrino event and a flaring blazar (Aartsen et al., 2018a), reported in detail in Chapter 6. In that case the neutrino came from a LSP/ISP blazar, considered a low-priority possible candidate as neutrino emitter because of the relatively poor environment surrounding the blazar jet. However, at the moment the statistics is too low to state a correlation between neutrinos and any class of blazar objects.

In the last years, the possible presence of hadronic processes in the blazar jets led some authors to look for a correlation between the direction of the neutrino events and the presence of nearby blazars. One of the main works is presented in Padovani et al. (2016).

This correlation was found by first deriving the number of neutrino events with at least one gamma-ray counterpart in the *Fermi* 3LAC catalog within the individual IceCube median angular error, and then by estimating the related chance probability using an ensemble of 10^5 - 10^6 random maps. This work resulted in the determination of a hint of correlation between HBL objects and neutrino events, as reported in **Figure** 4.3.

Performing an analysis of the hybrid photon-neutrino spectral energy distributions of the most likely candidates, they found a possible set of about five IceCube events which could be linked to the corresponding blazar sources:

- 1ES 1011+496 (EHBL),
- MKN 421 (HBL),
- H 2356-309 (EHBL, this source will be presented in Section 4.3),
- PG 1553+113 (HBL, this source has been presented in Section 3.2.6),
- 1H 1914-194 (EHBL),
- and 1ES 0414+009 (HBL/EHBL).

Some of these sources will be mentioned also in other parts of this Thesis, as turn out to be particularly interesting in this framework of correlation between blazars and neutrinos.

Furthermore, the statistical correlation of their work suggests that the more energetic EHBLs may show an even higher correlation with the neutrino events (Resconi et al., 2017), but to assess such results we need more statistics both in the neutrino event lists and in the EHBL object lists.

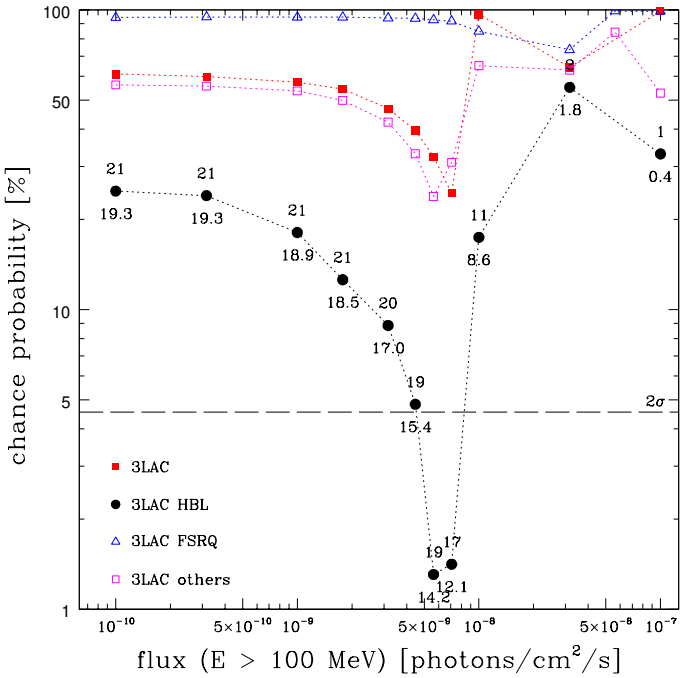

Figure 4.3: *Figure from Padovani et al. 2016 (their Figure 3). The chance probability of association of* Fermi*-LAT 3LAC clean sources with IceCube events for objects having flux above 100 MeV larger than the value on the x axis for the whole sample (filled red squares), HBL (black circles), FSRQ (blue triangles), and others (non-HBL and non-FSRQ: empty red squares). The numbers give the observed (above the points) and average random values (below the points) of N_ν for HBL. The dashed line denotes the 2σ value.*

4.1.6 Temporarily EHBLs

In recent observations of blazars performed with the IACTs, flares of HBL objects have been registered with a temporary extremely high synchrotron peak frequency exceeding 10^{17} Hz. Typically, during these flares also the high-energy peak moderately shifts to higher energies, and the total flux of the hump increases notably. During the low state of these sources, however, the spectrum does not present so extreme peak frequencies.

A typical example of this behaviour is the blazar Mrk 501, whose low-state SED is shown in **Figure** 4.6. This is a famous object with very low redshift and variable flux, and for this reason is studied by many observatories in all the wavelengths like an ideal extragalactic laboratory of physical processes. Its synchrotron peak during the low-activity phase of the source is located between 10^{16} and 10^{17} Hz, and does not reconciles with the definition of EHBL. However, during flaring episodes the source has shown huge enhancement of the flux and of both the peaks of the two SED humps. This source, during the huge flare of 1997 (measured by HEGRA in Aharonian 1999), when the source flux exceeded that of the Crab Nebula, has shown a shift of the synchrotron peak energy up to about 100 keV (Catanese et al., 1997), the highest value ever registered in blazars. The hard spectrum showed no sign of convergence up to the highest energy detected photons of about 20 TeV, shown in **Figure** 4.4. That was an historical event never repeated at that level on a timescale of thirty years. More recently, in Ahnen et al. (2018) is reported the detection of a notable flare during 2012 measured at several wavelengths. During that episode, the source temporarily became an EHBL during the flaring phase.

Beside Mrk 501, there are other blazars that show similar behaviour. Some of them are, for example:

- 1ES 1959+650 (one of the last ATEL is Kapanadze 2018, and a specific publication

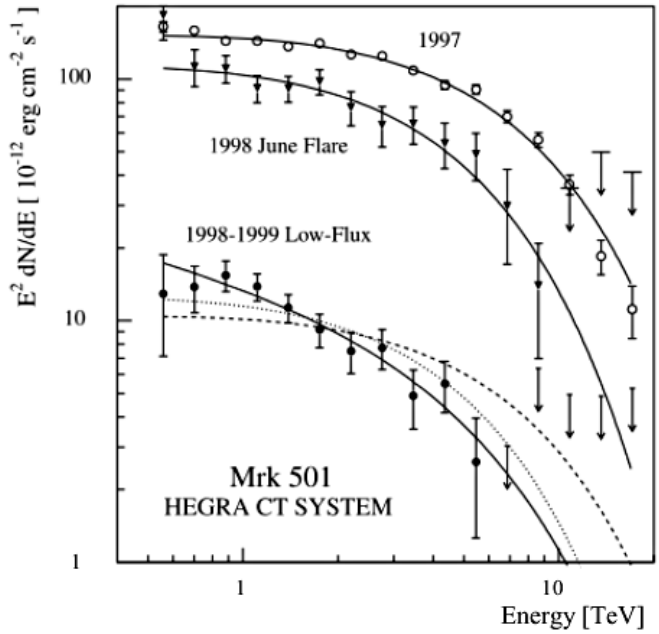

Figure 4.4: *Spectral energy distribution of Mrk 501 during the flares on 1997 and 1998. Figure adapted from Aharonian (1999).*

in the MAGIC Collaboration in preparation);

- and 1ES 2344+514 (e.g. Grube, 2008, and MAGIC Collaboration 2019d, in preparation).

On the modelling point of view, however, these different states of the sources are generally not challenging for the current theoretical emission models. During these high-state activities, the emission peaks do not shift much in the SED with respect to their position during the low state of the source. Conversely, the most important difference is the strongly enhanced flux, that is generally easily reproduced by the models.

Among these objects, one of them can be considered a sort of exception:

- 1ES 1218+304 (in the last high-state activity recorded during my last shift in La Palma, Mirzoyan 2019a).

This source is known for its notable flaring activities, but it always shows hard-TeV spectrum both in its "low state" and in its "high state".

4.1.7 Importance of the VHE gamma-ray band

The challenging interpretation of the SED of EHBLs is an important piece of the puzzle in the blazar context, and the VHE gamma-ray band is fundamental to study their enigmatic spectral properties.

The EHBL study in the VHE gamma-ray band is mainly performed by the current generation of major IACTs: H.E.S.S., MAGIC, and VERITAS. These telescopes detected more than 200 sources in the TeV gamma-ray band in the last fifteen years. Among them, about 70 sources are identified and classified as blazars – as reported in **Figure** 4.5 – the majority of them being HBLs. Given the relatively small field of view (3.5 to 5 degrees), IACTs operate mainly in pointing mode and (except for the Galactic survey of the H.E.S.S. telescope in Abdalla et al. 2018) cannot provide wide surveys of the whole sky in VHE gamma rays. On the other hand, due to their low flux in this energy band, EHBLs generally need large integration time to be detected.

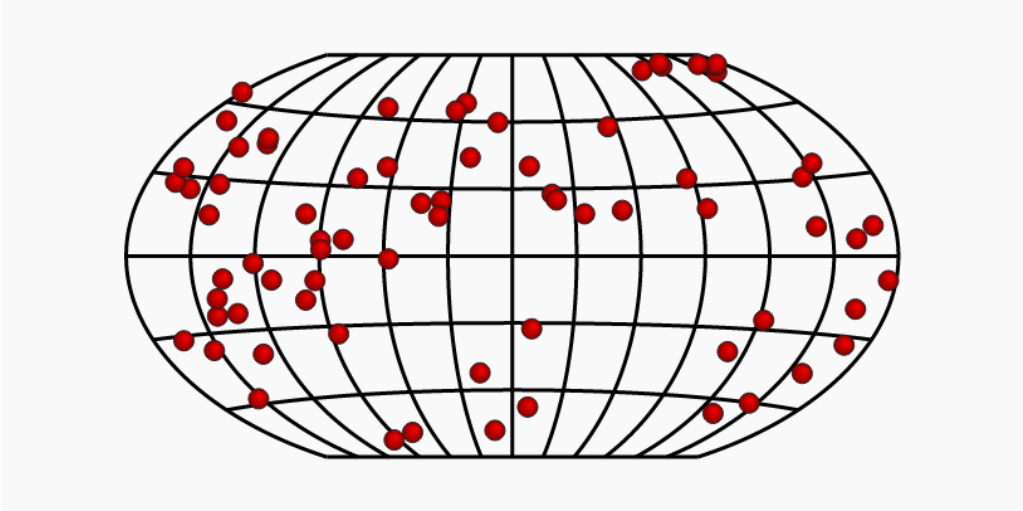

Figure 4.5: *Map of the 72 gamma-ray emitters of photons above 100 GeV in the Universe detected up to September 2019. Adapted from* http://tevcat2.uchicago.edu/.

Thus, only a few of them have been observed and characterized in the VHE gamma-ray regime. Among them, some objects show an extremely hard spectrum, the hard-TeV EHBLs presented in the last Section. On the other hand, as we have seen previously, some other blazars show temporary EHBL behaviour and not so hard TeV spectra.

This means that the definition of EHBL based on the synchrotron peak position is unveiling, as more sources are discovered especially in TeV gamma rays, a population of sources with different spectral properties. I report in **Figure** 4.7 an example of such difference. Two sources, both of them with synchrotron peak above 10^{17} Hz, are shown: 1ES 0229+200 and Mrk 501, with original SEDs shown in **Figure** 4.1 and **Figure** 4.6, respectively. The two SEDs are compared by normalizing the fluxes at the synchrotron peak of 10^{17} Hz. As we can see, there is some modest difference in the synchrotron peak location for these sources (however, above the threshold of 10^{17} Hz that defines the EHBLs), but the crucial difference is in the TeV gamma-ray behaviour. While 1ES 0229+200 is continuously increasing up to above 10 TeV, Mrk 501 is going down showing the high-energy peak at about few hundreds of GeV.

A more detailed study of this spectral behaviour will be presented in Section 4.3, but this example shows that also in the EHBL class there are spectral differences that are particularly interesting in the gamma-ray band. These differences show that the IACTs play a key-role in the characterization of the objects in this class, and for this reason we need a more detailed statistics that can be obtained only with more dedicated observations in this energy band.

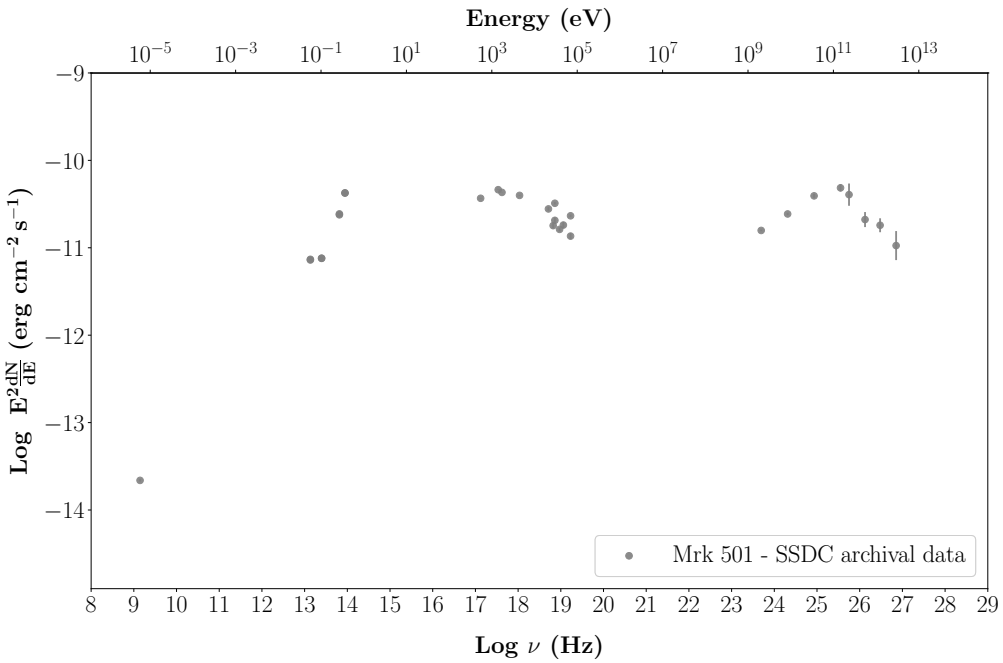

Figure 4.6: *Multi-wavelength archival SED of Mrk 501. The data have been chosen following* ***Figure*** *B.1. The spectrum has been de-absorbed by EBL effect with the model by Franceschini & Rodighiero (2017).*

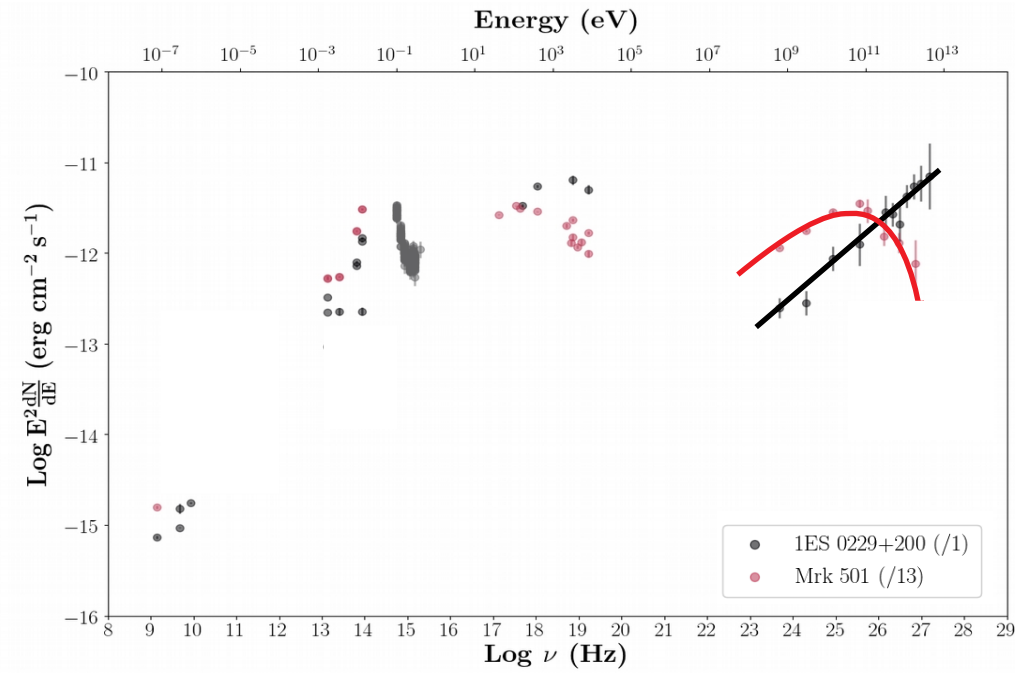

Figure 4.7: *Comparison of two SEDs of 1ES 0229+200 in* ***Figure*** *4.1 and Mrk 501 in* ***Figure*** *4.6 during their low-state activity and with flux normalization at about 10^{17} Hz. All spectra have been de-absorbed by EBL effect with the model by Franceschini & Rodighiero (2017). Red and black thick lines represent a sketch of the behaviour at TeV energies of the two sources.*

4.2 Previous selection methods of EHBLs

Considering the need for new sources to be classified as EHBLs and to be characterized at VHE gamma rays, in the last years several methods have been proposed in literature in order to increase the statistics. In this Section, I will present some of the main methods that have been used and referred to in this Thesis.

4.2.1 Correlation between different flux levels

One of the first selection methods of candidate TeV gamma-ray BL Lacs was suggested by Stecker et al. (1996).

This method is based on the SSC framework, and uses simple scaling arguments to predict the gamma-ray flux of HBL objects. At that time, the only HBL known both at GeV and TeV gamma-ray energies was Mkn 421. Using its SED as a template, they found a rough relation between the synchrotron and the high-energy hump: the latter results as the first one but upshifted by $\sim \gamma^2_{\rm peak}$ (in the Thomson regime), where $\gamma_{\rm peak}$ is the Lorentz factor of the electrons emitting at the peak. In the case of Mkn 421, they found two important values characterizing the SED:

- an upshifting factor of $\sim 10^9$;
- a ratio between the two luminosities at the peaks, $L_{\rm IC}$ of the high-energy hump and $L_{\rm syn}$ of the synchrotron, of $L_{\rm IC}/L_{\rm syn} \sim 1$.

Assuming then for simplicity similar properties to Mrk 421 for all HBL objects, the previous upshifting factor leads to the following relation between different points of the SEDs in the νF_ν representation:

$$\frac{\nu_{\rm o} F_{\rm o}}{L_{\rm syn}} \simeq \frac{\nu_{\rm GeV} F_{\rm GeV}}{L_{\rm C}}$$

and

$$\frac{\nu_x F_x}{L_{\rm syn}} \simeq \frac{\nu_{\rm TeV} F_{\rm TeV}}{L_{\rm C}} \ ,$$

where $F_{\rm o}$ is the flux at the optical frequency $\nu_{\rm o}$, and the same applies for the corresponding GeV lower-script that relates to the HE gamma-ray band, TeV lower-script that relates to the VHE gamma-ray band, and X that relates to the X-ray band.

When the ratio $L_{\rm C}/L_{\rm syn} \sim 1$ is known, then a direct relation for the energy fluxes with the GeV and TeV gamma-ray ranges is obtained:

$$\nu_{\rm GeV} F_{\rm GeV} \sim \nu_{\rm o} F_{\rm o} \ \text{ and } \ \nu_{\rm TeV} F_{\rm TeV} \sim \nu_x F_x \tag{4.1}$$

In conclusion, this model adopts as main selection criterion the X–ray flux: looking at the flux level at about 1-2 keV, one obtains the expected flux at around 0.2-0.3 TeV. In this framework, sources with the highest synchrotron $\nu_{\rm syn}$ are expected to show the highest flux in the TeV gamma-ray band (Costamante & Ghisellini, 2002).

4.2.2 Costamante+02: looking for high TeV gamma-ray fluxes

One of the first selection methods studied to extract good TeV candidate BL Lac objects (I refer to them as HBLs) was proposed is Costamante & Ghisellini (2002). It is worth to note that this method, as mentioned by the authors, is not expected to directly provide EHBLs. In fact, EHBLs generally are not the best candidates to be strong TeV emitters because their flux at TeV energies is expected to be relatively low. However, this method is useful to select some of the most luminous EHBLs with large $\nu^{\rm sync}_{\rm peak}$ and a sufficiently strong soft seed IR photon emission to be scattered in the TeV gamma-ray regime.

Their driving idea was to adapt the method by Stecker et al. (1996) to the SED of HBLs, shifted at even higher energies. The main problem is that the simple shift of the

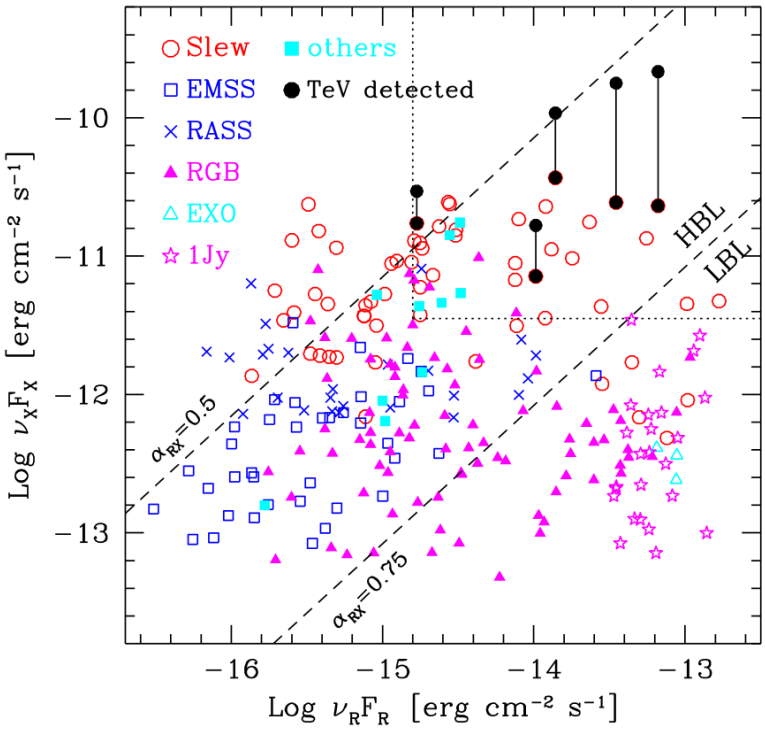

Figure 4.8: *BL Lac objects in the radio (5 GHz) and X–ray (1 keV) $\nu F(\nu)$ plane. Sources belonging to different samples have different symbols, as labeled. The objects marked with filled circles are those already detected at TeV energies (from left to right, 1ES 1426+428, 1ES 2344+514, PKS 2155–304, Mkn 421, Mkn 501). The vertical segment indicates two different X–ray states of the TeV detected sources. The dotted lines delimiting the rectangle are at $F_x = 1.46\ \mu Jy$ and $F_R = 31.6\ mJy$. Figure from Costamante & Ghisellini (2002).*

high-energy hump with respect to the synchrotron hump is no more reliable in the case of very large synchrotron peak frequencies. When the interaction process between ambient photons and very energetic electrons (producing the radiation of the synchrotron peak) is in the Thomson regime, the scattering is effective.

However, for larger synchrotron peak frequencies, the electrons enter the Klein-Nishina regime, and the scattering cross section between electrons and synchrotron photons decreases notably. This means that the TeV photons can be produced only by the scattering generated by electrons with energy lower than the maximum peak energy. Such photons, however, show a reduced energy density, and thus the TeV gamma-ray emission is not favoured.

Thus, the two ingredients that are necessary for the formation of a strong TeV emission thanks to SSC process are

- the density of electrons, enough energetic to produce TeV photons;
- the density of seed photons to be scattered.

The main idea is that, in order to produce large TeV gamma-ray fluxes, we need a good balance between very energetic electrons (related to very large synchrotron peak $\nu^{\rm sync}_{\rm peak}$) in a sufficient quantity (and this requires not extreme values of $\nu^{\rm sync}_{\rm peak}$).

4.2.2.1 Sample and results

In Costamante & Ghisellini (2002), the authors collect new TeV candidate BL Lac objects in a sample of several hundreds of sources. For such BL Lac objects, the spectral information in all the three energy bands radio, optical, and X–rays, was available.

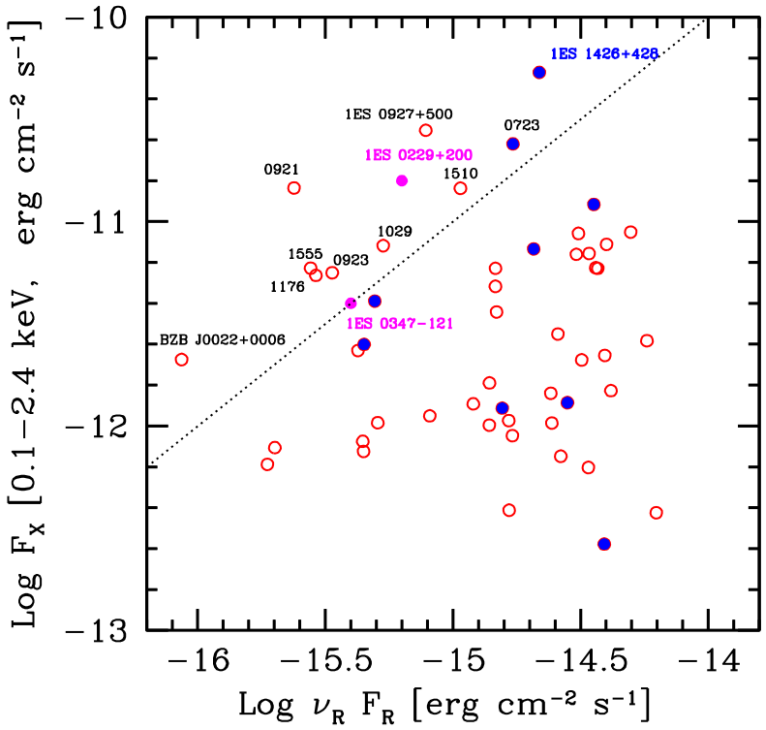

Figure 4.9: *F_X vs. F_R diagnostic plot. Red open circles represent the full sample; the blue filled circles are the* Fermi*-LAT detected ones. The 12 sources above the black dotted diagonal line have a high ($F_X/F_R > 10^4$) ratio of X–ray vs. radio flux. The magenta filled circles are the two archetypal TeV detected, but GeV faint extreme BL Lacs, 1ES 0229+200 and 1ES 0347-121. Figure from Bonnoli et al. (2015).*

The sources were then presented in a X–ray to radio flux plot, as reported in **Figure** 4.8. The main idea is the following. A large TeV gamma-ray flux is produced by IC process only in the case of a sufficient number of electrons with high energies. By considering electrons with typical Lorentz factors of the order $\gamma \sim 10^5$–10^6, they produce synchrotron radiation following the relation

$$h\nu = 1.5\, B\, (\gamma/10^5)^2\, (\delta/10)\ \text{keV}\ ,$$

with B in Gauss. This means that the most effective seed photons able to interact with these electrons and produce TeV gamma-ray photons have energies compatible with the IR–optical band (photons of higher frequencies scatter in the Klein Nishina regime). Since the IR-optical band is severely affected by the contamination from the host galaxy, the closest energy band useful to this scope is the radio band. Thus, the radio flux in this plot may represent a measurement of the relevant seed photons. Joining the idea of Stecker et al. (1996), by considering the higher X-ray to radio flux might select the most likely TeV gamma-ray emitters. It is worth to note that the already TeV-detected sources are located right among the brightest sources in both energy bands.

4.2.3 Bonnoli+15: searching for hard TeV spectra

More recently, Bonnoli et al. (2015) compiled a list of EHBL candidates looking for sources with high X-ray to radio flux ratio, and a dominant thermal radiation from the host galaxy in the optical range. While Costamante & Ghisellini (2002) basically looked for candidates with high TeV flux asking for dense seed photon fields, in Bonnoli et al. (2015) the authors selected sources (in more updated list of sources provided by Plotkin et al. 2011) aiming at identifying hard TeV spectra candidates. While Costamante & Ghisellini (2002) based the selection on sources with evidence of large X-ray and radio

fluxes, in Bonnoli et al. (2015) the authors look for sources requesting only a high X-ray to radio flux, without limiting it on high flux levels.

On the basis of a pure one-zone SSC model, they extract sources with an electron distribution characterized by high minimum ($\gamma_{\rm min}$) and break ($\gamma_{\rm b}$) Lorentz factors, that corresponds to large values of the synchrotron and IC peak frequencies, but dim and hard TeV spectra.

In **Figure** 4.9 is reported the sample of sources in the $F_X/F_{\rm R}$ plot. The oblique dashed line represents the criterion they adopt to propose good EHBL candidates. It corresponds to the fixed ratio $F_X/F_{\rm R} = 10^4$, and represents a rounded but somewhat arbitrary value suggested by the position of the two known EHBL in the plane.

4.3 Unveiling a population of EHBLs

Up to about twenty years ago (before Costamante et al. 2001), the EHBL class was not yet identified: all sources with synchrotron peak above 10^{15} Hz were part of the HBL category, without distinction between HBLs and EHBLs. In the recent literature, HBL objects have been studied deeply thanks also to their good statistics and spectral detection at different wavelengths. An important aspect in this topic is that such studies reveal several mis-classifications: in several cases some HBL sources have been classified as EHBLs, or in some other cases some EHBLs have been classified as HBLs. Additionally, some sources have been classified as EHBLs on the basis of their hard TeV spectrum on the high-energy hump rather than on the definition based on the synchrotron peak.

Thus, the classification of new sources in this category is encountering several difficulties. Considering the increasing interest in the study of these objects, it is clear that a more detailed selection and statistical analysis should be performed.

At the moment, the better known EHBL is 1ES 0229+200. This is probably the most energetic source both with regards to the synchrotron peak position and to the high-energy peak. The stability of the flux is a particular feature of this source and of all the hard-TeV EHBLs. During the last years, only few sources have been characterized in their broad-band SED with a similar spectral energy distribution, and probably no one of those is actually as extreme as 1ES 0229+200.

On the other side, there are sources that during their low-state activity do not show EHBL behaviour. However, such sources sometimes have reported notable flaring episodes that have shown shifts of their SED towards higher energies. During these episodes, the synchrotron peak exceeded several keV, and in some cases it reached about 100 keV.

Thus, the EHBL class itself is showing very different spectral properties (stable hard-TeV EHBLs or temporarily EHBLs) among its objects. These differences should be analysed and interpreted in a common picture.

Here I report a discussion based on the paper Foffano et al. (2019).

4.3.1 The hard-X ray selected sample

Extreme blazars are characterized by a peak emission in hard X-rays. In order to look for new candidates as hard-TeV emitters and to characterize this class of objects, we decided to take a look into the best catalogues in this energy band. The most unbiased survey of the sky in this energy band at the moment is provided by the BAT instrument on-board of the *Swift* telescope (see Section 2.2). We based our selection on the most recent survey of the *Swift*-BAT telescope represented by the BAT 105-months catalogue (Oh et al., 2018).

For the selection of EHBL candidates, we searched for sources with a firm detection in the hard X-ray energy range using the *Swift*-BAT 105-months catalog (also reported as BAT105) provided by the *Swift*-BAT instrument (see Section 2.2.1). On a practical point of view, the sensitivity of BAT is lower than that of *NuSTAR* (Harrison et al., 2013), and only sources with a moderate luminosity in this energy band can be detected. However, it represents a first step into the selection of sample of EHBL sources relatively unbiased by their properties in the gamma-ray spectrum. This instrument offers an all-sky survey in the ultra-hard X-ray band between 14 and 195 keV. The *Swift*-BAT telescope, with a wide field of view of about 60×100 degrees, continuously monitors the sky and this results in a catalog of the brightest sources in this energy range. BAT105 is - up to now - the most sensitive and uniform hard X-ray all-sky survey.

4.3.2 Source selection

4.3.2.1 *Swift*-BAT 105-months catalog

Among the 1632 sources of the *Swift*-BAT 105-months catalog, all the known TeV emitting EHBLs, namely 1ES 0229+200, 1ES 0347-121, RGB J0710+591, and 1ES 1101-232 are present, having their synchrotron peak located in the hard X-ray band. The *Swift*-BAT catalog, once properly exploited, can therefore allow us to obtain the up-to-now most complete and representative sample of EHBLs with bright flux in the hard X-ray band according to the *Swift*-BAT sensitivity.

To find at least a significant fraction of these sources, we have confined our analysis to the 158 objects that are classified as "Beamed AGN (Blazar/FSRQ)" (class number 80 of the *Swift*-BAT 105-months catalog), whose classification was confirmed among previously published catalogs of AGNs and blazars. The study of other sources of the catalog could provide new EHBL candidates. For example, this analysis may be applied to the 114 "unknown AGN" sources of the catalog (class 70), or even to the 129 completely "unknown class" objects (classes 10-11-12). However, such analysis would need a refined approach to validate the nature of each source, and it will be the subject of a future work.

4.3.2.2 *Fermi*-LAT 3LAC catalog

In order to study the nature of these 158 sources in the HE gamma-ray band, we considered data from the *Fermi*-LAT observatory (see Section 2.3). In particular, we adopted the *Fermi*-LAT 3LAC catalog (Fermi-LAT Collaboration, 2015b), the third catalog of AGNs detected by the *Fermi*-LAT telescope after four years of operation in which a detailed analysis of the AGN sources was performed.

The main aim driving this work, with respect to the previous methods presented in Section 4.2, is both to identify new EHBL sources (and in particular hard-TeV EHBLs) and study their broad-band emission. Since no complete catalog of EHBLs has been produced yet, first of all we aim at increasing the number of sources classified as EHBLs using the definition based on the synchrotron peak position. Secondly, given the observational evidence of different TeV spectral features (see Section 4.3.8), we aim at enlarging the statistics of the TeV population in order to identify a possible sub-classification inside the EHBL class.

The driving idea is that, since the SED peaks of EHBLs are located at higher energies with respect to HBLs ones, their synchrotron peak should be well detected in hard X-rays, and their high-energy hump should be rather faint in HE gamma rays in order to peak in the TeV gamma-ray band. To perform this selection, we identify sources with a high frequency of the synchrotron peak and high flux in the hard X-ray band. Moreover, we make use of the large integration time by the *Fermi*-LAT telescope to improve our data in HE gamma rays.

The main step of the selection procedure was the cross-match between the *Swift*-BAT 105-months catalog and the *Fermi*-LAT 3LAC catalog. We used a search radius of 20 arcmin corresponding to the maximum value of the error box distribution of the BL Lac objects reported in the *Fermi*-LAT 3LAC catalog. This operation resulted in two sub-samples of 86 *Fermi*-LAT 3LAC detected sources and 72 *Fermi*-LAT 3LAC undetected sources.

- ***Fermi*-LAT 3LAC detected sources.** Concerning the sample of 86 *Fermi*-LAT 3LAC detected sources, we plot the distribution of their synchrotron peak frequencies in **Figure** 4.10. Except for the three sources with unknown synchrotron peak frequency (set to zero), we notice that this sample is splitted in two main groups: the blazars with synchrotron peak around 10^{13} Hz, meaning a sample of LBL objects, and the blazars with synchrotron peak above 10^{15} Hz. We explain this fact as a selection effect due to the sensitivity of the BAT instrument around

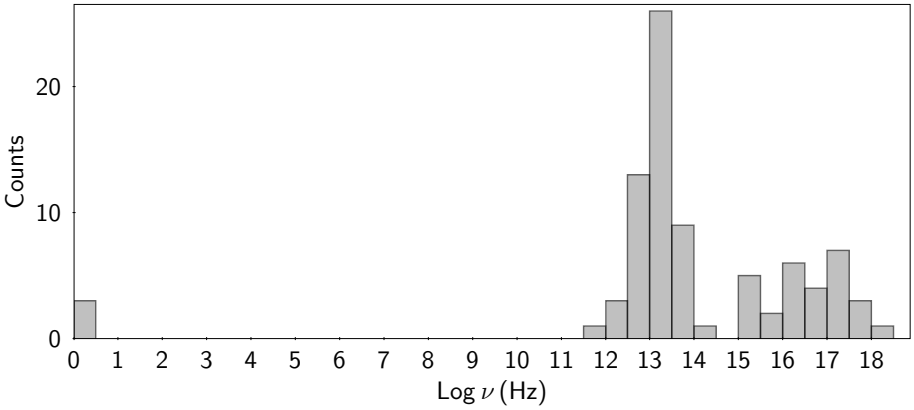

Figure 4.10: *Distribution of the synchrotron peak frequencies in the sample of 86 sources obtained cross-matching the* Swift*-BAT beamed AGNs and the* Fermi*-LAT 3LAC catalog.*

10^{-12} erg cm^{-2} s^{-1} in the hard X-ray band. This implies that this sample is composed by a group of HBL/EHBL objects of which the BAT instrument detects the last part of the synchrotron peak, and by a sample of LBL sources of which the BAT instrument already detects the second peak. Following this idea, IBL objects with synchrotron peak frequency around 10^{14} Hz are excluded from this distribution because the BAT energy range in the SED of those sources is located in the region between the two peaks and the instrument is not sensitive enough to detect them.

In our analysis, we decided to keep all sources with synchrotron peak exceeding at least 10^{15} Hz and not only 10^{17} Hz (definition of EHBL) because the estimation of the synchrotron peak position is commonly affected by large errors due to the data selection used to fit the polynomial to the MWL data (an introduction to this problem is reported in Section 4.1.2). For this reason, in this selection of 86 *Fermi*-LAT 3LAC detected sources, we selected all the objects with the synchrotron peak situated above 10^{15} Hz, excluding all ISP and LSP objects, reducing the sample to 28 sources. In this sample we decided to add the three sources with undefined synchrotron peak, and the sample increased to 31 objects.

Then, with a cross-match using a search radius of 10 arcmin corresponding the maximum value of the error box distribution of the BL Lac sources reported in the *Swift*-BAT 105 catalog, we checked in the 2WHSP catalog the synchrotron peak position of our previous sample of 31 *Fermi*-LAT 3LAC detected objects, finding 28 out of 31 sources whose updated value is reported in **Table** 4.2.

Exceptions

For some sources in the sample, we performed a detailed search in literature to check their classification. In particular, we noticed that the source RX J0324.6+3410 was classified as Sy 1 galaxy by Motch et al. (1998) and is now classified as NLSY1 galaxy (see Zhou et al. 2007 and Healey et al. 2007) in the *Swift*-BAT 105-month catalog. Thus, this source is not of interest for our work and has been excluded from our sample.

- ***Fermi*-LAT 3LAC undetected sources.** Coming now to the *Fermi*-LAT 3LAC undetected sources (72 sources), we decided to check if some new blazar of the 2WHSP catalog is present. We found three more sources PKS 0706-15, PKS 2300-18 and 1RXS J225146.9-320614, that additionally show association in the *Fermi*-LAT 3FGL catalog.

Exceptions

After a detailed search in literature, we noticed that the source PKS 2300-18 actually is not a blazar but is classified as Sy 1 galaxy by Healey et al. (2007), and it is not of interest for our work.

4.3.3 Final sample

Our selection resulted in a sample of 32 EHBL objects out of 158 of the reference *Swift*-BAT 105-months blazar sample, represented in **Table** 4.2 on page 170.

We complemented the SED data of these luminous objects in the hard X-ray band with archival radio, UV, optical, and soft X-ray data. For the HE gamma-ray band, we used the *Fermi*-LAT 3LAC catalog, and updated the results with a new ten-years *Fermi*-LAT analysis of our source sample. More information about the updated *Fermi*-LAT analysis is reported in Section 4.3.3.1.

Finally, to check if our 32 objects are already detected in the TeV gamma-ray band, we performed a cross-match between the main sample, the TeGeV catalog (Carosi et al., 2016), and the TeVCat catalog[2]. We found that 18 sources out of 32 are already known as TeV gamma-ray emitters. Within this sample, the objects show spectral properties similar to those of the archetypal EHBL 1ES 0229+200 at energies below about 100 GeV. Interestingly, sources with a TeV gamma-ray detection show also interesting differences in the VHE gamma-ray regime.

In summary, our main sample of 32 objects is composed of 18 TeV gamma-ray detected objects and 14 TeV gamma-ray undetected objects. This allows us to to study first the TeV detected sources in order to find spectral differences within this class, and then to apply such results to the TeV undetected sources in order to guess their detectability at VHE energies and provide a new sample of TeV EHBL candidates.

[2] http://tevcat.uchicago.edu

Fermi-LAT analysis

4.3.3.1 *Fermi*-LAT analysis

For all the sources in our final sample we performed an updated analysis over ten years of operation of the *Fermi*-LAT telescope using the data publicly available on the *Fermi* Science Support Center. The results are reported in **Table** 4.2.

We analyzed them using the *Fermi*-LAT Science Tools version `v10.r0.p5`, together with the Pass 8 instrument response functions, the corresponding `iso-P8R2-SOURCE-V6-v06` isotropic model and `gll-iem-v06` galactic diffuse background model. The event selection was based on Pass 8 reprocessed source (event type 3 and class 128) photons in the 1-300 GeV energy range, collected from 2008 August 4 (MET 239557417) to 2018 July 19 (MET 553654936) and coming from a 15° radius region of interest (ROI) centered at the nominal position of the source. The cut in energy above 1 GeV was set because, taking into account that the detector Point Spread Function improves with increasing energy and that the spectral slope of HSP sources is relatively hard, it helps to avoid contamination from nearby sources.
The events were selected and filtered through standard quality cuts. The target was modeled with *PowerLaw2*:

$$\frac{dN}{dE} = \frac{N_0(\Gamma+1)\,E^{\Gamma}}{E_{\rm max}^{\Gamma+1} - E_{\rm min}^{\Gamma+1}}$$

where N_0 is the normalization factor, Γ is the photon index $E_{\rm max}$ and $E_{\rm min}$ are fixed parameters representing the range where the integral flux is calculated.

Besides the target and backgrounds, all the *Fermi*-LAT 3FGL catalog point sources in the field were included in the model (Fermi-LAT Collaboration, 2015a). A standard binned analysis was then performed. The test statistic (TS) was used to verify the significance of excess signal of our sources. The TS is defined as (Mattox et al., 1996)

$$\mathrm{TS} = -2\,\ln\left(\frac{L_{\,null}}{L_{\,source}}\right)$$

where $L_{\,null}$ and $L_{\,source}$ are the likelihoods of observing a certain flux for a model respectively without the candidate source (the null hypothesis) and including the additional candidate source. This quantity allows to determine how much a source emerges from the background: a TS≈25 is equivalent to a 5σ detection (Abdo et al., 2010a), and only cases with TS>25 are considered as a positive detection of point-like source.

4.3.4 TeV gamma-ray information

In our sample of 18 TeV gamma-ray detected objects, we collected all the available TeV gamma-ray data in order to add them the MWL SEDs. However, only 13 sources had these data publicly available.

The TeV gamma-ray data were collected looking for data up to the highest available energy. We collected data regarding only the lower possible state of the sources, but some of them are known variable sources and may present strong fluctuations in this energy band in different observational campaigns.

In the case of some interesting sources like 1ES 0229+200 and 1ES 1426+428, the resulting spectra at TeV gamma-ray energies based on observations with the MAGIC telescopes – reported in Section 5.2 – are compatible with the values found in this work and agree with its conclusions.

In **Table** 4.1 I summarize the TeV gamma-ray data used in this work.

Source	Data reference	Considered period
1ES 0229+200	Aharonian et al. (2007d)	MJD 53614-54088
1ES 1426+428	Aharonian et al. (2003)	MJD 51179-51909
1ES 1959+650	Aliu et al. (2013)	MJD 54417
PKS 0548-322	Aharonian et al. (2010)	MJD 53279-54495
3FGL J0710.3+5908	Acciari et al. (2010)	MJD 54801-54891
Mrk 501	Anderhub et al. (2009)	MJD 54913
1ES 2344+514	Acciari et al. (2011)	MJD 54377-54476
1ES 0347-121	Aharonian et al. (2007c)	MJD 53973-54090
1ES 1101-232	Aharonian et al. (2007a)	MJD 53111-53445
1ES 1218+304	Acciari et al. (2009)	MJD 54115-54180
H 2356-309	H.E.S.S. Collaboration et al. (2010b)	MJD 53530-53615
PKS 2005-489	H.E.S.S. Collaboration et al. (2010a)	MJD 53171-54345
Mrk 421	Aharonian et al. (2005)	MJD 53107-53115

Table 4.1: *TeV gamma-ray data used in building the MWL SEDs of Appendix B.*

4.3.5 New synchrotron peak estimation

Considering that the synchrotron peak position is at the basis of the definition of EHBL (for more details see Section 4.1.2), this value plays an important role in classifying these sources. In order to consider the best values of $\nu_{\rm peak}^{\rm sync}$, we performed a log-parabolic fit of the form

$$\frac{dN}{dE} = N_0 \left(\frac{E}{E_0}\right)^{-\alpha-\beta\log\left(\frac{E}{E_{\rm cut\text{-}off}}\right)}$$

of the synchrotron peak in the X-ray band using for each source the available *Swift*-XRT, *Beppo*-SAX, and *Swift*-BAT 105-months archival data. We obtained overall good quality fits. All our results, reported in **Table** 4.2, are in general compatible with the values reported in the 2WHSP catalog (Chang et al., 2017). In some cases (e.g. in 1ES

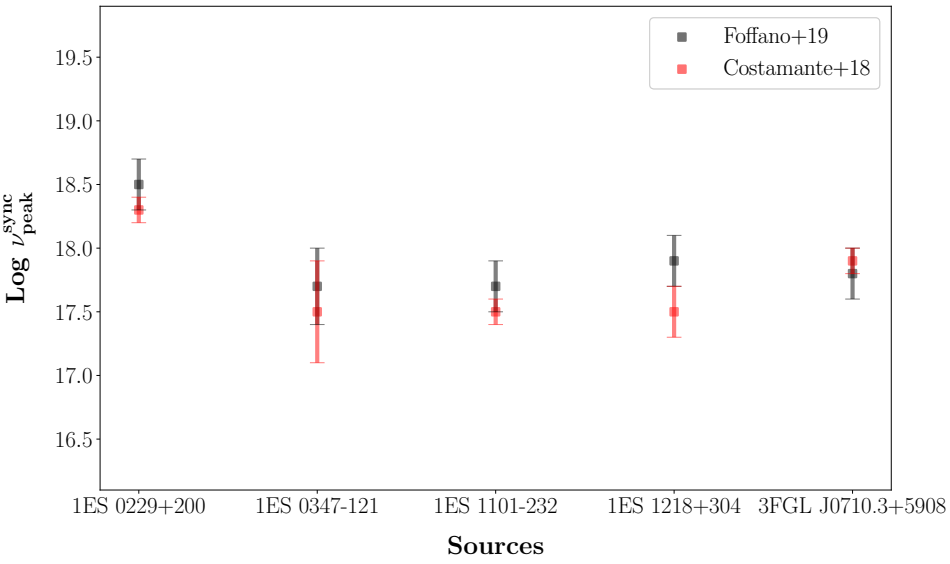

Figure 4.11: *Comparison of the synchrotron peaks estimated in our work n Foffano et al. (2019) and the ones in Costamante et al. (2018).*

1959+650) there is some tension with respect to the 2WHSP catalog that we attribute to the high variability of the sources and to the fact that these estimations are all based on non-simultaneous archival data. However, in the following analysis we adopt our estimation of the synchrotron peak position also because we are able to provide a statistical error.

It is worth to note that in our final sample 5 over 6 already known TeV EHBL emitters reported in Costamante et al. (2018) are present (the only one missing is 1ES 0414+009 because not detected by *Swift*-BAT 105-months). In that paper, they performed a detailed study of the synchrotron peak of these sources thanks to simultaneous *Swift*-XRT and *NuSTAR* (Harrison et al., 2013) observations. All their estimations are, however, compatible with our previous results (see **Figure** 4.11 for the comparison).

#	*Swift*-BAT name	Counterpart	RA (deg)	DEC (deg)	Redshift	*Swift*-BAT flux (10^{-12} erg/s/cm^2)	Δ flux$_{\rm BAT}$	*Fermi* variab.	*Fermi* flux (10^{-10} ph/s/cm^2)	*Fermi* spectral index	*Fermi* TS	Log $\nu^{\rm sync}_{\rm peak}$ (Hz)	TeV detect.
1	SWIFT J0232.8+2020	1ES 0229+200	38.188	20.29	0.140	$23.46^{+2.62}_{-2.27}$	4.9	130	2.7 $\pm$ 0.5	-1.74 $\pm$ 0.13	49	18.5 $\pm$ 0.2	D
2	SWIFT J2251.8-3210	1RXS J225146.9-320614	342.944	-32.096	0.246	$13.98^{+2.47}_{-1.92}$ (0.6)	4.4	47	1.1 $\pm$ 0.4 (0.4)	-1.55 $\pm$ 0.26 (0.7)	37	18.3 $\pm$ 0.3	N
3	SWIFT J0733.9+5156	3FGL J0733.5+5153	113.404	51.931		$8.17^{+2.27}_{-2.17}$ (0.3)	4.4	107	2 $\pm$ 0.4 (0.7)	-1.69 $\pm$ 0.13 (0.3)	41	18.3 $\pm$ 0.2	N
4	SWIFT J0244.8-5829	BZB J0244-5819	41.188	-58.299	0.265	$10.13^{+2.46}_{-1.13}$ (0.4)	3.6	429	5.1 $\pm$ 0.5 (1.9)	-1.65 $\pm$ 0.08 (0.6)	37	18.2 $\pm$ 0.3	N
5	SWIFT J1136.7+6738	RX J1136.5+6737	174.104	67.645	0.134	$12.73^{+2.24}_{-1.53}$ (0.5)	3.8	471	4.4 $\pm$ 0.4 (1.6)	-1.67 $\pm$ 0.07 (0.5)	51	18.2 $\pm$ 0.6	D
6	SWIFT J0709.3-1527	PKS 0706-15	107.329	-15.437		$7.37^{+1.99}_{-1.63}$ (0.3)	3.6	82	3.3 $\pm$ 0.8 (1.2)	-1.77 $\pm$ 0.15 (0.2)	39	18.0 $\pm$ 0.2	N
7	SWIFT J0156.5-5303	RBS 259	29.13	-53.036		$7.32^{+1.56}_{-2.46}$ (0.3)	4	361	5.5 $\pm$ 0.5 (2)	-1.89 $\pm$ 0.08 (1.0)	56	18.0 $\pm$ 0.2	N
8	SWIFT J1428.7+4234	1ES 1426+428	217.149	42.655	0.129	$20.85^{+1.5}_{-1.04}$ (0.9)	2.5	731	6.1 $\pm$ 0.5 (2.3)	-1.55 $\pm$ 0.06 (1.3)	59	18.0 $\pm$ 0.2	D
9	SWIFT J0353.4-6830	PKS 0352-686	58.28	-68.532	0.087	$12.24^{+1.67}_{-1.44}$ (0.5)	3.1	165	2.3 $\pm$ 0.4 (0.9)	-1.46 $\pm$ 0.11 (1.6)	42	18.0 $\pm$ 0.2	O
10	SWIFT J0710.3+5908	3FGL J0710.3+5908	107.635	59.14	0.125	$24.06^{+2.77}_{-2.3}$ (1.0)	5.1	445	4.4 $\pm$ 0.4 (1.6)	-1.57 $\pm$ 0.07 (1.2)	78	17.8 $\pm$ 0.2	D
11	SWIFT J0036.0+5951	1ES 0033+595	8.989	59.841	0.086	$25.96^{+1.13}_{-1.57}$ (1.1)	2.7	3138	32.2 $\pm$ 1.2 (11.9)	-1.7 $\pm$ 0.03 (0.3)	70	17.9 $\pm$ 0.2	D
12	SWIFT J0550.7-3212A	PKS 0548-322	87.689	-32.273	0.069	$18.21^{+6.16}_{-5.29}$ (0.8)	11.5	157	2.8 $\pm$ 0.5 (1)	-1.73 $\pm$ 0.12 (0.1)	48	17.8 $\pm$ 0.2	D
13	SWIFT J0122.9+3420	1ES 0120+340	20.776	34.371	0.272	$11.27^{+2.07}_{-1.62}$ (0.5)	3.7	132	1.9 $\pm$ 0.4 (0.7)	-1.49 $\pm$ 0.15 (1.3)	128	17.7 $\pm$ 0.2	O
14	SWIFT J1654.0+3946	Mrk 501	253.472	39.76	0.034	$71.58^{+2.23}_{-2.29}$ (3.1)	4.5	24696	107.8 $\pm$ 1.7 (39.9)	-1.76 $\pm$ 0.01 (0.2)	101	17.7 $\pm$ 0.2	D
15	SWIFT J2346.8+5143	1ES 2344+514	356.764	51.692	0.044	$10^{+2.13}_{-1.51}$ (0.4)	3.6	2986	28.9 $\pm$ 1.1 (10.7)	-1.88 $\pm$ 0.03 (1.0)	2935	17.7 $\pm$ 0.4	D
16	SWIFT J1417.7+2539	BZB J1417+2543	214.449	25.72	0.237	$5.93^{+1.77}_{-1.73}$ (0.3)	3.5	211	2.8 $\pm$ 0.4 (1)	-1.52 $\pm$ 0.1 (1.3)	43	17.7 $\pm$ 0.2	O
17	SWIFT J0640.3-1286	TXS 0637-128	100.07	-12.866		$7.87^{+2.51}_{-2.08}$ (0.3)	4.6	186	3 $\pm$ 0.6 (1.1)	-1.44 $\pm$ 0.1 (1.8)	51	17.7 $\pm$ 0.2	N
18	SWIFT J2246.7-5208	RBS 1895	341.661	-52.12	0.194	$6.97^{+1.76}_{-1.57}$ (0.3)	3.3	81	1.8 $\pm$ 0.4 (0.7)	-1.67 $\pm$ 0.15 (0.4)	37	17.6 $\pm$ 0.2	N
19	SWIFT J0213.7+5147	1RXS J021417.8+514457	33.553	51.772	0.049	$13.65^{+1.67}_{-1.81}$ (0.6)	3.5	157	4.1 $\pm$ 0.6 (1.5)	-1.88 $\pm$ 0.1 (0.9)	41	17.6 $\pm$ 0.2	O
20	SWIFT J2359.0-3038	H 2356-309	359.777	-30.579	0.165	$14.88^{+1.97}_{-1.85}$ (0.6)	3.8	292	4.6 $\pm$ 0.5 (1.7)	-1.8 $\pm$ 0.09 (0.4)	47	17.6 $\pm$ 0.2	D
21	SWIFT J1031.5+5051	1ES 1028+511	157.854	50.903	0.360	$7.85^{+1.68}_{-1.31}$ (0.3)	3	1130	9.4 $\pm$ 0.6 (3.5)	-1.72 $\pm$ 0.06 (0.1)	131	17.5 $\pm$ 0.2	O
22	SWIFT J1221.3+3012	1ES 1218+304	185.343	30.16	0.184	$10.62^{+1.29}_{-1.68}$ (0.5)	3	3971	33.3 $\pm$ 1.2 (12.3)	-1.68 $\pm$ 0.03 (0.4)	45	17.9 $\pm$ 0.2	D
23	SWIFT J0349.2-1159	1ES 0347-121	57.368	-11.983	0.180	$15.68^{+3.31}_{-2.25}$ (0.7)	5.6	190	2.9 $\pm$ 0.4 (1.1)	-1.64 $\pm$ 0.1 (0.6)	39	17.7 $\pm$ 0.4	D
24	SWIFT J1103.5-2329	1ES 1101-232	165.868	-23.471	0.186	$10.8^{+1.66}_{-3.01}$ (0.5)	4.7	241	4 $\pm$ 0.5 (1.5)	-1.6 $\pm$ 0.09 (0.9)	92	17.7 $\pm$ 0.2	D
25	SWIFT J0507.7+6732	1ES 0502+675	76.92	67.533	0.314	$9.03^{+2.18}_{-2.28}$ (0.4)	4.5	2292	15.4 $\pm$ 0.3 (5.7)	-1.47 $\pm$ 0.01 (2.1)	251	17.5 $\pm$ 0.2	D
26	SWIFT J0930.1+4987	1ES 0927+500	142.523	49.878	0.187	$7.44^{+2.22}_{-1.71}$ (0.3)	3.9	50	1.3 $\pm$ 0.4 (0.5)	-1.61 $\pm$ 0.2 (0.5)	44	17.4 $\pm$ 0.4	O
27	SWIFT J1959.6+6507	1ES 1959+650	299.973	65.158	0.047	$29.03^{+1.72}_{-1.83}$ (1.2)	3.6	17681	95.2 $\pm$ 1.7 (35.3)	-1.84 $\pm$ 0.02 (0.8)	158	17.4 $\pm$ 0.2	D
28	SWIFT J0326.0-5633	1RXS J032521.8-56354	51.47	-56.526	0.060	$8.49^{+2.35}_{-2.21}$ (0.4)	4.6	251	4.9 $\pm$ 0.5 (1.8)	-1.97 $\pm$ 0.1 (1.4)	755	17.4 $\pm$ 0.2	N
29	SWIFT J0136.5+3906	B3 0133+388	24.126	39.05		$7.91^{+2.28}_{-1.84}$ (0.3)	4.1	6511	42 $\pm$ 1.2 (15.6)	-1.72 $\pm$ 0.02 (0.2)	44	17.4 $\pm$ 0.2	D
30	SWIFT J2009.6-4851	PKS 2005-489	302.477	-48.866	0.071	$6.03^{+2.61}_{-3.07}$ (0.3)	5.7	2943	28.7 $\pm$ 1.1 (10.6)	-1.84 $\pm$ 0.03 (0.7)	55	17.0 $\pm$ 0.9	D
31	SWIFT J2056.8+4939	RX J2056.6+4940	314.202	49.665		$13.01^{+1.7}_{-2.02}$ (0.6)	3.7	610	16.3 $\pm$ 0.9 (6)	-1.81 $\pm$ 0.05 (0.5)	178	17.0 $\pm$ 0.9	D
32	SWIFT J1104.4+3812	Mrk 421	166.103	38.214	0.033	$141^{+1.11}_{-2.01}$ (6.0)	3.1	101631	344.7 $\pm$ 3.1 (127.7)	-1.77 $\pm$ 0.01 (0.2)	62	17.0 $\pm$ 0.3	D

Table 4.2: *List of all the 32 sources of our final sample selected in the* Swift*-BAT 105-months catalog (Oh et al., 2018) (see text for details). All of them are detected in the* Fermi*-LAT 3LAC catalog (Fermi-LAT Collaboration, 2015b), except for sources numbers 2 and 30 that have been selected using the 2WHSP catalog (Chang et al., 2017). In this table we report from the* Swift*-BAT catalog the name of each source, the counterpart, the galactic coordinates (in degrees), and the redshift (when known). Then we report the* Swift*-BAT flux and the* Δ *flux$_{BAT}$, that is a measure of variability computed as difference between the lowest flux and highest flux in the* Swift*-BAT catalog. After that, we present the updated ten-years* Fermi*-LAT TS, the 1-300 GeV flux, the spectral index and its compatibility with the one of 1ES 0229+200 (see text for details), and the* Fermi*-LAT 3FGL (Acero et al., 2015) variability index. In the last columns we present also the logarithm of the synchrotron peak frequency, that we estimated with a log-parabolic fit through X-ray and hard X-ray data. Finally, we indicate the TeV detection ("D" if already detected, "N" if not detected yet) reported in the TeGeV (Carosi et al., 2016) and TeVCat catalogs (`http://tevcat.uchicago.edu`) association. If the source has been observed by the current IACTs but without detection, we indicate it with "O".*

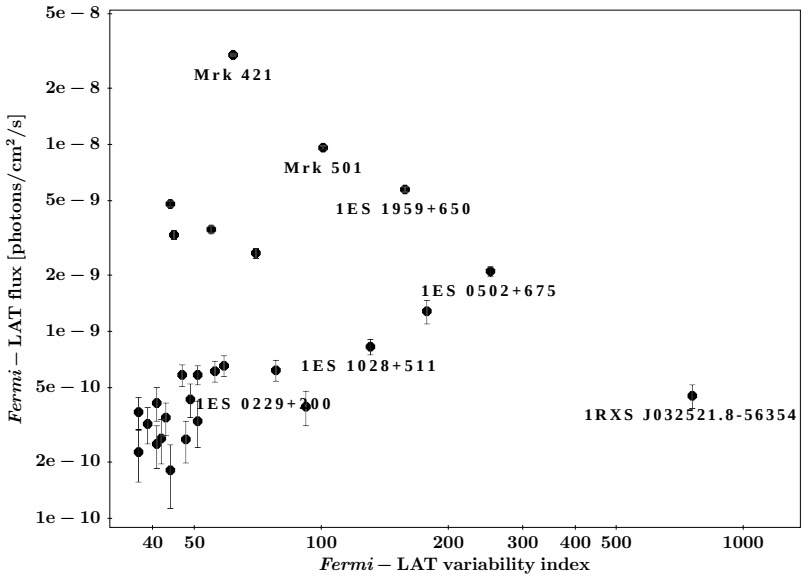

Figure 4.12: *Distribution of the* Fermi*-LAT 3FGL flux versus the corresponding variability index of the sources in the main sample (logarithmic scale).*

4.3.6 Broad-band SEDs

For each of our final EHBLs, in **Figure** B.1 in Appendix B we compiled the available MWL (not simultaneous) archival data from the ASI Science Data Center (SSDC) server (including our ten-years *Fermi*-LAT analysis). This let us to perform a visual inspection of the SEDs to check the extreme nature of the sources, comparing them with the data of the reference EHBL 1ES 0229+200.

According to the main idea driving our selection method, in the HE gamma-ray band these sources show the rising part of the second bump that finally peaks in the TeV band. Thus, this criterion by which the EHBLs may exhibit a rather faint detection in HE gamma rays could be a key feature in the selection and characterization of EHBLs. A more detailed discussion of this point is reported in the next Section.

The shift at higher energies of the two peaks in the SED provide access to the optical radiation of the host galaxy for low-redshift objects in our sample. This is an important feature of the so far studied EHBLs: the majority of our objects (81%) has a known redshift value, and the sources with unknown redshift may be good candidates to be addressed by specific optical campaigns.

4.3.7 Results

In **Table** 4.2 we report the results of our ten-years *Fermi*-LAT analysis and we list the main properties extracted from other catalogs for all the 32 sources of the final sample.

***Swift*-BAT fluxes.**
The *Swift*-BAT total flux in the 14-195 keV band shows that 31 out of 32 sources (97%) generally have an X-ray flux of the same order of 1ES 0229+200. Generally they show a flux of the synchrotron peak around 10^{-11} erg cm^{-2} s^{-1}, probably related to the sensitivity limit of the *Swift*-BAT 105-months catalog. We notice that the two Markarians (Mrk 421 and Mrk 501 from now on) make an exception and are particularly bright also in this energy band.

The following column $\Delta\,\mathtt{flux}_{\mathtt{BAT}}$ describes the variability of the hard X-ray flux of each source, calculated as difference between the highest and the lowest flux measured by *Swift*-BAT between December 2004 and August 2013 (see Oh et al. 2018). Almost all sources show an average stable flux in this energy band, very similar with respect to that

of 1ES 0229+200.

***Fermi*-LAT variability indices.**
We report also the *Fermi*-LAT variability indices as reported in the *Fermi*-LAT 3FGL catalog. We find that 27 out of 32 sources (84%) show values below the threshold of 72.44 and are considered not variable in the HE gamma-ray band (Acero et al., 2015). In **Figure** 4.12 we show a qualitative plot relating these two observables available from the *Fermi*-LAT 3FGL catalog: some interesting sources e.g. 1ES 1959+650 and Mrk 501 do not follow the mean low variability behavior.

***Fermi*-LAT flux.**
In **Table** 4.2 we report also our new estimation of the total flux in the 1-300 GeV band, showing in parentheses the ratio of the flux of each source with respect to the reference 1ES 0229+200. All sources show total fluxes of the same order of that of 1ES 0229+200, except for 1ES 1959+650 and the two Markarians that are particularly bright.

***Fermi*-LAT spectral index.**
In the following column we present the spectral index resulting from our analysis and in parentheses the compatibility

$$\lambda = \frac{|A - B|}{\sqrt[2]{\sigma_A^2 + \sigma_B^2}}$$

of the spectral index of each source (A) with that measured in 1ES 0229+200 (B). The *Fermi*-LAT spectral indices are generally very hard (lower than 2.0) and well compatible with the value -1.74 ± 0.13 of 1ES 0229+200.

***Fermi*-LAT TS values.**
The *Fermi*-LAT TS values are distributed over a wide range of values. Generally they are around few hundreds, but some very bright objects in HE gamma rays like 1ES 1959+650 and the two Markarians show TS values up to hundred thousands. On the other hand, some other sources like 1RXS J225146.9-320614 (TS=47) and 1ES 0927+500 (TS=49) show low TS values also after ten years of data. This can explain their absence in the 3FGL catalog.

Since we are looking for sources that should not show high signal in HE gamma rays due to hard spectrum of the IC bump that peaks above this energy band, we have to remember that some of the brightest sources may show mainly thanks to their high flux rather than to their extreme spectral properties. For example, the two Markarians are generally considered very bright HSP sources, even though in some cases they show strong variability and sometimes Mrk 501 behaves like an EHBL during some flaring episodes (Pian et al., 1998a; Ahnen et al., 2018). We will study this relation the next Section.

Synchrotron peak frequency.
The logarithm of the frequency of the synchrotron peak $\nu_{\rm peak}^{\rm sync}$ (see **Table** 4.2 for more details) ranges from 17 to 18.3. Thus, we confirm that all the sources in our sample can be classified as EHBL following the definition based on the synchrotron peak frequency.

4.3.8 TeV gamma-ray detected sources

The analysis of the previous Section reveals essentially a compatibility between the main observables of the EHBLs and our reference source 1ES 0229+200, at least up to GeV energies. This effect may be to some extent expected because we are dealing with sources that - in most of the cases - are at the limit of the sensitivity of our instruments. On the other hand, some sources with very bright and variable flux in these bands (e.g. 1ES 1959+650 and the two Markarians) seem to deviate from the mean values of the spectral parameters that the other EHBL objects show.

In order to find distinguishable features between our sources, we now try to further investigate the properties of the TeV gamma-ray band for the sources. The detailed list of TeV gamma-ray detected sources is reported in **Table** 4.3.

4.3.8.1 Broad-band spectra comparison

All the sources in our sample resulted very similar in their synchrotron peak properties. In order to exploit the relation between the main spectral properties of the sources at different wavelengths, we report in **Figure** 4.13a a comparison of the MWL SEDs of all the TeV gamma-ray detected sources with data from the SSDC database for which we have TeV data publicly available (13 out of 18). In this figure, all SEDs have been rescaled to the 1ES 0229+200 flux of $3.34 \cdot 10^{-12}$ erg cm^{-2} s^{-1} at $1.7 \cdot 10^{17}$ Hz, and the scaling factor for each source is reported in parentheses in the legend. All sources have been deabsorbed by EBL effect at their own redshift with the model by Franceschini & Rodighiero (2017) to obtain the intrinsic spectrum of the source. We chose a color scale that follows up-to-bottom **Table** 4.3, meaning that the color gradually goes from dark brown when the $\nu^{\rm sync}_{\rm peak}$ of the source is high to light yellow when its $\nu^{\rm sync}_{\rm peak}$ is low.

In the figure, all the sources share common features in their SEDs. For example, the logarithm of the frequency of the synchrotron peak $\nu^{\rm sync}_{\rm peak}$ lies in the narrow range from 17 to 18.3, and the synchrotron hump shape results quite similar for all the sources.

At optical wavelengths, they generally show the presence of the galaxy. This appearance of the galaxy depends on the distance of the source from the observer, and shows mainly in the case of low-redshift sources. The flux in radio and hard X-rays is scattered due to different slopes and brightness in these bands.

Thus, the analysis of all the sources in the wavelengths from radio to HE confirms essentially a compatibility between the main observables of the EHBLs and our reference source, 1ES 0229+200. This effect may be to some extent expected because we are dealing with sources that - in most of the cases - are at the limit of the sensitivity of our instruments. On the other hand, some sources with very bright and variable flux in these bands (e.g. 1ES 1959+650 and the two Markarians) seem to deviate from the mean values of the spectral parameters that the other EHBL objects show (see results of Section 4.3.7).

However, in HE gamma rays all sources are shaping the increasing flux of the second hump. Interestingly, even though the slopes in HE gamma rays are generally well compatible between each other, there is a moderate dispersion of the differential energy flux in this band. This spread seems to be amplified in VHE gamma rays above about 100 GeV, where the SED points for some sources diverge: some of them show continuously increasing hard-TeV spectra with peak located at higher energies, and some other show decreasing TeV spectrum with peak located at few hundreds GeV.

This tendency in the TeV gamma rays, in addition to some indicators like the TeV detection that is not uniform through the sample, suggest us that the properties of the EHBL objects in the TeV VHE are crucial.

In order to find distinguishable features between our sources, we tried to further investigate the properties of the TeV gamma-ray band for these sources.

#	*Swift*-BAT name	Counterpart	Log $\nu_{\rm peak}^{\rm sync}$ (Hz)	HE χ^2	HE-VHE slope	HE-VHE χ^2	IC peak (TeV)	TeV slope	TeV χ^2
1	SWIFT J0232.8+2020	1ES 0229+200	18.5 $\pm$ 0.2	1.1	0.43 $\pm$ 0.04	0.4	>10	0.49 $\pm$ 0.19	0.4
2	SWIFT J1136.7+6738	RX J1136.5+6737	18.2 $\pm$ 0.6	2.4					
3	SWIFT J1428.7+4234	1ES 1426+428	18.0 $\pm$ 0.2	0.7	0.47 $\pm$ 0.04	0.5	>10	0.58 $\pm$ 0.15	0.4
4	SWIFT J1221.3+3012	1ES 1218+304	17.9 $\pm$ 0.2	1.4	0.16 $\pm$ 0.02	2.1	>10	0.14 $\pm$ 0.22	0.6
5	SWIFT J0036.0+5951	1ES 0033+595	17.9 $\pm$ 0.2	0.5					
6	SWIFT J0710.3+5908	3FGL J0710.3+5908	17.8 $\pm$ 0.2	1.5	0.33 $\pm$ 0.03	0.4	>10	0.22 $\pm$ 0.16	0.3
7	SWIFT J0550.7-3212A	PKS 0548-322	17.8 $\pm$ 0.2	2.8	0.15 $\pm$ 0.04	1.9	0.3 $\pm$ 0.2	-0.47 $\pm$ 0.23	0.0
8	SWIFT J2346.8+5143	1ES 2344+514	17.7 $\pm$ 0.4	1.4	0.03 $\pm$ 0.01	6.7	0.3 $\pm$ 0.3	-0.41 $\pm$ 0.03	1.8
9	SWIFT J1654.0+3946	Mrk 501	17.7 $\pm$ 0.2	0.9	0.13 $\pm$ 0.01	13.9	0.2 $\pm$ 0.1	-0.52 $\pm$ 0.11	0.1
10	SWIFT J0349.2-1159	1ES 0347-121	17.7 $\pm$ 0.4	0.1	0.42 $\pm$ 0.04	0.6	>10	0.32 $\pm$ 0.16	0.6
11	SWIFT J1103.5-2329	1ES 1101-232	17.7 $\pm$ 0.2	1.0	0.40 $\pm$ 0.03	0.5	>10	0.34 $\pm$ 0.17	0.5
12	SWIFT J2359.0-3038	H 2356-309	17.6 $\pm$ 0.2	0.5	0.20 $\pm$ 0.04	0.3	>1	-0.14 $\pm$ 0.32	0.1
13	SWIFT J0507.7+6732	1ES 0502+675	17.5 $\pm$ 0.2	0.3					
14	SWIFT J1959.6+6507	1ES 1959+650	17.4 $\pm$ 0.2	1.4	0.03 $\pm$ 0.01	5.0	0.2 $\pm$ 0.2	-0.31 $\pm$ 0.06	0.8
15	SWIFT J0136.5+3906	B 30133+388	17.4 $\pm$ 0.2	61.7					
16	SWIFT J2009.6-4851	PKS 2005-489	17.0 $\pm$ 0.9	0.4	-0.11 $\pm$ 0.01	3.8	0.1 $\pm$ 0.1	-0.82 $\pm$ 0.12	0.9
17	SWIFT J2056.8+4939	RX J2056.6+4940	17.0 $\pm$ 0.9	6.0					
18	SWIFT J1104.4+3812	Mrk 421	17.0 $\pm$ 0.3	8.1		173.1	0.7 $\pm$ 0.1	-0.35 $\pm$ 0.01	85.3

Table 4.3: *List of all the 18 TeV gamma-ray detected sources of our final sample. We report here for convenience the synchrotron peak frequencies of* ***Table*** *4.2. In the* `HE` χ^2 *column, we present the* Fermi-*LAT curvature test estimated with a reduced* χ^2 *on the ten-years* Fermi-*LAT data. Then we show the* `HE-VHE slope` *and* `HE-VHE` *reduced-*χ^2 *test in the 100 MeV - 10 TeV range, and the* `TeV slope` *and* `TeV` χ^2 *test in the 100 GeV - 10 TeV range. The* `TeV slope` Γ *is related to the power-law spectral index* S *in the same energy band by* $S = 2.0 - \Gamma$.

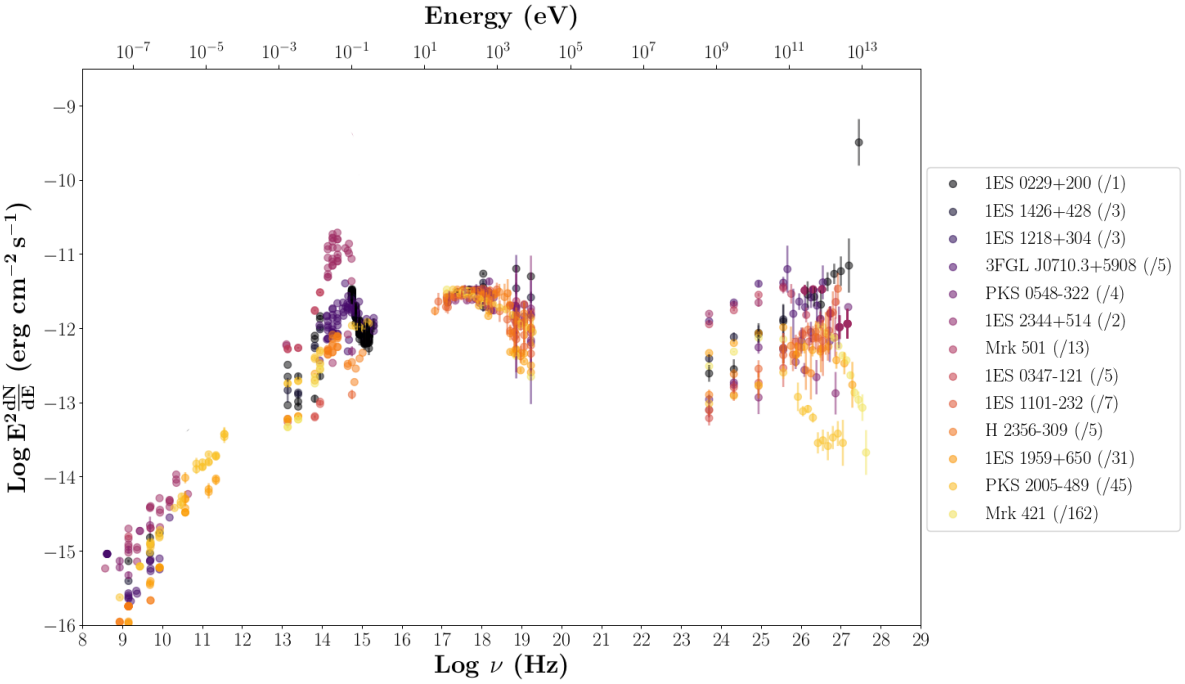

(a) Superimposition of the MWL SEDs of the 13 already TeV gamma-ray detected sources with publicly available TeV data. The fluxes have been rescaled to the 1ES 0229+200 flux of $3.34 \cdot 10^{-12}$ erg cm^{-2} s^{-1} at $1.7 \cdot 10^{17}$ Hz.

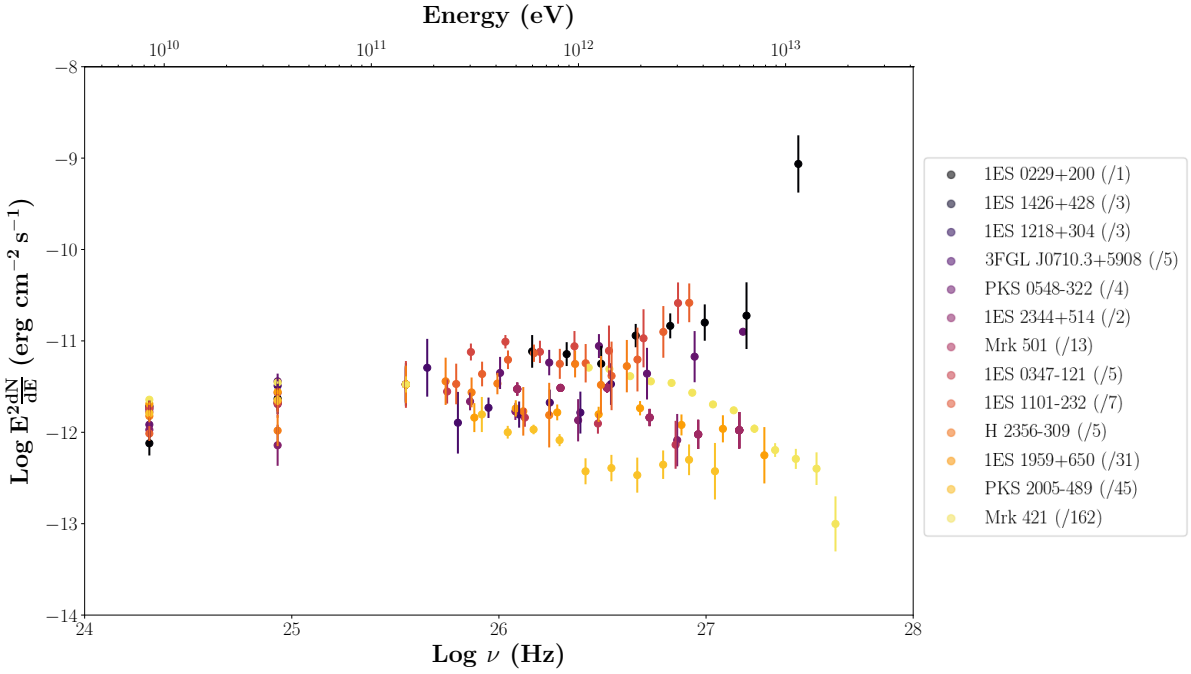

(b) Focus on the HE-VHE gamma ray range of the previous figure but with fluxes rescaled to the 1ES 0229+200 flux at 147 GeV with $1.93 \cdot 10^{-12}$ erg cm^{-2} s^{-1}.

Figure 4.13: *The color table follows up-to-bottom* ***Table*** *4.2 on page 170, meaning that the color gradually goes from dark brown when ν_{peak}^{sync} of the source is high to light yellow when its ν_{peak}^{sync} is low. In parentheses we report the ratio of the spectra of each source with respect to the 1ES 0229+200 spectrum. The plotted data are already corrected for EBL absorption with the model by Franceschini & Rodighiero (2017) to show the intrinsic spectrum of the source.*

4.3.8.2 A population of EHBLs

For all the TeV detected sources (for those objects with publicly available TeV data) we performed the following analysis on the TeV gamma-ray spectra:

- we first fitted the HE and VHE gamma-ray spectra with a power-law function in the region between 100 MeV and 10 TeV (the whole available data set in the gamma-ray range). This allowed us to look for statistical curvature of the data through the χ^2 test, and to find the sources possibly similar to the hard-TeV blazars with TeV spectra continuously increasing up to the $>$ 10 TeV energies.
- for all the sources, we applied a further fit in the range between 100 GeV and 10 TeV. This allowed us to find the VHE slope at the highest energies: the sources with clear curvature in the previous broad energy range had a clear down-going shape, whereas the sources with straight VHE spectra show an up-going spectrum up to the highest TeV energies.

This simple approach allowed us to determine the sources that show a gamma-ray spectral behaviour like 1ES 0229+200 in **Figure** 4.14a or like Mrk 501 in **Figure** 4.14b, that – as shown in in **Figure** 4.7 on page 158 – have crucial differences at TeV gamma-ray energies.

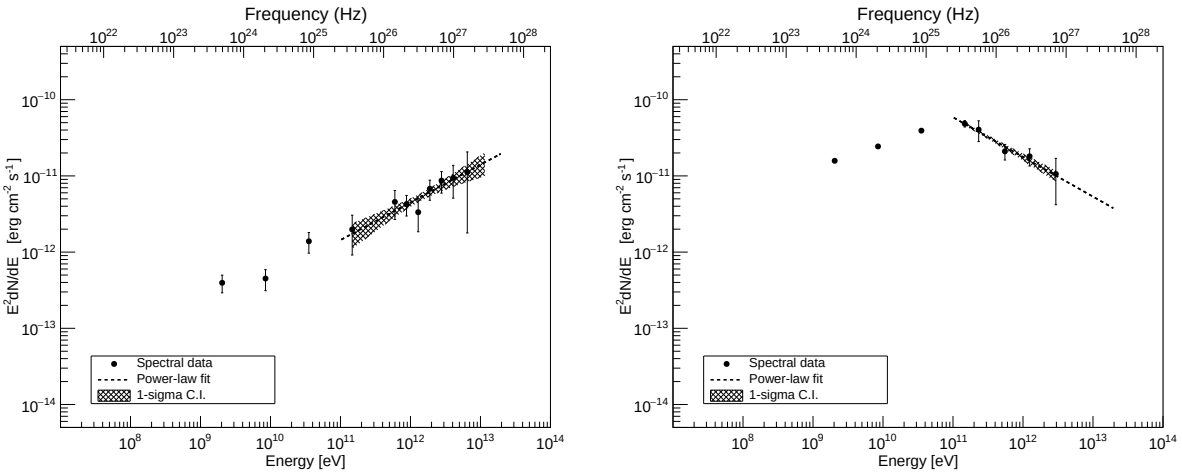

(a) 1ES 0229+200. **(b)** Mrk 501.

Figure 4.14: *TeV power-law fit of 1ES 0229+200 (a) and Mrk 501 (b) in the 100 GeV-10 TeV interval. These two sources show opposite behaviours in the TeV regime: while 1ES 0229+200 is compatible with the previous power-law fit all along the GeV - TeV band, Mrk 501 shows curvature in the spectrum that is down-going in the hard TeV gamma-ray band.*

This different VHE gamma-ray slope above 100 GeV was then plotted in **Figure** 4.15 versus the synchrotron peak position of all the sources. The main result in this plot is the clustering of the sources in two main areas. On the right hand side, the TeV slope is positive and means that the gamma-ray spectrum is continuously increasing up to the deep TeV regime (as in **Figure** 4.14a). This implies that here only the hard-TeV EHBLs are selected. A confirmation of this interpretation is the fact that indeed we obtain all the 5 hard-TeV sources of Costamante et al. (2018), and in particular here the 1ES 0229+200 is present. On the left-hand side, there is a cluster of the majority of the sources. Here the slope is negative, meaning that the sources are already showing the descending part of the high-energy hump and the peak is likely located at few hundreds of GeV or below.

These two main clusters of sources are probably only two extreme cases: in fact, there are sources that present intermediate near flat slopes in this energy band. For example, the source H 2356-309 may represent a transitional case because it is located, considering the errors, where the slope in this energy range is on average flat. Its position in this

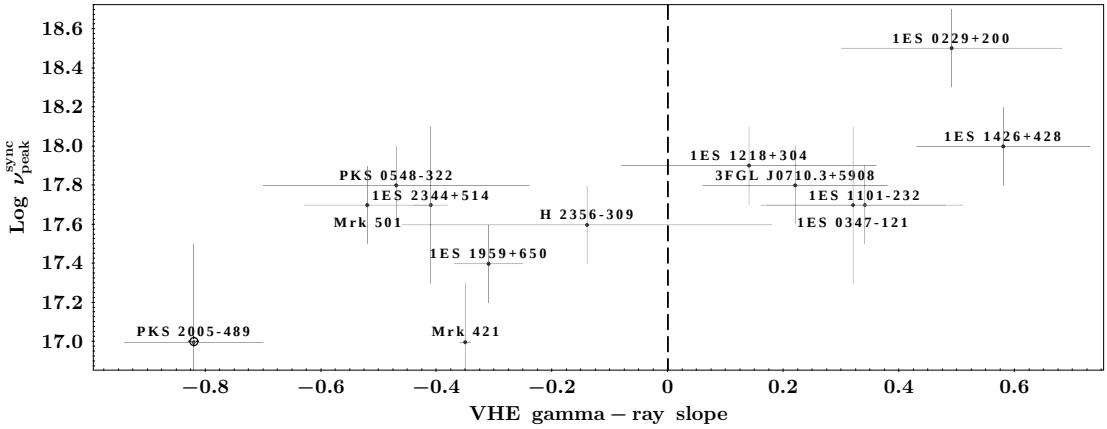

Figure 4.15: *Synchrotron peak position of the TeV gamma-ray detected sources with respect to the distribution of their slopes in the 0.1-10 TeV range.*

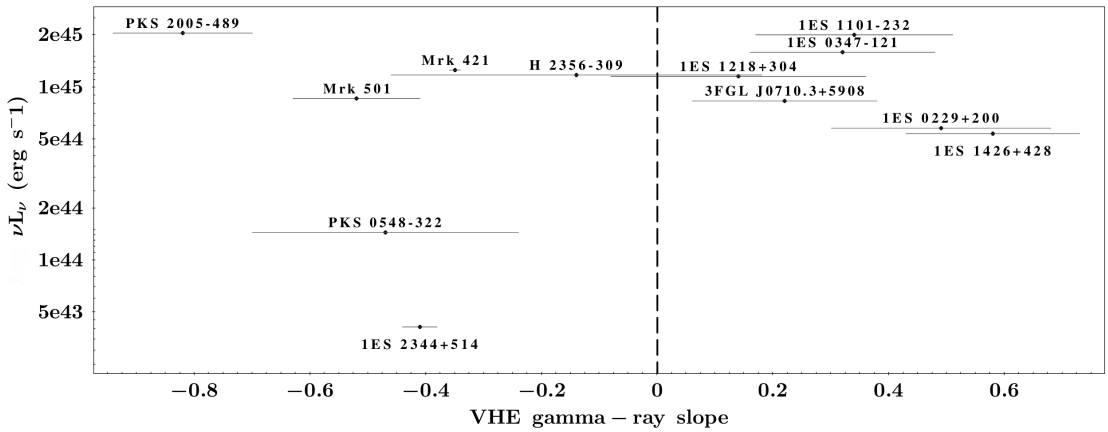

Figure 4.16: *Synchrotron peak luminosity of the TeV gamma-ray detected sources with respect to the distribution of their slopes in the 0.1-10 TeV range.*

plot suggests that the high-energy peak of this source is located in the region around few TeV, and that the source may be starting the descending part of the high-energy hump. The case of 1ES 1218+304 is probably more related to the right-hand side of this plot. Considering its average TeV spectrum harder than 2 in the majority of the recent measurements, it can be considered a hard-TeV EHBL. However, this interpretation at the moment lacks of precise and numerous TeV gamma-ray data. More observations of EHBLs in the TeV band will confirm this scenario and enrich this class of sources.

Except for H 2356-309, the objects on the right of the plot and those on the left are largely incompatible in their TeV slopes, and they support the evidence for two distinct populations of EHBLs.

Another interesting point when studying EHBLs, and in particular when comparing them to the blazar sequence, is the emitted total power with respect to their synchrotron peak frequency. This plot is presented in **Figure** 4.17 with the stacking of all the SED of the sources, and in **Figure** 4.16 as a diagnostic plot similar to **Figure** 4.15. All the sources are distributed over a tight range of synchrotron peak luminosities (especially the hard-TeV EHBLs on the right hand side) at about 10^{45} erg s^{-1}. Some sources like PKS 0548-322 and 1ES 2344-514 of the left-hand side of the plot show lower luminosity peak values.

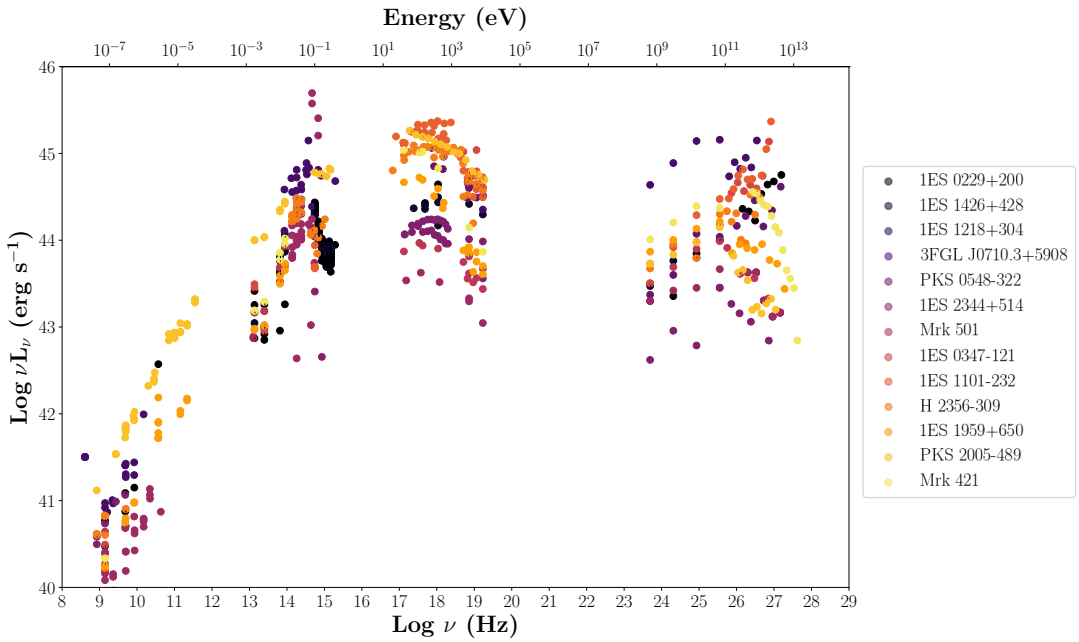

Figure 4.17: *Superimposition of the MWL SEDs of the 13 already TeV gamma-ray detected sources with publicly available TeV data. The fluxes have been converted in luminosity by considering the redshift reported in the* Swift*-BAT 105-months catalog. The plotted data are already corrected for EBL absorption with the model by Franceschini & Rodighiero (2017) to show the intrinsic spectrum of the source.*

4.3.8.3 Are EHBLs a unique population?

All these findings suggest us that EHBLs are not a homogeneous class. Considering that this sample is composed by sources that match the definition of EHBL based on the synchrotron peak location, the sample may be subdivided at least into two main sub-categories: EHBL sources peaking in the 0.1-1.0 TeV range (we will call them "HBL-like" EHBLs), and exceptional EHBLs peaking above 10 TeV (the known "hard-TeV" EHBLs).

The former seem to represent a sort of continuation of the HBL class, meaning with a high synchrotron peak above 10^{17} Hz but the high-energy peak located in a region compatible with HBL sources and with decreasing slope in the TeV gamma-ray band.

Most of these sources (like 1ES 1959+650, 1ES 2344+514, 1ES 1218+304, Mrk 501, Mrk 421) are also known to be showing moderate flux variability or even frequent flaring activity.

On the other hand, the latter show an high-energy hump peaking well above the 10 TeV band and represent the sample of hard-TeV blazars proposed also by Costamante et al. (2018). Looking also at **Figure** 4.16, these hard-TeV blazars seem to be a standalone category characterized by high total emitted power, rather stable flux, and hard TeV spectra.

Another important category that could emerge with a more detailed statistics of EHBL sources in the VHE gamma-ray regime could be represented by objects like H 2356-309. Such source, with its flat `TeV slope` value, is probably peaking at about 1 TeV and might represent a "transitional" type of EHBLs with spectral properties between the HBL-like and the hard-TeV EHBLs.

Interestingly, all these results regarding the sub-classification of EHBLs seem not to be strongly correlated with the synchrotron peak frequency in the SED.

4.3.9 TeV gamma-ray undetected sources

In our main sample of EHBLs, after having analysed the TeV-detected sources, we then studied the TeV gamma-ray undetected sources in order to guess their possible TeV detectability and their spectral properties at TeV energies. I report the list of TeV gamma-ray undetected sources in **Table** 4.4.

4.3.9.1 Importance of the cut-off at high energies

In order to investigate the VHE spectra of the TeV gamma-ray undetected sources, we performed a power-law extrapolation of the *Fermi*-LAT data obtained in a new analysis after ten years of observation. Such power-law extrapolation should resemble the second hump of the SED, and thus should show also the peak of such hump in order to be physically consistent with the expectations from the modelling of blazars. In order to mimic the second hump peak, we apply an exponential cut-off at the power-law extrapolation, following

$$\frac{dN}{dE} = N_0 \Big(\frac{E}{E_0}\Big)^{-\Gamma} \cdot \exp\Big(-\frac{E}{E_{\text{cut-off}}}\Big) ,$$

where N_0 is the normalization factor, E_0 is the pivot energy, Γ is the photon index. These parameters were estimated from the best fit of the spectral points of each target in the *Fermi*-LAT range above 1 GeV.

This formula has been applied because - under this assumption - while the power-law function describes the rising part of the high-energy hump (the hard-TeV EHBLs show power-law spectra up to the deep TeV range, as reported also in Costamante et al. 2018), the cut-off at energies above 10 TeV describes the expected peak of such high-energy emission.

Then, in order to consider also the correction for EBL absorption, each spectrum has been absorbed with the model by Franceschini & Rodighiero (2017) to show the observed spectrum of the source.

A particularly important role is played by the value of $E_{\text{cut-off}}$ we assume. The EBL absorption is higher as the energy of the emitted TeV photons increases. This implies that, assuming an higher cut-off, we produce more TeV photons. However, at the same time the interaction with the EBL of these TeV photons lowers the observed flux. This process continues up to values of $E_{\text{cut-off}}$ of some tens of GeV, when the EBL absorption becomes dominant and the observed flux is determined only by the distance of the source. A discussion about this effect is reported in Section 4.4.1.

An example of the application of a trustable $E_{\text{cut-off}}$ value can be seen in **Figure** 4.18, where we show an example of our extrapolation on 1ES 0229+200 together with the TeV data obtained by the SSDC website (Aharonian et al., 2007d). Considering in this plot $E_{\text{cut-off}} = 12$ TeV as reported in Costamante et al. (2018), as expected we see that our extrapolation matches the real TeV data (not EBL de-absorbed). Thus, the value of $E_{\text{cut-off}}$ strongly affects the TeV detectability of EHBLs. In Costamante et al. (2018), the authors show that in all the considered known TeV gamma-ray emitting EHBLs, the high-energy peak lies above 2 TeV. However, in our previous analysis with regard to the TeV gamma-ray detected sources, we have seen that some sources like H 2356-309 (and the case of PGC 2402248, reported in Section 5.1) may peak around 1 TeV. Thus, since for the TeV undetected sources we are missing this information, in our analysis we will adopt $E_{\text{cut-off}} = 1$ TeV as a conservative cut-off energy in their spectral extrapolations.

4.3.9.2 Implications of the redshift

The known redshift values of our sources are limited between 0.03 and 0.36. Since we are dealing with photons up to several TeV, in this redshift range the EBL absorption is expected to affect significantly the observability of our sources. This effect is evaluable in our figures: while the ones with redshift below 0.1 are not significantly affected by

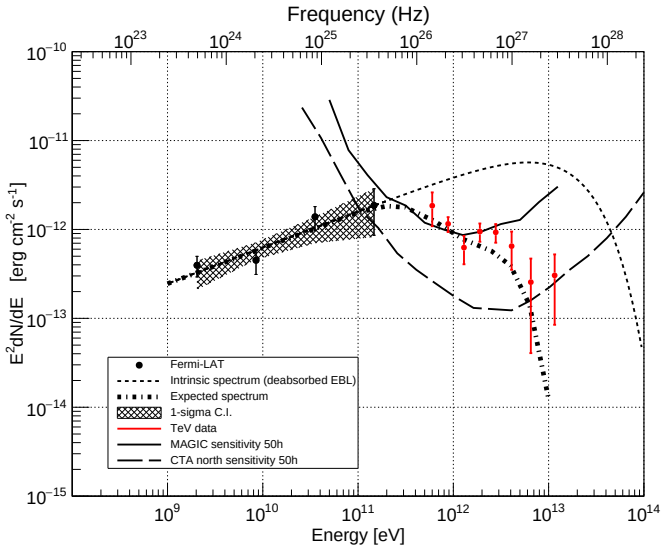

Figure 4.18: *Extrapolation at the VHE of the* Fermi*-LAT points obtained for 1ES 0229+200 with $E_{cut\text{-}off} = 12$ TeV. We report also the real TeV data (not EBL de-absorbed) of Aharonian et al. (2007d) to show that they match well our extrapolation only if considering the right value of the $E_{cut\text{-}off}$.*

EBL absorption in the HE and VHE bands up to some hundreds of GeV (see for example **Figure** B.3 in relation with other sources, considering the different spectral index and absolute flux), sources with higher redshift (z > 0.25-0.30) suffer a non negligible effect that decreases significantly the observed radiation in the same band. This EBL absorption affects the flux of these sources at Earth, and their detection for redshifts higher than about 0.5 would need a large amount of integration time from the current IACTs and, in some cases, also by the forthcoming CTA observatory.

4.3.9.3 Hint of high-energy gamma-ray curvature

In order to check the hypothesis of power-law behavior, for all sources we performed a curvature test on the *Fermi*-LAT data with a χ-square ratio test on the power-law model used for extrapolations in **Figure** B.3 in Appendix B. We report the results for both the TeV gamma-ray detected and undetected sources in **Table** 4.3 and **Table** 4.4, respectively. For 29 out of 32 sources (88%) no signs of curvature seem to be present in the second peak at high energies and the computed χ-square ratio test is of the order of 1. On the other hand, an hint of curvature is present in the *Fermi*-LAT SEDs of RBS 259, 1ES 1028+511, and RX J0324.6+3410. It is worth to note that an hint of curvature already in the *Fermi*-LAT data means that high-energy peak is probably located well below the energies of our reference 1ES 0229+200. This means that they are probably good candidates as *HBL-like* EHBLs, rather than hard-TeV EHBLs.

4.3.9.4 Resulting candidates for IACT observations

Thanks to the detailed study of each source in our sample and the extrapolation of the HE spectra to the VHE range, we were able to provide a list of good candidates for the current generation of IACT observations.

In particular, considering the combination of known redshift, hard spectra in HE gamma rays, and extrapolations to the VHE gamma-ray range, some sources like PKS 0352-686, 1RXS J225146.9-320614, BZB J1417+2543, and BZB J0244-5819, may be

#	*Swift*-BAT name	Counterpart	Log $\nu_{\rm peak}^{\rm sync}$ Hz	HE χ^2	IACT observations obs time (h)	signif.	UL 10^{-12} erg/s/cm^2
1	SWIFT J2251.8-3210	1RXS J225146.9-320614	18.3 ± 0.3	0.2			
2	SWIFT J0733.9+5156	3FGL J0733.5+5153	18.3 ± 0.2	0.1			
3	SWIFT J0244.8-5829	BZB J0244-5819	18.2 ± 0.3	0.2			
4	SWIFT J0709.3-1527	PKS 0706-15	18.0 ± 0.2	0.2			
5	SWIFT J0156.5-5303	RBS 259	18.0 ± 0.2	7.8			
6	SWIFT J0353.4-6830	PKS 0352-686	18.0 ± 0.2	0.6	15.0	0.1 σ	1.2 at 710 GeV
7	SWIFT J0122.9+3420	1ES 0120+340	17.7 ± 0.2	0.6	5.9	1.5 σ	3.2 at 283 GeV
8	SWIFT J1417.7+2539	BZB J1417+2543	17.7 ± 0.2	1.4	10.0	1.9 σ	2.9 at 327 GeV
9	SWIFT J0640.3-1286	TXS 0637-128	17.7 ± 0.2	0.1			
10	SWIFT J2246.7-5208	RBS 1895	17.6 ± 0.2	1.0			
11	SWIFT J0213.7+5147	1RXS J021417.8+514457	17.6 ± 0.2	2.4	5.1	0.3 σ	2.9 at 336 GeV
12	SWIFT J1031.5+5051	1ES 1028+511	17.5 ± 0.2	6.8	24.1	1.2 σ	1.9 at 305 GeV
13	SWIFT J0930.1+4987	1ES 0927+500	17.4 ± 0.4	0.1	11.7	-0.2 σ	2.1 at 346 GeV
14	SWIFT J0326.0-5633	1RXS J032521.8-56354	17.4 ± 0.2	1.4			

Table 4.4: *List of all the 14 currently TeV gamma-ray undetected sources of our final sample. We report here for convenience the synchrotron peak frequencies of* ***Table*** *4.2. In the* HE χ^2 *column, we show here the* Fermi-*LAT curvature test estimated with a reduced-*χ^2 *test on the ten-years* Fermi-*LAT data. The available upper-limits on the already observed sources by the VERITAS telescopes (Archambault et al., 2016) and by the H.E.S.S. telescopes (Abramowski et al., 2014a) are reported.*

good targets also for the MAGIC, the H.E.S.S., and VERITAS telescopes, likely detectable in less than 50 hours of observations.

I show in **Figure** 4.19 two promising candidates. These sources have spectra that should be detectable most probably in the energy range around few hundreds of GeV. This means that, in the case of IACTs, the observations should be performed with thresholds at maximum as high as 100-200 GeV. Thus, the IACTs should observe such sources with good weather conditions and dark nights.

Considering the results about several interesting sources of this sample, I decided to prepare a proposal of observations with the H.E.S.S. telescopes. I report in Section 5.4 details about two of the most promising candidates visible only from the southern hemisphere, namely PKS 0352-686 and 1RXS J225146.9-320614, that were proposed to be observed at VHE gamma rays by the H.E.S.S. telescope.

Finally, it is worth to note that the source PGC 2402248, discovered at TeV gamma-ray energies with the MAGIC telescopes (see Section 5.1), it is included in the final sample of this work as a TeV undetected EHBL candidate. Due to the fact that the redshift value was not established yet, we could not extrapolate its spectrum up to TeV gamma-ray energies. However, its detection with the MAGIC telescopes confirms the validity of our selection method and of its candidates.

4.3.10 Discussion and conclusions

Sub-classes of EHBLs

In this work we aimed at providing a sample of EHBL objects and studying their broad-band spectral features.

In our final sample of 32 EHBL objects, almost all the spectral properties through their MWL SEDs show comparable spectral observables. However, some discrepancies appear in their TeV gamma-ray spectra. Some indicators like the flux variability in hard X-rays and HE gamma rays, the curvature of their HE gamma-ray spectra, and the TeV

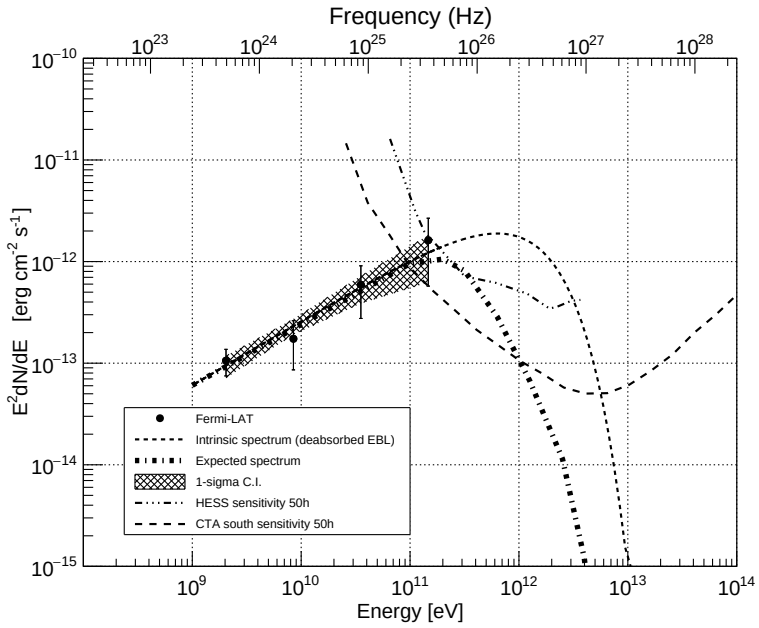

(a) 1RXS J225146.9-320614.

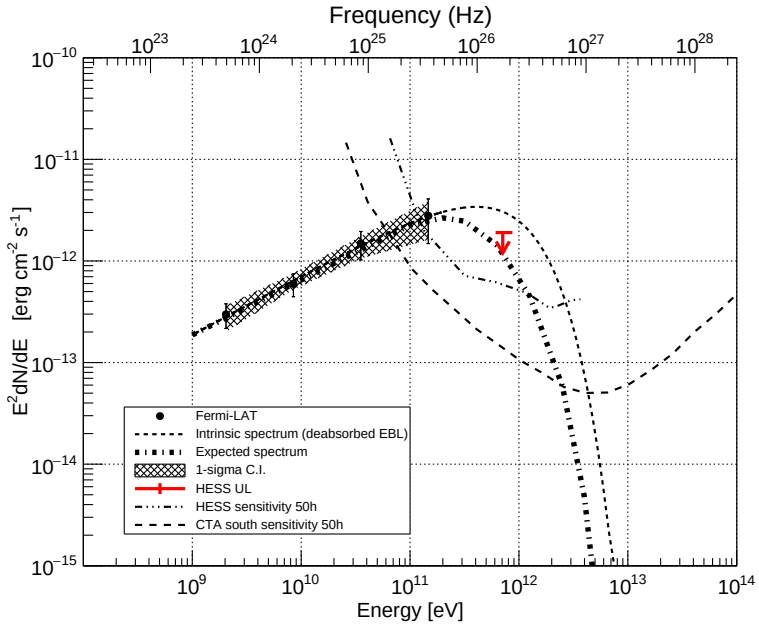

(b) PKS 0352-686.

Figure 4.19: *Power-law extrapolation above 1 GeV of the* Fermi*-LAT data after ten years of operation of two TeV gamma-ray undetected sources in our final sample in* ***Table*** *4.4. A cut-off energy of 1 TeV has been applied. The thicker dashed line is the power-law extrapolation absorbed for EBL using the model by Franceschini & Rodighiero (2017). CTA, MAGIC (Aleksić et al., 2016b), and H.E.S.S. (Holler et al., 2016) sensitivities for 50h of observations are also reported in the plots. The available upper-limits on the already observed sources by the H.E.S.S. telescopes (Abramowski et al., 2014a) are reported. Figures from our work in Foffano et al. (2019).*

detection, are not homogeneous in the sample. This fact inspired us to study the available VHE spectra of the TeV gamma-ray detected sources. We found that the sources seem to be subdivided at least into two main groups:

- *HBL-like* extreme blazars with VHE gamma-ray spectra peaking in the 0.1-1.0 TeV range;
- *hard-TeV* EHBLs peaking above about 10 TeV.

The former are probably the tail of the HBL class to sources with a high synchrotron peak above 10^{17} Hz, but with their high-energy hump peaking already in the near TeV gamma-ray band. These sources are characterized by moderate to high flux variability, and in some cases even notable flaring activity. Conversely, the latter show a rather stable flux and an IC peak energy exceeding the 10 TeV threshold.

Richer samples of sources will provide more information on weather the two sub-classes of sources form two distinct populations or a continuum transition. For example, in our sample the source H 2356-309 might represent a

- *transitional* type of EHBL

with high-energy hump peaking at few TeV and intermediate spectral features with respect to HBL-like and hard-TeV EHBLs. The case of PGC 2402248, as reported in Section 5.1, is an example of another source with similar properties and classification in the EHBL category.

The results obtained in this sample of objects confirm the features found in the literature with regards to the different high-energy peak locations of the EHBL sources and provide a first collection of such spectral differences in a unique sample of sources. Furthermore, we found that the TeV behaviour of the EHBL class seems not to be strongly correlated with both the synchrotron peak position and luminosity. All this considerations suggest us that EHBLs may not be a homogeneous class: these differences might support different approaches to the modelling of such sources, whose physical interpretation will be covered in a future work.

It is important to note that, considering that this sample is composed by sources that match the definition of EHBL based on the synchrotron peak location, all the spectral features characterizing EHBLs are generally compatible between these two categories (according to the sensitivity of our instruments), and only the TeV characterization of these sources is the key factor in this classification.

Possible bias effects

Another crucial point to mention is that, considering the difference between the two classes represented by the HBL-like and the hard-TeV EHBLs, the latter might represent only an integration of the flux over time of "low-power" HBL-like sources. Some studies in literature are going into this direction, but no conclusions have been reported so far. This might represent a bias effect in which the observed flux represents only the integration over time of high-state activity of these sources. For this reason, the study of the EHBL category with particular focus on the comparison between the low-state and the high-state activity of the HBL-like sources will be an important future step of this analysis.

1ES 1218+304: an interesting candidate

The case of the source 1ES 1218+304 represents an interesting point to be studied in detail with further future observations. This object is one of the hard-TeV sources with a spectral index of $\simeq 1.8 - 1.9$, but it is also a known variable source that has presented several flaring activities during the last years. Since some of the most recent high-state activities have not been analysed and published yet, I could not study in a deep way the possible relation of this source with the complex framework of a population of EHBLs. The point is that this source – being a hard-TeV object and assuming a spectral behaviour similar to the other objects of this class – should not present high flux variability. This

might be a key point that might provide further information on the relation between the different classes of EHBLs.

Towards future observations

The EHBLs in our list make a good sample to which TeV observational campaigns should be addressed. The combination of the shift to higher energies of the two humps and the relatively low redshift of all sources in our sample (below $z = 0.36$) makes the optical radiation by the host galaxy visible in the SEDs. For this reason, the majority of our objects (84%) shows a known redshift value, and the sources with unknown redshift are good candidates to be targeted by specific optical campaigns. Additionally, the low redshift of the sources implies that the EBL absorption of TeV gamma rays expected from their hard VHE spectra is not too severe, and the detection by the IACTs may need a reasonable exposure time.

In our EHBL list, some currently TeV gamma-ray undetected sources show particularly favourable spectral features that could make them well detectable also by the current generation of IACTs. An evolution in this field will certainly be played by the forthcoming CTA observatory, that with its improved sensitivity (almost an order of magnitude) will have a key-role in detecting new EHBLs. All these sources, both the ones already observed and those never observed by the current IACTs, are excellent targets for the CTA telescopes.

4.4 Extreme blazars and EBL interaction

EHBLs – with such a hard VHE gamma-ray spectrum as that observed in 1ES 0229+200 – are also important probes for testing models of EBL. Gamma rays with energy above tens of GeV may be absorbed along cosmological distances due to the interaction with the diffuse EBL in the intergalactic space, where electron-positron pairs are produced by γ-γ interaction (Hauser & Dwek, 2001).

Since EHBLs are expected to have their second hump peaking in the VHE gamma-ray band, where the imprint of the EBL absorption in the spectrum is more informative, the study of their spectral properties could help in the analysis of the EBL features, particularly at infrared wavelengths.

In this Section, I report the study published in Franceschini et al. (2019) to which I participated together with Alberto Franceschini, Fabrizio Tavecchio, and Elisa Prandini.

4.4.1 Constraints on the infrared EBL from Cherenkov observations

As outlined in Section 1.3.4, the most difficult region of the EBL to be measured is the wide interval from 3 to 300 μm, defined as infrared EBL (Franceschini et al., 2019). In that region, the observations are precluded by the overwhelming dominance of the infrared foreground from Galactic and interplanetary dust emission (composed by dusty particles that are illuminated by the Sun and emit thermal radiation at about 200 K).

The presence of interesting astrophysical and cosmological information in this spectral region have been confirmed by deep observations with infrared space and ground-based telescopes. Some very luminous sources located at high redshifts have been detected and identified, and are interpreted as likely tracing major episodes of the formation of galaxies, AGNs, and quasars (Franceschini et al., 2001; Blain et al., 2002; Madau & Dickinson, 2014).

The infrared telescopes are able to detect point-like sources, but cannot identify more diffuse or faint emissions. Thus, in order to measure the total infrared EBL from 3 to 300 μm, other indirect methods have to be used. One of the most promising indirect measurements of the IR EBL is through the interaction between gamma rays and IR EBL photons, following the reaction

$$\gamma_{\rm VHE} + \gamma_{\rm EBL} \rightarrow e^+ + e^- \ .$$

As a reference, the maximum cross section for the pair production between an EBL photon $\gamma_{\rm EBL}$ and a gamma-ray photon $\gamma_{\rm VHE}$ follows the relation

$$\lambda_{max} \simeq 1.24 \ E^{\gamma}_{\rm VHE} \ \ \mu m \ , \tag{4.2}$$

where $E^{\gamma}_{\rm VHE}$ is the photon energy of $\gamma_{\rm VHE}$ in TeV and λ_{max} is the wavelength of the foreground EBL photons $\gamma_{\rm EBL}$.
In **Table** 4.5 I report a typical subdivision of the infrared range in *near, mid, and far infrared*. Comparing **Table** 4.5 and Eq. 4.2, we can easily connect the gamma-ray energies corresponding to each infrared region: the interaction of photons of order few hundred GeV can study the NIR region, radiation of energy around few TeV allow to study the MIR range, and finally only photons with energies above several tens of TeV allow to investigate the FIR. In particular, the 3-300 μm range (corresponding to the MIR-FIR regions) can be investigated when photons above few TeV to several tens of TeV are emitted from the sources of interest.

This requirement strongly selects the number of sources that can contribute to this process. EHBLs, with their hard emission up to several TeV, are good candidates to study especially the MIR-FIR regions.

Spectral region	Wavelength
Near infrared (NIR)	0.7 - 5 μm
Mid infrared (MIR)	5 - 25/40 μm
Far infrared (FIR)	25/40 - 200/300 μm

Table 4.5: *Typical subdivision of the infrared energy range.*

4.4.1.1 Prospects for EHBLs

Given their relevance for the EBL constraints, we have investigated the opportunity of using EHBLs to characterize the EBL features with gamma rays with energies above ten TeV.

There is a major point that has to be considered in this discussion. The EBL absorption is an increasing function of the photon energy and of the distance of the emitting source, and this aspect represents a severe drawback in studying these sources. In general, the EHBLs are relatively faint sources when observed with the IACTs (observed flux). The absorption of TeV photons makes the EHBL difficult to be detected: the higher is their redshift, the lower is the TeV flux we can observe, and thus the detection itself of these sources can be difficult. For this reason, the most interesting EHBLs should have very low redshift and enhanced flux in this energy band.

In this Section, we study the emitted flux of EHBLs in the VHE regime. In particular, considering 1ES 0229+200 that has been detected by H.E.S.S. up to energies about 10 TeV (Aharonian et al., 2007d), its relatively high redshift of the source ($z = 0.139$) implies a fast drop-off above that energy, making it unsuitable for our analysis (see **Figure** 4.18 on page 180).

However, our analysis resulting in a sample of 32 new EHBL objects in Section 4.3 (and in Foffano et al. 2019) revealed some interesting sources with very low redshift, such as:

- 1RXS J032521.8-56354 at $z = 0.06$;
- 1RXS J021417.8+514457 at $z = 0.049$.

Since these sources have not been detected at TeV energies yet, we extrapolated in **Figure** 4.20 their HE spectra up to the TeV band. Such extrapolation has been performed by assuming a power-law formula with exponential cut-off, following Section 4.3.9.1. Under this assumption, while the power-law function describes the rising part of the high-energy hump (the hard-TeV EHBLs show power-law spectra up to the deep TeV range, as reported also in Costamante et al. 2018), the cut-off at energies above 10 TeV describes the possible peak of such high-energy emission.

Considering that the cut-off may be a very limitative parameter for the extrapolations (since we do not know where the source is peaking), we tried several values for it. In **Figure** 4.20, we assume for example three different values for cut-off at 10, 30, and 100 TeV. As the figure shows, after some 20/30 TeV the EBL interaction drives the observed spectrum and results to be the dominant factor that lowers the observed flux. This effect is visible in low-redshift objects, and it becomes worse and worse for objects located at higher redshift.

As shown here, also in the most optimistic conditions (nearby EHBL sources with strong intrinsic spectral emission), the observed spectrum above some 20/30 TeV results to be difficult to be detected in standard observing conditions also with the forthcoming CTA telescope (see Section 2.5). Thus, EHBLs are not good candidates to study the FIR at longer wavelengths, and can be used to study only up to the MIR region (e.g. Aharonian et al., 2007d).

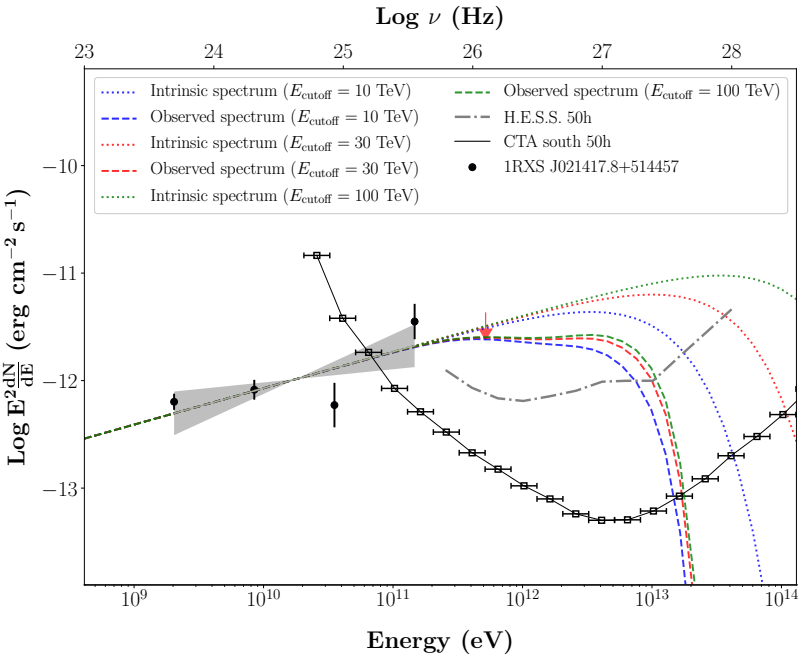

(a) 1RXS 021417.8+514457 at z=0.049.

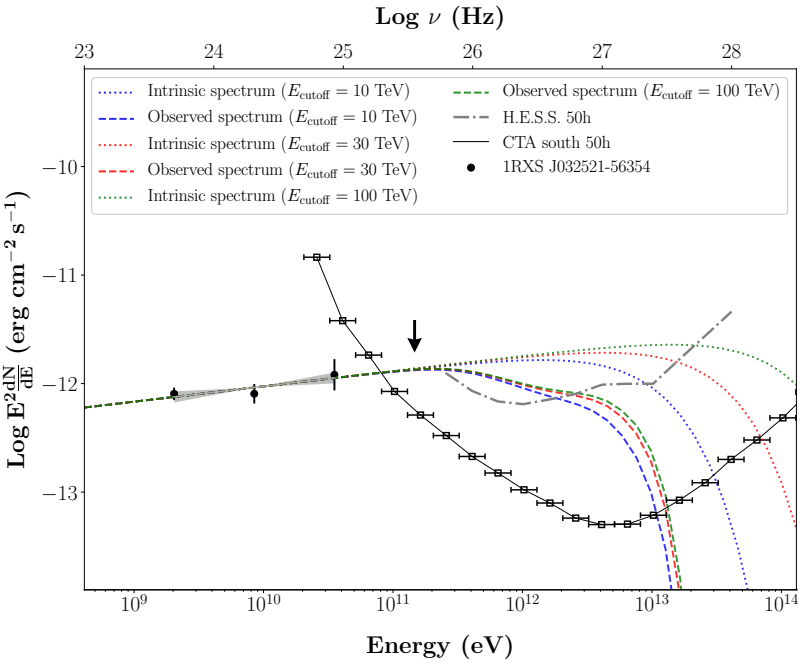

(b) 1RXS 032521.8-56354 at z=0.06.

Figure 4.20: *Extrapolation to the VHE of the spectrum of two promising EHBL objects, assuming an intrinsic power-law spectrum (dotted line) with a cut-off three different values for the cut-off at 10, 30, and 100 TeV. The short-dashed line is the EBL-absorbed spectrum with the model by Franceschini & Rodighiero (2017). Figures from my contribution to Franceschini et al. (2019).*

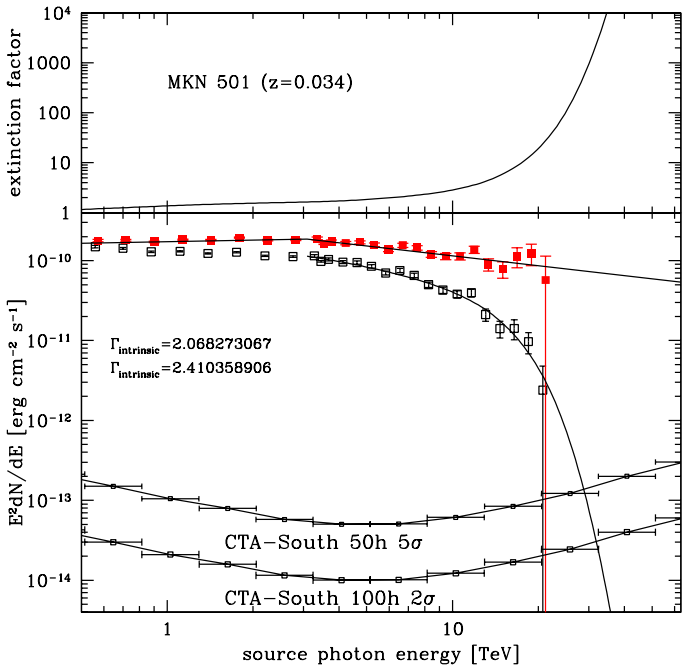

Figure 4.21: *Top panel: Photon–photon absorption correction $exp(\tau_{\gamma\gamma})$ for the source Mrk 501 at $z = 0.034$ based on the EBL model by Franceschini & Rodighiero (2017). Bottom: Observed (open black) and absorption-corrected (filled red) spectral data. Data are taken from Aharonian et al. (2001); see also Aharonian et al. (2006b). The intrinsic spectrum is fitted by a broken power-law with relatively flat photon spectral indices, as indicated in the insert. The energy-binned sensitivity limits for 50-hour 5 σ and 100-hour 2 σ of CTA South are also shown. Figure from Franceschini et al. (2019).*

4.4.1.2 Prospects for other blazars

Some information useful to constrain the EBL features above $\lambda > 10$ μm can be obtained by blazars only in the case of extremely energetic flares, like the one in **Figure** 4.21 representing a flare of Mrk 501 in 1997 (Aharonian et al., 2006b) that was detected up to 20 TeV. However, that was an historical event that has not been repeated on a timescale of thirty years, and the latest flares (for example in 2014 detected by H.E.S.S. in Abdalla et al. 2019) showed lower flux with respect that of the 1997 event. The forthcoming facilities like CTA (see Section 2.5) will improve sensibly the sensitivity at high energies, and probably it will detect flares like the one of 1997 of Mrk 501 up to 30 TeV at best. However, the strong EBL absorption at those energies kills the observed signal that could be received at Earth. Also an increased spectral coverage turns out to be very marginal, and the only solution is to look for sources located at very low distances.

Similar conclusions would apply for the other well-known low-redshift blazar, Mrk 421, in this case the situation being slightly less favourable because of its softer VHE spectrum.

In conclusion, blazars of all classes, even the closest ones in the most favourable conditions of an exceptionally excited state, cannot provide sufficiently high-energy photons to constrain the most interesting portion of the IR EBL at few tens of micrometers.

4.4.1.3 Prospects for local AGNs

From our previous analysis resulted that, independently on the source luminosities, the crucial parameter to constrain the IR EBL was the source distance. For this reason, we proposed the study of more local objects, like low-redshift radio galaxies as M87 and Centaurus A, where the deep integration in the VHE gamma-ray regime by the

forthcoming CTA telescope will provide detection of flux up to 30-50 TeV, and thus allowing us to study a wider region of the IR EBL.

Local radio galaxies

During the last years, several radio galaxies have been detected by the IACTs up to VHE gamma rays. Thanks to their relatively high number density, some of them populate the very local universe.

In order to find the more interesting ones to be further studied to constrain the EBL spectrum, we considered all such VHE sources in the TeVCat catalog[3] closer than 100 Mpc (the distance of the two closest Markarians is about 150 Mpc). Our selection ends with few potentially interesting objects, whose predicted sensitivity limits for future long observations are reported in **Figure** 4.22:

- **IC 310**

  This source is a TeV gamma-ray emitter located at very low-redshift ($z = 0.0189$). It is classified as radio galaxy, but it presents a complex morphology similar to a blazar but characterized by a kiloparsec-scale radio structure typical of radio galaxies.

  High variability both in flux and in maximum peak frequencies of the flaring events have been reported in the past. One of the main events was in November 2012, whose spectral data taken by MAGIC during the flare (Ahnen et al., 2017b) are reported in **Figure** 4.22a as blue datapoints: the spectrum is very hard with photon spectral index $\Gamma = 1.9$.

  Observations of the source in its high state by CTA might detect radiation up to 40 TeV by integrating about 50-100 hours of signal.

- **The Centaurus A core**

  This AGN is located an incredibly low distance from Earth of only 3.8 Mpc, and it is classified as a FR-I radio galaxy. It has been observed for several long campaigns by the H.E.S.S. observatory (e.g. Aharonian et al., 2009), reporting VHE gamma-ray emission. Remarkably, over a long integration lasted for about 6 years, no significant spectral or intensity variations were found. The complete data sample registered over a total observing time of about 213 hours is reported as black points in **Figure** 4.22c (H.E.S.S. Collaboration, 2018).

  The SED shows a complex structure: while most of it can be reproduced by a synchrotron self-Compton model, it presents and excess above 100 GeV.

  To simulate observations at the highest energies, we fitted and extrapolated the H.E.S.S. spectral data with a model similar to Fraija & Marinelli (2018). In this model, the complex MWL spectrum is fitted with a combination of a synchrotron self-Compton emission reproducing the whole SED from radio to gamma rays, and a hadronic component is used to fit the excess above 100 GeV. The latter would imply the acceleration of protons and production of neutral pions π^0 by interaction with ambient material or photons. The best-fit is reported in **Figure** 4.22b with a red line, including an extrapolation up to 100 TeV. The black line shows the EBL corrected spectrum.

  Thanks to the low distance, this source might be able to provide photon energies ideally up to $\sim$ 100 TeV, allowing us to constrain the IR EBL at the longest wavelengths of about $\lambda \sim 100$ μm. However, the source is faint in TeV gamma rays, and presents a soft spectrum in this energy band. CTA observations for about 50 h would measure the spectrum at 5σ only up to 10 TeV, too low to constrain the IR EBL at significative wavelengths.

[3] http://tevcat.uchicago.edu/

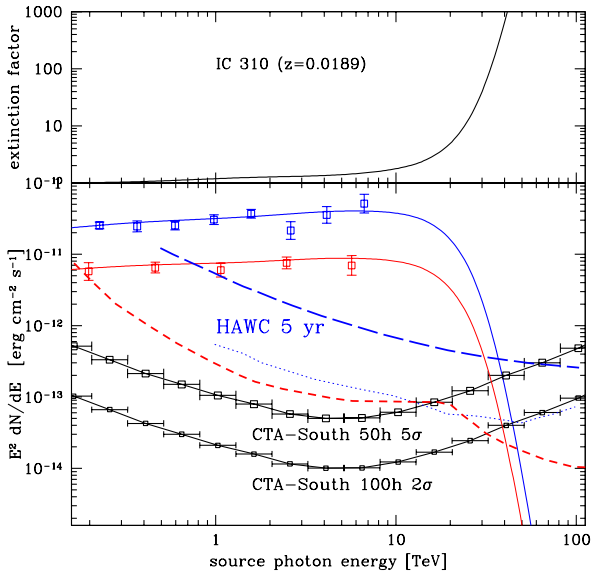

(a) *Top panel:* Photon–photon absorption correction $\exp(\tau_{\gamma\gamma})$ for the source IC 310 at $z = 0.0189$, based on the EBL model by FR2017. *Bottom:* The blue data-points and continuous line were taken during an outburst phase, the red data and continuous line during a prolonged high-state (see text). The 50-hour 5 σ and 100 hours 2 σ sensitivity limits for CTA, and the HAWC 5 years limits are shown. The blue dotted line and the red dashed one indicate the SWGO and LHAASO 5 years 5 σ limits, respectively.

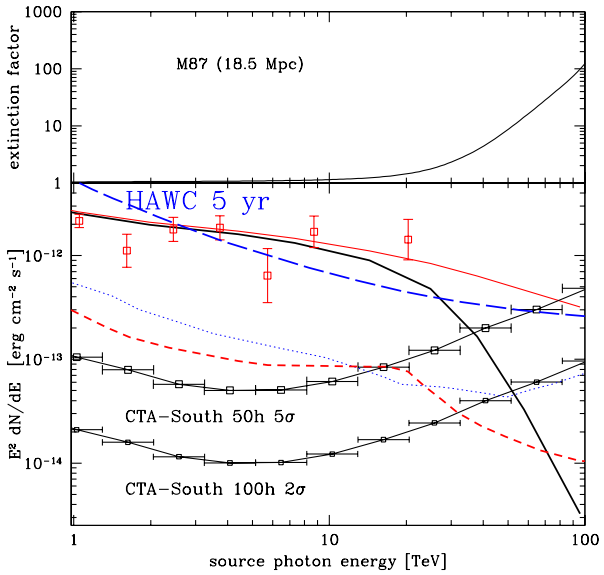

(b) Top panel: Photon-photon absorption correction $\exp(\tau_{\gamma\gamma})$ for the source M 87 at 18.5 Mpc, based on the EBL model by FR2017. *Bottom*: Observed (open red and continuous line) and absorption-corrected (black line) spectral data are reported. The 50-hour 5 σ and 100-hour 2 σ sensitivity limits for CTA, and the HAWC 5-year limit are shown. The blue dotted line and the red dashed line indicate the SWGO and LHAASO 5-year 5 σ limits, respectively.

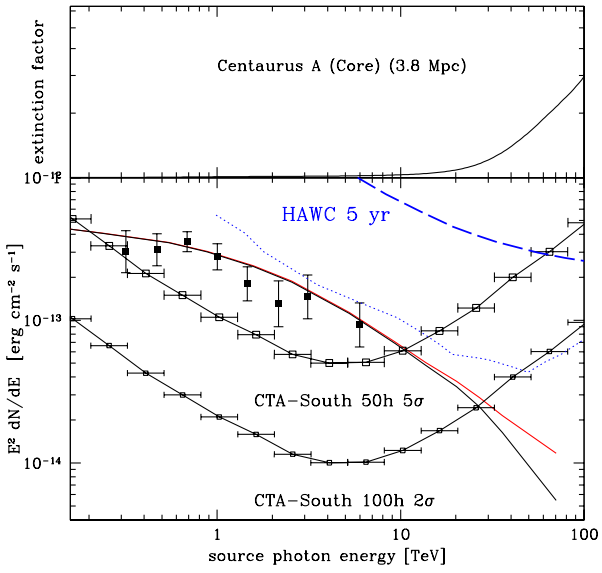

(c) *Top panel:* Photon–photon absorption correction $\exp(\tau_{\gamma\gamma})$ for the source Centaurus A at 3.8 Mpc, based on the EBL model by FR2017. *Bottom panel:* Observed (filled black squares) and model interpolated intrinsic spectrum (red line), and the absorption-corrected (black line) spectrum are reported. Two sensitivity limits for CTA are shown.

Figure 4.22: *Different extrapolations of TeV gamma-ray detected radio galaxies.*

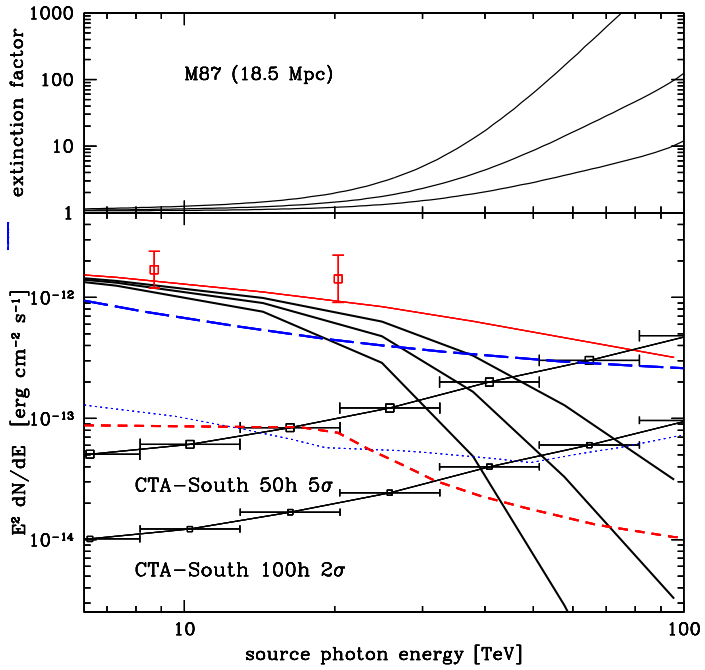

Figure 4.23: *Top panel: Photon–photon absorption correction to be applied to the M87 spectrum for three IR EBL adopted intensities. The intermediate curve corresponds to the model by Franceschini & Rodighiero (2017), and the upper and lower curves to IR EBL intensities a factor two higher and lower between 10 and 100 μm. Bottom panel: As in* ***Figure*** *4.22, for the three IR EBL models. The 50 h 5 σ and 100 h 2 σ sensitivity limits for CTA, and the HAWC and LHAASO five-year 5 σ limits are also indicated. Figure from Franceschini et al. (2019).*

- **Source M 87**

  This source is a FR-I radio-galaxy, located at a distance of 18.5 Mpc in the Virgo cluster. VHE gamma-ray emission has been detected by all major IACTs (HEGRA, HESS, VERITAS, MAGIC), showing strong flux variability. Moderate spectral changes have been registered (between $\Gamma \simeq 2.2$ and $\Gamma \simeq 2.6$) during the high-state and the low-state activity of the source, but always related to a hard spectrum in this energy band (Aharonian et al., 2006a). In **Figure** 4.22 we report the source as observed by H.E.S.S. in 2005, a high state that lasted for a few months early in that year. The combined data from H.E.S.S. and *Fermi* reveals a spectral hardening above 100 GeV. We fitted the gamma-ray spectrum with the previously presented model by Fraija & Marinelli (2018), showed with a red line in **Figure** 4.22. We then corrected this rest-frame spectrum by EBL absorption, and reported it in the figure as the black continuous line.

  Among all these candidates, this source is the most promising VHE emitter. Deep observations with the full CTA array will measure the spectrum of this source up to about 60-70 TeV, corresponding to IR EBL intensity up to the wavelengths of $\lambda \simeq 70 - 90$ μm, which is close to the expected IR EBL maximum.

4.4.1.4 Discussion and conclusions

The previous analysis reports on the possible detectability of photons with energy above some 10 TeV in order to disclose the unknown region of the EBL spectrum above $\lambda > 10$ μm. Constraining the IR EBL around its peak wavelength at ~ 100 μm therefore requires a delicate choice between the source distance, luminosity, and intrinsic spectral shape.

Sources like blazars, and including EHBLs, are generally too distant to provide enough photons to the IACTs, due to the strong EBL absorption at those high energies. Their flux is too dim to study the FIR EBL, but they are good candidates to study the MIR region of the EBL.

Only in the case of extraordinary (but yet rare) luminous flares might be possible to investigate the first part of the EBL spectrum above few $\lambda > 10$ μm. However, in general the only way to solve the problem would be to go for sources with lower redshift and located in the local Universe.

Radio galaxies seem to offer sufficiently high photon energies. Among them, M 87 appears to offer an ideal combination of properties, potentially allowing us to probe the IR EBL up to about 100 μm. This will require extensive monitoring of the source with state-of-the-art observatories. The best opportunity in this framework will be offered by CTA-South observations, particularly during the high-emission states of the sources.

4.5 Extreme blazars and IGMF estimation

Extreme blazars are also considered good astrophysical probes for constraining the intergalactic magnetic fields (IGMF).

Observational evidence confirms that inside galaxies and galaxy clusters there are non-negligible magnetic fields of the order of about 1 to 10 μG. The origin of such magnetic fields is largely unknown and represents one of the long-standing problems of astrophysics and cosmology (see e.g. Kronberg 1996; Grasso & Rubinstein 2001; Kulsrud & Zweibel 2008 for reviews). The most common interpretation of galactic magnetic fields is assumed to be due to the amplification of much weaker seed fields of extragalactic origin, whose origin is even more enigmatic.

The models that reproduce the extragalactic seed fields are divided in two main categories:

- the astrophysical models, which assume that the seed fields are generated by motions of the plasma in proto-galaxies;
- the cosmological models in which the seed fields are produced in the early Universe.

Very remarkably, the measurement of the IGMF can be performed indirectly through the study of the VHE radiation emitted by blazars. In fact, the VHE gamma-ray photons produced by these objects are supposed to interact with EBL creating e^+ - e^- pairs. When the e^+ - e^- pairs cool through IC scattering with photons of the cosmic microwave background, they emit a second generation of photons of lower energies. If the primary gamma-ray spectrum extends up to the VHE, part of this reprocessed radiation will still be above the threshold for EBL interaction, and will create further generations of e^+ - e^- pairs. Depending on the maximum energy of the primary gamma rays, this process can lead to the formation of further generations of pairs and of electromagnetic cascades, that produce radiation.

During this process, the charged particles diffuse in the intergalactic space and, if the IGMF is strong enough, it slightly deviates their trajectories off the main trajectory of the original gamma rays. This effect finally implies that the gamma-ray flux observed from these sources is not a typical point-source flux, and is actually spread over a cone depending on the intensity and direction of the intergalactic magnetic fields.

By comparing the observed flux (and its spread over the field of view around the source) and the predicted one allows us to estimate lower limits on the IGMF. It is possible to determine and constrain the presence of a cascade contribution in the spectra of distant TeV blazars by analysing *Fermi*-LAT and IACT data. All these analyses depend also on the assumption on the source flux activity (e.g. Dermer et al. 2011). In the following studies, the sources have been assumed to present a constant flux activity.

This approach has been tested by Neronov & Vovk (2010) on sources like 1ES 0229+200, 1ES 1101-232, 1ES 0347-121, and H 2356-309, and also by Tavecchio et al. (2011) for sources such as 1ES 0229+200, 1ES 0347-121, RGB J0152+017, and PKS 0548-322. Such sources, thanks to their relatively high redshift (for TeV gamma ray emitters) and their hard TeV spectra are good probes to study such extended emission.

Considering that the most stringent lower limits on the IGMF intensity are those obtained by the farthest sources, in the study by Tavecchio et al. (2011), this is provided by the source 1ES 0347–121. Thanks to the HE gamma-ray data offered by *Fermi*-LAT, the IGMF should not be lower than $B_{\rm IGMF} = 10^{-14}$ G. On the other hand, in the case of 1ES 0229+200 they get a worse lower limit of $B_{\rm IGMF} = 2 \times 10^{-15}$ G.

We have to remember, however, that these estimations depend on the primary gamma-ray spectrum. For this reason, HE and VHE gamma-ray data affect our results, and better measurements can provide more stringent constraints on the IGMF intensity. For example, I report in **Figure** 4.24 a comparison of emission models of 1ES 0229+200 including the IGMF effect with the real gamma-ray data offered by *Fermi*-LAT and IACTs, provided by Tavecchio et al. (2011). This example makes clear how the derivation of the intrinsic spectrum of the source (and hence of the physical

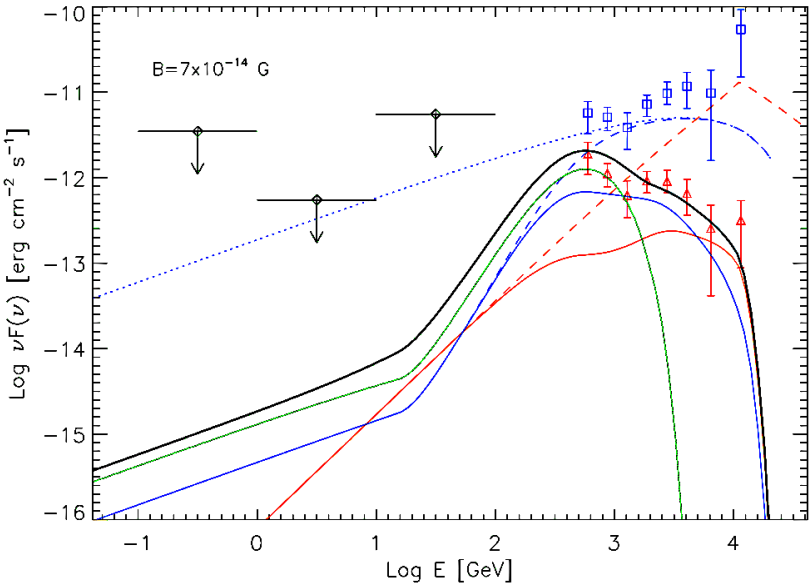

Figure 4.24: *Gamma-ray SED of 1ES 0229+200 composed of* Fermi-*LAT and H.E.S.S. data reported in Aharonian et al. (2010). It has been reproduced with a model assuming a large peak energy (10 TeV) for the primary SSC component. The consequent high level of the reprocessed emission (dominating the overall emission at TeV energies) requires a large value of the IGMF to not exceed the observational points below 5 TeV. The very large IGMF B is required not to exceed the level of the data around 200 GeV (not by the* Fermi-*LAT upper limits in black). Adapted from Tavecchio et al. (2011).*

parameters of the emitting region) and the estimate of the IGMF are connected: in order not to exceed the observational points below 5 TeV, the IGMF intensity has to respect a large value of $B_{\rm IGMF} = 7 \times 10^{-14}$ G.

The case of EHBLs if particularly interesting due to the unknown maximum frequency at which their high-energy emission is peaking. In fact, considering that the model we assume to interpret the reprocessed component strongly affects the estimates on the IGMF intensity, simple SSC models or more complex lepto-hadronic models change our conclusions. For example, in the case of the SSC model it is difficult to obtain SSC spectra peaking at 20/30 TeV. This implies that the total power that can be reprocessed into the GeV band is much lower, and for sources located at typical distance $z = 0.1 - 0.2$, the process of pairs-creation stops after the second generation of electron-positron pairs, and a real electromagnetic cascade does not develop. On the other hand, if the high-energy emission is the result of hadronic processes, the reprocessing could extend beyond the second generation of electron-position pairs, and electromagnetic cascade can develop and allow for a IGMF intensity estimation. In this case, if the primary spectrum extends well above 10 TeV with a hard slope, the total amount of reprocessed radiation increases, and a larger value of $B_{\rm IGMF}$ is required (Tavecchio et al., 2011).

In conclusion, the study of EHBLs is particularly useful for the IGMF intensity estimation. In order to improve this measurement, the observations should provide high-quality gamma-ray spectra of sources with moderate redshift, focusing the attention on constraining their peak emission.

4.6 Extreme blazars and the sensitivity of the current gamma-ray instruments

Extreme blazars are now facing with an increasing interest by the current generation of IACT collaborations.

However, considering that these instruments can only point at single sources and cannot provide wide all-sky surveys due to their pointing mode technique, the IACT collaborations require a pre-selection of the most interesting TeV-emitting EHBL candidates to be then pointed with their telescopes.

To provide such candidate list, a possibility is to perform a pre-selection through the study of the most informative instrument, whose sensitivity is located at the closest energy band to the VHE: the *Fermi*-LAT telescope in the HE gamma-ray band.

4.6.1 At the edge of *Fermi*-LAT sensitivity

In 2018, I was involved in an interesting project presented in Arsioli et al. (2018) regarding the study of sources that are difficult to be detected in HE gamma rays.

In this work, we presented for the first time the 1-100 GeV spectrum of 148 HBLs recently detected with *Fermi*-LAT as part of the named Brazil-ICRANet Gamma-ray Blazar catalogue (1BIGB catalogue, Arsioli & Chang 2017).

The 1BIGB sample was built based on the selection of 400 γ-ray objects from the 1WHSP and 2WHSP samples (Arsioli et al., 2015; Chang et al., 2017). Those candidates comprise HSPs with the brightest synchrotron peaks, but having no counterpart in previous *Fermi*-LAT catalogues – 1FGL, 2FGL and 3FGL. A likelihood analysis in the 0.3-500 GeV band, integrating over 9.3 years from August 04 2008 up to December 05 2017 of *Fermi*-LAT observations, and using the PASS8 data release, unveiled a total of 150 γ-ray new detections hint of detections.

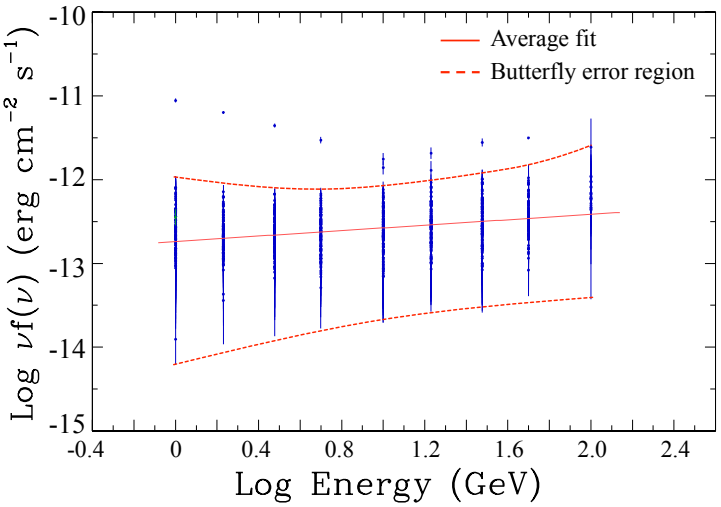

Figure 4.25: *Stacking of the 148 1BIGB SEDs in the 1-100 GeV energy band. Red dashed lines enclose the main flux density interval covered by the measured fluxes and its uncertainties, showing the main region in* log ν *vs.* log νf_ν *covered by the new gamma-ray spectrum. Red line is a average power-law fit considering all the 148 SEDs. Figure from Arsioli et al. (2018).*

In such study, a particular focus was paid to one of the main categories of blazars that can be unveiled by this process of new updated analysis of *Fermi*-LAT data, the EHBLs. Thanks to the dedicated analysis of faint sources in HE gamma rays , the 1BIGB catalogue contains information about possible new EHBLs, typically characterized by modest signal in this band.

In fact, in the 1BIGB sample there is probably a considerable amount of EHBL sources that might be particularly interesting for the forthcoming CTA telescope observations: in

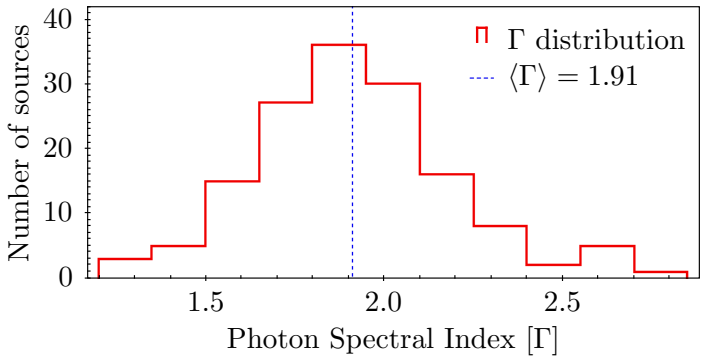

Figure 4.26: *Distribution of the photon spectral index* Γ *as derived from the broad-band analysis of 1BIGB sources, covering the 0.3-500 GeV energy range and integrating over 9.3 yrs of Fermi-LAT observations. Dashed line show the mean value for the distribution, calculated considering all 148 1BIGBs.*

the case of hard but faint HE gamma-ray spectra, these sources might be peaking in the VHE gamma-ray band, typical signature for EHBLs.

To this purpose, we present in **Figure** 4.25 the stacking of all HE gamma-ray data of the sources in the sample. When considering an individual power-law fit, the spectral index ranges between 1.26 and 2.81, with an average error on the slope of the order of 10%. The large spread in spectral slopes suggests that the objects in the catalogue do not present common spectral features in this energy band. The sample appears non-uniform, except for the faintness in flux, and there are 51 1BIGB sources ($\approx$1/3 of the sample) with $\Gamma > 2.0$.

However, by removing few sources with the highest or the lowest values of spectral slope, we fitted the clustered data points for the remaining sources. The power-law fit in **Figure** 4.25 results in an average photon spectrum slope of $\Gamma \sim 1.86$.

This fact suggests that for the selected sources the peak of the second bump in the SED is, on average, located at energies larger than those covered by our analysis. This means that the objects may peak in the VHE γ-ray regime, typical feature of EHBLs (and in particular with hard-TeV blazars), which should have a hard spectrum at high-energies.

4.6.2 EHBLs among faint *Fermi*-LAT sources

My main contribution in this work was to perform detailed power-law extrapolation of the new *Fermi*-LAT points and - depending on the location of each source in the sky - to compare such extrapolations with the sensitivity of instruments like the current IACTs and the next CTA telescopes.

The extrapolations, presented in **Figure** 4.27, show that the redshift is a very important factor that can affect sensibly the detectability of blazar candidates. This is particularly true for EHBLs with a high-energy peak exceeding TeV energies, because in this case, already at relatively small redshifts such as those considered here, the absorption strongly affects the spectrum. The effect is evident in the two sources with the highest assumed cut-off energy, namely 1BIGB J225147.5−320611 and 1BIGB J223301.0+133601, located at redshift 0.139 and 0.214. Thanks to the relatively high intrinsic emission, despite the EBL absorption severely affecting the observed flux, the extrapolations are still confidently within CTA detectability in both cases.

My analysis was performed by estimating the best cut-off energy expected for such objects. Differently from the analysis of Section 4.3.9.1 where the cut-off energy was chosen at 1 TeV as a conservative value in the case of no information about the TeV gamma-ray flux, in this case the cut-off energy of the extrapolation has been computed by considering the existing upper-limits on the observed spectrum available for most of these sources. This study confirmed that most of the sources selected in the 1BIGB sample are

detectable by the next generation of IACTs.

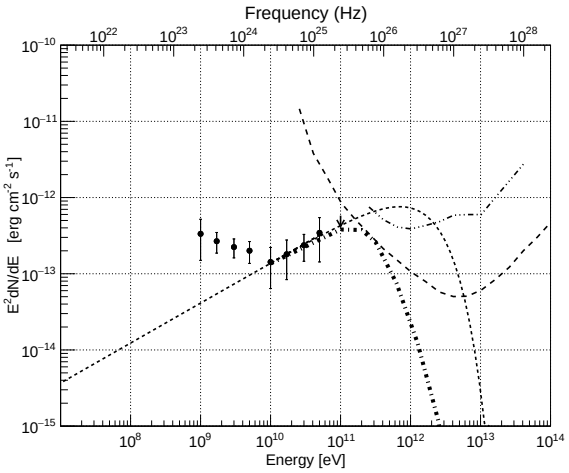

(a) 1BIGB J225147.5−320611 extrapolated with power-law and cut-off at 700 GeV.

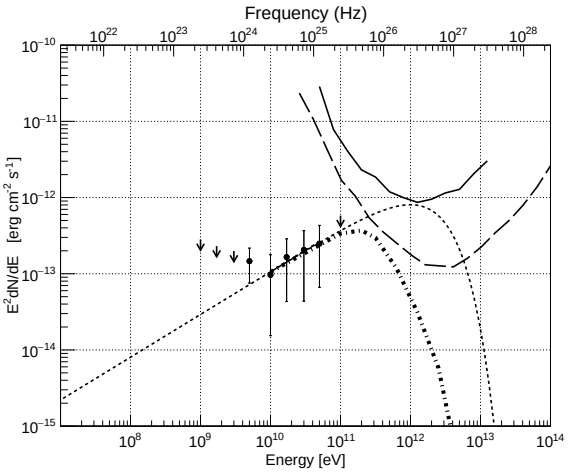

(b) 1BIGB J223301.0+133601 extrapolated with power-law and cut-off at 1 TeV.

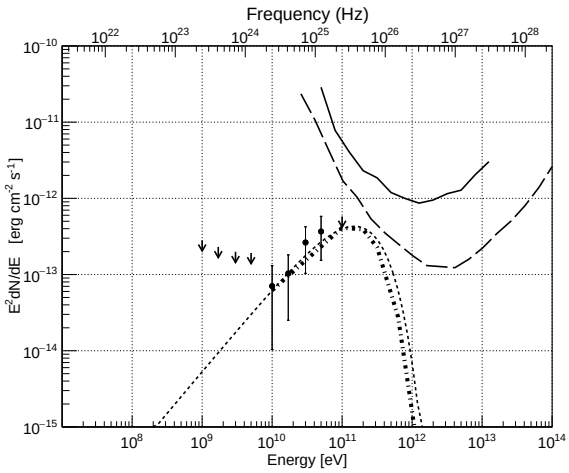

(c) 1BIGB J220155.8−170700 extrapolated with power-law and cut-off at 150 GeV.

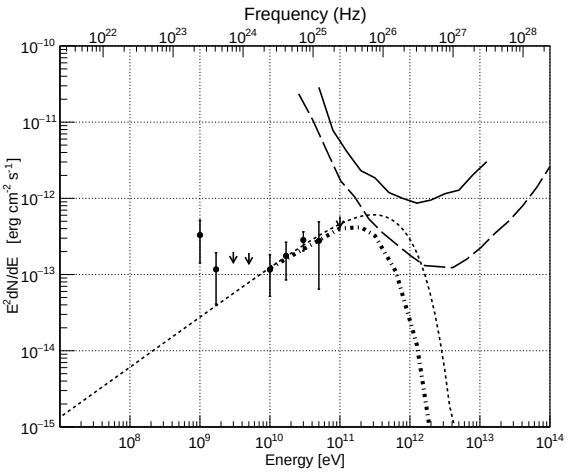

(d) 1BIGB J151041.0+333503 extrapolated with power-law and cut-off at 300 GeV.

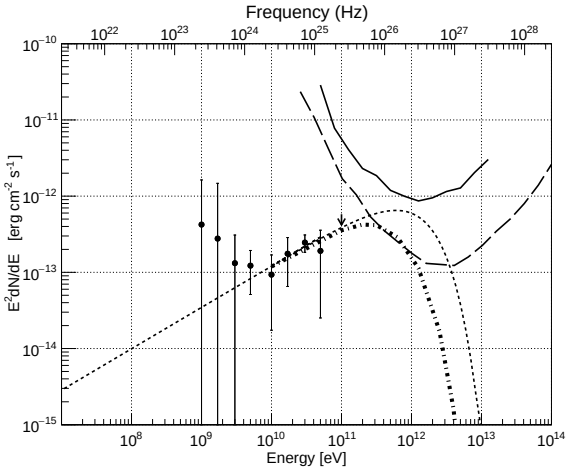

(e) 1BIGB J090802.2−095936 extrapolated with power-law and cut-off at 600 GeV.

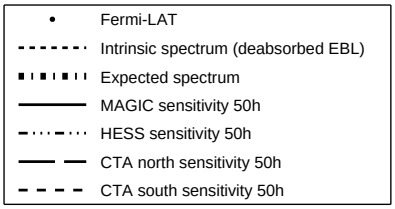

(f) Legend.

Figure 4.27: *Extrapolation of the gamma-ray spectrum of five selected sources of the 1BIGB catalogue. The intrinsic spectrum assumed is a power-law with an exponential cut-off (dashed line). The cut-off energy has been computed by considering the existing upper-limits on the observed spectrum. The resulting spectra, once corrected for EBL absorption, are presented with dashed-dotted lines. CTA, MAGIC (Aleksić et al., 2016b), and H.E.S.S. (Aharonian et al., 2006c) sensitivities for 50 h of observations are also reported in the plots.*

Chapter 5

Search for new extreme blazars in TeV gamma rays

In this Chapter, I will present my studies about the phenomenology of extreme blazars.

In the first Section, I will introduce the discovery of a new extreme blazar in the TeV gamma-ray range, named PGC 2402248. I had the opportunity to propose this blazar to be observed with the MAGIC telescopes. After a dedicated observational campaign, the source PGC 2402248 was finally detected at TeV gamma-ray energies. In this work, a detailed discussion about the variability of the source in the broad-band spectrum and its interpretation with several leptonic and hadronic models have been reported. The results about this blazar are included in the main framework concerning the possible emergence of a population of extreme blazars presented in Chapter 4.

In the second Section, I will report about my contribution to the analysis and discussion of a new set of sources that has been discovered by MAGIC in this energy band.

In the third Section, I will report the status of the observations of two extreme blazars that I proposed to the MAGIC Collaboration and are now being observed.

Finally, I will describe two sources in the southern sky that have been considered candidates for TeV gamma-ray observations and that have been proposed to the H.E.S.S. telescopes.

Source	z	Obs. time	Signif.	Integral flux > 200 GeV (10^{-13} ph cm^{-2} s^{-1})	$\Gamma_{\rm obs}$	$\Gamma_{\rm intr}$
PGC 2402248	0.065	23.38 h	6.76 σ	22.5 ± 0.60	2.41 ± 0.17	1.99 ± 0.16

Table 5.1: *Summary of the observational results obtained with the MAGIC telescopes. I report here the source name and the first redshift z estimation reported by Becerra Gonzalez et al. (2018). The information related to MAGIC observations includes the observation time, the resulting significance of the detection, and the integral flux above 200 GeV. Finally, the observed spectral index Γ_{obs} as measured by MAGIC in the VHE gamma-ray band is reported together with the intrinsic one Γ_{intr}, deabsorbed with the EBL model by Dominguez et al. (2011).*

5.1 Discovery of the extreme blazar PGC 2402248 at TeV gamma-ray energies

During my PhD activity in the MAGIC Collaboration, I had the opportunity to contribute to the *EHBL sources hunting project* - during Cycle 13$^{\rm th}$ as Co-Investigator (Co-I) and during Cycle 14$^{\rm th}$ as Principal Investigator (PI) - by proposing a list of interesting EHBLs to be further investigated at TeV gamma-ray energies. The successful acceptance of our proposals allowed us to perform observations of the proposed sources. In the ranking list of the interesting candidates to be observed within this project, the first was one of the sources I proposed, named PGC 2402248. This source was observed and finally detected with the MAGIC telescopes. The discovery of PGC 2402248 allowed me to add new statistics to the population of the transitional EHBLs, following my analysis reported in Section 4.3. This source has now been published in a paper by the MAGIC Collaboration in the MNRAS journal in which I am first corresponding author along with Josefa Becerra Gonzalez and Matteo Cerruti (MAGIC Collaboration, 2019b).

In this Section, I report a detailed report concerning the discovery of PGC 2402248 at TeV gamma-ray energies.

5.1.1 The blazar PGC 2402248

The blazar PGC 2402248 (RA=113.36125, DEC=51.89889) was selected in the 2WHSP catalog (Chang et al., 2017) under the name of 2WHSP J073326.7+515354. Some of the most interesting features of this object are:

- its high synchrotron peak frequency equal to $\nu^{\rm sync}_{\rm peak,2WHSP} = 10^{17.9}$ Hz, that makes it an EHBL object with high synchrotron maximum frequency;
- the high Figure of Merit (FoM). This parameter, used in the 2WHSP catalog in order to select the best candidates to be detected in gamma rays, is defined as the ratio between the synchrotron peak flux in the SED of the given source and that of the faintest blazar that has already been detected in TeV gamma rays in the catalog. The idea is to provide a parameter able to indicate if a certain blazar might be detectable at TeV gamma-ray energies or not.
- high X-ray and HE gamma-ray fluxes, with very good extrapolations up to the highest energies.

The source PGC 2402248 is a known HE gamma-ray source: it is associated with the *Fermi*-LAT source 3FGL J0733.5+5153 in the *Fermi*-LAT 3FGL catalog (Acero et al., 2015) and with the source 3FHL J0733.4+5152 in the *Fermi*-LAT 3FHL catalog ("Third

Catalog of Hard *Fermi*-LAT Sources", Ajello et al., 2017). The properties in the HE gamma-ray band are particularly promising thanks to the hard spectral index that, in the 3FHL catalog (that offers a better analysis at high energies), is $\Gamma_{HE} = 1.34 \pm 0.43$.

Additionally, the source PGC 2402248 results compatible with the position of the source SWIFT J0733.9+5156, that is reported also in the *Swift*-BAT 105-months catalog (Oh et al. 2018, from now on, I call it also BAT105). The distance from the nominal coordinates is about 2.39 arcmin, that is well inside the position uncertainty of 5.67 arcmin resulting in the BAT105 catalog. The association of a *Swift*-BAT counterpart confirms that the source is probably peaking with its synchrotron emission in the hard X-ray band, and this agrees with the expectations of an EHBL (as reported in Section 4.1.3).

It is worth to note that the source PGC 2402248 was included also in our selection described in Section 4.3 (source number 3 in **Table** 4.2 on page 170), and its detection confirms the robustness of the selection method of EHBLs based on their hard X-ray properties.

5.1.2 MAGIC data analysis

Observations

MAGIC observed the source PGC 2402248 for a total of 23.4 h in 2018 within the *EHBL sources hunting project* of Cycle 13$^{\text{th}}$ of observations. The observations were performed during 25 nights between January 23$^{\text{rd}}$ to April 19$^{\text{th}}$, 2018 (MJD 58141-58227), and resulted in a sample with good data quality.

The analysis of MAGIC data led to the first detection of this source in TeV gamma rays on April 19$^{\text{th}}$, 2018. Such discovery was also reported in the ATEL #11548 by Mirzoyan (2018). During the MAGIC observations, simultaneous observations were performed at different wavelengths with several other experiments like the *Swift*-XRT/UVOT, Kungliga Vetenskapsakademien Academy (KVA) system, and *Fermi*-LAT telescopes.

Additionally, during MAGIC observations some optical data were collected with the Gran Telescopio Canarias (GTC) in order to estimate the redshift of the source that was previously unknown. Such observations resulted in the first measurement of the redshift of the source PGC 2402248 that was reported as $z = 0.065$ (Becerra Gonzalez et al., 2018). This value results particularly affordable for the observation of this blazar with the IACTs thanks to the relatively low absorption effect related to the interaction with EBL photons (see Section 1.3.4).

Signal search

The MAGIC signal from the source PGC 2402248 was evaluated with the θ^2 plot (described in Section 2.4.3.7). For the claim of the detection, the θ^2 with standard cuts for the FR energy range cuts were applied. The resulting θ^2 plot for PGC 2402248 is shown in **Figure** 5.1. An excess of 95 ± 16 events in the standard fiducial signal region with $\theta^2 < 0.009$ deg^2 was found, corresponding to a significance of $6.8\,\sigma$.

Considering the fluctuation of the gamma-like events with respect to the background events in the region between 0.04 and 0.12 deg^2 we investigated whether this fluctuation was significant by comparing the θ^2 distribution for PGC 2402248 with regards to the reference Point Spread Function (PSF) obtained from a Crab Nebula data sample observed contemporaneously to PGC 2402248. Following Da Vela et al. (2018), the PSF and the θ^2 plot of PGC 2402248 were fitted with the King function, and a comparison among the parameters was performed. The PSF computed on PGC 2402248 results well consistent (χ^2/d.o.f. = 89/98) with the reference PSF of the instrument. This check confirmed that the excesses at large θ^2 values were not statistically significant, and were compatible with a random fluctuations of the background.

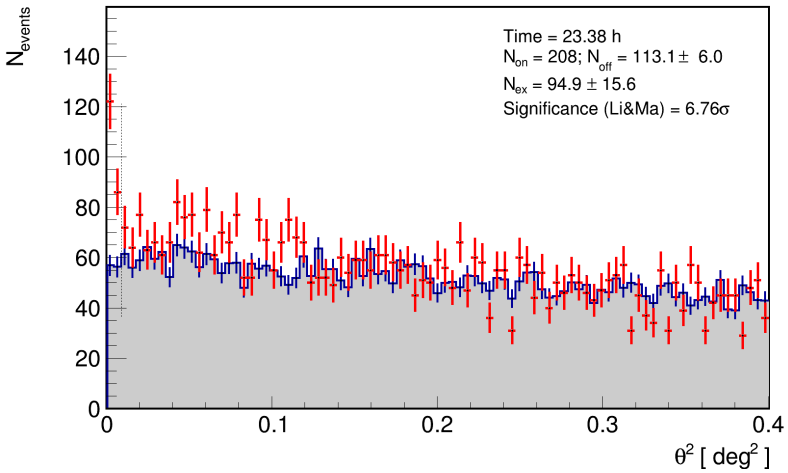

Figure 5.1: *θ^2 distribution of the PGC 2402248 events, signal (red) and background (shadowed grey), for the MAGIC observations. The vertical dashed line indicates the defined signal region to which the significance of the detection is calculated.*

Spectrum

The spectrum of the source PGC 2402248 as detected with the MAGIC telescopes is shown in **Figure** 5.2. It was reconstructed between 80 GeV and 8 TeV using the Tikhonov unfolding method (Albert et al. 2007a, and see Section 2.4.3.10), a method that allows us to consider migrations between true and reconstructed energy.
The spectrum can be described by a simple power-law model ($\chi^2/\mathrm{DOF} = 2.4/3$):

$$\frac{\mathrm{dN}}{\mathrm{dE}} = \mathrm{f}_0 \left(\frac{\mathrm{E}}{200\ \mathrm{GeV}} \right)^{-\Gamma} ,$$

where the observed photon index is $\Gamma_{\mathrm{obs}} = 2.41 \pm 0.17$, and the corresponding normalization constant $\mathrm{f}_{0,\mathrm{obs}} = (1.95 \pm 0.10) \times 10^{-11}$ ph cm^{-2} s^{-1} TeV^{-1} at the energy of 200 GeV. By applying a correction for the absorption due to the interaction with the EBL with the model by Dominguez et al. (2011), the intrinsic spectrum of the source was fitted with a power-law function ($\chi^2/\mathrm{DOF} = 2.8/3$) with a photon index $\Gamma_{\mathrm{intr}} = 1.99 \pm 0.16$ and a normalization constant $\mathrm{f}_{0,\mathrm{intr}} = (2.03 \pm 0.13) \times 10^{-11}$ ph cm^{-2} s^{-1} TeV^{-1} at the same energy of 200 GeV. A detailed discussion on the systematic uncertainties can be found in Aleksić et al. (2016b).

The SED of PGC 2402248 in the VHE gamma-ray band is particularly important to understand the role of this source within the extreme blazar subclasses, as introduced in Section 4.3. A detailed discussion is reported in Section 5.1.7.

Integral flux

The MAGIC observations were used to compute the mean integrated flux of PGC 2402248 above 200 GeV that was estimated in $\mathrm{F}(> 200\,\mathrm{GeV}) = 2.25 \pm 6.04 \cdot 10^{-13}\,\mathrm{ph\,cm^{-2}\ s^{-1}}$.

As shown in **Figure** 5.5, the source is detected above 2 σ C.L. only during four nightly observations (blue points and arrows). The rest of the observations yield upper limits. The fit of the daily light curve with a constant function yields a χ^2 /d.o.f. of 16/21, and it results in no hint of variability.

Due to the lack of strong variability detected from the nightly observations (constant fit with χ^2/DOF of 16/21) and the low photon statistics, the monthly light curve is also evaluated (black points). Also with larger time bins, the light curve does not show any hint of variability, and the average flux results in $(3.4 \pm 0.4) \times 10^{-12}$ ph cm^{-2} s^{-1} with χ^2/DOF of 1.2/4.

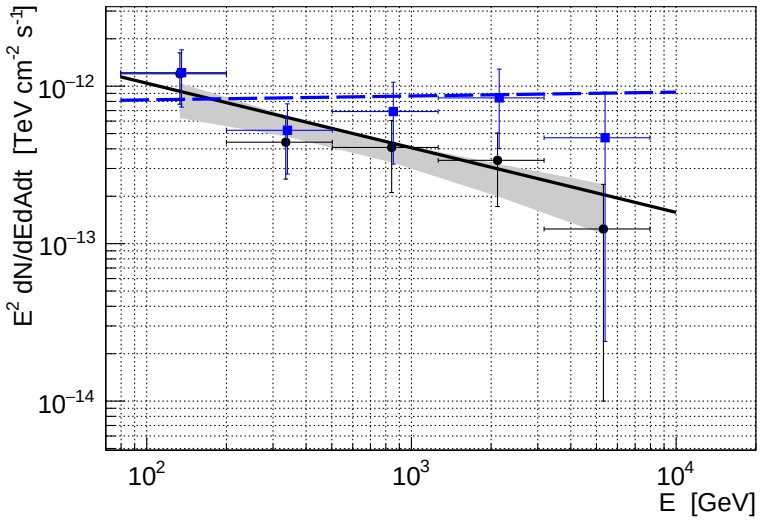

Figure 5.2: *MAGIC spectral energy points of PGC 2402248. The black markers and line represent the observed SED spectral points and fit. The points have already been deabsorbed with the model by Dominguez et al. (2011). The shaded area represent the uncertainty obtained from a forward folding method (Mizobuchi et al. 2005, and see Section 2.4.3.10).*

The emission of PGC 2402248 in this data sample is therefore compatible with a steady flux hypothesis.

5.1.3 Other wavelenghts

Thanks to the coordinated work of several other telescopes and observatories triggered by MAGIC observations, we collected a good MWL data sample. The broad-band SED of PGC 2402248, besides the MAGIC data, was complemented with data in the optical with the KVA, in optical/UV with *Swift*-UVOT, and in the X-ray band with *Swift*-XRT. Additionally, an analysis of the sample collected with *Fermi*-LAT during more than ten years of operation was performed.
The results for the different analyses are reported in Appendix C.

Fermi-LAT data analysis

With regards to the *Fermi*-LAT data, a standard analysis was performed. The analysis details have been reported in Appendix C.1 and results are collected in **Table** 5.2.

PGC 2402248 was detected with a TS=138.8, a flux of $F(0.5-300\text{GeV}) = (1.3 \pm 0.5) \times 10^{-9}$ ph cm^{-2} s^{-1} and a hard spectral index of $\Gamma = 1.73 \pm 0.11$ (compatible with the value reported in the 4FGL catalogue, $\Gamma_{4FGL} = 1.80 \pm 0.10$).

Considering that it is not possible to detect the source on daily basis, the *Fermi*-LAT light curve was computed on 2-year time bins to study the flux evolution of the source.

Swift data analysis

During the MAGIC observation campaign, simultaneous optical-UV and X-ray observations were performed with the *Swift observatory* via a Target of Opportunity request (see Section 2.2).

Eight good quality pointings were obtained between 2018, January 26$^{\text{th}}$ (MJD 58144.08) and 2018, April 29$^{\text{th}}$ (MJD 58227.92), reporting a total exposure time of ~ 2.7 h with an average of 1.2 ks per observation.

The spectra for each individual daily observation were fitted by power-law and log-parabola functions. In all cases, the log-parabola fit did not improve significantly the

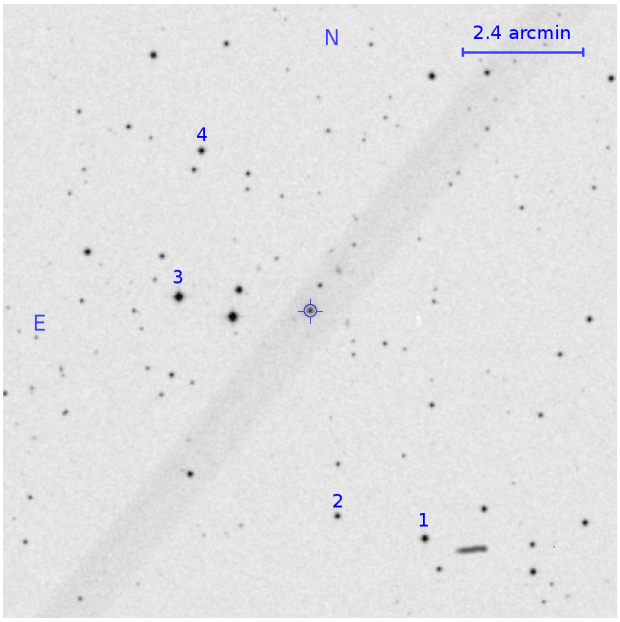

Figure 5.3: *Finding chart of PGC 2402248 for the optical photometry and host galaxy measurement.*

result (lower than 3 σ confidence level) with respect to the power-law fit. The results of this analysis are reported in **Table** C.2 together with data obtained with *Swift*-XRT since 2009. The X-ray spectrum of the source is hard, with a photon index $1.5 \leq \Gamma_X \leq 1.6$ on the data strictly simultaneous to the MAGIC campaign, but with hint of a softer spectrum in the archival data with larger uncertainty.

During the *Swift* pointings in 2018, the UVOT instrument observed PGC 2402248 in its optical (U) and UV (W1 and W2) photometric bands (Poole et al., 2008; Breeveld et al., 2010). We analysed the data, reporting the results for each individual observation in **Table** C.3.

KVA data analysis

Under the Tuorla blazar monitoring program[1], the finnish optical telescope named *Kungliga Vetenskapsakademien Academy (KVA) system* observed PGC 2402248 coordinated with the MAGIC observations since April 2018. These observations were performed in the R-band (Cousins) with a 35 cm telescope attached to the KVA. The data were analysed using the differential photometry method described by Nilsson et al. (2018). In order to perform differential photometry, the comparison stars were selected in the same field of view (reported in **Figure** 5.3).

The results of the Tuorla blazar monitoring are presented in **Table** C.4 in Appendix C. Data are corrected for Galactic extinction using values from Schlafly & Finkbeiner (2011) and the host galaxy contribution.

5.1.4 Variability

In the analysis of the simultaneous data of PGC 2402248, we verified the presence of spectral variability. At this scope, we report in **Figure** 5.5 on page 208 the multi-wavelength light curve from optical to VHE gamma rays collected during this analysis.

Each wavelength helps us in understanding the relative variability of this source during the MAGIC observations. This step is crucial in order to understand if a broad-band SED can be built with this data set.

[1] http://users.utu.fi/kani/1m

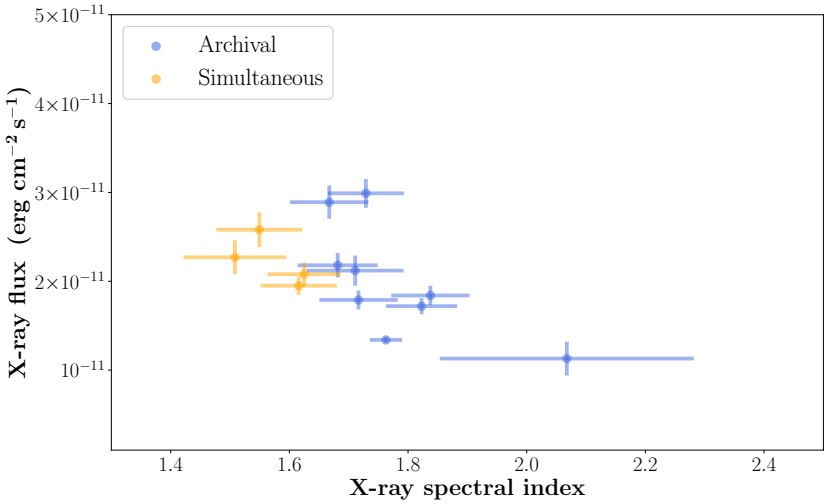

Figure 5.4: *The X-ray 0.3-10 keV integral flux as a function of the spectral index measured with Swift-XRT during the all the observations of the source (in blue) and the ones simultaneous to MAGIC observations (yellow).*

In particular, in a blazar we expect high variability in the SED regions close to the two peaks. For this reason, the X-ray observations are crucial to study the variability of the synchrotron flux and the peak of its emission. Additionally, the gamma-ray light curve from *Fermi* and MAGIC can be used to infer the flux evolution of the high-energy peak.

Synchrotron hump

In the optical band, we performed KVA observations simultaneous to the MAGIC window. The results confirm that the flux is compatible with a constant function of 3.74 ± 0.1 mJy, yielding a χ^2/DOF of 6.6/11.

In the UV data obtained with *Swift*-UVOT with filters U, W1, and W2, the statistics results pretty sparse. However, no strong flux variation was detected over the course of the MAGIC observations. The flux is compatible with a constant function of $(1.3 \pm 0.2) \times 10^{-12}$ erg cm^{-2} s^{-1} with χ^2/DOF of 0.5/3) and $(1.76 \pm 0.05) \times 10^{-12}$ erg cm^{-2} s^{-1} with χ^2/DOF of 4.6/4) for the bands W1 and U, respectively. In the case of W2 band, only one observation was performed, and thus no conclusion on variability can be derived.

We performed a comparison with historical observations from 2009, 2011, and 2014. During the MAGIC observations, the source PGC 2402248 shows compatible flux with the average historical fluxes of 2009 and 2011 in the UVOT bands. However, during January 2014, the source showed fluxes higher by a factor of about 4-5 times compared to the average flux during the MAGIC observation window in both the U and W2 bands. This means that a possible modest variability is present in these energy bands, but it was not recorded during our MWL campaign.

On the other side, the observations in X-rays performed with *Swift*-XRT during the MAGIC window (but the whole sample and not only strictly simultaneous data) present moderate variability. Looking at the X-ray light curve, we can discard a constant flux hypothesis at a 3.7 σ C.L. (χ^2/DOF of 29.6/8). Previous observations of the source carried on between 2009 and 2014 show a variable flux between 1 and 3×10^{-12} erg cm^{-2} s^{-1}.

However, when considering only strictly simultaneous XRT and MAGIC observations (MJD 58144, 58164, 58190, and 58227), the flux is compatible with a constant function and the averaged flux results in $(2.07 \pm 0.15) \times 10^{-11}$ erg cm^{-2} s^{-1} (χ^2/DOF of 6.8/4).

Another important point in the X-ray spectra study is the check for evolution in the

MJD_{start}	MJD_{stop}	Flux	Γ	TS
		10^{-10} ph cm^{-2} s^{-1}		
54682.7	55412.7	2.6 ± 1.1	1.4 ± 0.2	45.6
55412.7	56142.7	3.2 ± 1.4	1.6 ± 0.2	25.1
56142.7	56872.7	6.8 ± 2.0	1.8 ± 0.2	58.8
56872.7	57602.7	1.9 (U.L.)	1.7	0.4
57602.7	58332.7	1.6 ± 1.1	1.5 ± 0.4	15.9

Table 5.2: *Fermi-LAT light curve generated for 2-year time bin within 0.5-300 GeV energy band. In case of non significant detection (TS<4), a flux upper limit (U.L.) was estimated assuming the spectral index reported in the 4FGL catalog.*

ratio between the spectral index and the flux in this energy band. We verified the presence of a marginal "harder-when-brighter" trend in the *Swift* data, as shown in **Figure** 5.4. The data points can be fitted by a linear function (with χ^2/DOF of 1.3/13) with slope of -1.64 ± 0.62. This trend is quite typical in BL Lacs, and has been observed in several X-ray campaigns of Mrk 501 and Mrk 421 (e.g. Pian et al., 1998b; Ahnen et al., 2018). It is supposed to be correlated with the injection of freshly accelerated electrons in the blazar jet. This new population of electrons enhances the flux up to the highest energies of the synchrotron emission, and sometimes shifts its peak to higher energies.

Finally, in the *Swift*-BAT 105-months catalog the source is detected with a signal to noise ratio (SNR) of only 5.38, and no hint of variability is reported.

High-energy hump

Regarding the high-energy SED peak, we analysed the flux evolution in both *Fermi* and MAGIC data. The light curve from *Fermi*-LAT, receiving modest signal from the source, has been computed on large time bins of two years over all ten years of observations. For this reason, it cannot be plotted in **Figure** 5.5, and I report in **Table** 5.2 the flux and photon index measurements in this energy band. As shown in the latter table, probably due to the weak detection even in a two year timescale, the measured flux is affected by large error bars and is compatible with a constant flux during the first 10 years of operation of *Fermi*-LAT. This result agrees with the variability index equal to 39 reported in the *Fermi*-LAT 3FGL catalog (Acero et al., 2015). Such a value of the variability index is considered statistically consistent with a steady source, being the variability index threshold 72.44 as reported in the 3FGL catalog.

Moreover, the long-term SED measured by *Fermi*-LAT connects smoothly with the VHE gamma-ray SED observed with MAGIC as shown in **Figure** 5.6.

An important point that has to be considered is that in the HE gamma-ray band we are integrating data over long time. For this reason, we remind that the low photon statistics cannot exclude short term variability of the source and that such variability could be smoothen out on large integrations, but the stability of the light curve on the long term supports a steady flux condition of the source within the sensitivity of the instruments.

The MAGIC observations report the detection of the source during daily observations only during 4 nights, as shown in **Figure** 5.5 (blue points and arrows). Most of the data only yield to flux upper limits. However, the constant fit applied to these nightly observations confirm the lack of strong variability (constant fit with χ^2/DOF of 16/21).

For this reason, we had to compute the light curve based on wider time bins. We report in black the monthly light curve of the source. Actually, also larger time bins do not show any hint of variability, and the average flux results in $(3.4 \pm 0.4) \times 10^{-12}$ ph cm^{-2} s^{-1} with χ^2/DOF of 1.2/4.

The summary of our analysis of variability of the collected dataset implies that, when considering only the MWL data simultaneous to the MAGIC observations, no significant variability has been recorded. Therefore, we consider that during the MAGIC observation campaign the source remained in a stable flux state. Only some moderate variability has been measured by *Swift*-UVOT/XRT when comparing with historical observations, and for this reason we used all this dataset to build the MWL SED.

5.1.5 Multi-wavelength SED

Considering that we detected only moderate variability in the MWL dataset collected for PGC 2402248, we can now build the broad-band SED that is presented in **Figure** 5.6. In grey, we show the selected archival SSDC data, then in orange the KVA data, in blue the *Swift*-UVOT data, in light red the *Swift*-XRT data, in dark red the *Swift*-BAT data, in violet the *Fermi*-LAT data, and in dark green the MAGIC data. In order to account for the modest variability found with the *Swift* data, we considered only its data strictly simultaneous to MAGIC observations (MJD 58144, 58164, 58190, and 58227).

One of the main points when discussing about EHBLs is the estimation of the synchrotron peak position $\nu^{\rm sync}_{\rm peak}$, that is at the basis of the definition of EHBL. In this case, we were able to collect enough X-ray data (XRT simultaneous, BAT archival) in order to measure $\nu^{\rm sync}_{\rm peak}$. We fitted the data of the synchrotron peak with a log-parabolic function, as illustrated in **Figure** 5.7a.
The resulting new estimation leads to

$$\nu^{\rm sync}_{\rm peak} \simeq 10^{17.8\pm0.3}\ {\rm Hz},$$

with χ^2/DOF of 19/39. This value is well compatible with the estimation reported in the 2WHSP catalog (Chang et al., 2017) of $\nu^{\rm sync}_{\rm peak,2WHSP} = 10^{17.9}$ Hz, and confirms the classification of PGC 2402248 as an EHBL. Additionally, this value is fully compatible with the estimation performed in **Table** 4.2 on page 170 (source number 3), where the estimation was performed on the basis of an archival set of X-ray data.

Another point of EHBLs is that, having their synchrotron hump shifter at higher energies with respect to conventional blazars, the SED exhibits the optical radiation of the host galaxy (that helped also in the first determination of the redshift for this source, see Becerra Gonzalez et al. 2018). The combination of the simultaneous KVA and *Swift*-UVOT data allows us to build a good template for the host galaxy radiation in the optical range of the SED.

The adequate set of MAGIC and *Fermi*-LAT SED points enabled us to constrain also the frequency of high-energy peak $\nu^{\rm IC}_{\rm peak}$, reported in **Figure** 5.7b. In the HE gamma-ray band, the *Fermi*-LAT points present a hard spectral index of $\Gamma_{HE} = 1.67 \pm 0.11$. This implies that they are on the rising part of the second SED hump that finally peaks in TeV gamma rays. For this reason, given the hard gamma-ray spectrum, we fitted the intrinsic spectrum through the entire gamma-ray band with a power-law model, reporting a (χ^2/DOF of 5.2/7) and a slope of 1.87 ± 0.04. This means that the experimental points allow for a continuously increasing gamma-ray spectrum.

Alternatively, the intrinsic spectrum can be fitted also with a power-law model with exponential cut-off (χ^2/DOF of 4/8). This methods adds a degree of freedom, but it allows for an estimation of the cut-off $\nu^{\rm IC}_{\rm cutoff} 10^{27.2\pm0.2}$ Hz, and thus that the second SED hump peaks at

$$\nu^{\rm IC}_{\rm peak} = 10^{26.4\pm0.6}\ {\rm Hz}.$$

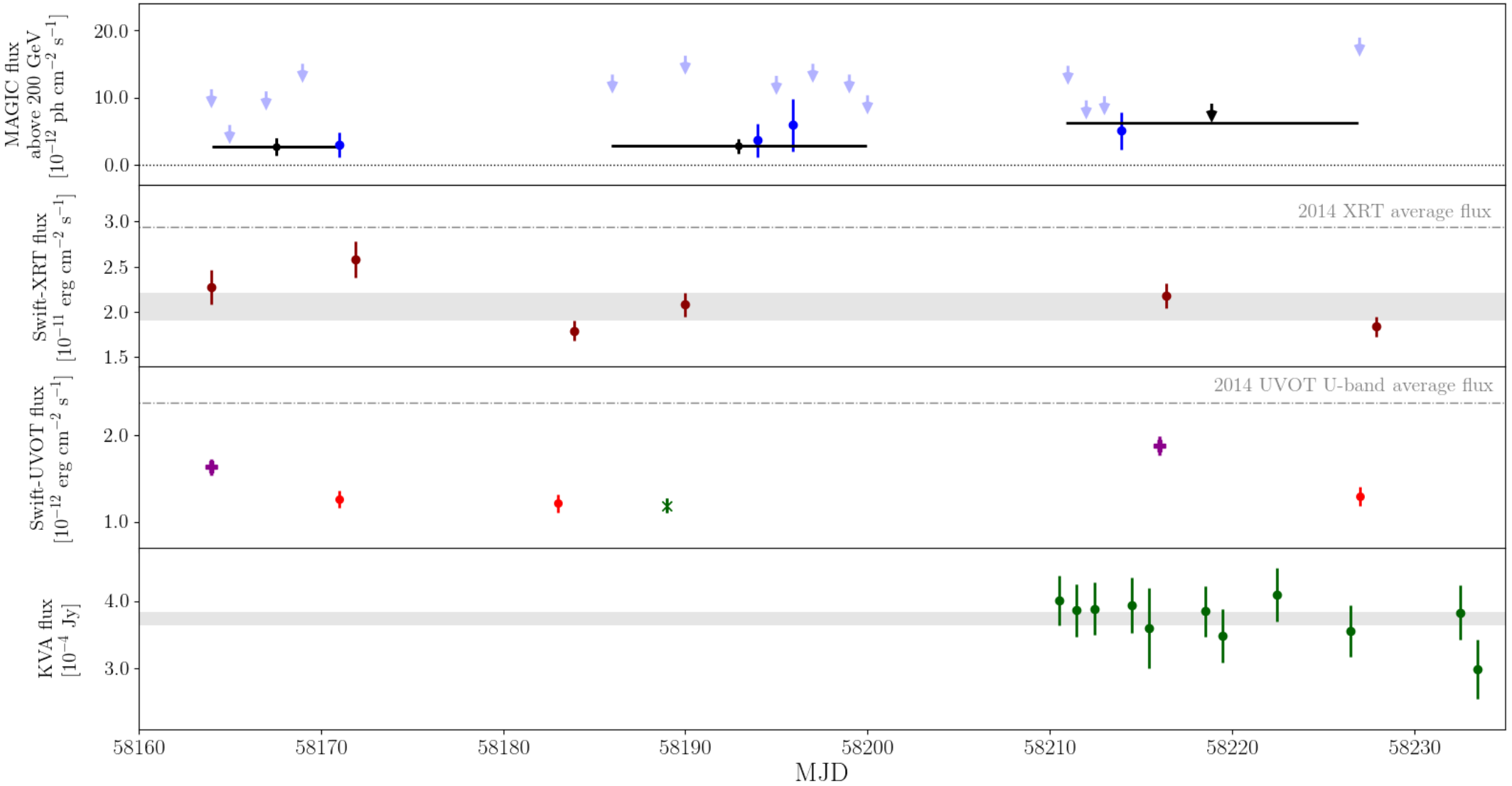

Figure 5.5: *MWL light curve of PGC 2402248 during the MAGIC observation campaign. In order from top to bottom, we present the MAGIC flux and upper-limits (arrows) above 200 GeV, the* Swift-*XRT 0.3-10 keV flux points, the* Swift-*UVOT points (in the U-band in violet, W1-band in red, and W2-band in dark green), and the KVA optical flux points (after host galaxy subtraction). For the X-ray and optical energy bands, we report in light grey the 1σ-band around the average flux. The MAGIC flux has been computed in night-wise (in blue) and monthly binning (black). For the X-ray and UV energy bands, we report in dashed light grey lines the higher average flux obtained during observations in 2014. For the X-ray and UV energy bands, we report in dashed light grey lines the highest average flux obtained during 2014 observations. Due to the low flux emitted by the source in the HE band, the light curve as observed by the Fermi-LAT can only be produced in large time bins larger than the scale shown in this figure. Figure taken from my contribution to MAGIC Collaboration (2019b).*

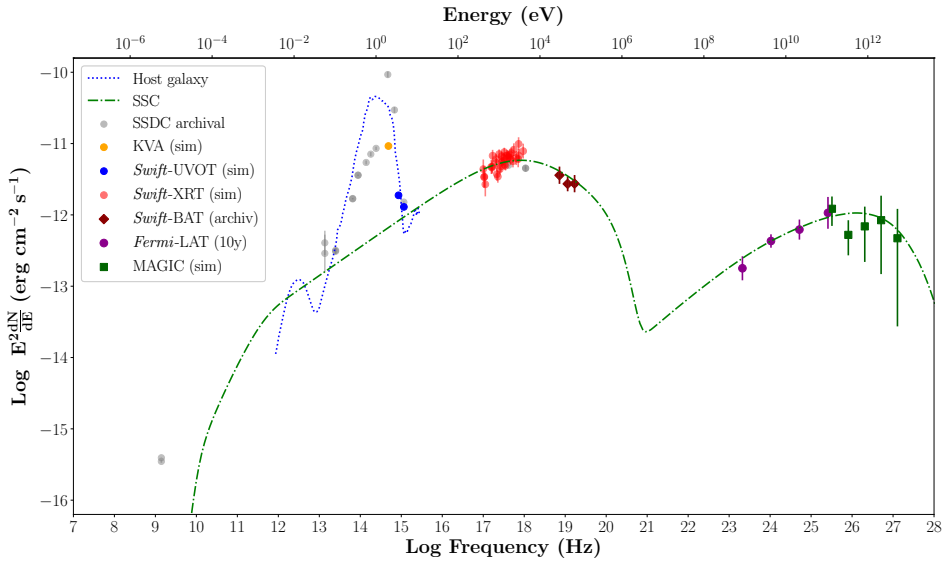

(a) SSC model.

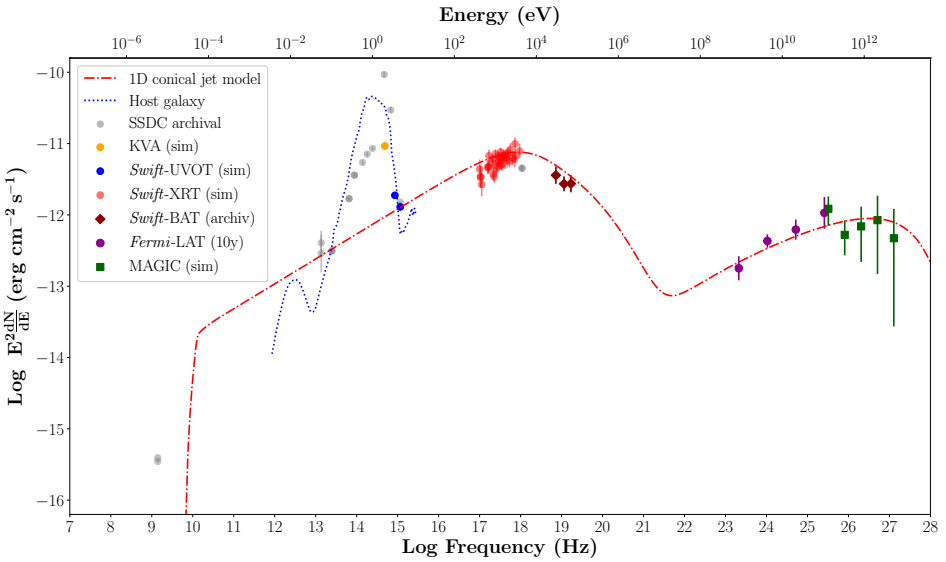

(b) 1D conical jet model.

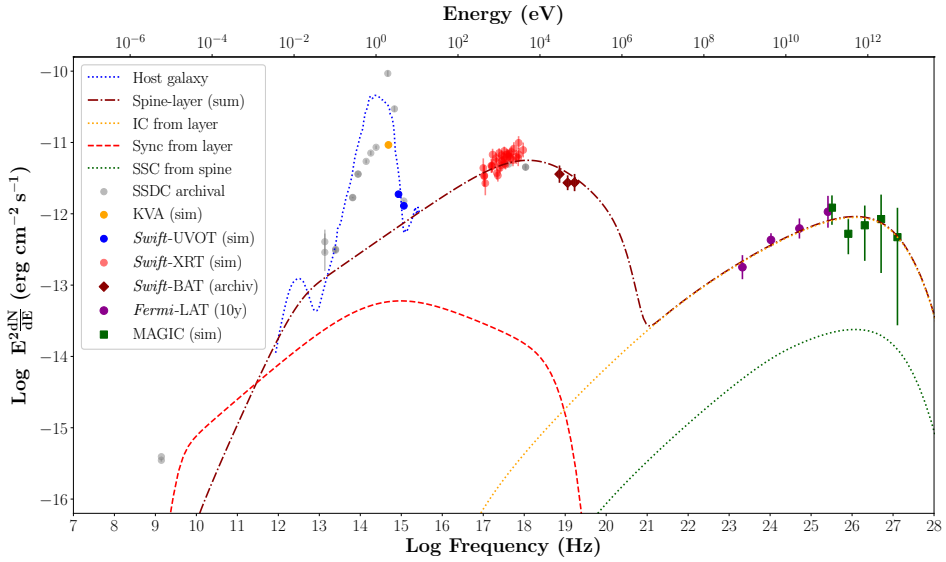

(c) Spine-layer model.

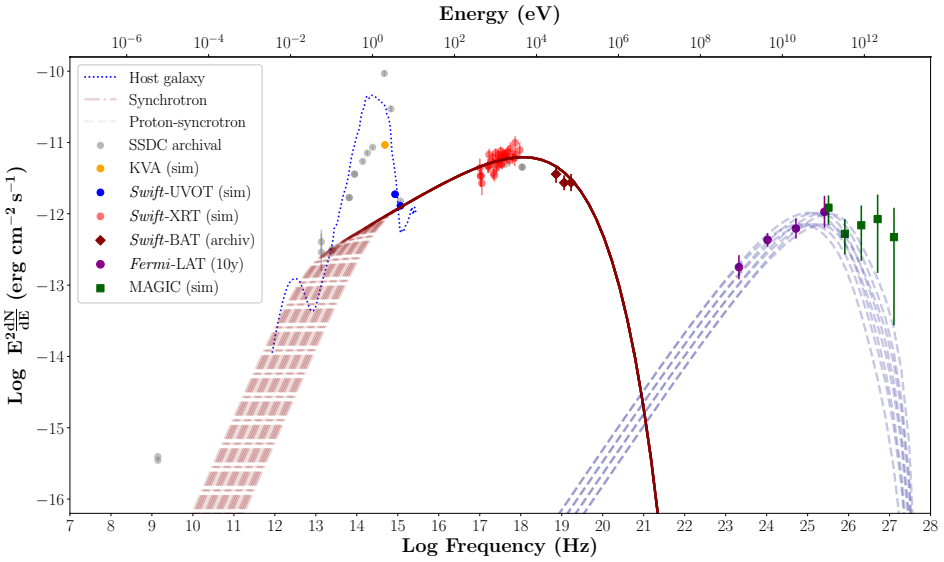

(d) Hadronic model. **Here we report all the models that survived the χ^2 cuts.**

Figure 5.6: *MWL intrinsic SED of PGC 2402248. The data have been EBL de-absorbed using the model by Dominguez et al. (2011). In grey, we report the selected archival SSDC data (First data on MJD 49078 in White et al. (1997), WISE data between MJD 55287-55479), in orange the KVA data, in light red the* Swift-*XRT data, in dark red the* Swift-*BAT data, in light green the* Fermi-*LAT data, and in dark green the MAGIC data. Arrows represent upper-limits. Figure taken from my contribution to MAGIC Collaboration (2019b).*

Model	Comp.	Γ	K	B	R	L_e	γ_{min}	γ_{br}	γ_{max}	p_1	p_2	CD	U_B/U_e
				G	cm	erg s^{-1}							
One-zone SSC		30	7.7×10^3	0.01	1×10^{16}	6.2×10^{43}	500	1×10^6	1×10^7	2.2	4.0	0.12	5×10^{-4}
1D SSC		30		0.005	2.1×10^{16}	1.2×10^{45}	20	2×10^6	2×10^7	2.3	3.5	0.12	7×10^{-5}
Spine-layer	spine	30	7.5×10^1	0.02	3×10^{16}	1.2×10^{45}	1000	9×10^5	8×10^6	2.2	4.1	0.14	0.26
	layer	5	1×10^1	0.1	3.5×10^{16}		1	1×10^4	3×10^6	2	3.5		

Table 5.3: *Resulting values of the parameters used by the three leptonic models in the paper. We report the radius of the emitting region (R_0/Γ in 1D SSC model), the bulk Lorentz factor Γ, the magnetic field B, and the electron luminosity L_e. The electron distribution is assumed to have an index of p_1 between γ_{min} and γ_{br}, and an index of p_2 up to the maximum γ_{max}. Then, we report the Compton dominance parameter CD (the ratio of νL_ν at $\varepsilon_{IC,pk}$ to that at $\varepsilon_{syn,pk}$), and the energy density ratio of the magnetic field to that of the non-thermal electron distribution (U_B/U_e) at the radius where the electron injection terminates.*

Compton dominance

Considering the previous estimations of the SED peaks, the CD parameter for PGC 2402248 (see Section 3.2.3.5) results in $CD = 0.12$. This value is compatible with the CD observed for the gamma-ray blazar sample detected by *Fermi*-LAT reported in Finke (2013). In general, the CD value becomes lower when the frequency of the synchrotron peak increases, and in EHBLs it turns to be of the order of $\sim 0.1 - 0.2$. The low value for the CD parameter is interpreted in the scenario of low or rich environment around the blazar jet. If one considers an environment around the EHBL relativistic jets poor of low-energy photon fields, such environment should not favour the high-energy emission via EC scattering due to the lack of target photons (contrary to the rich external fields in FSRQs, for instance).

5.1.6 Modelling and physical interpretation

In MAGIC Collaboration (2019b), we discussioned in detail about the application of different theoretical models on the experimental data of PGC 2402248. In particular, the MWL SED composed of simultaneous data has been tested with two one zone models, the standard SSC and the 1D conical jet model (see description respectively in Section 3.2.4.1 and Section 3.2.4.2). Considering the physical results coming out of these one zone models, we have tested the SED also with the two-zone spine-layer model (Section 3.2.4.3) and with an example of hadronic model (Section 3.2.5.1). In this Section, I report a summary of the results emerging from this analysis.

One-zone leptonic models

All the one-zone models we have tested, namely the standard SSC and the 1D conical SSC jet model, reported quite similar results. In **Table** 5.3, I summarize the resulting parameters.
Both the SSC-based models present

- a low magnetic field B, of the order of 10^{-2} G;
- a relatively large Doppler factor, of about 30;
- a high value of the minimum energy of the electrons $\gamma_{\rm min}$, above some hundreds.

These extreme resulting parameters are non-standard values within the SSC model when compared to "standard" HBLs, and turn out to be common in the modeling of EHBL objects (Tavecchio et al. 2010, but see also Cerruti et al. 2015 for a comparison of some results on the modelling of other known EHBLs). These values are generally required

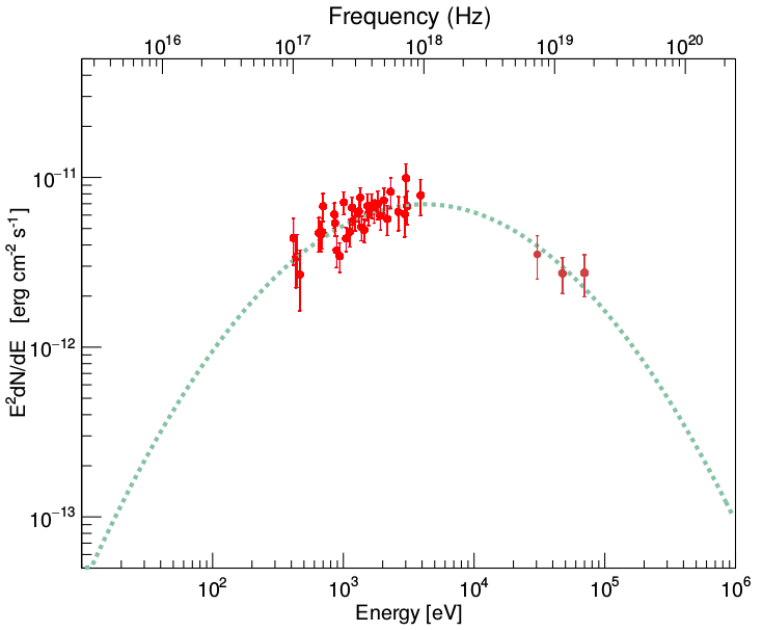

(a) Synchrotron peak of PGC 2402248. The log-parabolic model fits the simultaneous *Swift*-XRT data (violet dots) and the archival BAT105 catalog data (dark red dots).

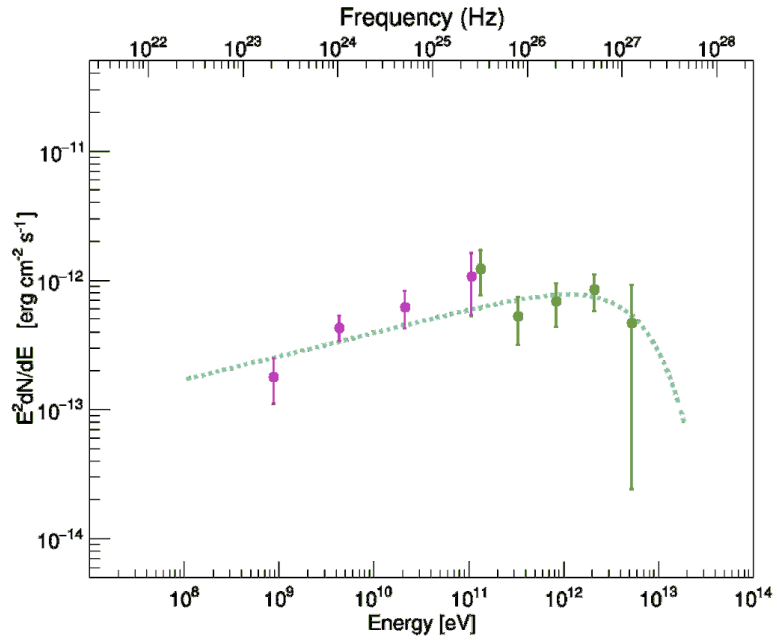

(b) High energy SED peak of PGC 2402248. The MAGIC spectral points (blue dots) are EBL-corrected using the model from Dominguez et al. (2011). The power-law model fits the *Fermi*-LAT data (red dots) and the MAGIC data applying an exponential cut-off.

Figure 5.7: *Synchrotron (a) and high-energy (b) hump of PGC 2402248. Figure taken from MAGIC Collaboration (2019b).*

by the SSC modelling in order to account for the large separation between the two SED peaks.

By applying the SSC model to the data, we can provide an estimation of the synchrotron peak located at $\nu^{\rm sync}_{\rm peak} = 10^{18}$ Hz ($\simeq$ 4.0 keV) and an high-energy peak located at $\nu^{\rm IC}_{\rm peak} = 10^{26.4}$ Hz ($\simeq$ 1.2 TeV). On the other side, the 1D conical SSC jet model provides an estimated synchrotron peak frequency $\nu^{\rm sync}_{\rm peak} = 10^{18}$ Hz ($\simeq$ 4.0 keV) and an high-energy peak frequency $\nu^{\rm IC}_{\rm peak} = 10^{26.5}$ Hz ($\simeq$ 1.25 TeV). These values are in agreement with the observational fits we reported in Section 5.1.5.

The energy equipartition issue

In this one-zone leptonic framework, both the models request for an extremely low magnetic field B of the emitting region that results in a low U_B/U_e ratio. Such low value results far from the equipartition limit that is generally supposed to apply in blazar jets. In particular, such condition is particularly interesting because we are considering a stable state of the sources, and they are not only related to temporary flaring episodes. This fact implies that, in the case of leptonic scenarios, a mechanism is expected to continuously keep the emission out of equipartition.

In order to increase the U_B/U_e ratio, one can adopt few solutions. The easiest solution is to decrease the number of radiating electrons (by lowering the electron density) and increase the minimum Lorentz factor $\gamma_{\rm min}$.

Alternatively, another solution would be to modify the size of the emitting region. A larger size of the emitting region R and smaller Doppler factors δ may be an alternative solution, but these *ad-hoc* values would not help enough in bringing the conditions much closer to equipartition, accounting only for few times closer, and not orders of magnitude (e.g. Costamante et al. 2018). Additionally, one would need to respect the values of emission region sizes that have been proposed in the literature by studying the fast variability time-scales of several blazars (see Section 3.2.3.2). Since in our case the variability is low, we apply $R \simeq 10^{16}$ cm, that is a common value used in the blazar literature.

Alternative solutions that require less extreme parameters can be found by modifying the main hypotheses behind the one-zone leptonic models. For example, the structure of the jet itself can be though as composed of several components (in the two-zone spine-layer model) or there might be contribution of hadronic processes to the emission mechanisms.

Two-zone spine-layer model

Interestingly, the structured jet proposed in the spine-layer model allows to obtain less extreme values of U_B/U_e. Additionally, the introduction of a structured jet allows for a more relaxed fit of all the physical parameters in the case of fit of EHBLs SEDs.

These results can be obtained thanks to the increased energy density of the radiation field (supposed to be dominated by the radiation provided by the layer) that the spine-layer model offers due to the relative motion of the spine and the layer. This allows us to lower the electron density needed to produce a given IC luminosity. In turn, in order to account for the reduced number of electrons, the model slightly increases the magnetic field B to keep the same synchrotron luminosity. This fact increases the previous U_B/U_e ratio and brings it closer the equipartition limit, reconciling it with the theoretical expectations.

A particularly interesting comparison can be performed between the application of the structured jet model on the hard-TeV blazars reported in Costamante et al. (2018) and other less extreme EHBLs. In fact, the spine-layer model provides a larger magnetic field. This implies that there is a more efficient cooling of the TeV electrons, and thus a softer spectrum at TeV energies. Such soft TeV spectrum cannot reconcile with the one found in the hard-TeV blazars seen in Costamante et al. (2018), and thus cannot fully explain their emission.

However, such a softer spectrum at TeV energies is observed in more standard HBL-like EHBLs, like for example PGC 2402248. This source, is an EHBL object that presents an

high-energy peak detected at few TeV, and thus the application of the spine-layer model might be still able to fit the SED (especially the high-energy hump). Therefore, the case of PGC 2402248 might be an intermediate case in the EHBL population with a high synchrotron peak but not extremely hard TeV gamma-ray spectrum. This result confirms the great difference that might be hidden in the EHBL population due to different spectral properties in the TeV gamma-ray band.

	Proton-synchrotron
δ	*30*
R [10^{16} cm]	$0.1 - 14.6$
$^{\star}\tau_{\rm obs}$ [hours]	$0.3 - 48.0$
B [G]	$1.2 - 46.8$
$^{\star}u_B$ [erg cm^{-3}]	$0.06 - 87$
$\gamma_{e,\rm min}$	200
$\gamma_{e,\rm break}$	$= \gamma_{e,\rm min}$
$\gamma_{e,\rm max}$ [10^4]	$2.5 - 15.6$
$\alpha_{e,1} = \alpha_{p,1}$	1.3
$\alpha_{e,2} = \alpha_{p,2}$	2.3
K_e [10^{-3} cm^{-3}]	$0.015 - 311$
$^{\star}u_e$ [10^{-7} erg cm^{-3}]	$0.013 - 249$
$\gamma_{p,\rm min}$	1
$\gamma_{p,\rm break}$[10^9]	$= \gamma_{p,\rm max}$
$\gamma_{p,\rm max}$[10^9]	$2.2 - 15.7$
η [10^{-5}]	$0.26 - 2.6$
$^{\star}u_p$ [10^{-4} erg cm^{-3}]	$0.009 - 10.7$
$^{\star}U_B/U_p$ [10^3]	$0.9 - 120$
$^{\star}L$ [10^{46} erg s^{-1}]	$0.2 - 10.3$

Table 5.4: *Parameters used for the hadronic model. u_B, u_e, and u_p are the energy densities of the magnetic field, the electrons, and the protons, respectively. The quantities flagged with a star (*) are derived quantities, and not model parameters.*

Proton-synchrotron model

Without asking for a more complex structure of the jet, another solution in order to interpret the SED of PGC 2402248 without using extreme physical parameters can be found considering a hadronic origin for the gamma-ray component. In this work, we applied the proton-synchrotron model (see Section 3.2.5.1).

We produced 350 hadronic models scanning the following parameter space: the radius of the emitting region $R \in [10^{14}\text{cm} - 1.46 \times 10^{17}$ cm], the proton peak synchrotron frequency $\nu_{p,syn} \in [4\times10^{24} - 4\times10^{26}]$ Hz, and the proton normalization $K_p \in [K^{\star}/3, 3K^{\star}]$, where $K^{\star}$ corresponds to the proton density such that the peak of the proton synchrotron component is at the level of the MAGIC data. A χ^2 test is used to select the solutions which correspond to a 1 σ C.L., obtaining a best χ^2/DOF of 46/42. The proton-synchrotron models which describe the SED are shown in **Figure** 5.6d and the corresponding model parameters are reported in **Table** 5.4. These models provide acceptable values for the

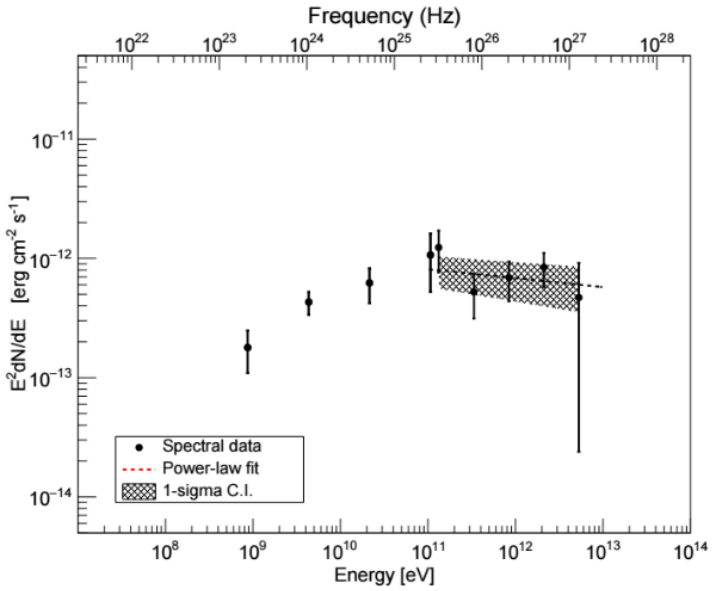

Figure 5.8: *Fit of the high-energy hump of PGC 2402248 in the 0.1-10 TeV range.*

Doppler factor (equal to 30) and the jet luminosity (which can be as low as 10^{45} erg s^{-1}, that is about 0.01 $\times$ $L_{\rm Edd}$ for a typical supermassive black hole mass of 10^9 solar masses).

An important feature of this model, however, is that the emitting region remains extremely out of energetic equipartition, being dominated by the magnetic energy density with $U_B/U_p \simeq 0.6 - 250 \times 10^3$. The synchrotron radiation spectrum is affected by a typical degeneracy that implies that the parameters of the emitting region cannot be constrained, and indeed all studied values of the size of the emitting region from $R_{min} = 10^{14}$ cm, to $R_{max} = 1.46 \times 10^{17}$ cm can provide a good solution. The same is true for the values of the magnetic field, which can take any value between 1.0 and 50.5 G. The only parameter which takes unusual values is the index of the injected particle population, $\alpha = 1.3$: such a hard injection index is not consistent with standard shock acceleration, although it can be achieved, if particles are accelerated via magnetic reconnection (Sironi & Spitkovsky, 2014). On the other hand, it is important to underline that this value does not come from the SED fitting, but is a direct consequence of the two assumptions on co-acceleration of electrons and protons, and that only synchrotron and adiabatic cooling terms shape the stationary particle distribution. Removing one of these assumptions (or both) can lead to softer particle injection indices still in agreement with the observations.

The hadronic model provides an estimated synchrotron peak located at $\nu^{\rm sync}_{\rm peak} = 10^{18}$ Hz ($\simeq 4.1$ keV) and a gamma-ray peak located at $\nu_{\rm peak} = 1 - 6\ \ 10^{25}$ Hz ($\simeq 0.25$ TeV). The latter range of values represents the result for the best-fit solutions whose χ^2 is dominated by the *Fermi*-LAT data.

5.1.7 Discussion and conclusions

Thanks to the wide coverage of data through the MWL SED, four different emission models have been applied to PGC 2402248: three leptonic and one hadronic.

The results of both the leptonic SSC models substantially agree on the extreme spectral parameters needed to fit the SED of this source. The high Doppler factor δ, the low magnetic field B of the emitting region, and the minimum Lorentz factor γ_{min}, are common resulting parameters. However, for the one-zone leptonic framework an extremely low magnetization is required, in both models being very far from equipartition.

In order to overcome this problem, two different alternative models were investigated: a two zone leptonic model (spine-layer), and a hadronic scenario.

While the one-zone leptonic models result in a ratio between the energy density of the

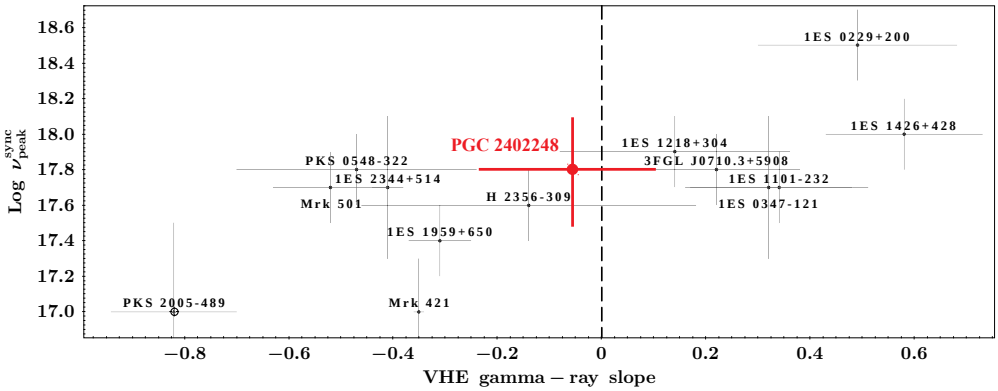

Figure 5.9: *Synchrotron peak position of the TeV gamma-ray detected sources with respect to the distribution of their slopes in the 0.1-10 TeV range. In this plot, differently from* ***Figure*** *4.15 on page 177, the source PGC 2402248 has been added.*

particles and the magnetic field (U_e/U_B) of several orders of magnitude, the spine-layer model results in a value close to the theoretical expectations. Another interesting point is that equipartition is not reachable with the spine-layer model in other EHBLs like the "hard-TeV" blazars (e.g. 1ES 0229+200), and this implies that this object might represent an exception or a transitional case in the EHBL class where the spectral properties are sufficiently extreme but the equipartition regime still holds with respect to hard-TeV blazars (compare with Costamante et al. 2018).

The relatively low luminosity of EHBLs and their modest variability make the application of hadronic modelling successful with reasonable physical parameters. Therefore, in addition to the leptonic models, we presented another model in which a hadronic contribution is considered in the emission mechanism. While the hadronic scenario is able to produce a plausible fit to the MWL SED, the opposite problem for equipartition w.r.t one-zone leptonic models is found. The parameter space able to fit the SED results in a ratio U_B/U_e far from equipartition, with the jet highly magnetized in this case.

In conclusion, while the four SED modelling scenarios provide compatible models for the MWL SED of PGC 2402248, extreme physical parameters would be required for three of them. The model that better matches with the theoretical predictions is the spine-layer scenario, which provides a reasonable framework to explain the broad-band SED. Its application is possible because, differently from the hard-TeV blazars in Costamante et al. (2018), the TeV spectrum of this source is not extremely hard as in the case of the hard-TeV blazars.

The roughly flat slope at TeV energies states the difference with respect to the hard-TeV blazars of Costamante et al. (2018), which show continuously increasing flux up to above several TeV and hard spectral index of the order of 1.5 ∼ 1.7. On the other side, this source is particularly interesting because its flat slope at TeV energies could make it a good candidate as *transitional* EHBL blazar, following the classification reported in Section 4.3.8. In fact, by fitting the spectrum in the 0.1-10 TeV range as performed in Section 4.3.8 and reported in **Figure** 5.8, we obtain a TeV slope Γ of

$$\Gamma = -0.07 \pm 0.18 \, .$$

If we recover the plot in **Figure** 4.15 on page 177 representing the synchrotron peak position of the TeV gamma-ray detected sources of that sample of sources with respect to the distribution of their slopes in the 0.1-10 TeV slope parameter there computed, we can adapt the plot as represented in **Figure** 5.9. Here the source PGC 2402248 appears clearly located exactly in the region of the plot of the *transitional* EHBLs. This conclusion is confirmed by the modest variability of the source at some wavelengths, together with the moderately high synchrotron peak and the moderately hard TeV spectrum typical of this class. Additionally, this is an example of the importance of new observations in the

TeV gamma-ray band: thanks to the discovery of this source in VHE gamma rays, we have added a new point in this plot and a new source in the EHBL category, increasing the statistics and the emergence of a population of EHBLs.

Finally, it is worth to note that the spectral properties of the source PGC 2402248 resulting from this analysis confirm the robustness of the selection method of EHBLs based on their hard X-ray properties described in Section 4.3. In that case, however, the redshift value was not available yet, and the analysis could not evaluate its TeV gamma-ray detectability by the IACTs.

5.2 MAGIC observations of extreme blazars

The MAGIC Collaboration focused particular interest on the observations concerning the search for new EHBLs emitting at TeV gamma-ray energies. This program started in 2013, and led to the discovery of several new sources on this category and to the determination of new upper-limits of some low-flux sources.

Since the beginning of my PhD activity, I had the opportunity to being involved in the EHBL project within the MAGIC Collaboration. Additionally, in Cycle 14^{th}, I was asked to contribute to the project as Principal Investigator (PI) for the related observational proposal.

In this Section, I report a summarized discussion regarding the paper on the discovery of new EHBLs by the MAGIC Collaboration just published by ApJ journal (MAGIC Collaboration, 2019a). I contributed directly to the analysis of several of these sources and to the review of the discussion.

5.2.1 Source selection

In this work, the selection of candidates was based on different selection methods. They are mainly based on phenomenological results, and are expected to provide a sample of EHBLs with favourable spectral properties to make them detectable at TeV energies. The criteria are based on properties at different wavelengths: the X-ray spectral behaviour, the soft HE gamma-ray spectral behaviour, and the X-ray-to-radio flux ratio.

1. The first criterion is based on the properties of the source in X-rays. Considering that EHBLs are defined on the basis of the synchrotron emission peaking in X-rays, an EHBL candidate with a hard spectral index like $\Gamma \leq 2$ in the soft X-ray band covered by *Swift*-XRT is favoured.

2. The second method is related to the spectral properties in HE gamma rays. Since the second hump of the SED is shifted to the highest energies, it shows relatively low luminosity in the HE gamma-ray band. For this reason, their flux in HE gamma rays might be faint or not detectable below a hundred GeV. This is, for example, the case of 1ES 0229+200. On the other hand, the detection in HE gamma rays (even if faint) of a source is useful to characterize the spectral behaviour in the whole gamma-ray band, and especially to perform extrapolations to VHE.

3. The third criterion was based on previous selections provided by Bonnoli et al. (2015) and presented in Section 4.2, where the authors propose new TeV-emitting EHBL candidates according to the high X-ray-to-radio flux ratio.

In this sample, other properties of the candidates were used in order to provide higher priority observation lists: sources located at low distance and observable at low zenith were favoured.

In the sample also the archetypal EHBL source 1ES 0229+200 was included, which has been deeply observed by MAGIC between 2013 and 2017 and was added as a reference source (Acciari et al., 2019, MAGIC Coll. in prep.).

The final list of objects observed with the MAGIC telescopes is summarized in **Table** 5.5.

Source	RA [deg]	DEC [deg]	l [deg]	b [degree]	z	N_H $\times 10^{21}$ [cm^{-2}]	log $\nu_{\rm peak}^{\rm sync}$ [Hz]
TXS 0210+515	33.57	51.75	135.74	-9.05	0.049[1]	1.440	17.3
TXS 0637-128	100.03	-12.89	223.21	-8.31	0.136[2]	2.990	17.4
BZB J0809+3455	122.41	34.93	186.48	30.35	0.082[3]	0.432	16.6
RBS 0723	131.80	11.56	215.46	30.89	0.198[3]	0.317	17.8
1ES 0927+500	142.66	49.84	168.14	45.71	0.187[3]	0.138	17.5
RBS 0921	164.03	2.87	249.28	53.28	0.236[3]	0.382	17.9
1ES 1426+428	217.14	42.70	77.48	64.90	0.129[3]	0.113	18.1
1ES 2037+521	309.85	52.33	89.69	6.55	0.053[1]	4.360	N.A.
RGB J2042+244	310.53	24.45	67.77	-10.80	0.104[4]	1.010	17.5
RGB J2313+147	348.49	14.74	90.5	-41.91	0.163[5]	0.514	17.7
1ES 0229+200	38.20	20.29	152.94	-36.61	0.140[1]	0.792	18.5

Table 5.5: *Sample of EHBLs observed with MAGIC from 2010 to 2017. Columns from left to right: source name, equatorial (RA and DEC) and J2000 Galactic coordinates (l and b), redshift (z), equivalent Galactic hydrogen column density reported by Kalberla et al. (2005), and synchrotron peak frequency* log ν_{peak}^{sync} *reported by Chang et al. (2017). 1ES 0229+200 reported in the last line is the prototype of EHBL sources and is considered in our work as reference source.*

5.2.2 MAGIC observations and results

A summary of the results about observations with the MAGIC telescopes are reported in **Table** 5.6. More than 262 h of good quality data were collected and analysed with observations started from 2010. The data were collected both under dark time and under good quality moon time, with respectively low and higher threshold for the analyses.

In the following sections, I will report a short description of the sources and a summary of the analyses I contributed to.

5.2.2.1 1ES 0229+200

One of the main targets that MAGIC observed is the source 1ES 0229+200, the archetypal EHBL. A dense monitoring of the source on the long-term was performed during more than five years of observations between 2013 and 2018, reporting a total good quality data of more than 117 h. During a so long exposure time, the MAGIC telescopes were upgraded both in the hardware and in the software. For this reason, the analysis of this source was particularly complex due to the quantity of data and different analysis periods (and thus different RFs) that have been used.
In particular, the data analysis has been divided into five different analysis periods:

- year 2013: ST.03.03 Monte Carlos;
- year 2014: ST.03.05 Monte Carlos;
- year 2015: ST.03.06 Monte Carlos;
- year 2016: ST.03.07 Monte Carlos;
- year 2017: ST.03.07 Monte Carlos.

Additionally, for some of these periods the data were separated depending on the moon level under which the observations were performed. While the standard dark observations were present in all the previous analysis periods, during some periods also non-standard observations performed under moon light were performed (see Section 2.4.3.12).

Signal search

Once collected all the data, I computed the signal estimation thanks to the `odie` program. Though, since the signal was collected during several analysis periods, we had to collect all the `odie` results on the individual analysis periods, and then merge all of them through a particular configuration in the `odie` program that allows the stacking of different outputs of the same program.

Finally, our analysis results in the stacked θ^2 plot reported in Figure 5.13a that shows the θ^2 distribution of the events. We found an excess of about 325 events in the fiducial signal region with $\theta^2 < 0.009$ deg^2, corresponding to a significance of $8.96\,\sigma$.

Although the second SED peak lies in the TeV gamma-ray range, its overall luminosity is low, following the blazar sequence, and therefore it does not reach a very high significance despite the long exposures.

Spectrum and integral flux

The spectrum of the source 1ES 0229+200 observed by the MAGIC telescopes was reconstructed between 0.1 and 10 TeV. It was reconstructed using the Tikhonov unfolding method (Albert et al., 2007a) and it can be described by a simple power-law model (χ^2/d.o.f. = 2.4/3) with formula:

$$\frac{dN}{dE} = f_0 \left(\frac{E}{E_0}\right)^{-\Gamma} , \tag{5.1}$$

Source	Obs. periods	Time [h]	Significance [σ]	$E_{\rm th}$ [GeV]	$\mathrm{Flux}_{\geq E_{\rm th}}$ $\times 10^{-12}[\mathrm{cm}^{-2}\mathrm{s}^{-1}]$	$\mathrm{L}_{\geq 200\mathrm{GeV}}$ $\times 10^{43}[\mathrm{erg\,s}^{-1}]$	VHE?
TXS 0210+515	2015, 2016, 2017	28.6	5.9	200	1.6 ± 0.5	0.6 ± 0.2	Y
TXS 0637-128	2017	12.8	1.7	300	$<8.9^{\star}$	<50.9	N
BZB J0809+3455	2015	21.8	0.4	150	$<3.7^{\star}$	<3.0	N
RBS 0723	2013, 2014	45.3	5.4	200	2.6 ± 0.5	24.8 ± 4.8	Y
1ES 0927+500	2012, 2013	26.2	1.2	150	$<5.1^{\star}$	<24.2	N
RBS 0921	2016	13.9	-0.4	150	$<8.6^{\star}$	<68.5	N
1ES 1426+428	2010	6.51	2.1	200	$<9.3^{\dagger}$	<27.7	N
	2012	8.7	6.0	200	6.1 ± 1.1	18.4 ± 3.4	Y
	2013	5.9	1.8	200	$<5.1^{\dagger}$	<14.2	N
1ES 2037+521	2016	28.1	7.5	300	1.8 ± 0.4	1.3 ± 0.3	Y
RGB J2042+244	2015	52.5	3.7	200	1.9 ± 0.5	3.4 ± 0.8	H
RGB J2313+147	2015	11.5	-0.9	200	$<1.5^{\star}$	<7.0	N
1ES 0229+200	2013–2017	117.5	9.0	200	2.1 ± 0.3	7.6 ± 1.1	Y

Table 5.6: *Results of the signal search and integral flux analysis of the MAGIC data for the ten EHBLs considered in this study. The results for 1ES 0229+200 are also reported for comparison, bottom row. Columns from left to right: source name, year(s) of observation, effective exposure time after quality cuts, significance of the signal in σ, assumed energy threshold for integral flux calculation, flux measured above the energy threshold, VHE gamma-ray luminosity over 200 GeV, and the source detection status at VHE gamma rays (Y: detected, N: not detected, and H: hint of signal). In case of non-detection (see text for details), an integral-flux upper limit is reported instead, assuming a simple power-law spectrum of spectral index Γ (see Equation 5.2 and the text for further details).*

where the spectral index Γ is $\Gamma_{\rm observed} = 2.6 \pm 0.1$, and the normalization constant $f_0 = 3.4 \pm 0.4 \cdot 10^{-12}$ ph cm^{-2} s^{-1} TeV^{-1} at $E_0 = 521\ GeV$.

Correcting for the absorption due to the interaction with the EBL according to the model by Dominguez et al. (2011), we obtain a power-law fit with spectral index of $\Gamma_{\rm intrinsic} = 1.8 \pm 0.1$.

Finally, the mean integrated flux above 200 GeV has been estimated in $F(> 200\,{\rm GeV}) = 3.58 \pm 0.37 \cdot 10^{-12}\,{\rm ph\,cm^{-2}\,s^{-1}}$.

5.2.2.2 TXS 0210+515

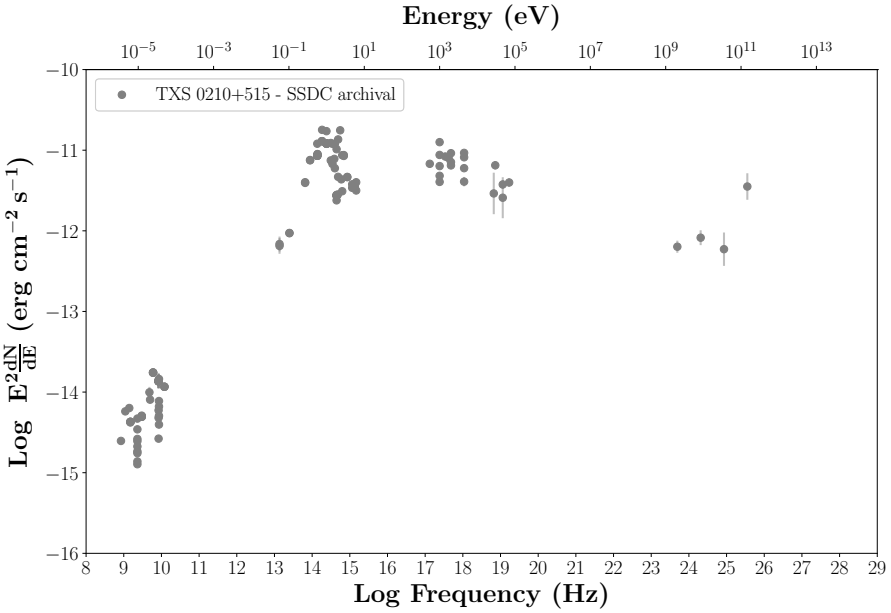

Figure 5.10: *MWL SED of TXS 0210-515 as collected from archival data of SSDC.* Fermi-*LAT data taken from my ten-years analysis.*

TXS 0210+515 is a very interesting target that has been observed and recently detected by the MAGIC Collaboration (PI: Shimpei Tsujimoto and Elisa Prandini).

This source has been selected from the *Fermi*-LAT 2FHL catalog and the ROMA-BZB catalog (Massaro et al., 2015) as a hard spectrum source at X-rays and HE gamma rays.

The SED of TXS 0210+515, reported in **Figure** 5.10, shows a synchrotron peak energy above 1 keV, making it a good EHBL candidate. The high-energy peak goes above several hundreds GeV. The *Fermi*-LAT 2FHL catalog shows a spectral index of this source of 1.9 ± 0.5 at E>100 GeV. This hard spectral index at high-energy gamma rays suggests a possibly hard-TeV nature of this source.

Thanks to the detection at TeV gamma rays obtained in the previous cycle, this source will be proposed for deep observations in the next cycles of the MAGIC telescopes.

Observations

Also this analysis was performed with several MC periods:

- year 2015: ST.03.06 Monte Carlos;
- years 2016 and 2017: ST.03.07 Monte Carlos.

Additionally, some of these periods were separated depending on the moon level under which the observations were performed. While the standard dark observations were present

in all the previous analysis periods, during some periods also non-standard observations performed during the moon light were given to this source (see Section 2.4.3.12).

Signal search

Once collected all the data, we computed the signal estimation thanks to the `odie` program. Also in this case we had to perform a stacking of the `odie` results on all the individual analysis period.

Finally, our analysis results in the stacked θ^2 plot reported in **Figure** 5.13b that shows the θ^2 distribution of the events. After 28.65 h of observations, we found an excess of about 92 events in the fiducial signal region with $\theta^2 < 0.009$ deg^2, corresponding to a significance of 5.96 σ.

Spectrum and integral flux

The spectrum of the source TXS 0210+515 observed by the MAGIC telescopes was reconstructed in the VHE gamma-ray range using the Tikhonov unfolding method (Albert et al., 2007a) and it can be described by a simple power-law model with formula Eq. 5.1 where the spectral index Γ is $\Gamma_{\text{observed}} = 1.9 \pm 0.3$, and the normalization constant $f_0 = 1.65 \pm 0.54 \cdot 10^{-12}$ ph cm^{-2} s^{-1} TeV^{-1} at $E_0 = 972\ GeV$.

Correcting for the absorption due to the interaction with the EBL according to the model by Dominguez et al. (2011), we obtain a power-law fit with spectral index of $\Gamma_{\text{intrinsic}} = 1.6 \pm 0.7$.

Finally, mean integrated flux above 200 GeV has been estimated in $F(> 200\,\text{GeV}) = 1.65 \pm 0.54 \cdot 10^{-12}$ ph cm^{-2} s^{-1}.

5.2.2.3 RGB J2042+244

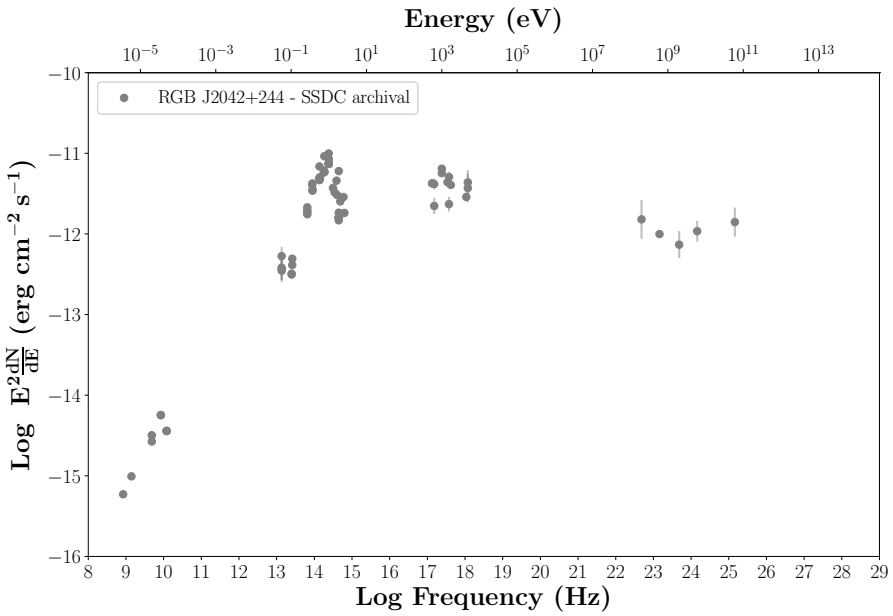

Figure 5.11: *MWL SED of RGB J2042+244 as collected from archival data of SSDC.* Fermi-*LAT data taken from the 3FGL catalog.*

The source RGB J2042+244, also named 1RXS J204206.3+242655, is an interesting target that was observed with the MAGIC telescopes (PI: Francesco Borracci and Elisa Prandini).

The archival MWL SED in **Figure** 5.11 suggests a synchrotron peak above 10^{17} Hz, making it a good candidate as EHBL and a candidate VHE gamma ray emitter thanks to the hard spectrum in gamma rays.

Observations and signal search

The source RGB J2042+244 was observed with the MAGIC telescopes for 52.51 h during 2015 (RF ST.03.06). Once collected all the data, we had the opportunity to compute the signal estimation thanks to the `odie` program. Also in this case we had to perform a stacking of the `odie` results on all the individual analysis period.

Finally, our analysis results in the θ^2 plot reported in **Figure** 5.13c that shows the θ^2 distribution of the events.

The overall signal search with `odie` reported only 3.7 σ in the FR range, and thus only an hint of detection can be claimed. Thanks to the `flute` macro, we computed the flux above 150 GeV, as $\mathrm{F}(> 150\,\mathrm{GeV}) = 1.91 \pm 0.46 \cdot 10^{-12}\,\mathrm{ph\,cm^{-2}\,s^{-1}}$.

5.2.2.4 BZB J0809+3455

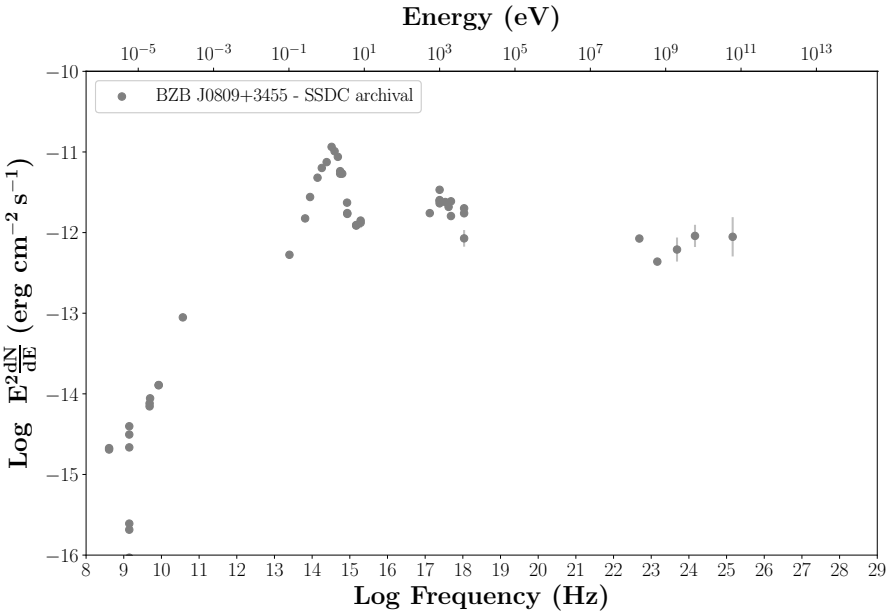

Figure 5.12: *MWL SED of BZB J0809+3455 as collected from archival data of SSDC.* Fermi-*LAT data taken from the 3FGL catalog.*

The source BZB J0809+3455 (PI: Antonio Stamerra) is a blazar with redshift $z = 0.086$ and it was observed with the MAGIC telescopes for 21.76 h during 2015 (RF ST.03.06).

The archival MWL SED in **Figure** 5.12 suggests a synchrotron peak above 10^{17} Hz, making it a good candidate as EHBL and a candidate VHE gamma ray emitter thanks to the hard spectrum in gamma rays.

Signal search and flux upper limit

Once collected all the data, we computed the signal estimation thanks to the `odie` program. Finally, we the overall signal search with `odie` reported only 0.4 sigma in the FR range, and thus no hint of signal has been detected.

The upper limit on the flux above 150 GeV was estimated with the `flute` executable, and resulted in $F(> 150\,\mathrm{GeV}) = 3.66 \cdot 10^{-12}\,\mathrm{ph\,cm^{-2}\,s^{-1}}$, assuming a power-law spectrum with index $\Gamma = 2$.

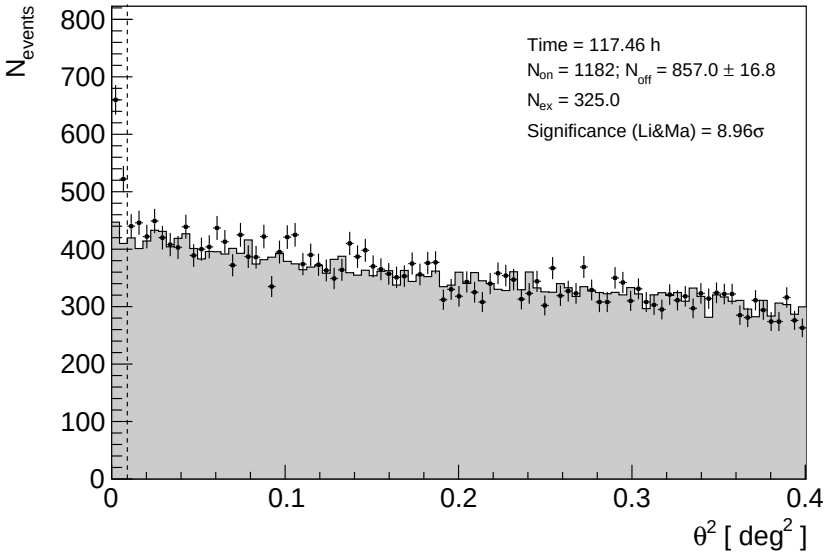

(a) 1ES 0229+200.

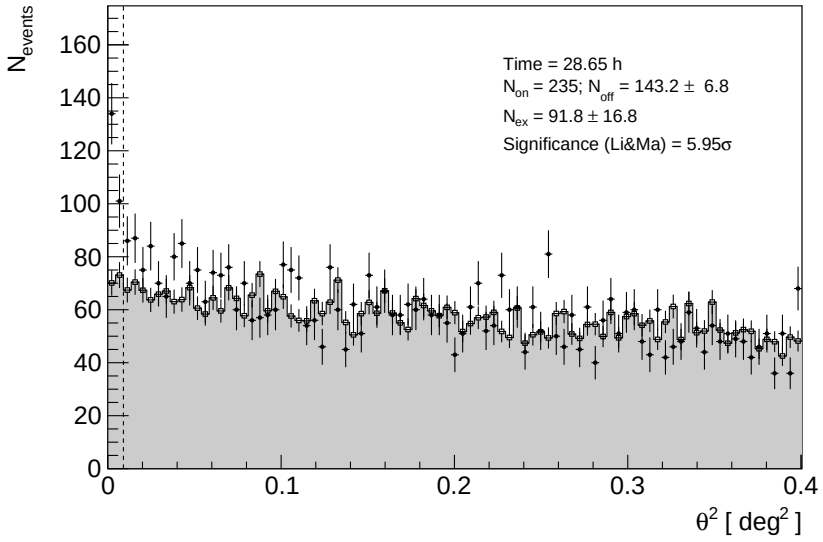

(b) TXS 0210+515.

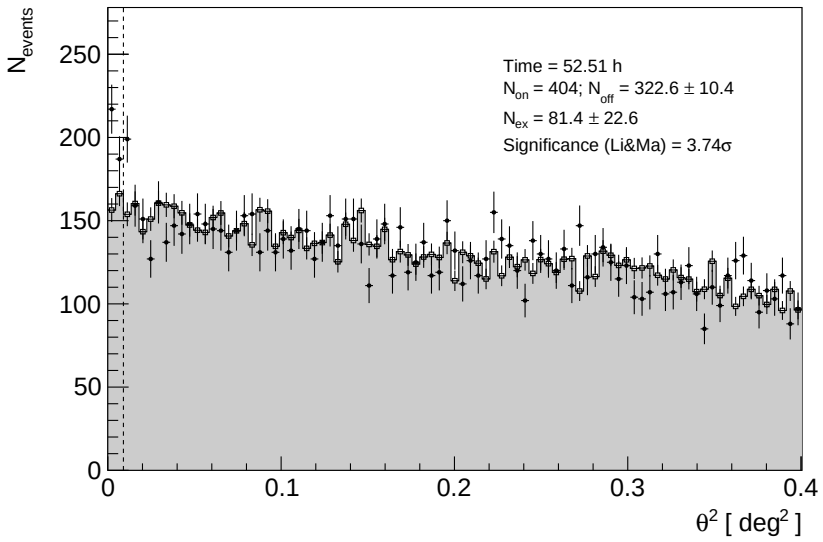

(c) RGB J2042+244.

Figure 5.13: *θ^2 distribution of the EHBLs that have been detected thanks to the MAGIC analyses I contributed to during my PhD activity. From MAGIC Collaboration (2019a).*

Source	z	$E_{\rm dec}$ [GeV]	$F_0 \times 10^{-12}$ [cm^{-2}s^{-1}]	$\Gamma_{\rm obs}$	$\Gamma_{\rm int}$
TXS 0210+515	0.049	1574	0.10 ± 0.03	2.0 ± 0.3	1.6 ± 0.3
RBS 0723	0.198	300	10.0 ± 2.0	3.6 ± 0.8	2.7 ± 1.2
1ES 1426+428*	0.129	242	25.6 ± 0.1	2.6 ± 0.3	1.8 ± 0.5
1ES 2037+521	0.053	400	5.6 ± 0.6	2.3 ± 0.2	2.0 ± 0.5
RGB J2042+244†	0.104	379	2.6 ± 0.5	2.3 ± 0.3	1.7 ± 0.6
1ES 0229+200	0.140	521	3.6 ± 0.4	2.6 ± 0.1	1.8 ± 0.1

Table 5.7: *Results of the MAGIC spectral analysis of the EHBLs detected at VHE gamma rays together with the one which shows hint of signal (RGB J2042+244) and 1ES 0229+200, the reference source. Columns from left to right: Source name, redshift, decorrelation energy, differential energy flux derived from the observed spectrum at the decorrelation energy, spectral index of the observed spectrum, spectral index of the intrinsic spectrum corrected for EBL absorption with the model by Franceschini et al. (2008b).*

5.2.2.5 Discussion of MAGIC results

Signal search

The analysis of the signal revealed the detection at VHE gamma rays of three new sources: TXS 0210+515, RBS 0723, and 1ES 2037+521. Additionally, a hint of signal was registered from the source RGB J2042+244, and a confirmation of the detection of the known TeV emitter 1ES 1426+428 was found in the 2012 dataset. A summary of the MAGIC results is reported in **Table** 5.7.

Thanks to a dedicated analysis, no variability in the flux of the sources was found. This agrees with the usual low-flux variability of EHBLs, and in particular of hard-TeV EHBLs: since these sources are faint TeV emitters, modest variability of the signal could be undetectable due to the instrument sensitivity limit. Only in the case of 1ES 1426+428 was found a hint of variability, however not statistically significant (constant-flux hypothesis cannot be excluded: $\chi^2/\text{d.o.f} = 8.4/2$).

Spectral properties

I report in **Figure** 5.14 the observed spectra (gray markers) of all the sources detected or with hint of detection by MAGIC.

The spectra have been fitted with a power law of the form

$$\frac{dN}{dE} = F_0 \cdot \left(\frac{E}{E_{\rm dec}}\right)^{-\Gamma} , \tag{5.2}$$

where F_0 and Γ are fit parameters representing the flux at the decorrelation energy $\rm E_{dec}$ and the spectral index, respectively, for the observed $\Gamma_{\rm obs}$ and intrinsic spectrum $\Gamma_{\rm int}$. The fit parameters are presented in **Table** 5.7.

Remarkably, all the sources except the most distant one RBS 0723, show data up to more than 1 TeV, which excludes severe cutoff below this energy as expected for this class of sources, in particular the hard-TeV EHBLs.

The resulting observed spectra are quite soft, with a spectral index softer than 2, and reaching in the case of RBS 0723 the value 3.60 ± 0.79.

However, after correcting for the EBL absorption effect with the model by Franceschini et al. (2008a), the intrisinc spectral indices are very hard (except for RBS 0723) and generally compatible or lower than 2. This feature confirms the possible nature of hard-TeV blazars of these sources.

It is important to note that some interesting sources like 1ES 0229+200 and 1ES 1426+428 reported resulting spectra at TeV gamma-ray energies compatible with the values and

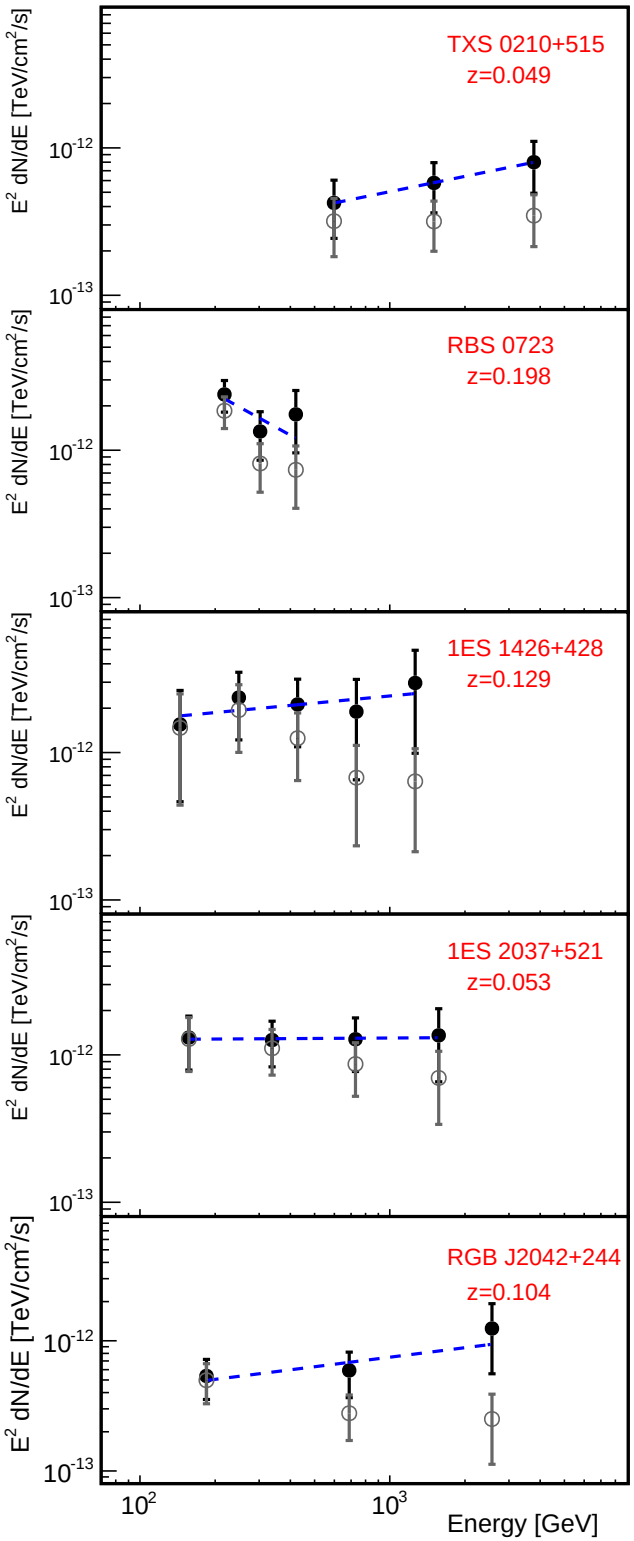

Figure 5.14: *SEDs of the four extreme blazars detected with the MAGIC telescopes and for the hint-of-signal source in E^2 dN/dE representation: observed data (open gray markers) and EBL-corrected data (filled black markers) using the Franceschini et al. (2008a) model. The dashed lines represent the power-law fit to the EBL-corrected data. From MAGIC Collaboration (2019a).*

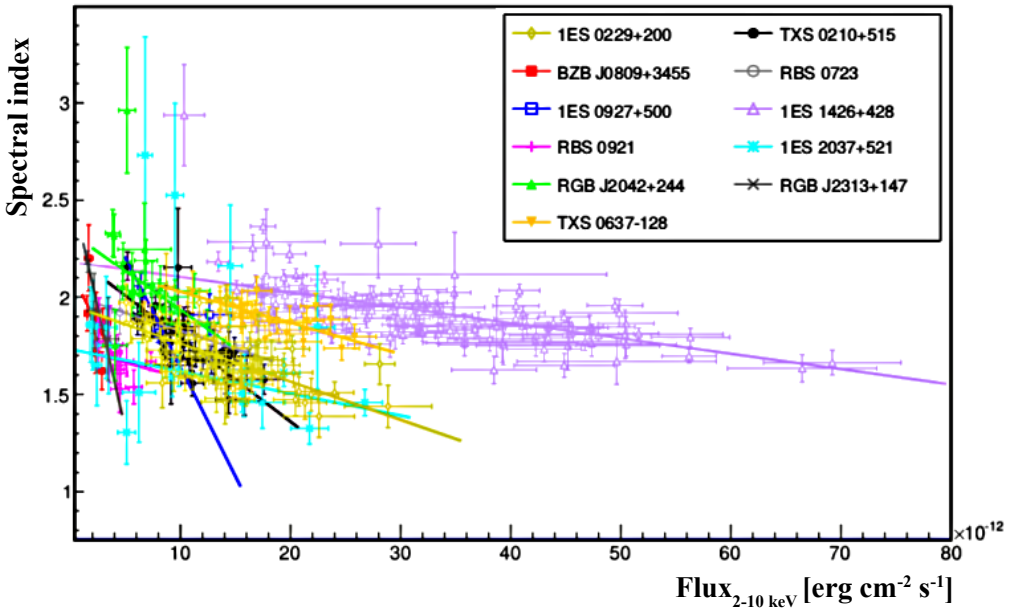

Figure 5.15: *The X-ray 2-10 keV flux as a function of the spectral index* Γ *measured with Swift-XRT during the all the observations of the sources. Almost all the sources show a clear harder-when-brighter trend.*

the conclusions reported in Section 4.3.

Upper limits

When no detection could be claimed, upper limits on the flux of the sources were computed, as reported in **Table** 5.6 on page 220. Assuming a spectrum similar to the reference 1ES 0229+200, an observed photon index of 2 was adopted for the upper limit calculations.

Some of these sources were already observed by other IACTs, with reported upper limits. In particular, the source TXS 0210+515 measured during MAGIC campaign is in agreement with the upper limit reported by VERITAS (Archambault et al., 2016). Conversely, for the other three sources that have not been detected yet, namely BZB J0809+3455, 1ES 0927+500, and RBS 0921, MAGIC computed upper limits that are in agreement but more precise with respect to the ones computed by VERITAS, this effect being related to the much longer exposures.

5.2.3 Results in other energy bands

***Fermi*-LAT**

For each of the sources, a dedicated *Fermi*-LAT analysis has been performed. The analysis has been performed also thanks to my implementation of the *Fermi* and *Enrico* softwares in the cloud system of the MAGIC-CTA Padova group (see Section 2.3.2.4 and Appendix A). The chosen time intervals were selected in such a way to cover, when the detection (TS $>$ 25) was possible in short time intervals, the simultaneous MAGIC observations (the minimum interval considered was as long as 1 year).

As reported in **Table** 5.8, the resulting TS values of the sources, representing the detection level of the signal, are quite low. This confirms that they are faint sources in the HE gamma-ray band, as expected by EHBLs.

Only the source RBS 0921, is not reported in any *Fermi*-LAT catalog yet. Remarkably, the analysis of more than 8 years of data indicates a TS of 23, corresponding to a significance of about 4 σ, near the threshold used to define a source detected at HE. The

source therefore shows a hint of signal at HE with this deep exposure and will be possibly detected in the near future. The fluxes vary in a relatively narrow range between 1.4 to $6.7 \cdot 10^{-10}$ cm^{-2}s^{-1}.

The observed spectral indices are quite soft, and all of them below 2. Interestingly, all *Fermi*-LAT spectral indices reported are compatible with the indices measured at higher energies with MAGIC in **Table** 5.7. This result agrees with the hypothesis of continuously increasing hard gamma-ray spectrum, typical feature of the hard-TeV blazars. However, this compatibility might be favoured by the relatively large error bars due to the faintness of these objects, and only further observations might confirm this hypothesis.

***Swift*-XRT**

During the MAGIC campaign, several simultaneous *Swift* observations have been requested via Target of Opportunity (ToO) observations (see Section 2.2). These data were added to the already available archival data, and all together were analysed.

The overall results are reported in the left panel of **Table** 5.8. All the spectra have been fitted with a power law, reporting spectral indices $\Gamma \lesssim 2$. This fact suggests that, according to the expectations of EHBLs, the synchrotron hump of the sources peaks around or above this energy range (with the only exception of RGB J2313+147, see next Section).

As shown in **Figure** 5.15, a general harder-when-brighter behaviour is found. This means that the photon index decreases when the flux increases, and is interpreted as the emerging of an additional population of accelerated electrons in the jet during high-activity states.

***Swift*-UVOT**

When triggering a ToO request to the *Swift* observatory, also UVOT data have been collected. Together with the already available archival data, they were analysed and reported in the MWL SEDs. These data were useful to constrain the radiation coming from the host galaxy of each source, that in EHBLs is generally visible.

***Swift*-BAT**

In the sample of **Table** 5.5 on page 218, five sources have been detected also in the *Swift*-BAT 105-Month hard X-ray catalog: they are TXS 2010+515, TXS 0637-128, 1ES 0927+500, 1ES 1426+428, and 1ES 0229+200.

It is worth to note that three of these sources have been detected also by MAGIC. This fact suggests that EHBL candidates with detection in hard X-rays, as performed in Section 4.3, represents a good selection criterion for VHE observations.

Thanks to new data collected by the *NuSTAR* satellite (Harrison et al., 2013), two sources, namely TXS 0210+515 and RGB J2313+147, were characterized also in the hard X-ray band (3-79 keV). The *NuSTAR* satellite is particularly useful to characterize EHBLs in this crucial energy band, and provide excellent spectra that constrain the synchrotron emission.

Simultaneously to *NuSTAR* observations, also *Swift*-XRT observations of TXS 0210+515 and RGB J2313+147 were performed. This allowed us to study the complete X-ray spectra of each source, presented in **Figure** 5.16.

In the case of TXS 0210+515, a clear evidence for a curved X-ray spectrum was found. The spectrum is well described by a log-parabola model, suggesting a position of the synchrotron peak at $7.1^{+1.5}_{-1.2}$ keV. This confirms the extreme-synchrotron nature of the source, similar (but still less extreme) than 1ES 0229+200, for which a synchrotron peak at about 10 keV has been estimated by Costamante et al. (2018). For RGB J2313+147, the X-ray flux observed with *NuSTAR* is a factor of ten lower with respect to that of TXS 0210+515, preventing us to carefully test a curved model in X-rays. The combined X-ray data, however, suggest a synchrotron peak well below 10^{17} Hz indicating that this source was very likely a standard HBL and not an EHBL during the observations.

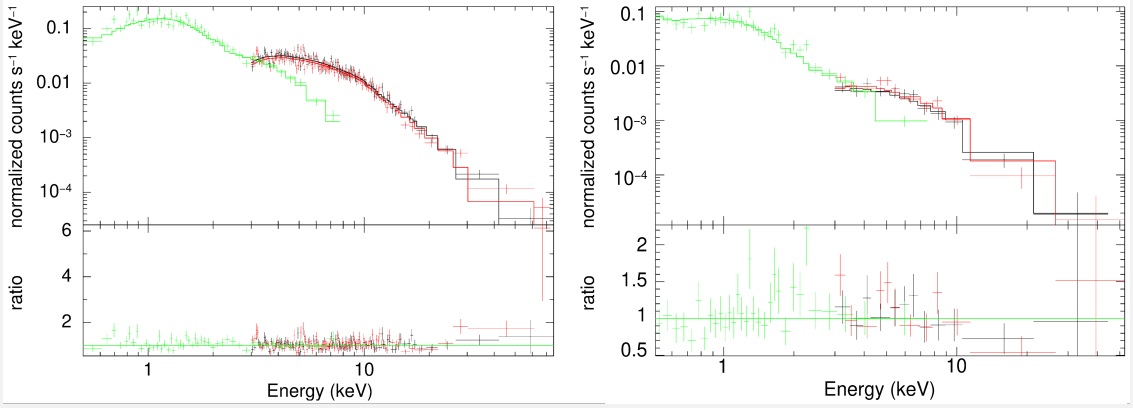

Figure 5.16: *Left: NuSTAR (black, FPMA, and red, FPMB, points) and Swift-XRT (green points) spectra and residuals for TXS 0210+515 collected on 2016 January simultaneously fitted with a log-parabola model. Right: NuSTAR (red and black points) and Swift-XRT (green points) spectra and residuals of RGB 2313+147 collected on 2015 May 30 simultaneously fitted with a power-law model. From MAGIC Collaboration (2019a).*

Source	*Swift*-XRT				*Fermi*-LAT			
	Obs. date [MJD]	$F_{(2-10\,keV)}\times10^{-12}$ [erg cm^{-2}s^{-1}]	Γ	χ^2/d.o.f.	Interval [MJD]	$F_{(1-300\,GeV)}\times10^{-10}$ [cm^{-2}s^{-1}]	Γ	TS †
TXS 0210+515	57417	8.6 ± 0.4	1.71 ± 0.04	119.4/77	57388–58118	4.3 ± 1.3	1.8 ± 0.2	42
TXS 0637-128	57784	15.6 ± 1.0	1.96 ± 0.07	32.1/32	54682–58318	3.4 ± 1.1	1.5 ± 0.2	60
BZB J0809+3455	57126	2.1 ± 0.3	1.89 ± 0.08	9.5/17	56658–57753	2.4 ± 0.8	1.9 ± 0.2	39
RBS 0723	57761	13.0 ± 0.7	1.68 ± 0.04	55.3/54	56108–57203	2.8 ± 0.8	1.6 ± 0.2	53
1ES 0927+500	55648	6.4 ± 0.7	2.06 ± 0.07	38.8/26	55562–57022	1.4 ± 0.6	1.5 ± 0.2	30
RBS 0921	57434	4.2 ± 0.6	1.63 ± 0.09	10.7/14		-	-	23
1ES 1426+428	56064	47.4 ± 1.4	1.84 ± 0.02	171.2/172	55927–56292	6.7 ± 1.7	1.4 ± 0.2	94
1ES 2037+521*	57660	10.7 ± 1.0	1.93 ± 0.13	18.7/17	57203–57934	4.6 ± 1.5	1.7 ± 0.2	46
RGB J2042+244	57192	9.2 ± 0.8	1.93 ± 0.07	29.5/27	56838–57569	4.6 ± 1.4	1.7 ± 0.2	58
RGB J2313+147	57172	1.6 ± 0.1	2.18 ± 0.06	30.5/32	56838–57569	3.6 ± 1.1	1.7 ± 0.2	34
1ES 0229+200	56264	13.1 ± 1.0	1.79 ± 0.07	43.5/41	56293–58118	2.3 ± 0.7	1.5 ± 0.2	78

Table 5.8: *Main spectral parameters resulting from the analysis of Swift-XRT and Fermi-LAT data. Columns from left to right: source name; Swift-XRT observation dates (selected for the SED modelling); X-ray flux in the 2-10 keV energy range; spectral index of X-ray spectrum; fit-statistics parameters; date for Fermi-LAT data (centered on the MAGIC observation window); HE gamma-ray flux in range of 1-300 GeV; spectral index of HE gamma-ray spectrum; likelihood TS of the fitted model.*

5.2.4 SED modelling and discussion

The intrinsic broad-band SEDs of each target were assembled complementing the MAGIC, *Swift*-XRT, *NuSTAR*, and *Fermi*-LAT data with archival data from the ASI Space Science Data Center (SSDC)[2].
In order to interpret the data, several emission models have been applied to the data:

- 1D conical jet model;
- spine-layer model;
- proton-syncrotron model.

All these models have been reported in Section 3.2.4.

The application of the models to the MWL SEDs is shown in **Figure** 5.18. All the resulting parameters have been reported in Appendix D. While all the SEDs were modelled with the 1-D conical-jet SSC model, the five sources detected at VHE gamma rays and the source RGB J2042+244 with hint-of-signal were also modelled with the other two alternative scenarios. All the models provide a good description of the quasi-simultaneous multi-wavelength observational data. However, the resulting parameters differ substantially in the three scenarios.

One of the main results of the 1D conical-jet SSC model applied to the data is that a critically low magnetization is requested (see **Figure** 5.17). The spine-layer model provides a satisfactory quasi-equipartition of the energetics and a good value for the magnetization. The proton-synchrotron model, instead, while still providing a good fit to the multi-wavelength data, results in a highly magnetized jet, still far from equipartition. Therefore, with the current data set we cannot favour or disfavour any model considered.

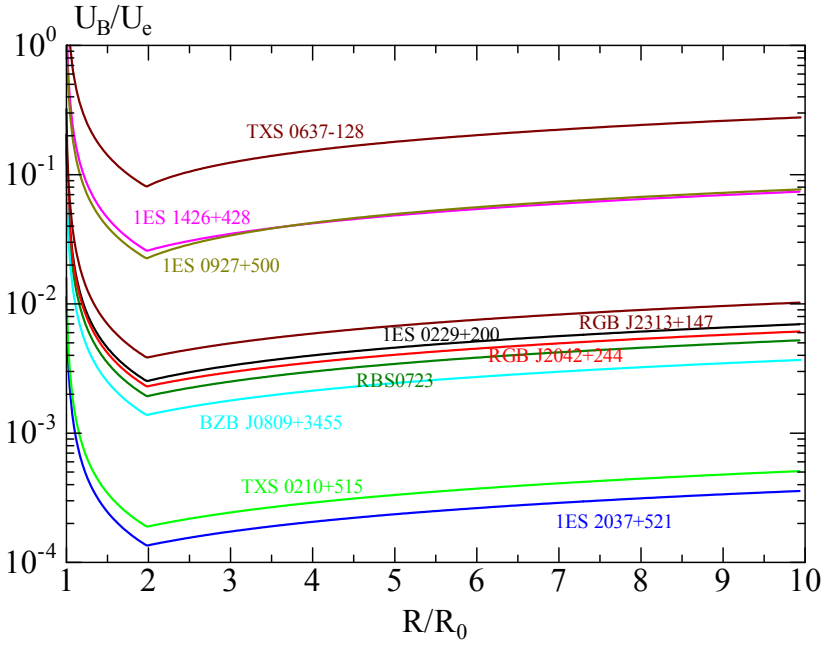

Figure 5.17: *U_B/Ue distribution as a function of R/R_0 for the sources considered in this study in the 1D conical jet SSC model (see* ***Table*** *D.1). From MAGIC Collaboration (2019a).*

[2] http://www.asdc.asi.it

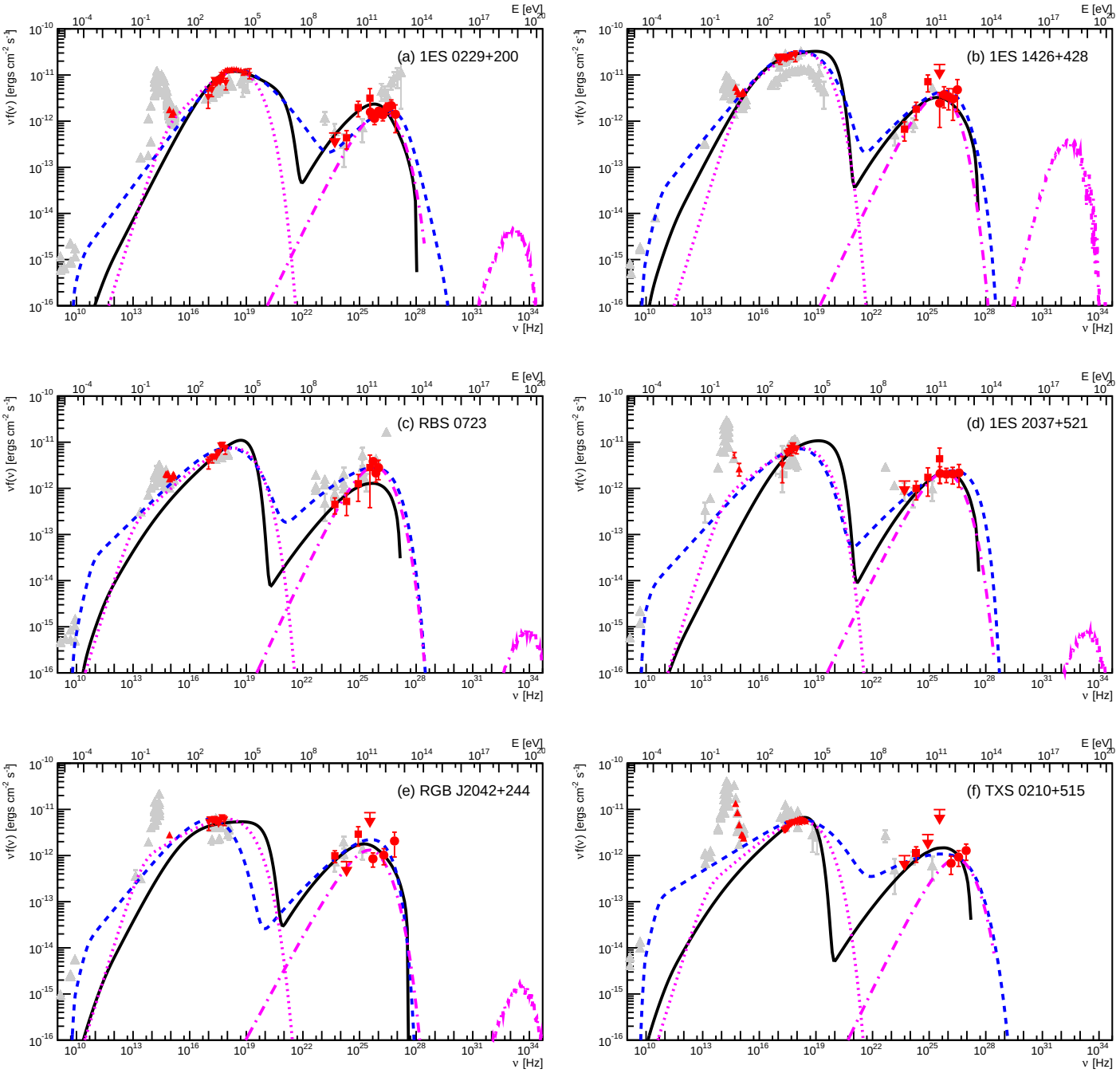

Figure 5.18: *Broad-band SED and modelled spectrum for 1ES 0229+200 (archetypal EHBL) and the four VHE gamma-ray sources detected with MAGIC presented in the study. The broadband SED of RGB J2042+244, for which a hint of signal was detected at VHE gamma-rays is also shown. Red points represent contemporaneous UVOT, XRT, NuSTAR, Fermi-LAT and MAGIC data considered in the fit. Gray markers are archival data from ASDC website. Blue, dashed line is the result of the conical-jet SSC model. Black continuous line represents the outcome of the spine-layer model. Dashed-dotted magenta line is the outcome of the proton-synchrotron model. The third bump in the proton-synchrotron model is the expected neutrino flux produced by secondary lepto-hadronic interactions resulting from the best fit solution proposed. From MAGIC Collaboration (2019a).*

5.3 Searching for new TeV gamma-ray emitting EHBLs with MAGIC

In this Section, I will present a summary of the main sources that I have proposed for observations with the MAGIC telescopes under Cycle 14$^{\text{th}}$. During that observation cycle, I was PI of the related proposal for observations of new EHBLs in TeV gamma rays, that has been approved.

These analyses are preliminary and are presented here only to show the current status of the project.

5.3.1 1RXS J081201.8+023735

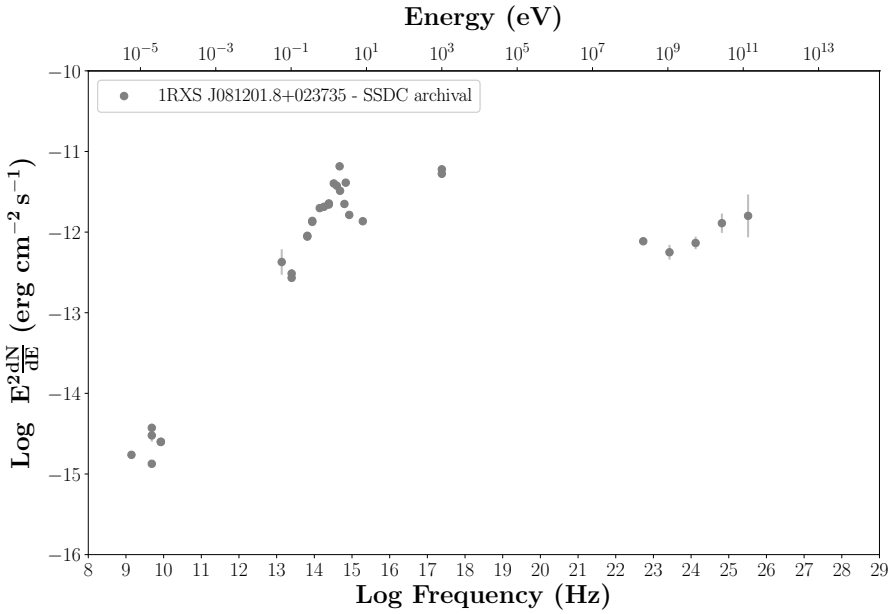

Figure 5.19: *MWL SED of 1RXS J081201.8+023735 as collected from archival data of SSDC.* Fermi-*LAT data taken from my ten-years analysis.*

1RXS J081201.8+023735 (PI: Luca Foffano) is a very promising source with radio, X-ray, and HE gamma-ray fluxes comparable with 1ES 0229+200 ones. The MWL SED, reported in **Figure** 5.19, shows the synchrotron peak exceeding $10^{17.5}$ Hz. The *Fermi*-LAT analysis over ten years of observations reports a robust detection with a TS=230, and a very hard spectrum with slope $\Gamma = -1.76 \pm 0.12$.

The redshift was previously unknown, but the appearance of the host galaxy at optical wavelengths suggested the relatively low redshift of the source In fact, an estimated value of the redshift based on optical spectroscopic observations given by J. Becerra and R. Clavero gives $z = 0.17$ (preliminary, private communication), a good value for detectable TeV emitting EHBLs.

Thanks to this redshift value, I was able to extrapolate my ten-years *Fermi*-LAT spectrum at TeV gamma-ray energies. As shown in **Figure** 5.20a, the extrapolation results compatible with the detectability of the current IACTs. A dedicated macro included in the MARS software allowed me to compute the estimated detectability of the source by comparing the expected signal with the sensitivity of MAGIC. As shown in **Figure** 5.20b, the source should be detectable in about 25 h of observations. However, this is only an estimate related to good data quality and dark observations (low threshold). Additionally, it is severely affected by the assumed spectral shape. As mentioned in Section 4.3.9.1,

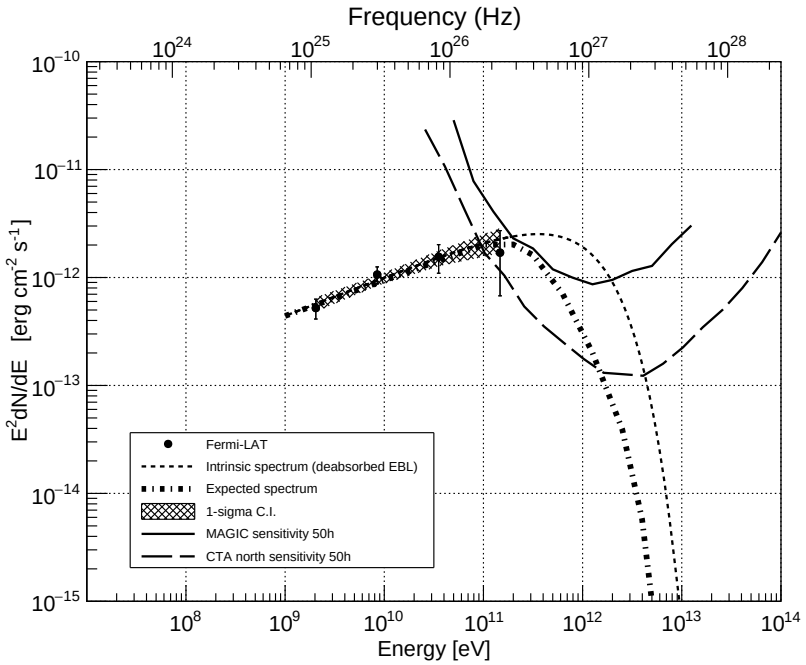

(a) Power-law extrapolation at TeV energies. I adopt here $E_{\text{cut-off}}$ =1 TeV as a conservative cut-off energy as reported in Section 4.3.9.1.

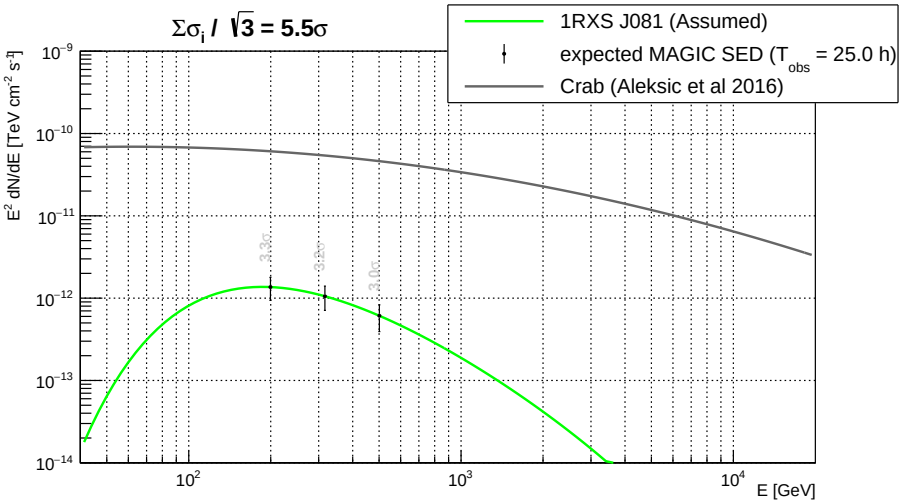

(b) Computation of the estimated detectability of the source with the MAGIC telescopes.

Figure 5.20: *1RXS J081201.8+023735.*

I applied a cut-off a 1 TeV to the power-law extrapolation, and this implies that the extrapolation results very conservative.

Signal search

The source 1RXS J081201.8+023735 was observed with the MAGIC telescopes for about 38 h during 2018 (RF ST.03.07). Once collected all the data, I had the opportunity to compute the signal estimation thanks to the `odie` program. Also in this case I had to

perform a stacking of the `odie` results on all the individual analysis period.

Finally, our analysis results in the θ^2 plot reported in **Figure** 5.21 that shows the θ^2 distribution of the events. The overall signal search with `odie` reported 3.8 sigma in the FR range. However, the signal represents an excess that might be related to a hint of detection of the source. Even if the detectability estimated in **Figure** 5.20b reported more than five sigma in about 25 hours, this hint of signal suggests that probably the non-optimal atmospheric conditions, the spectral properties, or some flux variability, might have diluted the signal. For this reason, more observations will be requested in the next observation cycle.

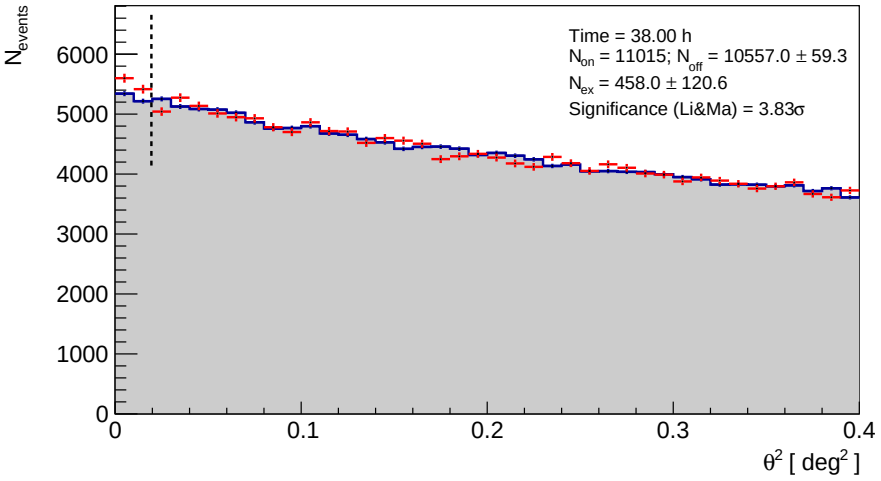

Figure 5.21: *θ^2 distribution of 1RXS J081201.8+023735 that have been observed with the MAGIC telescopes. The signal (red) and background (shadowed grey) are reported in each figure. The vertical dashed line indicates the defined signal region to which the significance of the detection is calculated.*

5.3.2 1RXS J055717.0-061705

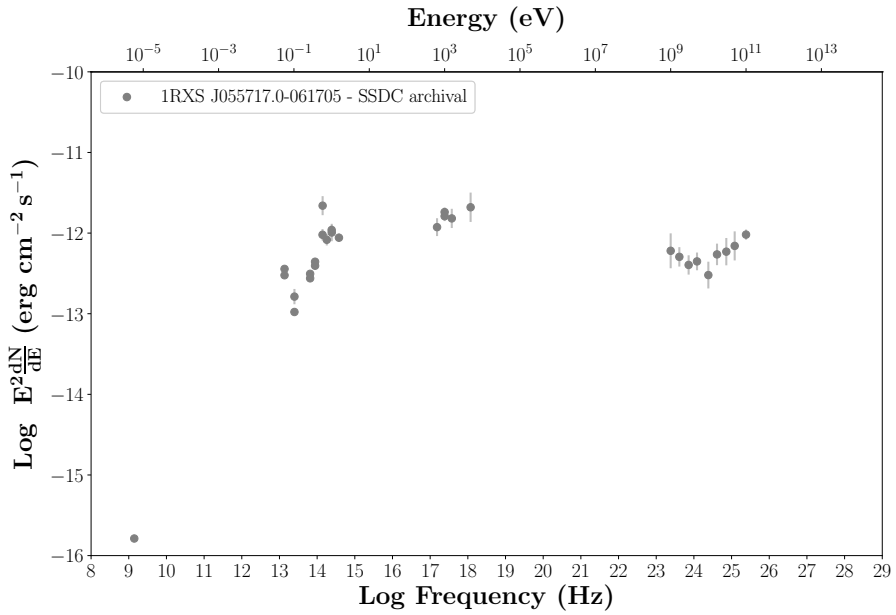

Figure 5.22: *MWL SED of 1RXS J055717.0-061705 as collected from archival data of SSDC.* Fermi-*LAT data taken from the 1BIGB catalog (Arsioli et al., 2018).*

The MWL SED of 1RXS J055717.0-061705 (PI: Luca Foffano), reported in **Figure** 5.22, shows synchrotron peak exceeding 10^{18} Hz. The ten-years *Fermi*-LAT analysis above 1 GeV gives TS=58 and confirms the detection in this band, but with relatively faintness that follows the typical properties of the EHBLs. The *Fermi*-LAT analysis reports also a hard spectrum with slope $\Gamma = -1.84 \pm 0.19$.

The redshift is currently unknown, but the optical points in the SED match a giant elliptical galaxy template with an approximate redshift value of $z \sim 0.2$.

This redshift value was adopted in order to extrapolate my ten-years *Fermi*-LAT spectrum at TeV gamma-ray energies. As shown in **Figure** 5.23a, the extrapolation results compatible with the detectability of the current IACTs but quite challenging. A dedicated macro included in the MARS software allowed me to compute the estimated detectability of the source by comparing the expected signal with the sensitivity of MAGIC. As shown in **Figure** 5.23b, the source should be detectable in about 25 h of observations. This estimation is based on the signal provided by the lowest part of the spectrum at few hundreds of GeV. For this reason, observations with dark conditions are strongly requested. However, since in our proposal I obtained also some spare time under moon light, part of this source was observed in these conditions. This implied longer exposure time but with challenging observation of a part at higher energies of the spectrum (above about 300 GeV). Additionally, the extrapolation is particularly uncertain due to the unknown value of the redshift and the conservative cut-off (see Section 4.3.9.1) at 1 TeV to the power-law extrapolation.

Signal search

The source 1RXS J055717.0-061705 (PI: Luca Foffano) was observed with the MAGIC telescopes for more than 15 h during 2018 (RF ST.03.07). Once collected all the data, we had the opportunity to compute the signal estimation thanks to the `odie` program. Also in this case I had to perform a stacking of the `odie` results on all the individual analysis period.

Unfortunately, the overall signal search with `odie` reports no hint of detection in the FR range yet, but the exposure time is still too low for the detection of EHBLs.

Considering the preliminary status of the analysis, I do not have computed a upper limit on the flux.

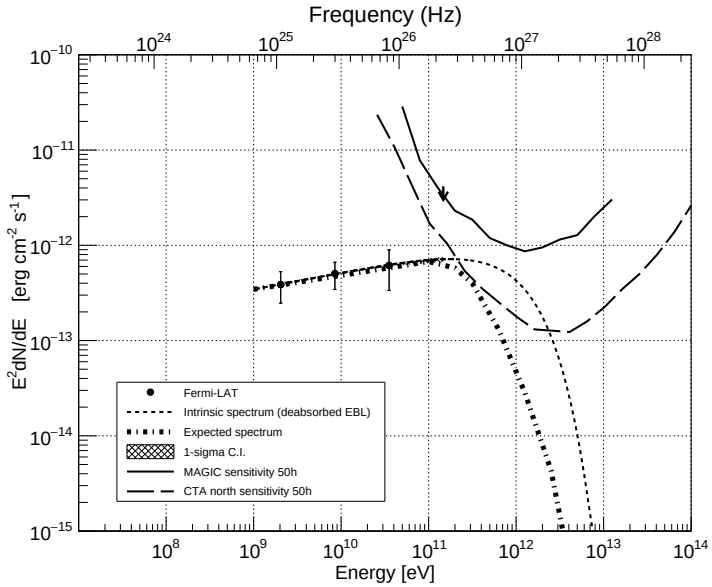

(a) Power-law extrapolation at TeV energies. I adopt here $E_{\text{cut-off}}$ =1 TeV as a conservative cut-off energy as reported in Section 4.3.9.1.

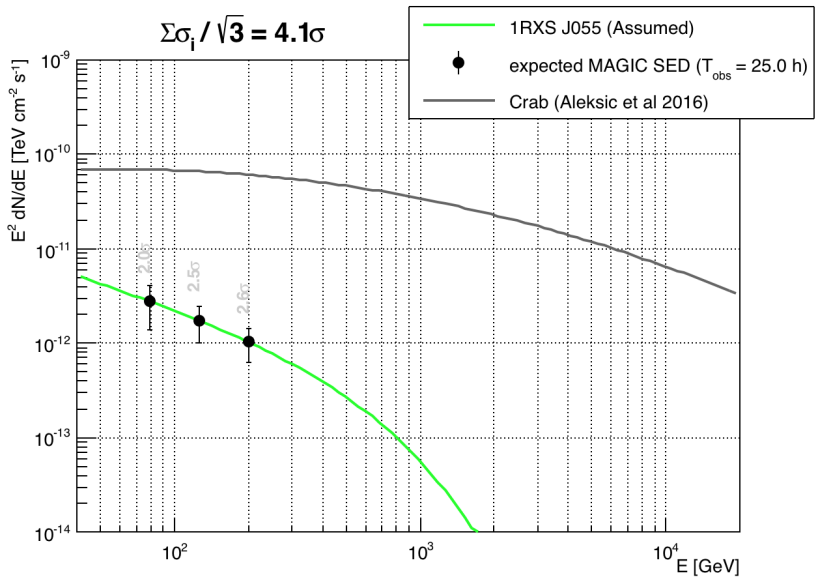

(b) Computation of the estimated detectability of the source with the MAGIC telescopes.

Figure 5.23: *1RXS J055717.0-061705.*

5.3.3 BZB J1417+2543

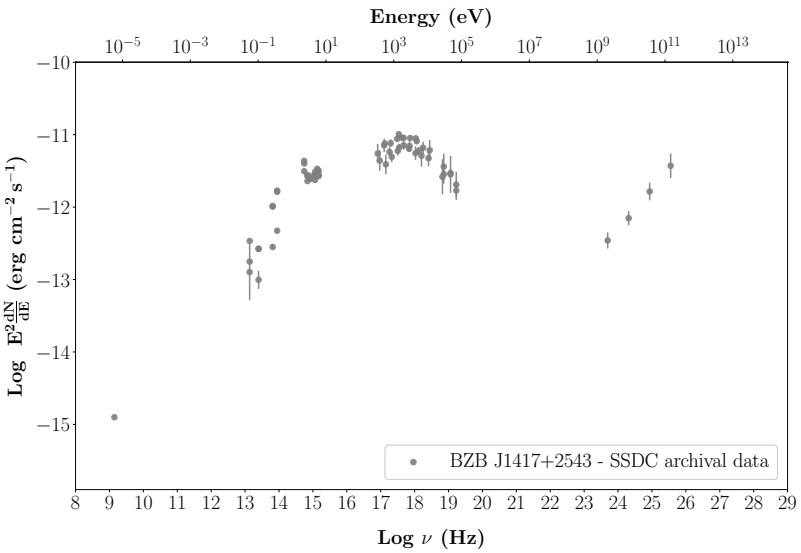

Figure 5.24: *MWL SED of BZB J1417+2543 as collected from archival data of SSDC.* Fermi-*LAT data taken from my ten-years* Fermi-*LAT analysis.*

The MWL SED of BZB J1417+2543 (PI: Luca Foffano), reported in **Figure** 5.24, shows synchrotron peak exceeding $10^{17.5}$ Hz. The ten-years *Fermi*-LAT analysis above 1 GeV gives TS=211 and confirms the detection in this band, but with relatively faintness that follows the typical properties of the EHBLs.

The redshift $z = 0.237$ of the source is relatively high for an EHBL. This means that the EBL absorption might be quite high, and the detectability challenging. However, the *Fermi*-LAT analysis reports a very hard spectrum with slope $\Gamma = -1.52 \pm 0.10$. This hard spectrum and the high flux in GeV gamma rays make this source promising if observed in the first part of the spectrum at few hundreds of GeV. Also in this case, moon observations (with higher threshold above about 300 GeV) are strongly discouraged.

In fact, the extrapolations of my ten-years *Fermi*-LAT spectrum at TeV gamma-ray energies, shown in **Figure** 5.25a, results compatible with the detectability of the current IACTs. A dedicated macro included in the MARS software allowed me to compute the estimated detectability of the source by comparing the expected signal with the sensitivity of MAGIC. As shown in **Figure** 5.25b, the source should be detectable in about 25 h of observations. This estimation is based on the signal provided by the lowest part of the spectrum at few hundreds of GeV. For this reason, observations with dark conditions are strongly requested.

The observations of this source are still ongoing, and no data are ready to be analysed yet.

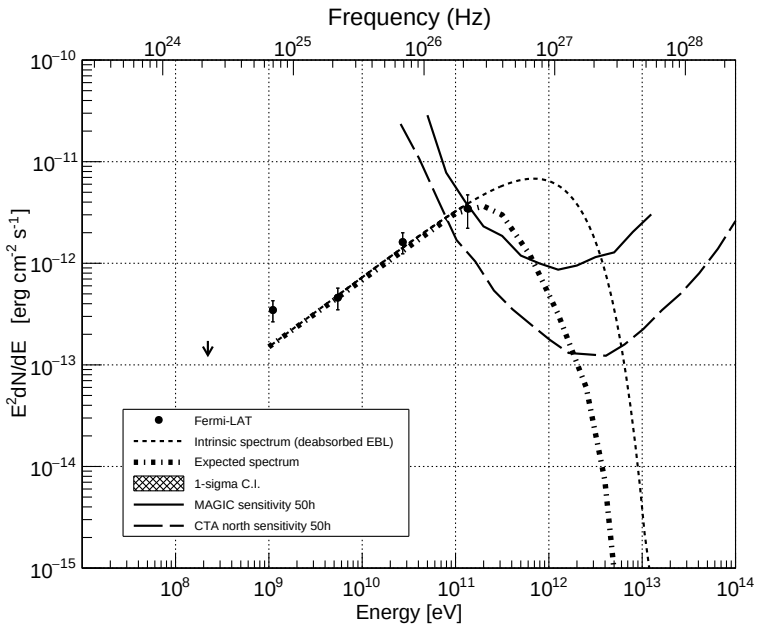

(a) Power-law extrapolation at TeV energies. I adopt here $E_{\text{cut-off}}$ =1 TeV as a conservative cut-off energy as reported in Section 4.3.9.1.

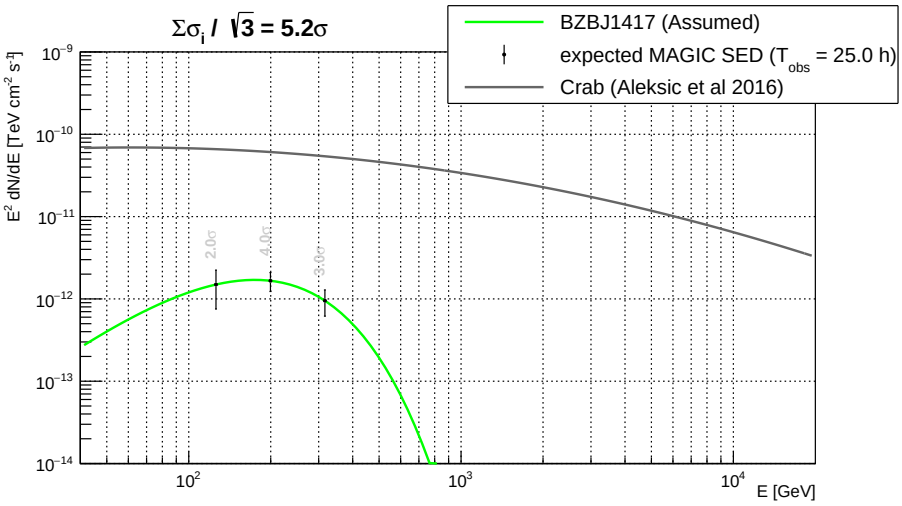

(b) Computation of the estimated detectability of the source with the MAGIC telescopes.

Figure 5.25: *BZB J1417+2543.*

5.4 TeV gamma-ray candidate EHBLs from the southern hemisphere

My activity in the search for new EHBLs, especially in the TeV gamma-ray band, led me to the preparation of list of good candidates. Some of these sources are located in the northern hemisphere, and for this reason the most interesting candidates were proposed to the MAGIC Collaboration. However, some other sources are observable only from the southern hemisphere. For this reason, I decided to submit a proposal to observe some of the best candidates with the H.E.S.S. telescopes.
In this Section, I will report a summary of two sources that have been proposed. The observational proposal is still under evaluation.

The selection of the best candidates was performed with an analysis of the most interesting objects of the *Swift*-BAT 105-months hard X-ray catalog, following Section 4.3. For each of the candidates in the source sample, I performed an updated ten-years *Fermi*-LAT analysis in order to characterize the spectral emission in the HE gamma-ray band. Their high synchrotron peak frequency, the relatively low redshift, and their hard spectrum in HE gamma-rays, make them good EHBL candidates. Additionally, the relatively high flux in X-rays and HE gamma-rays suggests a promising detectability of these objects by the current generation of IACTs in a moderate exposure time. These objects present good visibility from the H.E.S.S. site, and up to now have not been detected in TeV gamma rays.

5.4.1 PKS 0352-686

This is a very promising source with integral flux that, in comparison with that of 1ES 0229+200, is comparable in radio and X-rays, and higher in HE gamma rays. The updated ten-years *Fermi*-LAT analysis (see **Table** 4.2) indicates a very hard spectrum in HE gamma rays with index $\Gamma = 1.46 \pm 0.11$. The MWL SED (**Figure** 5.27a) shows that the synchrotron peak is exceeding 10^{18} Hz, making it one of the sources with the highest synchrotron peak energy among the EHBLs visible from the southern hemisphere. The redshift $z = 0.086$ is particularly low and makes the expected TeV gamma-ray spectrum of this source relatively less affected by the EBL absorption up to $E > 1$ TeV and particularly suitable for IACTs observations.

This BL Lac object has already been pointed by the H.E.S.S. telescopes and the upper limit is reported in Abramowski et al. (2014b). It was observed with a total exposure of 15 h and an integral flux of $I_{>thr} = 0.40 \times 10^{-12} cm^{-2} s^{-1}$ above the threshold of 710 GeV. However, it is worth to note that - looking at **Figure** 5.26a - the source is well detectable by the H.E.S.S. telescopes, but most part of the flux is located in the low energy band below the selected threshold of 710 GeV. In the high energy part of the H.E.S.S. sensitivity, the source is more affected by the EBL absorption and, in addition to the mid zenith observations under which it was observed, the detectability was probably compromised. Additionally, the upper limit provided by the previous observations is compatible with the extrapolation in **Figure** 5.26a. For this reason, I asked for new observations of this source with a longer exposure in a good data quality framework. Lower zenith observations performed during dark time should lower the threshold of the analysis, allowing us to detect it and characterize its spectrum.

5.4.2 BZB J0244-5819

BZB J0244-5819 is a promising source with radio, X-ray, and HE gamma-ray fluxes comparable to the 1ES 0229+200 ones. The MWL SED (**Figure** 5.27b) presents a synchrotron peak even higher with respect to the previous candidate, and exceeding $10^{18.2}$ Hz. Conversely, the redshift of $z = 0.286$ is higher, but it is still a good value for detectable TeV EHBLs. The updated ten-years *Fermi*-LAT analysis presents a spectrum in HE gamma rays of 1.65 ± 0.08 that may show an hint of curvature. This suggests

that this source is probably peaking with the second hump in the TeV region, and it may represent a non hard-TeV example of EHBL with extremely high synchrotron peak frequency. This source has not been detected in the TeV gamma-ray band yet, and **Figure** 5.26b confirms the promising extrapolation of the *Fermi*-LAT data to the VHE, and a good detectability of the source in the low-enegy band of the instrument sensitivity.

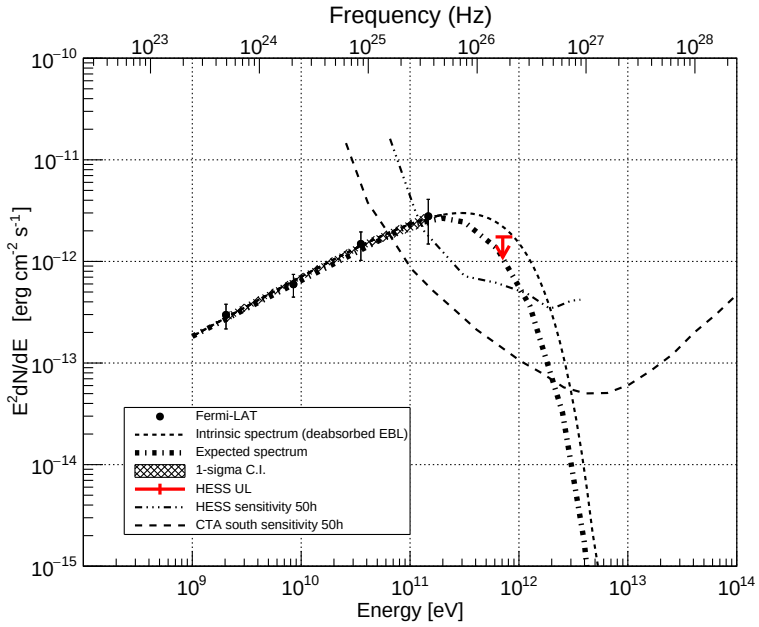

(a) PKS 0352-686.

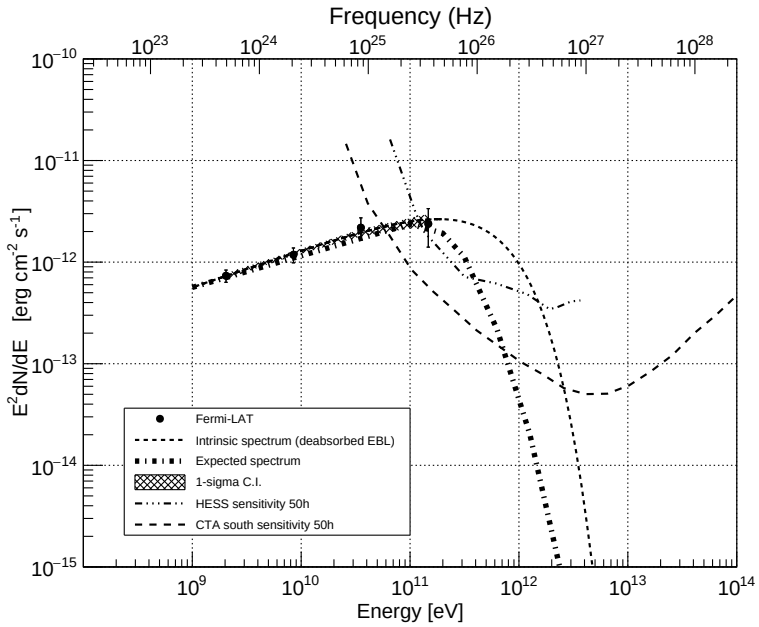

(b) BZB J0244-5819.

Figure 5.26: *TeV gamma-ray extrapolation of the updated ten-years* Fermi-*LAT points of PKS 0352-686. The fit was performed using a power-law function and applying a conservative cut-off at 0.5 TeV for both of them (in order to respect the upper limit on the observed flux of PKS 0352-686). The thicker dashed line is the power-law extrapolation absorbed for EBL using the model by Franceschini & Rodighiero (2017). The H.E.S.S. upper limit for PKS 0352-686 is reported from Abramowski et al. (2014b). The CTA-south and H.E.S.S. (Holler et al., 2016) sensitivities for 50h of observations are also reported in the plots.*

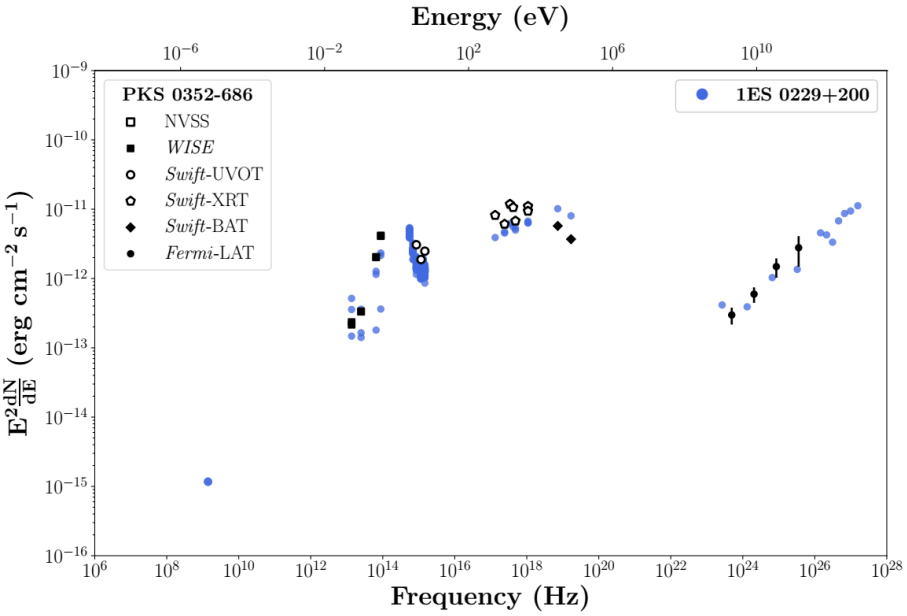

(a) PKS 0352-686.

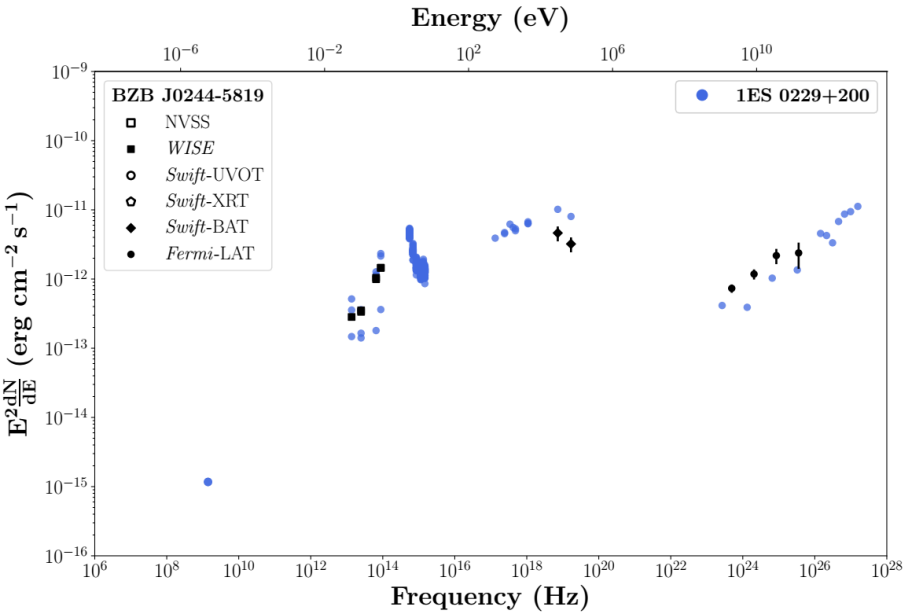

(b) BZB J0244-5819.

Figure 5.27: *Multi-wavelength SEDs of the two best candidates PKS 0352-686 (a) and BZB J0244-5819 (b). I indicate in black the source points, and in blue the reference EHBL 1ES 0229+200 for comparison. The data have already been deabsorbed by EBL effect with the model by Franceschini & Rodighiero (2017).*

Chapter 6

Towards an understanding of the origin of UHECRs

In the previous Sections I presented some of the main properties of the AGNs, with a particular focus on blazars. This is a huge topic that has been continuously developing in the last almost fifty years. Its role in astrophysics has been confirmed with several recent discoveries in the multi-wavelength and multi-messenger context.

Thanks to their emission throughout the whole electromagnetic spectrum, AGNs are powerful "outdoor" laboratories where we can test the most extreme and energetic processes that we cannot replicate on Earth. Additionally, the emission mechanisms at work in the AGN jets seem to be much more complex than expected. Several leptonic and hadronic processes have to be invoked in order to explain their spectral emission among the objects of the different subclasses of AGNs.

In this Section, I will introduce what was one of the most important steps in multi-messenger astrophysics: the first known coincidence between a highly energetic neutrino and a flaring blazar. This event happened unexpectedly in September 2017, and after more than two years several aspects have still to be clarified. In particular, the emission mechanism related to the production of gamma rays and neutrinos is still under debate. I had the opportunity to participate directly to this discovery, being the main data analyser for the MAGIC Collaboration that detected a clear VHE gamma-ray signal from the direction of the neutrino event. In spite of some residual uncertainties and limited significance, the event is considered an important insight onto processes originating the UHECRs, in extragalactic sources of the blazar kind.

6.1 TXS 0506+056 and the first neutrino-blazar association

On September 22nd, 2017, a major breakthrough opened a new era in the history of astronomy and astrophysics. The detection of a high-energy neutrino in coincidence with a flaring blazar was the first event in which the scientific community was able to pinpoint with high probability the incoming direction of a neutrino and to identify it with an extragalactic source. Such type of events are considered the smoking gun for hadronic processes taking place in the blazar jets, that for many years in the past have been thought to be able to produce neutrinos. In fact, as introduced in Section 1.2.1.3, the main contributors to the emission of light from blazars are probably electrons. However, also heavier particles might be accelerated in the jet, and especially protons. Their accelerated motion produces synchrotron light as in the case of electrons, but at higher energies (as in the proton-synchrotron model in Section 3.2.5.1). Their presence might would also additional interactions with the ambient photons through photo-hadronic processes, and in this case also neutrinos are produced. However, till now the detection of neutrinos and light coming from a common extragalactic source has never been registered, and in the community there was the feeling that the status of the neutrino experiments were not enough advanced to provide such information.

In this Section, I describe the first event of coincidence between the high-energy neutrino EHE-170922A and the flaring blazar TXS 0506+056 (also called *neutrino-blazar event*) to which I participated. My role was to provide the main analysis of the MAGIC data that confirmed the presence of VHE gamma-ray radiation coming from the flaring blazar TXS 0506+056. The results were reported in the paper Aartsen et al. (2018b) published on the Science magazine (here mentioned also as Paper I).

A more detailed study of the long-term observations of the blazar TXS 0506+056, presented in Section 6.2, was reported in the paper Ansoldi et al. (2018) by the MAGIC Collaboration (here mentioned also as Paper II).

6.1.1 History of the detection

Among the different activities carried out by the MAGIC Collaboration, one of the most important is the follow-up observation of different types of transient events such as GRB, FRB, GW, and neutrinos. The MAGIC telescopes are part of the Gamma-ray Coordinates Network (GCN), a world-wide connection between many observatories in different energy bands that, in case of alert, can point to the suggested direction in the sky and try to get the best possible scientific content.

On September 22nd, 2017, an alert from the IceCube observatory (see Section 2.6) informed all the members of the GCN network that a particularly favourable extremely high-energy (hereafter EHE, see Section 2.6.2 for details) event was detected by the detector 43 s before. This type of alerts comes with a frequency of about 4/6 alerts per year, and in some cases the errors attributed to the determination of the incoming direction are too large to be easily followed-up by other telescopes like MAGIC. However, this alert was particularly well reconstructed in the IceCube detector, and the error on the incoming direction was of only about 15 arcmin.

MAGIC suddenly triggered the alert on September 22nd, 2017, but the observations were not possible because of strong wind at the site. The observations were resumed on September 24th, 2017, when the weather conditions became more favourable. In that case, MAGIC observations were however partly affected by low sky transmission due to passing clouds. Only about half of the exposure time resulted in good quality data (about 1 h). The consequent analysis reported no signal from the source.

On September 27th, 2017, an alert by the *Fermi*-LAT telescope was sent alerting the scientific community that the TXS 0506+056 was flaring in the HE gamma-ray band. The blazar was incredibly close to the position of the incoming neutrino that provided the alert of EHE-220917A event. The very same night the MAGIC telescopes started a deep

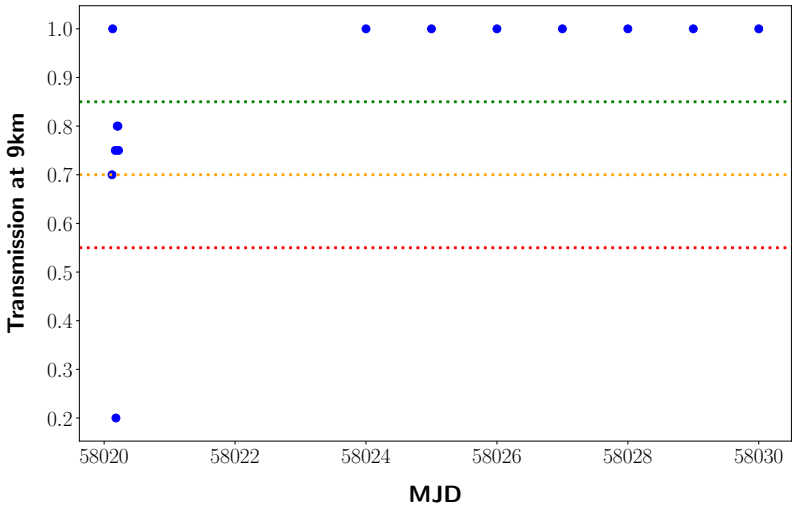

Figure 6.1: *Distribution of reports from LIDAR transmission as measured at a distance of 9 km. Green, yellow, and red dashed lines show the sky transmission levels at 85%, 70%, and 55% respectively.*

follow-up program that resulted in the detection of VHE gamma rays from the direction of the blazar TXS 0506+056 in less than five days, ended in the publication of the ATEL #10817 (Mirzoyan, 2017). In that moment, I was responsible of the fast analysis of the MAGIC data regarding this alert, and from then I continued to analyse the data related to this source. The details on such analysis are reported in the next Section.

6.1.2 MAGIC data analysis

Data quality and data selection

The first MAGIC observations of TXS 0506+056 that resulted in the ATEL #10817 were performed during the period from September 28$^{\text{th}}$ to October 4$^{\text{th}}$, 2017 (MJD 58020 - 58030). During this period, the weather conditions on the MAGIC site were particularly stable and favourable to the observations.

In the previously mentioned ATEL, also the very first day of observations September 24$^{\text{th}}$, 2017 was included. During that day, the sky transmission was affected by passing clouds. The values of the sky transmission measured by the MAGIC LIDAR (see Section 2.4.1.9) in the overall dataset are reported in **Figure** 6.1. The data selection was performed using the following cuts:

- transmission of the signal in the sky above 0.7;
- mean DC in the camera below 2 μA, to select only dark data;
- zenith range between 5 and 50 degrees, that allows for low-threshold observations.

These cuts were then used for all the analysis of the following periods for this source. The analysis of September 24$^{\text{th}}$ (MJD 58020), 2017 left only about 50% of the data available. The total time before quality cuts was about 2 h, while after quality cuts was about 1 h.

The data from September 24$^{\text{th}}$ were analysed with the standard procedure, reporting no signal. However, the data on that day were used in order to put an upper limit on the expected flux in VHE by TXS 0506+056.

The following data registered between September 28$^{\text{th}}$ and October 4$^{\text{th}}$, 2017 were instead particularly useful for the estimation of the flux variation of the source up to the flare of October 4$^{\text{th}}$, 2017. I report in **Table** 6.1 a main summary of the observations

Date	MJD	Effective time	Mean DC current M1	Significance LE	Data quality
24/09/17	58020	1.15 h	0.8-1.4	-1.30 σ	Moderate
28/09/17	58024	1.27 h	0.9-1.0	2.77 σ	Good
29/09/17	58025	2.91 h	0.9-1.0	0.85 σ	Good
30/09/17	58026	3.03 h	0.9-1.0	0.77 σ	Good
01/10/17	58027	2.87 h	0.9-1.0	3.58 σ	Good
02/10/17	58028	0.81 h	0.9-1.0	2.18 σ	Good
03/10/17	58029	1.30 h	0.8-1.2	2.97 σ	Good
04/10/17	58030	0.65 h	0.9-2.6	5.32 σ	Good

Table 6.1: *Summary of the data quality during the MAGIC first observations of TXS 0506+056 published in the paper Aartsen et al. (2018b). Here I report information on the day, the effective time, the mean current in the camera of MAGIC-1 (to indicate the dark conditions of the nights), the significance in the LE range, and an indication of the data quality (green means that all data were selected, yellow means that we had to apply quality cuts).*

during those first eight nights that lead to the ATEL. During these days, in fact, the weather conditions were good and no data quality cuts were needed. In particular, considering also the first day September 24$^{\text{th}}$ 2017, a total exposure time of 13.9 h was reported. After the quality cuts, the observing time used for the ATEL was of 12.9 h.

Signal search

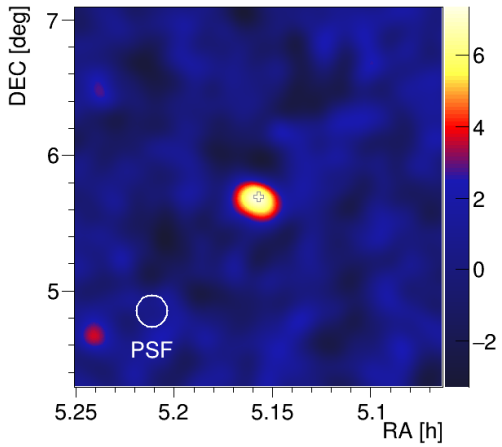

Figure 6.2: *First TS sky map above 90 GeV of the field of view registered by the MAGIC telescopes containing in the center the source TXS 0506+056.*

The analysis chain of the MAGIC data led me to study first the significance of such signal. The first step was to perform the estimation of the signal using the `caspar` program in order to perform the TS sky map of the field of view. This was particularly useful because the very first day of observations September 24$^{\text{th}}$, 2017, the MAGIC telescopes followed the direction of the incoming neutrino reported in the IceCube GCN. After few days, the *Fermi*-LAT alert on the increasing flux in the HE band from the direction of the blazar TXS 0506+056, led the MAGIC telescopes to follow the more precise direction of that blazar. However, the two directions are well inside the PSF of the MAGIC telescopes.

Thus, a blind skymap – as reported in **Figure** 6.2 – was particularly useful to verify the presence of excesses in the field of view of MAGIC and that those excesses were compatible with the incoming direction of the EHE neutrino (central cross). As reported in the Figure, the signal registered by the MAGIC telescopes and the direction of the incoming neutrino were perfectly compatible.

A more detailed study of the significance of the detection was performed using the `odie` program, in order to provide a θ^2 plot. After the quality cuts (as reported in the previous Section), I applied the standard LE cuts at the θ^2 plot (for more information see Section 2.4.3.7). The final significance of the signal resulted in 6.2 σ using the Li&Ma formula. The final θ^2 plot I produced for the Science publication is shown in **Figure** 6.3.

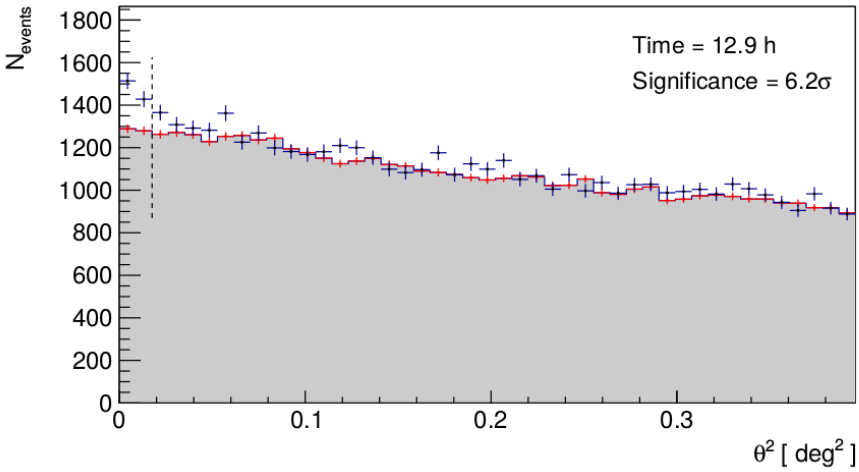

Figure 6.3: *θ^2 plot of the VHE gamma-ray signal from TXS 0506+056 as measured by MAGIC and published in Paper I.*

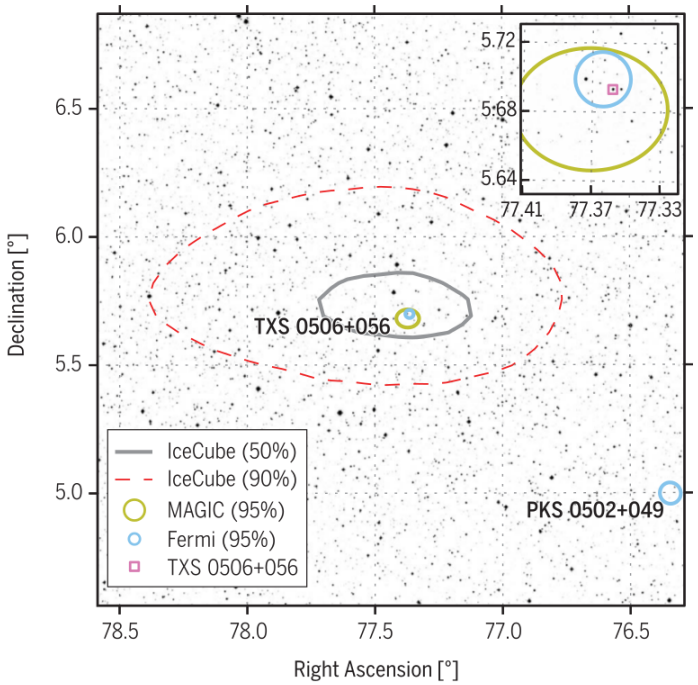

Figure 6.4: *Skymap of the multi-messenger observations of the blazar TXS 0506+056 taken by Aartsen et al. (2018b). The 50% and 90% containment regions for the neutrino IceCube-170922A (dashed red and solid gray contours, respectively), overlain on a V-band optical image of the sky. Gamma-ray sources in this region previously detected with the Fermi spacecraft are shown as blue circles, with sizes representing their 95% positional uncertainty and labelled with the source names. The IceCube neutrino is coincident with the blazar TXS 0506+056, whose optical position is shown by the pink square. The yellow circle shows the 95% positional uncertainty of very-high-energy gamma rays detected by the MAGIC telescopes during the follow-up campaign. The inset shows a magnified view of the region around TXS 0506+056 on an R-band optical image of the sky.*

Light curve

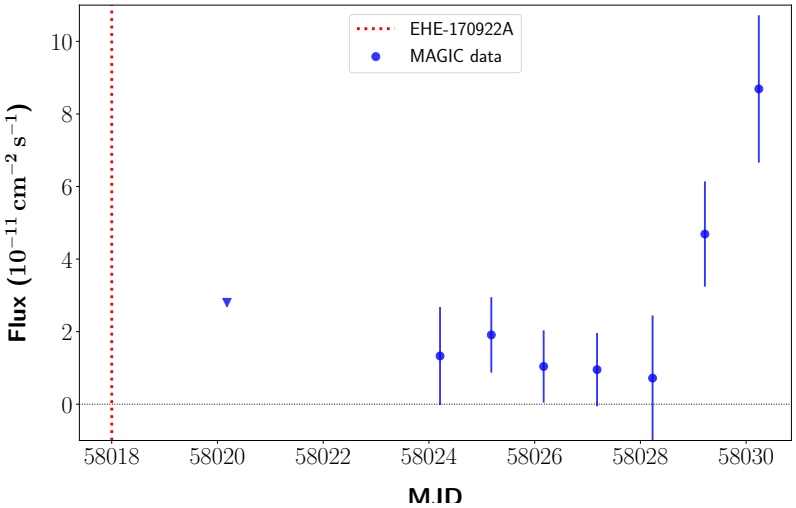

Figure 6.5: *Light curve of the data related to the ATEL analysis (MJD 58020 - 58030).*

The successful detection of the signal led us to perform an high-level analysis of the data. The first step was to reconstruct the flux of the source during the days reported in the ATEL.
Here I present the light curve associated to this analysis. The main plot is presented in **Figure** 6.5, where I show the upper limit of September 24$^{\text{th}}$ (MJD 58020) and the flux values of the days between September 28$^{\text{th}}$ (MJD 58024) and October 4$^{\text{th}}$ (MJD 58030). The first day of observations the MAGIC telescopes followed-up the IceCube alert, but there was not signal detected, and for this reason only the upper-limit is reported. The first enhanced emission phase appears to start already on October 2$^{\text{nd}}$ (about 10 days after the neutrino alert) and lasts at least for the following two days (then no more data are available due to the moon break).

The light curve was produced considering a lower threshold of 90 GeV, which has been chosen to be the common threshold energy between the two internal cross-check analyses (selected as reported in Section 2.4.3.9).

The mean integrated flux above 90 GeV has been estimated in $F(> 90\,\text{GeV}) = 1.59 \pm 0.21 \cdot 10^{-11}\,\text{ph}\,\text{cm}^{-2}\,\text{s}^{-1}$. Fitting the daily light curve with a constant function yields a $F(> 90\,\text{GeV}) = 2.04 \pm 0.46 \cdot 10^{-11}\,\text{ph}\,\text{cm}^{-2}\,\text{s}^{-1}$. The probability of the flux being constant is 0.46%. Thus there is an evident hint of variability in this energy band, and the emission of TXS 0506+056 in this data sample was not compatible with the steady flux hypothesis.

SED

The second step of the high-level analysis of the data was to reconstruct the SED of the source during the days reported in the ATEL (MJD 58020 - 58030).

The spectrum of the source observed by the MAGIC telescopes was reconstructed between 90 and 400 GeV using the Tikhonov unfolding method Albert et al. (2007a). The final SED points we reported in **Figure** 6.9 are the official ones that were reported in the Science publication.
The spectrum can be described by a simple power-law model with formula:

$$\frac{dN}{dE} = f_0 \left(\frac{E}{0.146\ \text{TeV}} \right)^{-\Gamma} ,$$

where the photon index Γ is $\Gamma_{\rm obs} = 3.93 \pm 0.37$, and the normalization constant $f_{0,\rm obs} = 1.29 \pm 0.26 \cdot 10^{-10}$ ph cm^{-2} s^{-1} TeV^{-1} at the decorrelation energy. The decorrelation energy was specifically calculated as in Abdo et al. (2010b), and assumed the value of $E_{\rm dec} = 146$ GeV.

Considering that before the Science publication the redshift was not known yet, the EBL de-absorbed spectrum was not available at that time.

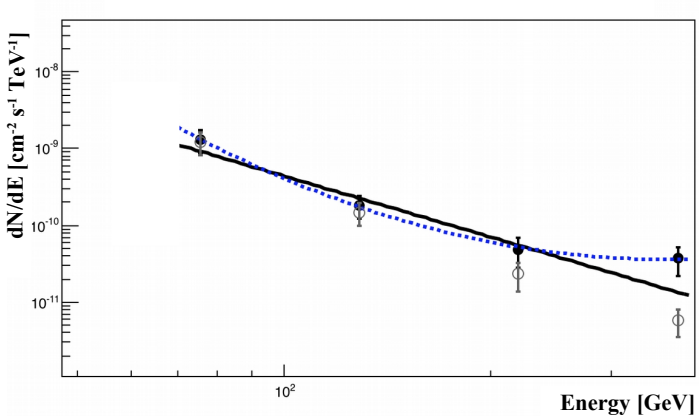

Figure 6.6: *Plot showing the procedure to compute the first upper-limits on the redshift of TXS 0506+056 based on the method by Prandini et al. (2011) and a preliminary MAGIC spectrum computed above 70 GeV. Empty circles represent the observed spectrum, filled black circles represent the intrinsic spectrum after EBL deabsorption. The assumed redshift is changed gradually. When the blue line fitted to the intrinsic spectrum disagrees statistically with the hypothesis of absence of pile-up in the VHE gamma-ray spectrum of the blazar, an upper-limit on the redshift is set.*

First redshift estimations

At the moment of the first ATEL analysis the redshift of the source was still unknown. The redshift estimation is particularly important in the VHE gamma-ray regime because of the absorption between EBL and TeV gamma rays. The observed spectrum of the source has to be corrected in order to provide the intrinsic spectrum of the source, that can then be modelled.

However, the MAGIC Collaboration decided to apply a phenomenological method to provide upper limits on the redshift that has been studied in Prandini et al. (2011), introduced in Section 3.2.6.1. By assuming a power-law spectrum of the source and an absence of pile-up (never observed in blazars at gamma-ray energies), one can deabsorb the spectrum until it starts to take over the power-law spectrum. When this happens (on a statistical basis), the corresponding value of redshift can be considered a good upper-limit on the true redshift.

Applying the de-absorption by EBL effect at the spectrum for several values of the tentative redshift, we could check if a flux pile-up appear in the SED. Assuming a slope in the HE part of the spectrum of -2.01 ± 0.03 (obtained from the analysis of *Fermi*-LAT data covering the last 100 days of observations), and using a preliminary MAGIC spectrum computed above 70 GeV, we got:

- $z^* = 0.68 \pm 0.30$ (redshift at which the slope of the MAGIC spectrum equals the *Fermi*-LAT slope)
- 2 σ upper-limit on the redshift: 1.29 (including *Fermi* and MAGIC statistical errors)
- $z_{\rm rec} = 0.40 \pm 0.17$ (reconstructed redshift). This value is considered as upper limit on the true redshift value.

The representation of the procedure is shown in **Figure** 6.6.

By the end of February 2018, the redshift of the source was independently measured using the specific optical spectroscopy by the GTC telescope by Paiano et al. (2018), yielding a value of $z = 0.3365 \pm 0.0010$. This value is well in agreement with our expectations during the analysis and with the expectations of the previous method by Prandini et al. (2011).

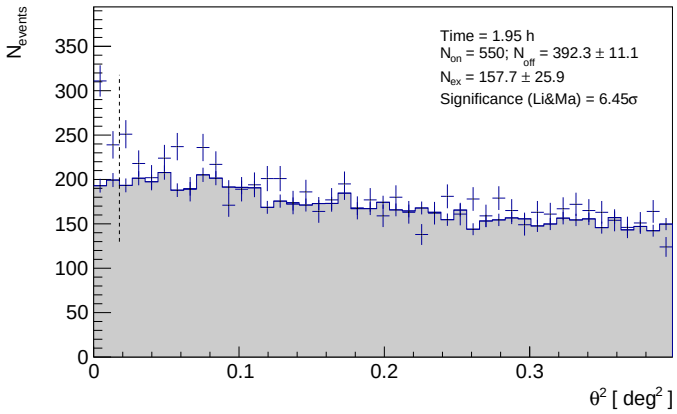

(a) Period A - first flare October 4^{th}, 2017.

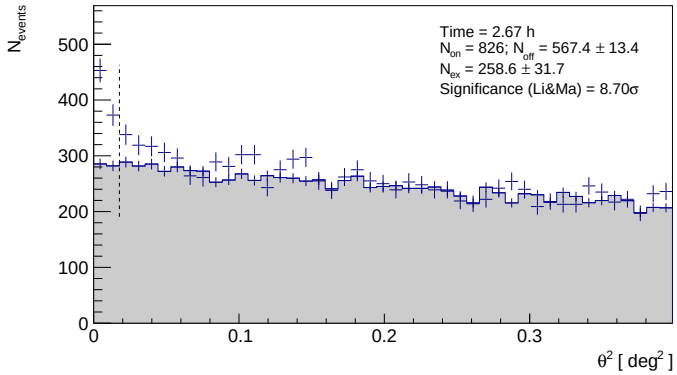

(b) Period B - second flare October 31^{st}, 2017.

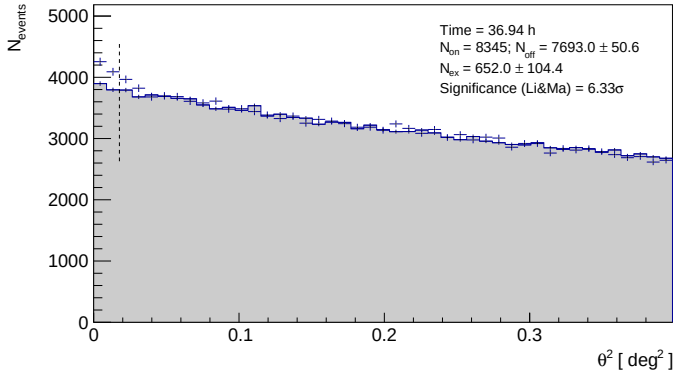

(c) Period C - quiescent state.

Figure 6.7: *θ^2 plots of different high-state and low-state activity of the TXS 0506+056 during the long-term analysis.*

	First flare Oct 3-4th	Second flare Oct 31st	Low state
	A	B	C
Effective time	2.0 h	2.7 h	35 h
Significance	5.7 σ	7.7 σ	5.6 σ
Normalization	2.91 $\pm$ 0.62	3.22 $\pm$ 0.59	0.54 $\pm$ 0.13
Spectral index	-3.86 $\pm$ 0.32	-4.00 $\pm$ 0.27	-3.52 $\pm$ .39

Table 6.2: *MAGIC spectral fit parameters. Normalization is fixed at the decorrelation energy of* $E = 146$ *GeV in units of* 10^{-10} TeV^{-1} cm^{-2} s^{-1}.

6.2 Long-term analysis

In the months following the first detection and the ATEL publication, the MAGIC Collaboration performed a deep monitoring of the source TXS 0506+056. This led to a rich data sample in which was possible to analyse in great detail the VHE gamma-ray signal of the blazar over more than two months.

Here I report some of the main specific results of Ansoldi et al. (2018).

6.2.1 Signal

During the long-term monitoring of the source, the MAGIC Collaboration was able to register a large data sample of more than 41 h good quality data of observations. This made possible to detect two different states of the source: the high state and the low state.

The complete dataset of this larger data sample goes from September 24th (MJD 58020) up to November 2nd, 2017 (MJD 58059), with a total exposure of about 47 h. After data quality cuts based on the atmospheric conditions, about 41 h of data were selected for further analysis. The data quality selection was performed at the same way as it was performed during the first ATEL analysis.
Within these observations, we detected two flares of the source:

A) the flare on October 3rd (already reported in the ATEL analysis) and October 4th: this event was reported in the Paper I.

B) an additional more intense flare registered on October 31st, never mentioned before.

Additionally, the large data sample allowed us to detect also

C) the lower state of the source (when not flaring or quiescent) over about 36 h of good quality data.

All the corresponding θ^2 plots are reported in **Figure** 6.7.

6.2.2 Light curve

The successful detection of the signal led us to perform a high-level analysis of the data. The first step was to reconstruct the light curve of the source.

Here I present the light curve associated to this analysis on the long-term exposure on TXS 0506+056. The main plot, produced considering an energy threshold of 90 GeV, is presented in **Figure** 6.8, where arrows represent upper limits.

Thanks to the detection of the flares, the VHE gamma-ray flux of this source is clearly variable, and fitting the daily light curve with a constant function implies that the probability of the constant flux hypothesis is as low as 0.3%. Additionally, the detected flares had increasing flux by a factor of up to about 6 within one day, and this allowed

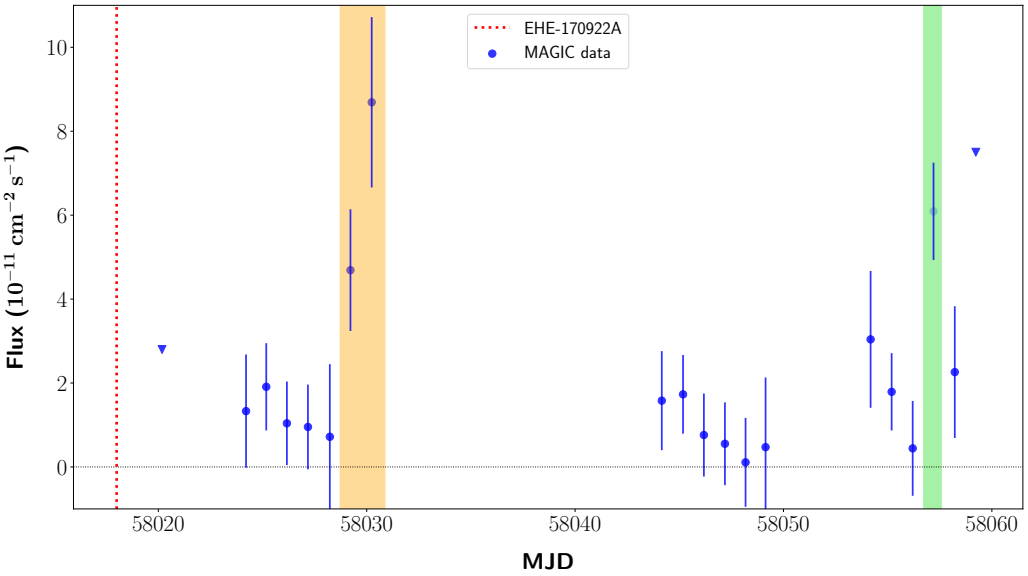

Figure 6.8: *Long-term light curve of the data related to the TXS 0506+056. The orange box puts in evidence the first flare (period A), and the green band the second flare (period B).*

the collaboration to compute the size of the emitting region as low as $R \sim 10^{16}$ cm (see Section 3.2.3.2 for more information about this procedure).

The mean integrated flux of the low state of the source above 90 GeV was estimated in $F(> 90\,\mathrm{GeV}) = 4.5 \cdot 10^{-11}\,\mathrm{ph\,cm^{-2}\,s^{-1}}$.

6.2.3 SED

The second step of the high-level analysis of the data was to reconstruct the SED of the source during the long-term exposure. Thanks to detection of the three states of the source, three values of the spectral index were obtained. In **Table** 6.2, I report a summary of the spectral indices.

The main result of this analysis was the absence of a detectable spectral shape variability during the flaring events and the low state of the source. The measured differential energy photon spectrum could be described between 90 GeV and 400 GeV by a simple power-law model with formula:

$$\frac{dN}{dE} = f_0 \left(\frac{E}{0.146\ \mathrm{TeV}} \right)^{-\Gamma} ,$$

where Γ is the photon index and f_0 is the normalization constant. As reported in **Table** 6.2, the observed spectral index (also when deabsorbed by EBL effect with the model by Dominguez et al. 2011) is significantly steeper than the spectrum measured by the *Fermi*-LAT telescope, with spectral index $\Gamma = -2.0 \pm 0.2$ between 100 MeV and 300 GeV.

6.2.4 Physical interpretation

The MAGIC Collaboration, by considering the new added value offered by the extended dataset collected just after the discovery of Ansoldi et al. (2018), tempted the description of an interesting interpretation of the processes that might have produced the neutrino coming from the TXS 0506+056 as well as the MWL data collected.

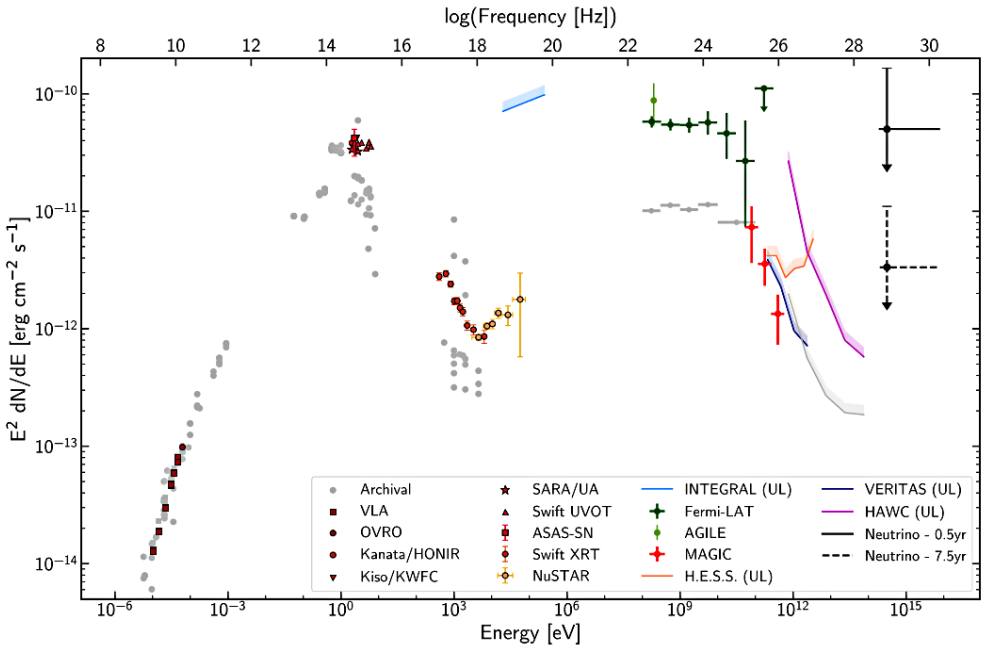

Figure 6.9: *Multi-wavelength SED of the data related to the neutrino-blazar coincidence. Upper limits at the 95% CL are shown as coloured bands and indicated as "UL" in the legend. Archival observations retrieved from ASDC website are shown in gray to illustrate the historical flux level of the blazar The gamma-ray observations have not been corrected for absorption due to the EBL. Figure adapted from Paper I.*

The main issue in the interpretation of this particular neutrino emission is that the theoreticians did not expect such neutrino coming from a BL Lac objects. In fact, the more likely sources to be neutrino producers have always been the FSRQs, that offer a richer environment around the blazar jets and interpreting the neutrino emission as the product of $p\gamma$ interactions of the jet with the surrounding matter and radiation fields.

This means that the interpretation of this neutrino emission has been recognized as absolutely not trivial, and many models have been proposed in order to explain this phenomenon. For sure, the models considering a hadronic emission component are favoured. Generally, the drawback of hadronic models is that they usually allow for neutrino production at the expense of relatively large values for the power in accelerated protons that may not be so favourable from an energetics perspective.

For this reason, the MAGIC Collaboration proposed a modified version of the so-called spine-layer model, in which the external photons might be naturally provided by the two-zone structure assumed for the blazar jet (see Section 3.2.4). In this scenario, the structured jet is composed by a faster core (or spine) surrounded by a slower sheath (or layer). The significant relative motion between the two structures implies that the density of photons originating from the slower sheath appears highly boosted in the frame comoving with the faster jet. This photon density exceeds that of the synchrotron photons arising within the jet, and thus enhances the rate of $p\gamma$ reactions and the consequent neutrino emission.

Considering this scenario, the interpretation of the neutrino emission should also imply another important observational consequence in the spectrum of the source. In fact, the high density of external photons would imply the presence of a strong $\gamma\gamma$ absorption effect within the jet, considering that the cross section for $\gamma\gamma$ interaction is about 10^3 times larger than the $p\gamma$ reactions. Thus, the strong absorption in gamma rays should be revealed through a steep spectrum at few hundreds of GeV, the energy range better reconstructed by MAGIC. Such spectral feature was actually detected by the MAGIC telescopes, and this confirms the availability of this interpretation.

6.3 Consequences on the multi-messenger era

The first identification of the incoming direction of a high-energy neutrino and the presence of an extragalactic object in particular high-state gamma-ray activity for sure will be remembered as the event opening a new era in the multi-messenger astrophysics. This event follows the detection of the GRB 170817A in coincidence with a gravitational wave, that confirmed the connection between short gamma-ray bursts and the merging of two stellar mass black holes, and the detection of the GRB 190114C, which confirmed the first revealed sub-TeV emission from GRBs.

After these discoveries, in the near future it will be possible the study of astrophysical phenomena by applying the combined information of completely different messengers: the gravitational waves, the neutrinos, and the classical electromagnetic light.

In the neutrino-blazar event, the importance of this detection is that it reveals the first extragalactic object able to provide neutrino emission (now added to the neutrino detection coming from the Sun and the Galaxy center). The study of this event would not have been possible if the information coming from the three major experiments IceCube, *Fermi*-LAT, and MAGIC was not combined. In fact – at a first sight – the probability of the neutrino EHE-170922A of about 50% to be extragalactic could be not enough to claim such discovery. However, the complete reading of the paper Aartsen et al. (2018b) reveals that the combined information coming from the neutrino and from the light (especially the one at high- and very-high energies) led to the reasonable detection of such coincidence. This event was not only the first association between a neutrino and an extragalactic object, but it was also the first event to confirm the crucial role of the combined information coming from different messengers.

For sure, the development of the observatories detecting gravitational waves, neutrinos, and light, will increase our capabilities of associating such events and their scientific outcome.

Conclusions

In this Thesis, I presented the research activity performed during my PhD course at the University of Padova. Most part of my scientific results were focused on the study of extreme blazars, with a particular effort on the characterization of their spectral properties in TeV gamma rays and on the detectability of new sources of this class by the Cherenkov telescopes.

My research work started with the implementation of a new selection method aimed at selecting extreme blazars on the basis of their high synchrotron emission in hard X-rays. This method allowed me to collect the up-to-now largest sample of EHBLs. The study of their spectral properties led me to find systematic differences that are emerging in the EHBL class, especially in TeV gamma rays. This suggests the possible emergence of a sub-classification: the EHBLs may be a population of objects, with a gradual sequence of objects that goes from the sources that behave like EHBLs only temporarily when flaring up to the more stable hard-TeV EHBLs characterized by high-energy emission peaked at more than 10 TeV.

An additional aspect of my analysis was to predict the feasibility of observations of EHBL objects with the current and next generation of Cherenkov telescopes. Thanks to the study of refined high-energy spectra, I contributed to the analysis of faint sources in the high-energy gamma-ray band in order to find new candidates to be observed at TeV gamma rays.

In the MAGIC Collaboration, I had the opportunity to propose a list of EHBL candidates for observations. Among them, several candidates are now being observed with the MAGIC telescopes with good preliminary results. In particular, a source named PGC 2402248 was observed and eventually detected in TeV gamma rays. This result has been recently published together with a detailed discussion on the comparison between several theoretical models proposing different interpretations of the spectral properties of this source. These results, besides the detection of a new EHBL in this energy band, confirm the analysis I reported in the hard X-ray selected sample, adding new statistics to an intermediate class of objects in the EHBL class with high-energy emission peaking at few TeV.

A second part of my work was the contribution to the discovery of the first coincidence between the high-energy neutrino EHE-170922A and the flaring blazar TXS 0506+056. This event, together with the first detection of a gravitational wave coming with electromagnetic radiation happened in the event GW 170817A, opened the new era of multi-messenger astrophysics. I had the opportunity to live, on the front line, one of the most important event in the recent history of astrophysics, one of those events that confirm how Science can always shock us with unexpected confirmations of theories we would not have trusted much up to some time before.

These two main parts of my Thesis, together with the opportunity to work on several other projects that complemented my preparation in this field, increased my motivation in the study of the multi-messenger and multi-wavelength approaches to astrophysics. Both the extreme blazars and the connection between blazars and neutrinos are two important examples of this new approach to the discipline.

Overall, this Thesis gave me the opportunity to contribute in a field which is performing the most innovative research in gamma-ray astronomy and astrophysics, by connecting different messengers of the Universe. The recent discoveries, for example the recent

GRB 190114C detection at TeV gamma-ray energies with the MAGIC telescopes, are suggesting us that this research field will continue giving us extraordinary news. The great effort of the scientific community in gathering for a new multi-wavelength and multi-messenger approach to this discipline is working, and will be a fantastic instrument to open new windows in this branch of Science. This work will for sure be the starting point for future improvements. I am sure that, in the next few years, great developments in this scientific area will make this Thesis only an old manuscript. And I think this is the greatest honour a scientist could get: to live in an era of fantastic scientific discoveries.

Acknowledgements

To be honest, after my Master's degree, I would not have believed to be accepted at a PhD course at the University of Padova. It was at the same time an unexpected and fantastic event. For this reason, I did my best to get the maximum result from this experience. Now, that I am completing this course, I can summarize the last three years as follows: it was hard work, but it was also an amazing adventure. However, besides my personal efforts, this experience was possible only thanks to the fantastic people I knew and who made me better than I was before.

My supervisor Prof. Alberto Franceschini gave me not only the support a supervisor should generally provide. He stimulated me in continuing to work hard and to point at the best results, also when it was not absolutely obvious to get a happy ending at the end of a project. His suggestions and advices led me to the right direction in my scientific career. I became so enthusiastic for this job because I saw that – while things were going – all the efforts were launched in the right direction, and all of them have eventually produced great results. This is absolutely not obvious when you do research, because you do not know when you will finish with your project. His great experience in the field helped me in doing the right things at the right moment.

Additionally, he always gave me all the opportunities to present my results and to explore new topics. I always got "yes" from him when asking for suggestions about presenting my results at some conferences or participating to meetings. He created such atmosphere that, when you ask for something, he says yes knowing that you will do all your best to take advantage of that opportunity. Personally, I am generally quite autonomous and I do not like being under a boss in a workplace. But this was absolutely not the case. I was basically free of doing what I though was the best thing to do, but I knew that in case he was always ready to give me suggestions on how to proceed, and I made use a lot of this opportunity. When the enthusiasm drives you on what you are doing, you work better and with more energy. This is not common in a workplace. I thank him for creating such relaxed atmosphere where people can work and express themselves without any constraint.

Special thanks are then devoted to Dr. Elisa Prandini, my co-supervisor during the entire PhD course. She was not only a mentor during my activities, but she was an extraordinary source of enthusiasm and energy. She had the patience to teach me all about our research field, from the most basic things up to the more political attitude in facing some problems: and I do not mean only the scientific stuff, but also the standard daily procedures on how to work and how to behave with people when working (and there is so much I have still to learn!). She carried me during this PhD course by helping me every day, until when – during the last part of the third year – I really felt on myself the huge help she gave me during this experience. I think that thanking her is not enough, because most things I know are only thanks to her.

During my PhD I had the opportunity to be a member of the MAGIC Collaboration. It was not only a team of people working together, but several of them became my friends. Among them, I want to thank Michele Peresano, who was the other analyser that with me worked on the neutrino-blazar coincidence in MAGIC. With him, I shared very stressful moments of hard work, but – besides the great results obtained and the opportunity to

being involved in such great discovery – thanks to that experience we knew each other and became great friends. After that period, we shared several other experiences when participating to conferences, but also travelling and climbing in the Alps.

In MAGIC I found great scientists believing in young people, and giving them the best opportunities. Thanks to the fantastic atmosphere in the Collaboration, I learnt a lot, both on the scientific and on the personal point of view. I also worked a lot, but I got fun, I travelled a lot, and I knew a lot of new people coming from all over the world. During the shifts in La Palma, I had the opportunity to work directly with the telescopes, but those experiences became really unforgettable thanks to the people who shared with me those shifts. The long nights of observations, the breathtaking sunrises, the nice moments at the beach before buying food and driving up to the Roque de los Muchachos to prepare the telescopes for observations during the incoming night. I will always keep my datataking shifts in good memory. In particular, I want to thank Massimo Persic and Vandad Fallah Ramazani for the nice moments we shared during my first shifts.

I really want to express my appreciation to the MAGICians, for giving me all these opportunities in a nice atmosphere.

While doing the PhD course, I had the opportunity to get involved in the MAGIC-CTA group at the INFN of Padova. I want to thank a lot all of them for the opportunities they gave me: Alessandro De Angelis, Michele Doro, Mosè Mariotti, Giovanni Busetto, Elisa Bernardini, Manuela Mallamaci, Alessia Spolon, Ruben Lopez, and Elisa Prandini.

I thank a lot also Simona Righini and Riccardo Rando for their useful comments on part of this Thesis, and Eugenio Bottacini for his suggestions on the development of part of this work. A special acknowledgement goes to Luigi Costamante and Markus Ackermann, the two external referees of this Thesis who contributed with insightful and valuable comments to the improvement of the manuscript.

I apologise if your name did not appear in this particular circumstance. There are so many people that, for different reasons, I would like to thank! Please know that I remember all the moments of this PhD course, all the experiences, and that your contribution is in my heart.

Dear reader, please remember that all these people are the main reason why I want to continue doing Science as much as possible!

Finally, I want to express my gratitude to something that is not a person, but a place. During this PhD, I had the opportunity to do also the sport I like most, alpinism (mountaineering). The mountains taught me a lot, and the experiences I had during these three years were a continuous increasing of enthusiasm and adventure. I spent in the mountains really nice moments, with good friends. I think that the mountains helped me a lot during these three years: they taught me not to give up, also in the worst circumstances, and that your efforts always pay back. I am not sure that this always happens, but I will continue to act as it was.

This year, while finishing my PhD, I had the opportunity to climb the Mont Blanc, after several preparatory ascents. As the great effort in preparing your body and your mind for such difficult climbing, the PhD introduced me into a new world that I would have never expected to participate. As the summit of Mont Blanc represents a symbol I will always keep in my heart, the PhD is an achievement and an experience I will never forget.

I leave these final words for my family, to remark all the love and support during all these years. This Thesis is dedicated to my parents, Arianna and Roberto, and my sister Claudia.

Thank you.

Appendix A

The cloud system in the MAGIC-CTA group in Padova

During the second year of my PhD, I had the opportunity to work on the implementation of a cloud computing system in the MAGIC-CTA group in Padova (Italy).

Before the development of the cloud system, the group has been working on few machines, called `photon13` and `photon15`. These machines were provided with quite powerful 32 cores, allowing the parallel computation or the execution of macros in background in a multi-user configuration.

Such machines, as indicated by their own names, were part of a big cluster with several machines working with hard disks attached, which were accessible to all users of the group. The maintenance of the hardware was responsibility of some computer technicians working for the INFN. Considering the continuous upgrades and maintenance needed by the software of the group, asking the intervention of computer technicians was not the most efficient procedure and was causing delays. The ideal solution would have been to have a computing infrastructure easy to use for the general users and in which the maintenance could have been carried on by few expert people of the group. Additionally, after some years of operations, several machines stopped working and only `photon13` and `photon15` were kept working.

Recently, the new cloud-based computing system of the INFN of Padova – named *Cloud Veneto*[1] – has notably improved its capacities and performances. The MAGIC-CTA group started to participate to this facility by acquiring a notable amount of resources able to build a network of machines and volumes (hard disks). Considering the relevant computing performances (both software and hardware) needed to perform a notable number of MAGIC and *Fermi* analyses, I was particularly interested in the development of this technology in order to facilitate the operations for the users of the MAGIC-CTA group. For this reason, the managers of the MAGIC-CTA group let me to contribute to the project, giving me the opportunity to have access to all the resources and to think how to improve at best the network infrastructure.

A.1 The idea behind a cloud

The main idea behind a network based on the cloud is that the manager gives you a certain amount of *resources*, both disk space or machines. Thanks to the great flexibility of the system, you can use the resources in such a way to build your own machines in a dedicate space in the network. When you build and launch your machine, you can decide its performances, such as number of CPUs, RAM, etc. After launching the machine, it works like a normal laptop, like being connected via *ssh* connection. In that machine, you are the `root` and you can install your preferred software, or attach how many volumes (hard disks) of different capacities.

[1] http://cloudveneto.it/

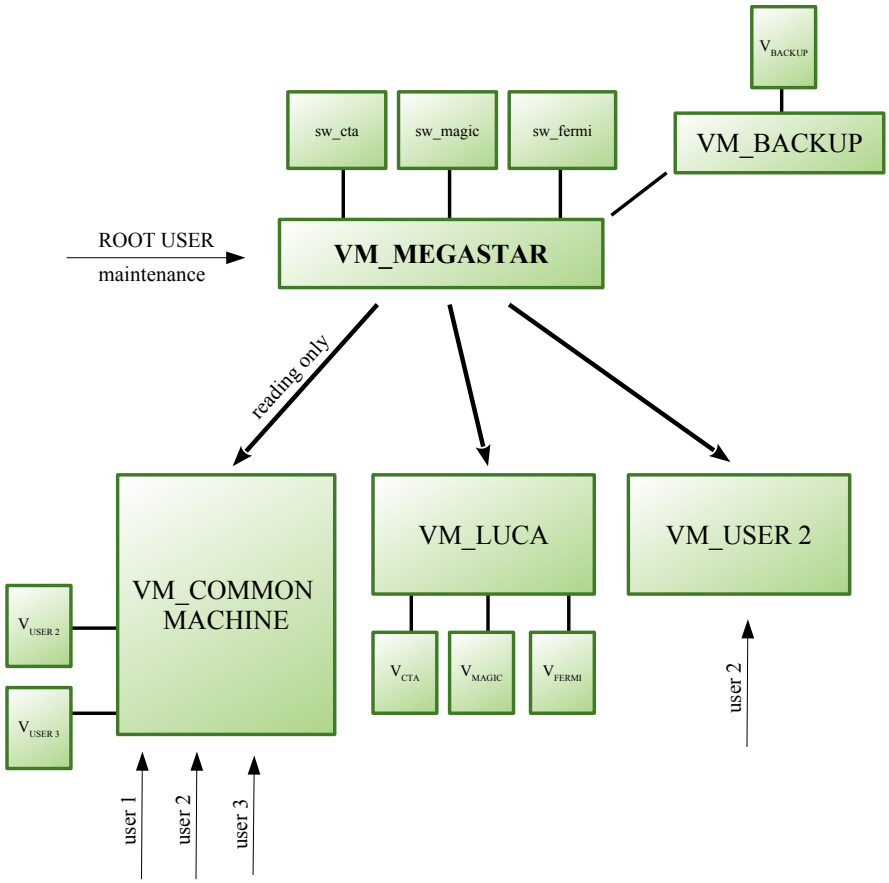

Figure A.1: *A schematic representation of the cloud system developed for the MAGIC-CTA group at the INFN of Padova.*

The maintenance of the hardware, to which the user has no direct access, is responsibility of the managers of the cloud system. The most interesting aspect is that the maintenance – if the structure is adequately built – can be completely invisible by the user, and generally does not interrupt its normal operations. In fact, the managers can temporarily *move* your virtual machines to other *nodes* (main physical machines where the virtual machines are created and hosted), and perform the maintenance of your typical *node*.

A.2 Desidered requirements and performances

The cloud system represents a powerful tool to manage resources in the more efficient way according to your needs. For sure, the structure of the cloud itself has to be projected on the needs of the group and of its users. In the case of our MAGIC-CTA group, the software generally used provides some ideal priorities:

- the software the users adopt is generally the same, and for this reason it can be installed in a common point and then shared;
- every user needs quite powerful machines, but it is rare to run continuously macros for more than some days. For this reason, the users need a lot of computational power, but for short time intervals;
- the number of users is quite limited (between 5 and 20), and they should not be worried about the cloud structure: they should be able to simply enter some machines and work in the most efficient and easy way.

Keeping in mind the previous main ideas on how the structure of the cloud should have been built, and thanks to the valuable suggestions of the cloud manager Massimo Sgaravatto, I developed a network of machines and volumes as represented in **Figure** A.1.

A.3 Structure of the cloud system in Padova

The main idea is that the `root` user is only one (generally, myself), and he takes care of the maintenance of the common software. In order to share the common software, the cloud is provided with a main machine, called `VM_MEGASTAR`. This machine is accessible only to the `root` user, and the software for the different experiments is installed there. In fact, the machine is provided with three main volumes attached:

- `sw_magic` is the volume with all the software needed for the MAGIC analyses,
- `sw_fermi` contains the software needed for the *Fermi* analyses (included the *Enrico* software, see Section 2.3.2.4),
- `sw_cta` is the volume with all the software needed for the CTA simulations and pipelines.

The software in `VM_MEGASTAR` is then shared via `nfs` network in read-only configuration to all the machines of the group. This read-only configuration is crucial for the stability of the whole cloud system and to avoid that the users modify the common software.

All the users of the MAGIC-CTA group can enter the cloud system and create their own machine. For example, in the right-hand side of **Figure** A.1, `user 2` can create its new machine called `VM_USER_2`. When the machine is created and launched into the network, few lines of code – reported in the *bash.rc* file in the user's home – attach the volumes with the common software (e.g. `sw_magic`) shared by the machine `VM_MEGASTAR` to the private machine. This simple procedure is reported in an online guide[2] that we have prepared. An example of how my machine called `VM_LUCA` works is also reported in the figure.

Thanks to the ready availability of the common software, the user can quickly start to work by first creating his own machine, and then by installing there the private software needed in dedicated volumes attached to the machine. Thanks to this method, the beginner user of the cloud system can start very quickly his analyses, without need to install the common software (every installation may take up to few hours).

Additionally, in order to simplify even further the usage of the cloud system, I created some powerful common machines – such as `VM_COMMON_MACHINE` – that all users of the group can access. By creating a home to the user, he can quickly start to work without even need to create his own machine.

In order to perform a regular backup of the common software, I created a machine called `VM_BACKUP` that manages the different backup configurations that each machine/user can request, and stores the data in a volume, named $\texttt{V}_{\texttt{backup}}$.

This represents only a schematic explanation of the main structure of this cloud system. After several months of test and problem solving phase, it has been implemented with several further simplifications and improved performances. Thanks to this computing infrastructure of the group, several students and postdocs have started working with the common software, and can perform analyses in a network of high-performances machines. At the moment, the cloud system of the MAGIC-CTA group in Padova works perfectly.

[2] https://sites.google.com/site/magicpadova/internal/come-fare-per/cloud-pd?pli=1&authuser=1

Appendix B

Unveiling a population of extreme blazars

In this Appendix, I will report some additional material concerning the hard X-ray selected sample of EHBLs presented in Section 4.3.

B.1 Multi-wavelength SEDs of the sample

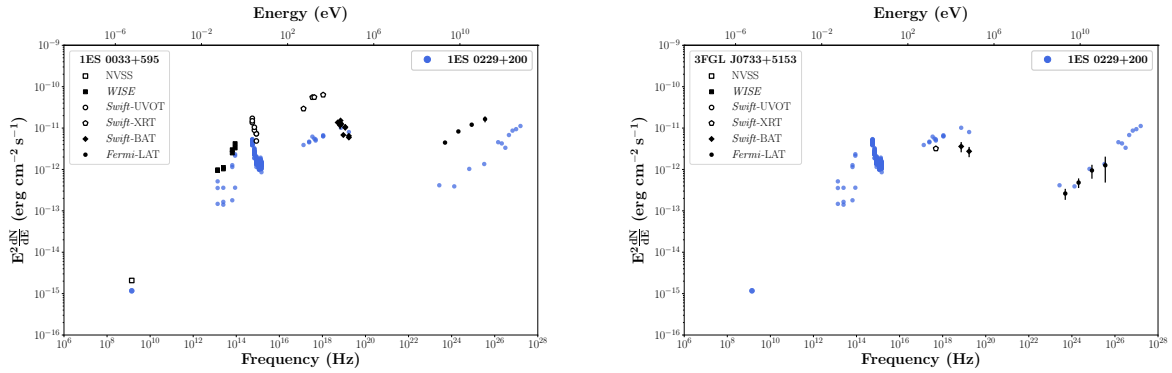

(a) 1ES 0033+595 (left) and 3FGL J0733+5153 (right).

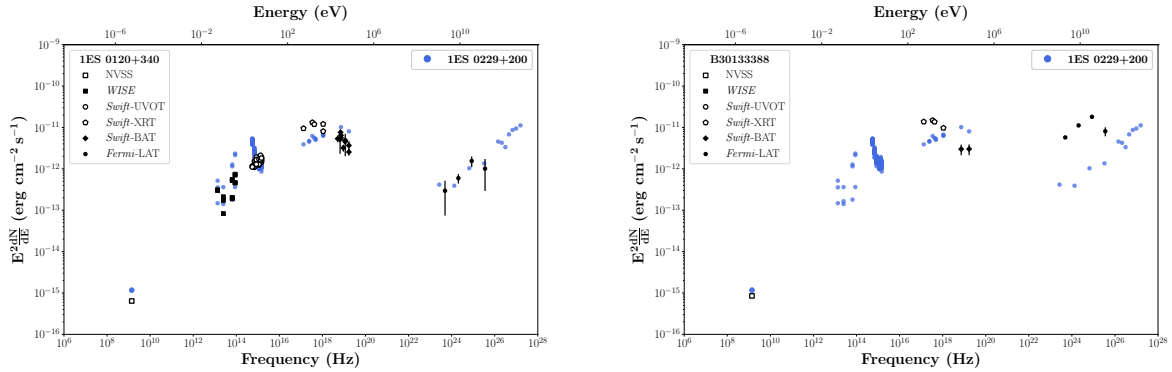

(b) 1ES 0120+340 (left) and B3 0133+388 (right).

Figure B.1

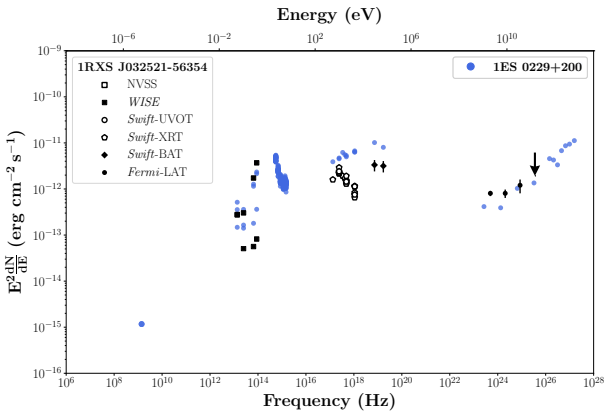

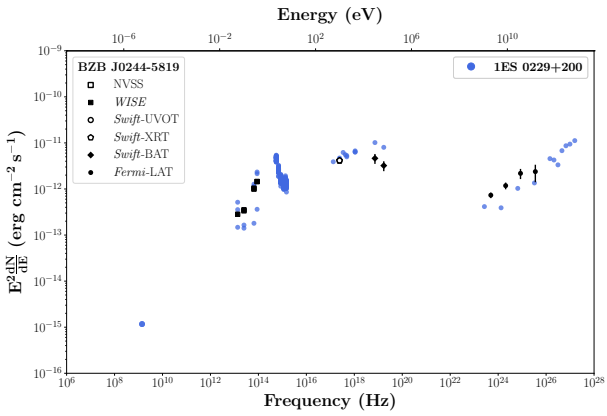

(a) 1RXS J032521-56354 (left) and BZB J0244-5819 (right).

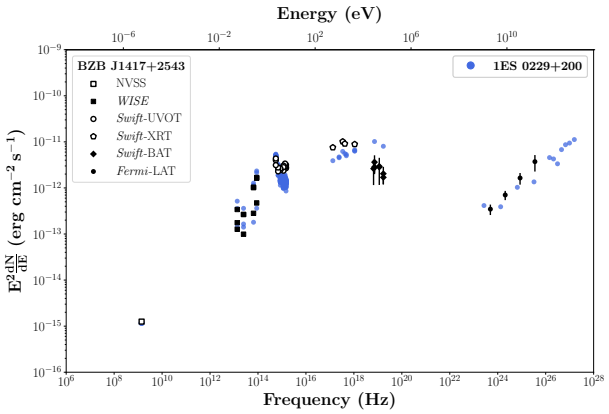

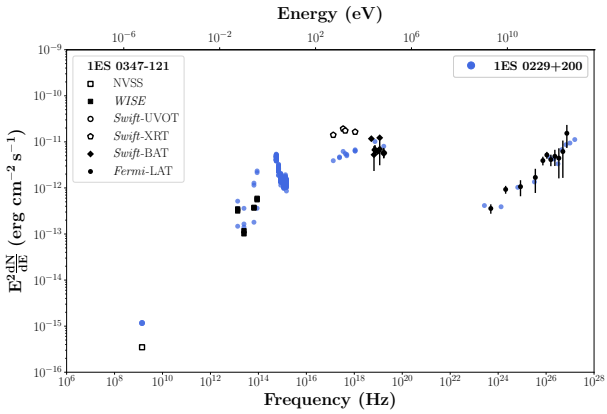

(b) BZB J1417+2543 (left) and 1ES 0347-121 (right).

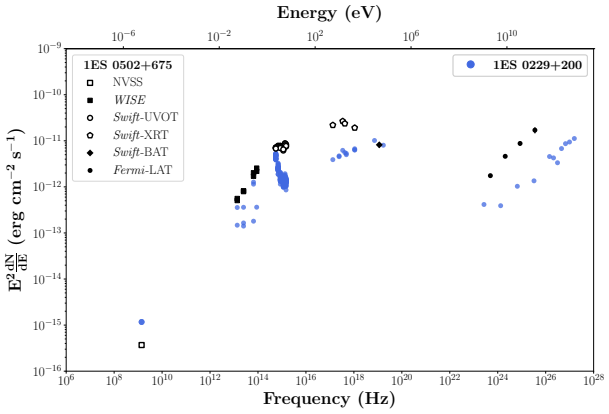

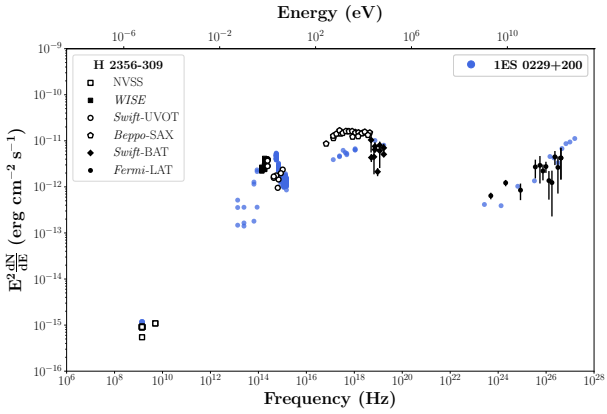

(c) 1ES 0502+675 (left) and H 2356-309 (right).

Figure B.1

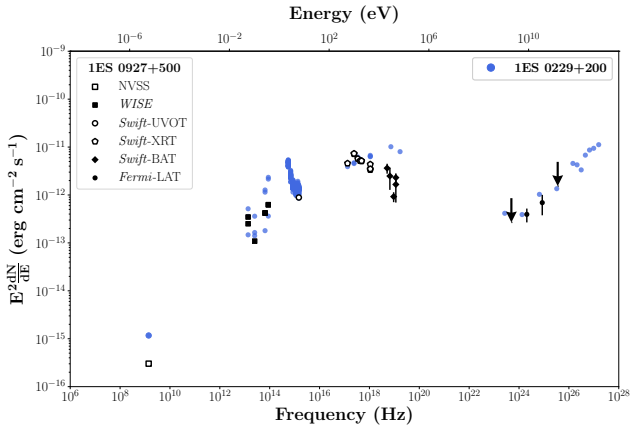

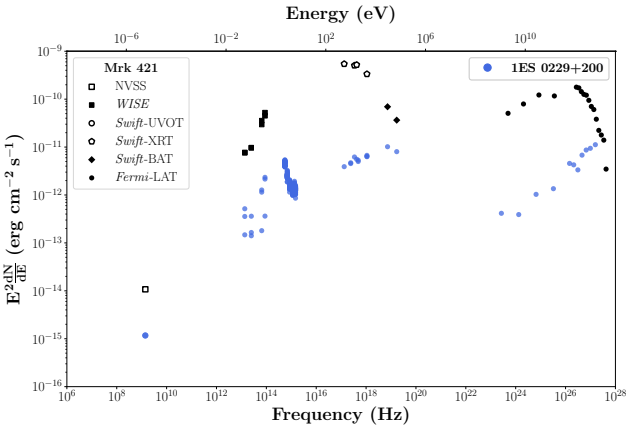

(d) 1ES 0927+500 (left) and Mrk 421 (right).

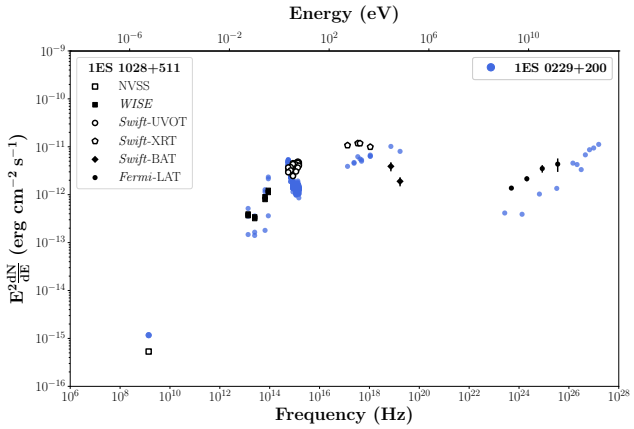

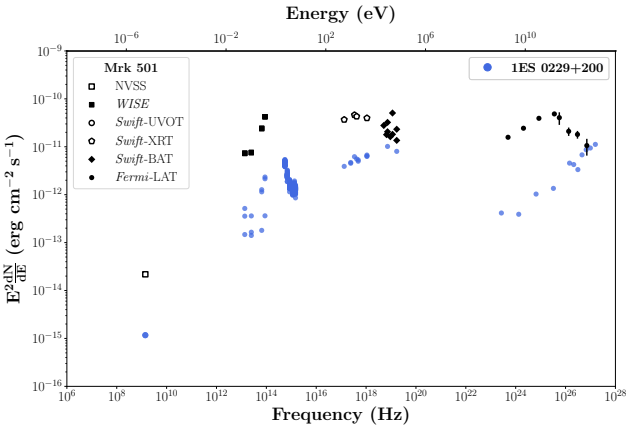

(e) 1ES 1028+511 (left) and Mrk 501 (right).

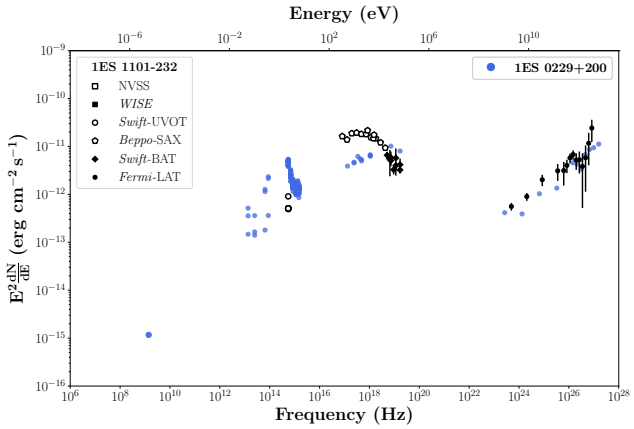

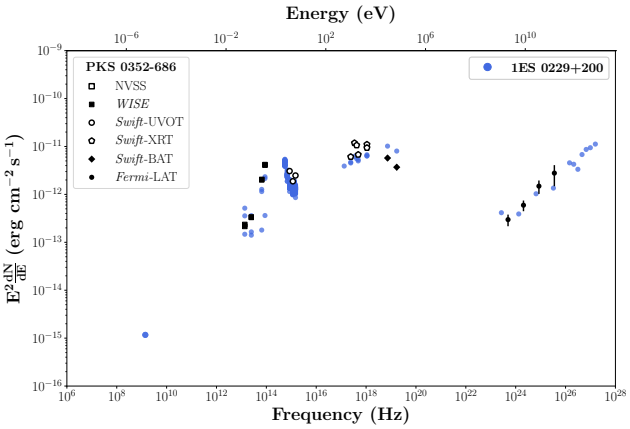

(f) 1ES 1101-232 (left) and PKS 0352-686 (right).

Figure B.1

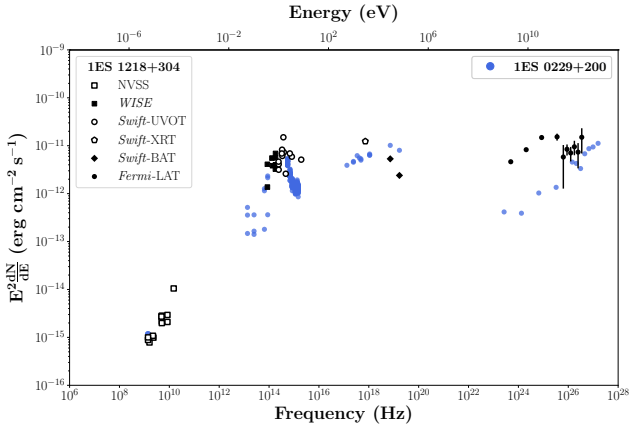

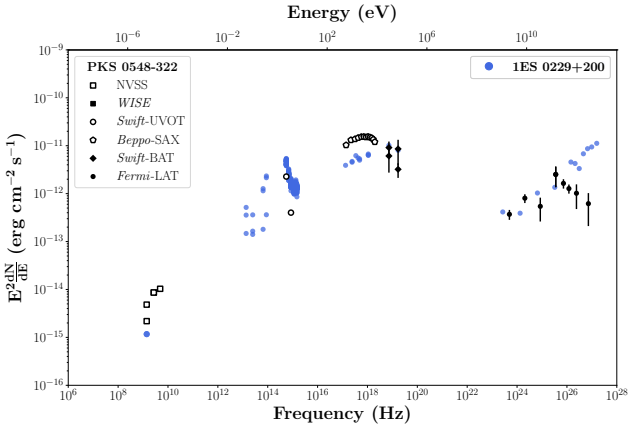

(g) 1ES 1218+304 (left) and PKS 0548-322 (right).

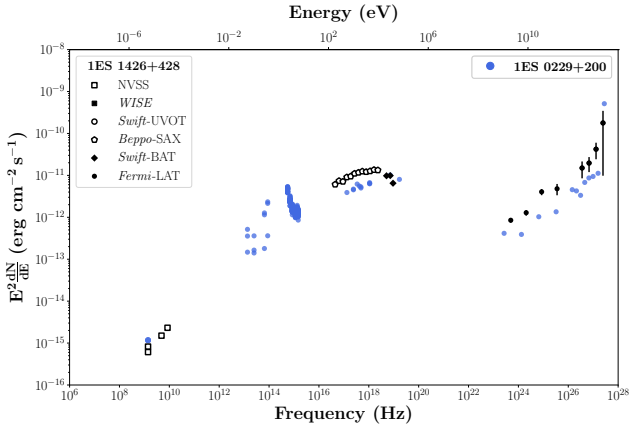

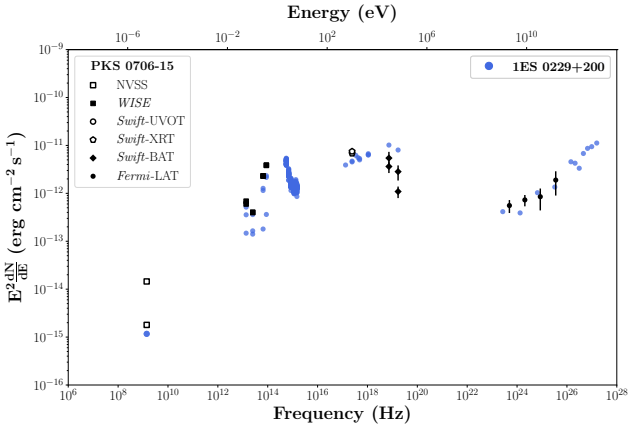

(h) 1ES 1426+428 (left) and PKS 0706-15 (right).

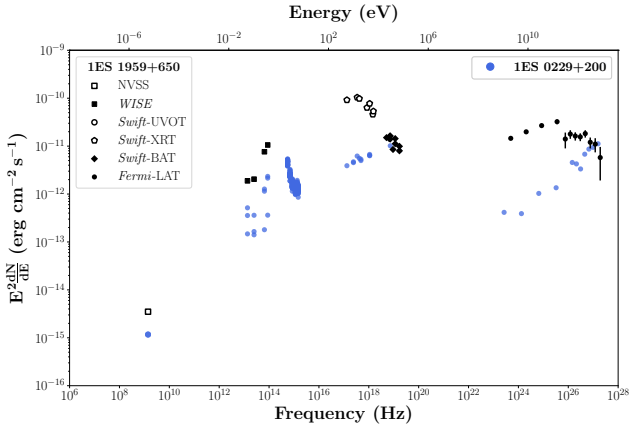

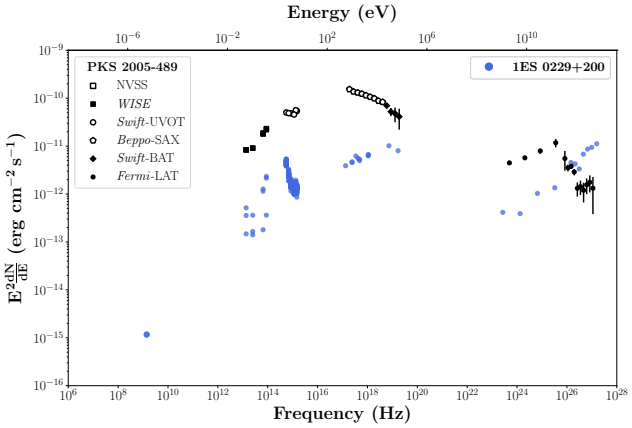

(i) 1ES 1959+650 (left) and PKS 2005-489 (right).

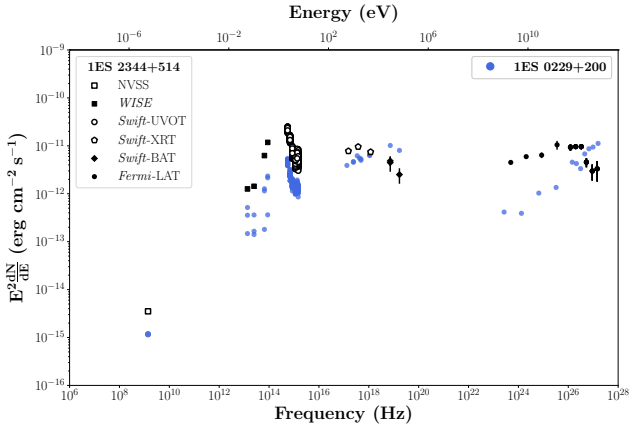

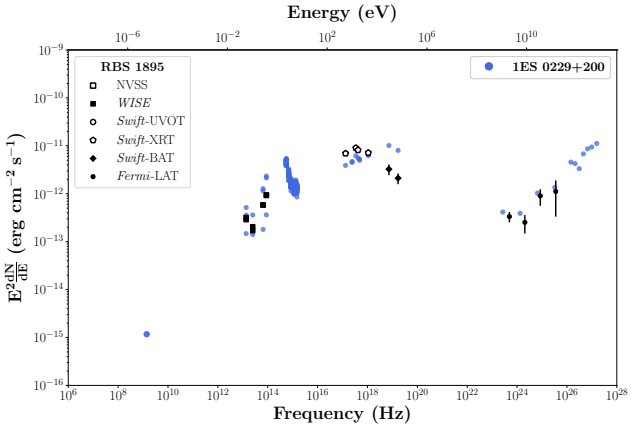

(j) 1ES 2344+514 (left) and RBS 1895 (right).

Figure B.1

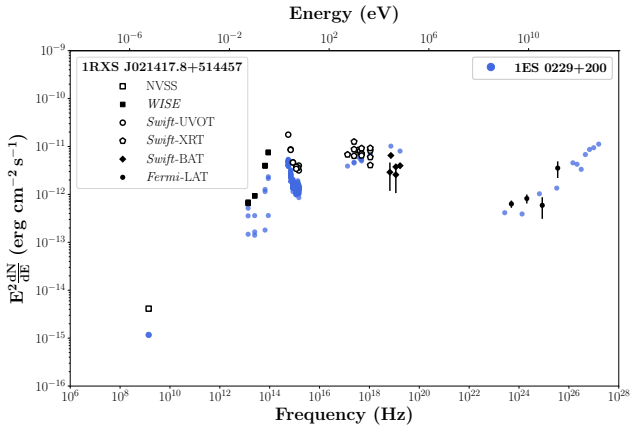

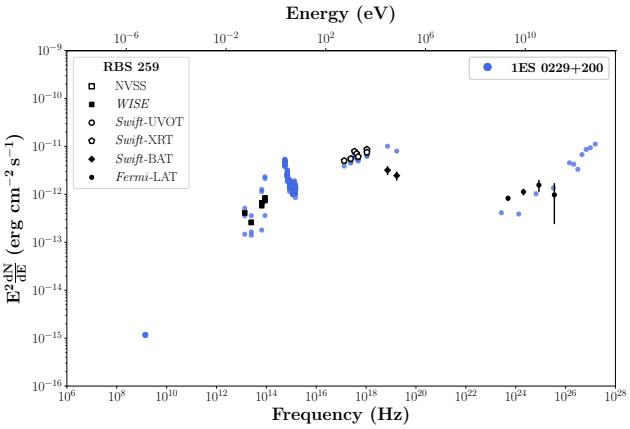

(k) 1RXS J0214178+514457 (left) and RBS 259 (right).

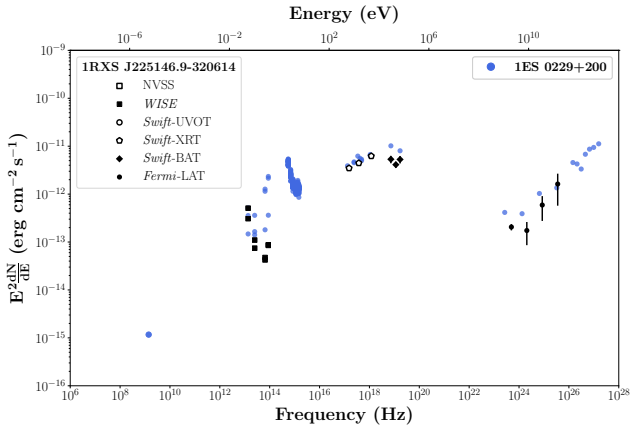

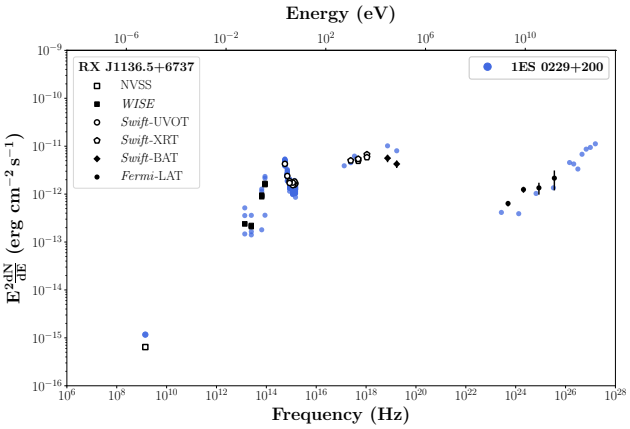

(l) 1RXS J225146.9-320614 (left) and RX J11365+6737 (right).

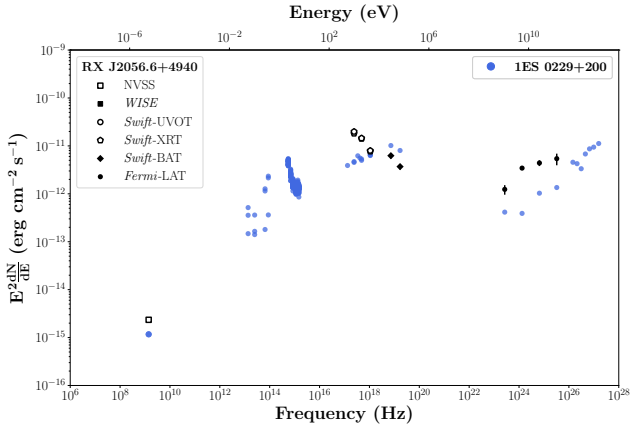

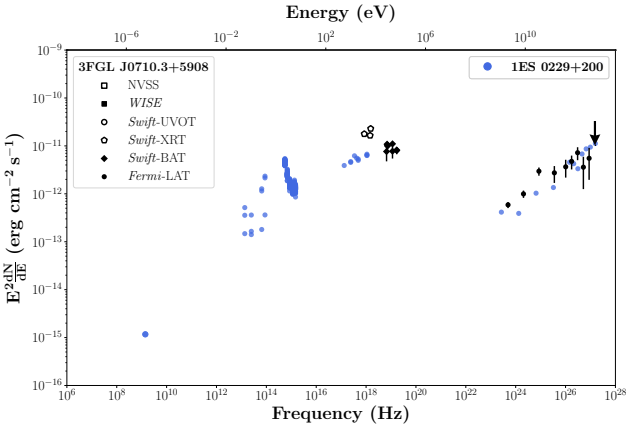

(m) RX J2056.6+4940 (left) and 3FGL J0710.3+5908 (right).

Figure B.1: *SED superimposition of SSDC (not simultaneous) archival data of EHBL objects in our sample (black symbols) and 1ES 0229+200 (blue circles), where data of 1ES 0229+200 are drawn without error bars to be better readable. We show NVSS (Condon et al., 1998) points for radio band,* WISE *points for the infrared band,* Swift-*UVOT (Giommi et al., 2012) points for the optical-UV band,* Swift-*XRT (D'Elia et al., 2013) points or the* Beppo-*SAX (Giommi et al., 2002) data (when available) for the soft-X-ray band, and* Swift-*BAT 105-months points for the hard-X-ray band. Arrows represent upper limits. Data in the HE and VHE gamma-ray bands are de-absorbed using Franceschini & Rodighiero (2017) model with the source redshift z to show the intrinsic spectra. In the HE gamma-ray band the ten-years* Fermi-*LAT data are reported. See text for further information about TeV data.*

B.2 TeV gamma-ray extrapolations

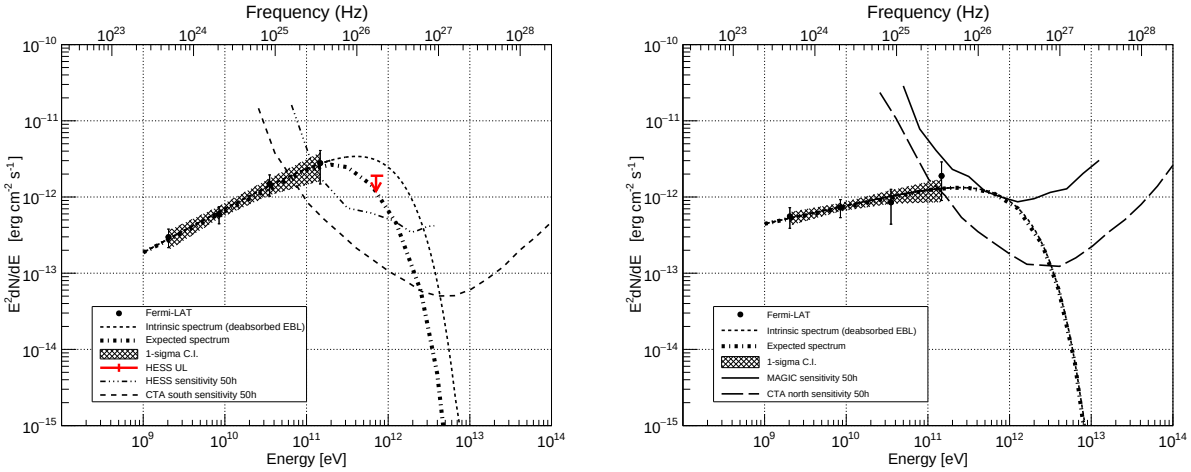

(a) PKS 0352-686 with $z = 0.085$ (left) and PKS 0706-15 with $z = 0.001$ (right).

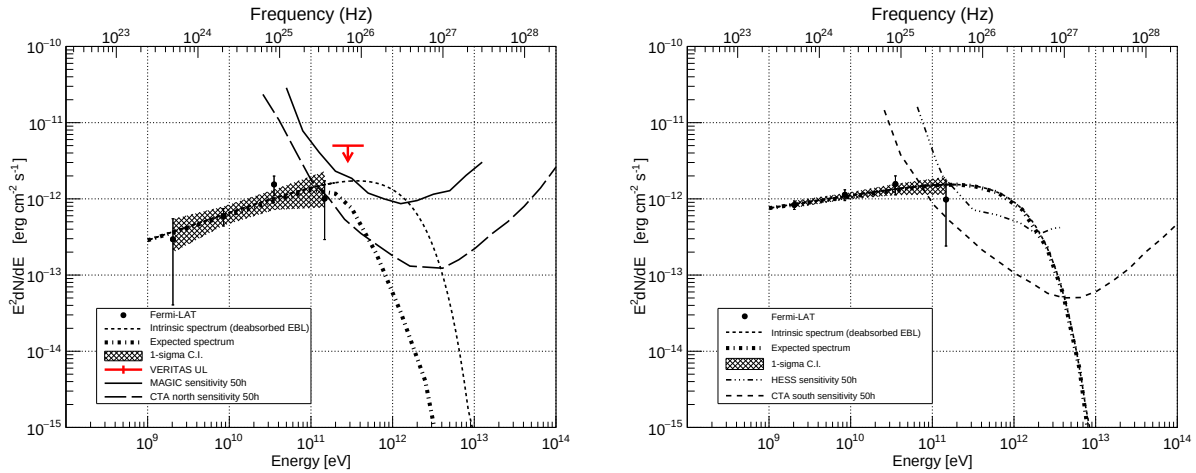

(b) 1ES 0120+340 with $z = 0.272$ (left) and RBS 259 with $z = 0.001$ (right).

Figure B.3

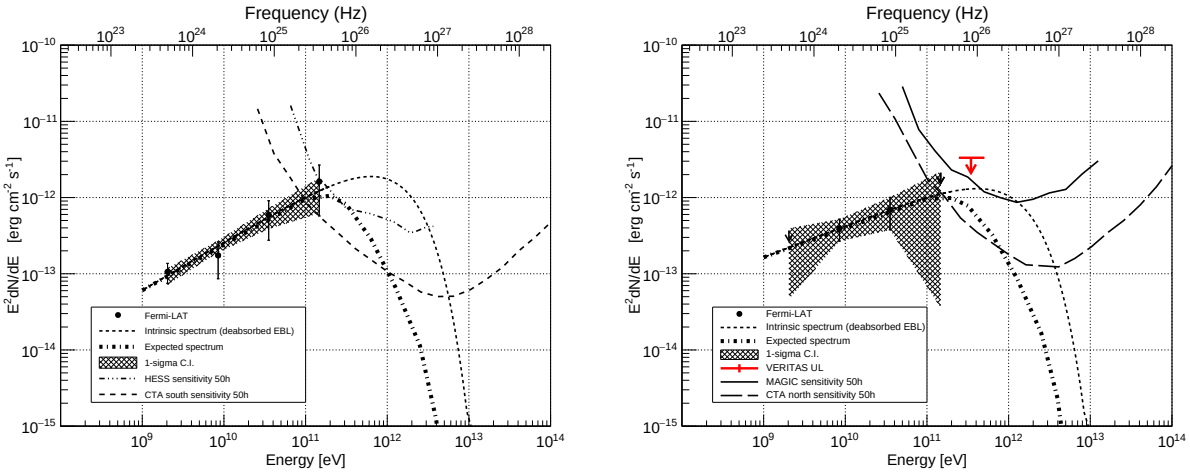

(c) 1RXS J225146.9-320614 with $z = 0.246$ (left) and 1ES 0927+500 with $z = 0.187$ (right).

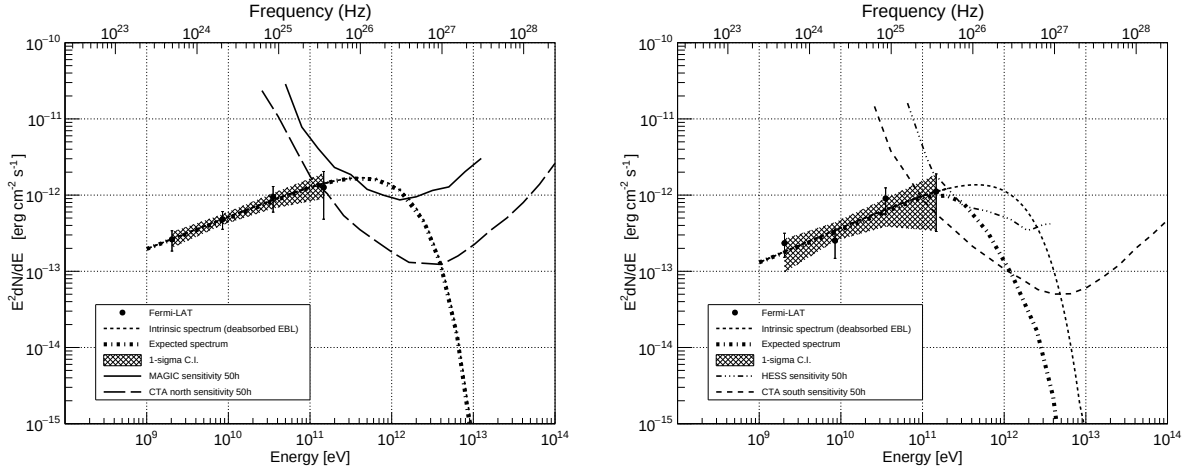

(d) 3FGL J0733.5+5153 with $z = 0.001$ (left) and RBS 1895 with $z = 0.194$ (right).

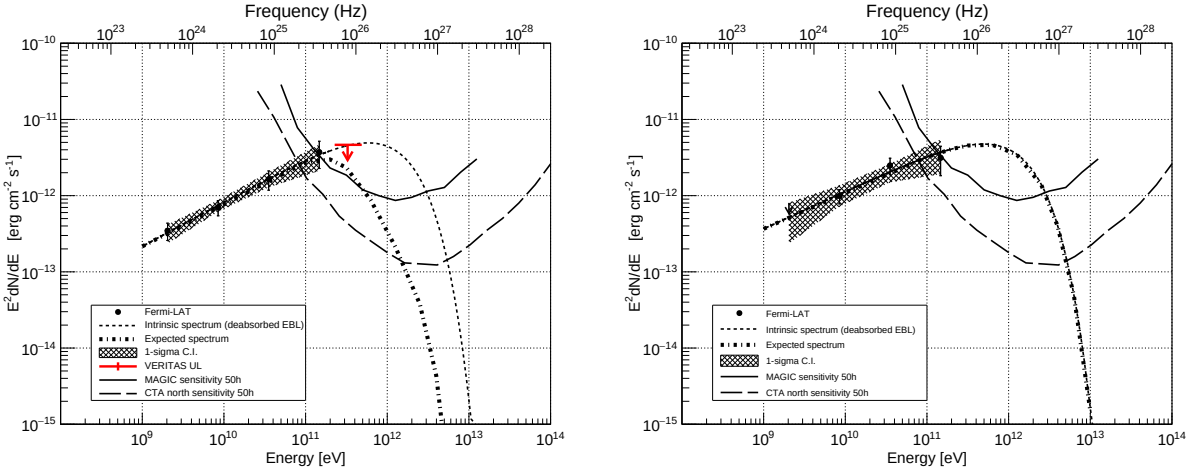

(e) BZB J1417+2543 with $z = 0.23$ (left) and TXS 0637-128 with $z = 0.001$ (right).

Figure B.3

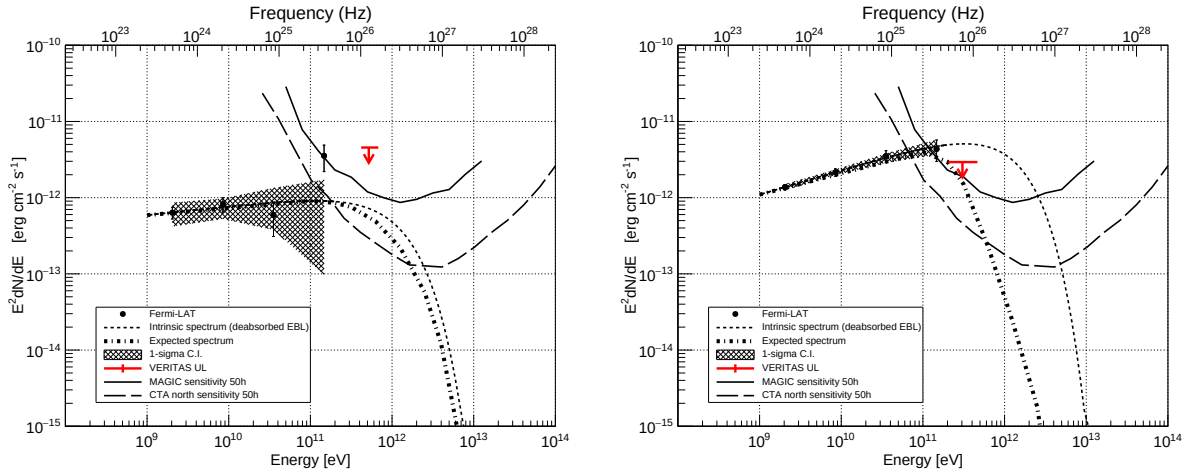

(f) 1RXS J021417.8+514457 with $z = 0.049$ (left) and 1ES 1028+511 with $z = 0.36$ (right).

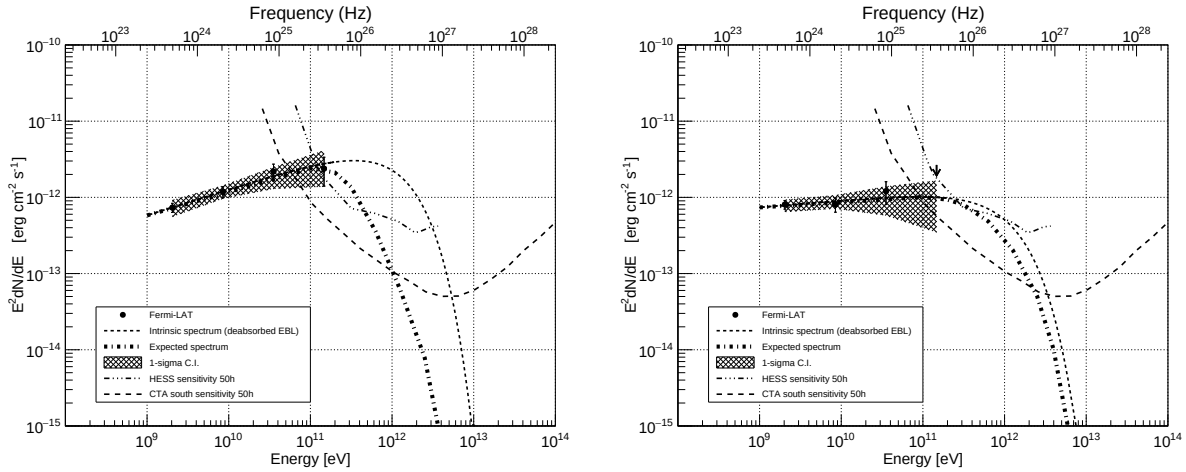

(g) BZB J0244-5819 with $z = 0.265$ (left) and 1RXS J032521.8-56354 with $z = 0.06$ (right).

Figure B.3: *Power-law extrapolation above 1 GeV of the* Fermi*-LAT data after ten years of operation (not EBL de-absorbed) of all 14 TeV gamma-ray undetected sources in our final sample in* ***Table*** *4.4. The thicker dashed line is the power-law extrapolation absorbed for EBL using the model by Franceschini & Rodighiero (2017). CTA, MAGIC (Aleksić et al., 2016b), and H.E.S.S. (Holler et al., 2016) sensitivities for 50h of observations are also reported in the plots. The available upper-limits on the already observed sources by the VERITAS telescopes (Archambault et al., 2016) and by the H.E.S.S. telescopes (Abramowski et al., 2014a) are reported.*

Appendix C

MAGIC paper on PGC 2402248

In this Appendix, the results of the MWL observations concerning the MAGIC paper on the discovery of the EHBL PGC 2402248 at TeV gamma-ray energies are included. The nightly fluxes obtained in the VHE band as observed by MAGIC telescopes are given in **Table** C.1. The 2-year fluxes obtained in the HE band with the *Fermi*-LAT telescope are reported in **Table** 5.2 on page 206. In **Table** C.2 and **Table** C.3 I report the information from all the observations of the source with the *Swift*-XRT and *Swift*-UVOT instruments, respectively. The details of the optical observations performed with the KVA telescope are reported in **Table** C.4.

C.1 *Fermi*-LAT analysis

For this work, a region of interest (ROI) centered around PGC 2402248 (4FGL J0733.4+5152) with a radius of 7° was selected. The data sample included more than ten years of data collected by *Fermi*-LAT, from 2008 August 4 to 2019 June 24 (MJD 54682-58658). The data reduction of the events of the Pass8 `source` class was performed with the Science-Tools software package version v11r5p3 in the energy range 0.5-300 GeV. To reduce Earth limb contamination a zenith angle cut of 90° was applied to the data. The binned likelihood fit of the data was performed using the recommended Galactic diffuse emission model (see e.g., Acero et al., 2016) and isotropic component recommended for Pass8 (P8R2) `source` event class[1].

The normalizations of both diffuse components in the source model were allowed to freely vary during the spectral fitting. In addition to the source of interest, all the sources included in the 4FGL catalogue (*Fermi*-LAT collaboration, 2019) within a distance of 14 degrees from the source of interest were included. We build the likelihood model including all the 4FGL sources within 14 degrees from the position. For the likelihood minimization we leave free to vary the spectral parameters of the sources in the region within 5 degrees from the centre of the RoI and fixed them to their catalogue. values outside. The binned likelihood fit was carried out in two steps, After a first fit, the targets with Test Statistics (TS) < 2 were removed from the model. After that cut, a final likelihood fit was carried out. We did not find significant residuals, which could suggest the presence of additional sources in the ROI. PGC 2402248 was detected with a TS=138.8, a flux of $F(0.5-300\text{GeV}) = (1.3\pm0.5)\times10^{-9}$ ph cm^{-2} s^{-1} and a hard spectral index of $\Gamma = 1.73 \pm 0.11$ (compatible with the value reported in the 4FGL catalogue, $\Gamma_{4FGL} = 1.80 \pm 0.10$). The same analysis is carried out in 2-year time bins to study the flux evolution of the source. The results are shown in **Table** 5.2 on page 206.

[1] `https://fermi.gsfc.nasa.gov/ssc/data/access/lat/BackgroundModels.html`

C.2 Tables

Date	Effective time	$\text{Flux}_{>200\ \text{GeV}}$
MJD	s	10^{-12} ph cm^{-2} s^{-1}
58141.1	2762	< 9.46
58142.1	2584	< 12.35
58143.1	2331	< 19.45
58144.1	2392	< 16.00
58164.1	2350	< 8.41
58165.1	2350	< 3.09
58167.1	2442	< 8.09
58169.0	3355	< 12.23
58171.0	7938	2.97 ± 1.86
58185.9	1363	< 10.59
58190.0	3126	< 13.40
58194.0	5047	3.68 ± 2.51
58194.9	4372	< 10.41
58195.9	2350	5.92 ± 3.92
58196.9	2350	< 12.20
58198.9	4598	< 10.64
58199.9	5550	< 7.50
58210.9	3496	< 11.93
58211.9	7010	< 6.75
58213.9	4682	5.11 ± 2.77
58226.9	2342	< 16.05

Table C.1: *Flux (points and 95% C.L. upper limits) and effective observing time of the source PGC 2402248 registered by the MAGIC telescopes.*

Date	MJD	Exposure	$F_{2-10keV}$	$F_{0.3-10keV}$	Γ_X	χ^2/d.o.f.	Obs. ID
		s	10^{-11} erg cm^{-2} s^{-1}	10^{-11} erg cm^{-2} s^{-1}			
2009-12-30	55195.8	1061	1.36 ± 0.16	2.12 ± 0.17	1.71 ± 0.08	15.59/17	00038675001
2011-02-20	55612.2	9872	0.84 ± 0.03	1.34 ± 0.04	1.76 ± 0.03	117.16/112	00045364001
2011-02-24	55616.4	492	0.57 ± 0.18	1.13 ± 0.19	2.07 ± 0.21	0.38/3	00045364002
2014-01-11	56668.7	1096	1.90 ± 0.16	2.99 ± 0.16	1.73 ± 0.06	20.17/25	00048299002
2014-01-12	56669.7	994	1.91 ± 0.17	2.89 ± 0.19	1.67 ± 0.07	17.44/21	00048299003
2018-01-26	58144.1	1326	1.32 ± 0.11	1.95 ± 0.10	1.62 ± 0.06	27.66/25	00010541001
2018-02-07	58156.0	1364	1.03 ± 0.09	1.72 ± 0.09	1.82 ± 0.06	22.24/26	00010541002
2018-02-15	58164.0	1059	1.62 ± 0.20	2.27 ± 0.19	1.51 ± 0.09	20.33/16	00010541003
2018-02-22	58171.9	1004	1.80 ± 0.19	2.58 ± 0.20	1.55 ± 0.07	19.94/18	00010541004
2018-03-06	58183.9	1441	1.14 ± 0.10	1.79 ± 0.11	1.72 ± 0.07	26.28/25	00010541006
2018-03-12	58190.0	1419	1.40 ± 0.12	2.08 ± 0.13	1.62 ± 0.06	22.83/29	00010541007
2018-04-08	58216.4	1094	1.42 ± 0.12	2.18 ± 0.14	1.68 ± 0.07	29.56/23	00010541009
2018-04-19	58227.9	1136	1.09 ± 0.09	1.84 ± 0.11	1.84 ± 0.07	38.97/24	00010541010

Table C.2: *Results of Swift-XRT data analysis for the observations of PGC 2402248. I report for each observation the MJD, the exposure obtained by XRT, and the two integral fluxes between 2-10 keV and 0.3-10 keV. Every individual spectrum can be well fitted by a power-law function with spectral index Γ_X and good reduced χ^2. In addition to the simultaneous observations with MAGIC, the results from historical observations are also included for comparison purposes.*

Band	Date	MJD	Flux	Compatibility
			10^{-12} erg cm^{-2} s^{-1}	with average flux
U	2011-02-20	55612	1.79 ± 0.10	0.4
	2011-02-24	55616	1.76 ± 0.11	0.1
	2014-01-11	56668	2.38 ± 0.10	5.8
	2018-01-26	58144	1.74 ± 0.08	0.1
	2018-02-07	58156	1.82 ± 0.09	0.7
	2018-02-15	58164	1.63 ± 0.10	1.1
	2018-04-08	58216	1.88 ± 0.11	1.1
W1	2009-12-30	55195	1.40 ± 0.11	0.6
	2018-02-22	58171	1.26 ± 0.10	0.0
	2018-03-06	58183	1.21 ± 0.11	0.2
	2018-04-19	58227	1.29 ± 0.11	0.1
W2	2011-02-20	55612	1.15 ± 0.10	0.3
	2014-01-12	56669	1.83 ± 0.11	4.6
	2018-03-12	58189	1.18 ± 0.08	

Table C.3: *Results of Swift-UV data analysis for the observations of PGC 2402248. I report the energy band of the UVOT instrument, the date and MJD of the observation, the integral flux, and the compatibility between each value and the average flux for only 2018 data simultaneous to MAGIC observations. The compatibility has been computed as $\lambda = \frac{|A-B|}{\sqrt{\sigma_A^2+\sigma_B^2}}$, for a given two fluxes with values A and B and their respective uncertainties (σ_A and σ_B). where for example A is a flux value and B is the average flux reported in the text.*

MJD	Flux
	10^{-4} Jy
58210.500	4.01 ± 0.38
58211.462	3.87 ± 0.39
58212.467	3.89 ± 0.39
58214.479	3.94 ± 0.41
58215.455	3.61 ± 0.60
58218.508	3.85 ± 0.37
58219.465	3.48 ± 0.40
58222.487	4.10 ± 0.40
58226.473	3.55 ± 0.39
58232.497	3.84 ± 0.41
58233.469	2.98 ± 0.44
58241.482	4.00 ± 0.39
58403.851	4.07 ± 0.38
58423.835	3.98 ± 0.39
58471.822	4.41 ± 0.38
58478.822	4.09 ± 0.38
58481.804	4.00 ± 0.38
58482.743	3.94 ± 0.38
58488.802	3.92 ± 0.37

Table C.4: *Optical R-band flux of PGC 2402248 as measured by the KVA telescope. The data have already been corrected by host galaxy subtraction.*

Appendix D

MAGIC paper on new EHBLs in TeV gamma rays

In this Appendix, I will report some additional material concerning the sample of new TeV gamma-ray detected EHBLs presented in Section 5.2.

D.1 Tables

Source name	$\gamma_{\rm br}$ [$\times 10^5$]	$\gamma_{\rm max}$ [$\times 10^6$]	p_1	p_2	B_0 [G]	$L_{\rm e} \times 10^{44}$ [erg s^{-1}]	Γ	$\log^\star \nu^{\rm sync}_{\rm peak}$ [Hz]	$\log^\star \nu^{\rm IC}_{\rm peak}$ [Hz]	CD*†	$U_B/U_{\rm e}^\star$ [$\times 10^{-3}$]	VHE?
TXS 0210+515	10.0	20.0	2.5	3.0	0.04	6.50	20	18.3	25.7	0.18	0.19	Y
TXS 0637-128	5.0	20.0	1.8	3.0	0.25	0.80	10	17.7	25.4	0.2	81.00	N
BZB J0809+3455	1.0	3.0	1.8	3.0	0.04	0.89	10	16.4	25.4	0.84	1.40	N
RBS 0723	—	2.0	2.2	—	0.11	4.90	20	18.1	25.8	0.37	1.90	Y
1ES 0927+500	3.0	3.0	1.5	2.5	0.13	0.71	10	17.6	25.9	0.25	23.00	N
1ES 1426+428	—	2.0	2.0	—	0.20	1.30	20	18.2	25.8	0.14	26.00	Y
1ES 2037+521	—	2.0	2.1	—	0.02	2.30	20	18.1	26.4	0.33	0.14	Y
RGB J2042+244	—	0.3	2.0	—	0.07	1.80	20	17.1	25.6	0.36	2.30	H
RGB J2313+147	0.8	20.0	2.0	3.5	0.09	1.60	20	16.5	25.3	0.37	3.90	N
1ES 0229+200	10.0	300.0	1.9	3.0	0.06	1.10	20	18.6	26.6	0.13	2.50	Y

Table D.1: *Model parameters and obtained physical values for the SSC conical jet scenario. Columns from left to right: source name; break and maximum electron Lorentz factor; spectral index of the electron energy distribution below and above $\gamma_{\rm br}$; magnetic field; electron luminosity; bulk Lorentz factor of the jet; synchrotron and IC peak frequency resulting from the model; Compton dominance parameter; ratio between the magnetic and electron energy density evaluated at the radius where the electron injection shuts down; and the source detection status at VHE gamma rays (Y: detected, N: not detected, and H: hint of signal)*

Source name	$\gamma_{\rm b}$ $[\times 10^4]$	$\gamma_{\rm max}$ $[\times 10^6]$	n_1	n_2	B [G]	K [cm^{-3}]	$R \times 10^{15}$ [cm]	$U_B/U_{\rm e}^{\star}$	$L_{\rm j}^{\star} \times 10^{42}$ [erg s^{-1}]
TXS 0210+515	33.0	0.8	1.40	2.30	0.15	25.0	5.1	1.25	2.50
RBS 723	0.3	0.8	1.40	2.30	0.35	15.0	5.1	1.17	14.60
1ES 1426+428	3.0	2.0	1.40	2.90	0.34	3.5	7.1	1.07	20.50
1ES 2037+521	13.0	2.0	1.40	3.00	0.40	2.9	1.3	0.75	0.97
RGB J2042+244	2.0	2.0	1.40	2.95	0.30	3.0	4.8	1.21	7.00
1ES 0229+200	13.0	6.0	1.40	3.40	0.40	2.6	3.2	0.74	6.30

Table D.2: *Model parameters and obtained physical values for the spine-layer scenario for the sources with VHE gamma rays spectral determination. Columns from left to right: source name; break and maximum electron Lorentz factor; spectral index of the electron energy distribution below and above $\gamma_{\rm b}$; magnetic field; normalization of the electron distribution; radius of the emission zone; ratio between the magnetic and electron energy density of the layer; kinetic luminosity of the jet.*

Source name	$\gamma_{e,\max}$	α_1	α_2	B	$K_e \times 10^{-3}$	$R \times 10^{14}$	$\gamma_{p,\max}$	η	$u_B^\star$	$u_p/u_B^\star$	$L^{\star\dagger} \times 10^{46}$
	$[\times 10^4]$			[G]	[cm^{-3}]	[cm]	$[\times 10^9]$	[erg cm^{-3}]	$[\times 10^{-5}]$	$[\times 10^{-5}]$	[erg s^{-1}]
TXS 0210+515	1.0–15.9	1.30	2.30	1.9–468	0.002–4890	1–1480	1.7–48.9	0.06–4.9	0.15–8710	0.008–47.8	0.10–48.1
RBS 0723	1.1–16.5	1.25	2.25	2.1–468	0.035–68640	1–1300	1.6–28.0	0.12–3.5	0.18–8710	1.1–1300	0.10–32.4
1ES 1426+428	1.2–15.9	1.25	2.25	2.0–344	0.09–120000	1–1380	1.6–21.0	0.07–1.7	0.17–4710	2.8–1070	0.11–18.2
1ES 2037+521	1.1–15.6	1.30	2.30	2.0–401	0.002–7810	1–1480	1.6–29.2	0.16–6.6	0.15–6410	0.06–103	0.10–35.3
RGB J2042+244	1.0–15.6	1.50	2.50	2.0–468	0.09–150000	1–1410	1.6–33.5	0.80–38.0	0.16– 871	0.06–234	0.11–46.5
1ES 0229+200	1.1–13.7	1.10	2.10	2.8–468	0.004–11130	1–1360	1.9–33.2	0.004–0.14	0.31–8710	0.11–140	0.15–45.6

Table D.3: *Model parameters and obtained physical values for the hadronic scenario for the sources with VHE gamma rays spectral determination. Columns from left to right: minimum electron Lorentz factor; spectral index of the electron/proton energy distribution below and above γ_{break}; magnetic field; normalization of the electron distribution; radius of the emission zone; maximum proton Lorentz factor; efficiency of the acceleration mechanism ; magnetic energy density; ratio between the proton and magnetic energy density; luminosity of the emission region.*

Acronyms

1FGL	First *Fermi*-LAT catalog
2FGL	Second *Fermi*-LAT catalog
3FGL	Third *Fermi*-LAT catalog
4FGL	Fourth *Fermi*-LAT catalog
a.s.l.	above sea level
ACD	Anti-coincidence
ACS	ALMA Common Software
ADC	Analog-to-Digital Converter
AGILE	Astrorivelatore Gamma ad Imagini Leggero
AGN	Active Galactic Nucleus
ALMA	Atacama Large Millimeter/submillimeter Array
AMC	Active Mirror Control
AP	After Pulse
ARC	Astrophysical Research Consortium
ASIC	Application-Specific Integrated Circuit
ATEL	The Astronomers' telegram
Az	Azimuth
BAT	Burst Alert Telescope
BGO	Bismuth germanate scintillators
BH	Black Hole
BLR	Broad line region of AGNs
BZB	BZB catalog
C	Carbon
C.L.	Confidence Level
C.U.	Crab Units
CALLISTO	CALibrate LIght Signals and Time Offsets
CC	Central Control
CCD	Charge-Coupled Device
CH	Counting House
ClusCo	Cluster Control
CMB	Cosmic Microwave Background
CORSIKA	COsmic Ray SImulations for KAscade
CR	Cosmic Ray
CTA	Cherenkov Telescope Array
CTAC	Cherenkov Telescope Array Consortium
CTAO	Cherenkov Telescope Array Observatory
CV	Cataclysmic Variable
DAQ	Data AcQuisition
DC	Direct Current
DISP	Distance between the Image centroid and the Source Position
DM	Dark Matter
DOF	Degree of freedom
DOM	Data Operation manual

DRS4	Domino Ring Sampler version 4
DT	Discriminator Threshold
EAS	Extended Air Shower
EBL	Extragalactic Background Light
EC	External Compton
ECC	Embedded Camera Controller
EGMF	Extragalactic Magnetic Field
EHBL	Extreme High-energy peaked BL Lac object
EHSP	Extreme High-synchrotron peaked BL Lac object
EHT	Event Horizon Telescope
EM	Electromagnetic
ERIC	European Research Infrastructure Consortium
ESA	European Spatial Agency
ESCS	Enhanced Single-dish Control System
ESO	European Southern Observatory
FADC	Flash Analog-to-Digital Converter
Fe	Iron
FIR	Far Infrared
Flute	FLUx vs Time and Energy
Fluxlc	FLUX and Light Curve
FoV	Field of View
FPGA	Field Programmable Gate Array
FR	Full Range Energy
FRB	Fast Radio Burst
FSRQ	Flat Spectrum radio quasars
FWHM	Full Width Half Maximum
GBM	GLAST Burst Monitor
GCN	Gamma-ray Coordinate Network
GPS	Global Positioning System
GRB	Gamma-Ray Burst
GZK	Greisen-Zatsepin-Kuzmin
H	Hydrogen
H.E.S.S.	High Energy Stereoscopic System
HAWC	High Altitude Water Cherenkov
HBL	High-energy peaked BL Lac object
HE	High Energy
He	Helium
HGPS	H.E.S.S. Galactic Plane Survey
HID	Hardness-Intensity Diagram
HJD	Heliocentric Julian Day
HPD	Hybrid Photo Detector
HS	Hard State
HSP	High-synchrotron peaked BL Lac object
HV	High Voltage
IACT	Imaging Atmospheric Cherenkov Telescope
IBL	Intermediate High-energy peaked BL Lac object
IC	Inverse Compton
IFAE	Institut de Fisica d'Altes Energies
INAF	Istituto Nazionale di Astrofisica (Italian National istitute of Astrophysics)
INFN	Istituto Nazionale di Fisica Nucleare (Italian National istitute of Nuclear Physics)
IPR	Individual Pixel Rate
IPRC	Individual Pixel Rate Control
IR	Infrared
IRA	Istituto di Radio Astronomia (Italian Istitute of Radio Astronomy)
IRF	Instrument Response Function
ISM	Interstellar Medium

ISP	Intermediate-synchrotron peaked BL Lac object
JD	Julian Day
KoP	Key Observation Program
L_{Edd}	Eddington luminosity
L0	Trigger Level 0
L1	Trigger Level 1
L3	Trigger Level 3
LAT	Large Area Telescope
LBL	Low High-energy peaked BL Lac object
LE	Low Energy
LED	Light-Emitting Diode
LGS-AO	Laser Guide Star Adaptive Optics
LHC	Large Hadron Collider
LIDAR	LIght Detection And Ranging
LMXB	Low-Mass X-ray Binary
LSP	Low-synchrotron peaked BL Lac object
LST	Large Size Telescope
LUT	Look-Up Table
LVDS	Low-Voltage Differential Signaling
MAGIC	Major Atmospheric Gamma-ray Imaging Cherenkov
MARS	MAGIC Analysis and Reconstruction Software
MC	Monte Carlo
MERPP	MERging and Prepoccesing Program
MHD	Magnetohydrodynamic
MJD	Modified Julian Day
MOLA	MAGIC OnLine Analysis
MoU	Memorandum of Understanding
MRK	Markarian
MST	Medium Size Telescope
NIR	Near-infrared
NN	Next Neighbour
NS	Neutron Star
NSB	Night Sky Background
O	Oxygen
OfWP	Off from Wobble Partner
OVRO	Owens Valley Radio Observatory
PACTA	Pre-Amplifier for the Cherenkov Telescope Array
PCB	Printed Circuit Board
PDB	Power Distribution Box
PDF	Probability Density Function
phe	photoelectrons
PMT	Photomultiplier Tube
PSF	Point Spread Function
PSU	Power Supply Unit
PWN	Pulsar Wind Nebula
QC	Quality Control
QE	Quantum Efficiency
RF	Random Forest
RMS	Root Mean Square
RoI	Region of Interest
RPP	Rotation-Powered Pulsar
SCT	Schwarzschild-Couder Telescope
SDM	Standard Disk Model
SED	Spectral Energy Distribution
Si	Silicon
SMBH	Super-Massive Black Hole

SN	Supernova
SNR	Signal to Noise ratio
SORCERER	Simple, Outright Raw Calibration; Easy, Reliable Extraction Routines
SPD	Surge Protection Device
SPE	Single Photoelectron
SS	Soft State
SSC	Synchrotron Self Compton
SSDC	Science Space Data Center
SSRQ	Steep Spectrum radio quasars
SST	Small Size Telescope
SUMT	SumTrigger
TIB	Trigger Interface Board
TNG	Telescopio Nazionale Galileo (National Italian Telescope Galileo)
TPU	Trigger Processing Unit
TS	Test Statistics
UHE	Ultra-High-Energy
UL	Upper limit
UPS	Uninterruptible power supply
UV	Ultraviolet
VERITAS	Very Energetic Radiation Imaging Telescope Array System
VHE	Very High Energy
VLBI	Very-long-baseline interferometry
VLZA	Very-large-zenith observations
WCD	Water Cherenkov Detector
WIMP	Weakly interaction massive particles
Zd	Zenith distance

Bibliography

Aartsen M. G., et al., 2017, Journal of Instrumentation, 12

Aartsen M. G., et al., 2018a, Adv. Space Res., 62, 2902

Aartsen M. G., et al., 2018b, Science, 361, eaat1378

Abdalla H., et al., 2018, A&A, 612, A1

Abdalla H., et al., 2019, ApJ, 870, 93

Abdo A. A., et al., 2010a, ApJS, 188, 405

Abdo A. A., et al., 2010b, ApJ, 708, 1310

Abdo A. A., et al., 2010c, ApJ, 716, 30

Abdo A. A., et al., 2011a, ApJ, 736, 131

Abdo A. A., et al., 2011b, The Astrophysical Journal, 736, 131

Abramowski A., et al., 2012, ApJ, 746, 151

Abramowski A., et al., 2014b, Astron. Astrophys., 564, A9

Abramowski A., et al., 2014a, A&A, 564, A9

Acciari V. A., et al., 2009, Astrophys. J., 695, 1370

Acciari V. A., et al., 2010, ApJ, 715, L49

Acciari V. A., et al., 2011, ApJ, 738, 169

Acciari V. A., et al., 2019, MNRAS, 486, 4233

Acero F., et al., 2015, ApJS, 218, 23

Acero F., et al., 2016, ApJS, 223, 26

Ackermann M., et al., 2015, ApJ, 813, L41

Actis M., et al., 2011, Exper. Astron., 32, 193

Aharonian F. A. e. a., 1999, A&A, 342, 69

Aharonian F. A., 2000, New Astron., 5, 377

Aharonian F., 2007, ApJ, 664, L71

Aharonian F. A., et al., 2001, A&A, 366, 62

Aharonian F., et al., 2003, A&A, 403, 523

Aharonian F., et al., 2004, A&A, 425, L13

Aharonian F., et al., 2005, A&A, 437, 95

Aharonian F., et al., 2006a, Science, 314, 1424

Aharonian F., et al., 2006b, Nature, 440, 1018

Aharonian F., et al., 2006c, A&A, 457, 899

Aharonian F., et al., 2007a, A&A, 470, 475

Aharonian F., et al., 2007c, Astron. Astrophys., 473, L25

Aharonian F., et al., 2007b, A&A, 473, L25

Aharonian F., et al., 2007d, A&A, 475, L9

Aharonian F., et al., 2009, ApJ, 695, L40

Aharonian F., et al., 2010, A&A, 521, A69

Ahnen M. L., et al., 2017a, Astropart. Phys., 94, 29

Ahnen M. L., et al., 2017b, A&A, 603, A25

Ahnen M. L., et al., 2018, Astron. Astrophys., 620, A181

Ajello M., et al., 2017, ApJS, 232, 18

Albert J., et al., 2007a, Astropart. Phys. (submitted)

Albert J., et al., 2007b, Nuclear Instr. in Physics Research A, 583, 494

Albert J., et al., 2008, Nucl. Instrum. Meth., A588, 424

Aleksić J., et al., 2012a, Astroparticle Physics, 35, 435

Aleksić J., et al., 2012b, A&A, 541, A99

Aleksić J., et al., 2015, MNRAS, 450, 4399

Aleksić J., et al., 2016a, Astroparticle Physics, 72, 61

Aleksić J., et al., 2016b, Astroparticle Physics, 72, 76

Aliu E., et al., 2008, Science, 322, 1221

Aliu E., et al., 2009, Astroparticle Physics, 30, 293

Aliu E., et al., 2013, ApJ, 775, 3

Aliu E., et al., 2014, ApJ, 782, 13

Aliu E., et al., 2015, ApJ, 799, 7

Alvarez-Muniz J., et al., 2020, Sci. China Phys. Mech. Astron., 63, 219501

Alves Batista R., et al., 2019, Frontiers in Astronomy and Space Sciences, 6, 23

Anderhub H., et al., 2009, ApJ, 705, 1624

Ansoldi S., et al., 2016, A&A, 585, A133

Ansoldi S., et al., 2018, Astrophys. J. Lett.

Antoni T., et al., 2005, Astropart. Phys., 24, 1

Antonucci R., 1993, Ann. Rev. Astron. Astrophys., 31, 473

Antonucci R. R. J., Miller J. S., 1985, ApJ, 297, 621

Archambault S., et al., 2016, AJ, 151, 142

Arsioli B., Chang Y. L., 2017, A&A, 598, A134

Arsioli B., Fraga B., Giommi P., Padovani P., Marrese P. M., 2015, A&A, 579, A34

Arsioli B., Barres U., Prandini E., Fraga B., Foffano L., 2018, MNRAS, 480, 2165

Asano K., Hayashida M., 2015, ApJ, 808, L18

Asano K., Hayashida M., 2018, preprint, (arXiv:1805.09953)

Asano K., Takahara F., Kusunose M., Toma K., Kakuwa J., 2014, ApJ, 780, 64

Atwood W. B., et al., 2009, ApJ, 697, 1071

Barthelmy S. D., et al., 2005, Space Sci. Rev., 120, 143

Becerra Gonzalez J., et al., 2018, The Astronomer's Telegram, 11621

Bell A. R., 1992, MNRAS, 257, 493

Bird D. J., et al., 1995, ApJ, 441, 144

Blain A. W., et al., 2002, Phys. Rept., 369, 111

Blazejowski M., Sikora M., Moderski R., Madejski G., 2000, ApJ, 545, 107

Boettcher M., 2010, p. arXiv:1006.5048

Boettcher M., Reimer A., Sweeney K., Prakash A., 2013, ApJ, 768, 54

Bonnoli G., Tavecchio F., Ghisellini G., Sbarrato T., 2015, MNRAS, 451, 611

Breeveld A. A., et al., 2010, MNRAS, 406, 1687

Bretz T., Dorner D., Wagner R. M., Sawallisch P., 2009, Astropart. Phys., 31, 92

Camenzind M., 1992, in Interface of Astrophysics with Particle Physics. pp 251–280

Caproni A., Abraham Z., Motter J. C., Monteiro H., 2017, ApJ, 851, L39

Carosi A., Lucarelli F., others. 2016. (arXiv:1510.08681)

Catanese M., et al., 1997, ApJ, 487, L143

Cerruti M., Zech A., Boisson C., Inoue S., 2015, MNRAS, 448, 910

Chang Y. L., Arsioli B., Giommi P., Padovani P., 2017, A&A, 598, A17

Cherenkov P. A., 1934, Dokl. Akad. Nauk SSSR, 2, 451

Chhotray A., et al., 2017, MNRAS, 466, 3544

Cologna G., Mohamed M., Wagner S., others. 2016, PoS, ICRC 2015, 762

Condon J. J., et al., 1998, AJ, 115, 1693

Cooray A., 2016, Royal Society Open Science, 3, 150555

Costamante L., Ghisellini G., 2002, A&A, 384, 56

Costamante L., et al., 2001, A&A, 371, 512

Costamante L., Bonnoli G., et al., 2018, MNRAS, 477, 4257

Covino S., et al., 2013, MNRAS, 432, 1231

D'Elia V., et al., 2013, A&A, 551, A142

Da Vela P., et al., 2018, Astroparticle Physics, 98, 1

Danforth C. W. a. a., 2010, ApJ, 720, 976

De Angelis, A. and Pimenta, M. 2018, *Introd. to Part. and Astropart. Physics*, Springer

Dermer C. D., Schlickeiser R., 1993, ApJ, 416, 458

Dermer C. D., Cavadini M., Razzaque S., 2011, ApJ, 733, L21

Dominguez A., et al., 2011, MNRAS, 410, 2556

Doro M., 2014, Nuclear Instr. in Physics Research A, 742, 99

Einstein A., 1915, Sitzungsber. Preuss. Akad. Wiss. Berlin (Math. Phys.), 1915, 778

Event Horizon Telescope Collaboration et al., 2019, ApJ, 875, L1

Fermi E., 1949, Phys. Rev., 75, 1169

Fermi-LAT Collaboration 2015a, ApJS, 218, 23

Fermi-LAT Collaboration 2015b, ApJ, 810, 14

Fermi-LAT Collaboration et al., 2018, Science, 362, 1031

Fermi-LAT collaboration 2019, arXiv e-prints, p. arXiv:1902.10045

Finke J. D., 2013, ApJ, 763, 134

Foffano L., Prandini E., Franceschini A., Paiano S., 2019, MNRAS, 486, 1741

Fossati G., Maraschi L., Celotti A., Comastri A., Ghisellini G., 1998, MNRAS, 299, 433

Fraija N., Marinelli A., 2018, ApJ, in press

Franceschini A., Rodighiero G., 2017, A&A, 603, A34

Franceschini A., Aussel H., Cesarsky C. J., Elbaz D., Fadda D., 2001, A&A, 378, 1

Franceschini A., Rodighiero G., Vaccari M., 2008a, A&A, 487, 837

Franceschini A., Rodighiero G., Vaccari M., 2008b, A&A, 487, 837

Franceschini A., Foffano L., Prandini E., Tavecchio F., 2019, Astron. Astrophys., 629, A2

Franceschini lecture notes A., 2016, *Notes of high-energy Astrophysics*

Fruck C., et al., 2014, in Proceedings ICRC 2013. p. 1054 (arXiv:1403.3591)

Galante N., 2006, PhD thesis, U. Siena

García J. R., et al., 2014, arXiv e-prints, p. arXiv:1404.4219

Gehrels N., 2004. pp 637–641 (arXiv:0405233)

Gelmini G. B., 2009, in Journal of Physics Conference. (arXiv:0903.4716)

Ghisellini G., 1999, Astropart. Phys., 11, 11

Ghisellini G., 2013, Radiative Processes in High Energy Astrophysics. Vol. 873

Ghisellini G., Tavecchio F., 2008, MNRAS, 387, 1669

Ghisellini G., Tavecchio F., Chiaberge M., 2005, A&A, 432, 401

Ghisellini G., Tavecchio F., Foschini L., Ghirlanda G., 2011, MNRAS, 414, 2674

Ghisellini G., Righi C., Costamante L., Tavecchio F., 2017, MNRAS, 469, 255

Ginzburg V. L., Syrovatskii S. I., 1964, *The Origin of Cosmic Rays*

Giommi P., et al., 2002, in Blazar Astrophysics with BeppoSAX. p. 63 (arXiv:0209596)

Giommi P., et al., 2012, A&A, 541, A160

Grasso D., Rubinstein H. R., 2001, Phys. Rept., 348, 163

Grube J., 2008, AIP Conference Proceedings, 1085

Gu M. F., Ai Y. L., 2011, A&A, 534, A59

H.E.S.S. Collaboration 2018, A&A, 619, A71

H.E.S.S. Collaboration et al., 2010a, A&A, 511, A52

H.E.S.S. Collaboration et al., 2010b, A&A, 516, A56

H.E.S.S. Collaboration et al., 2018, A&A, 620, A66

Harrison F. A., et al., 2013, ApJ, 770, 103

Hauser M. G., Dwek E., 2001, Ann. Rev. Astron. Astrophys., 39, 249

Hayashida M., et al., 2012, ApJ, 754, 114

Healey S. E., et al., 2007, Astrophys. J. Suppl., 171, 61

Heck D., Knapp J., Capdevielle J. N., Schatz G., Thouw T., 1998

Hess V. F., 1912, Phys. Z., 13, 1084

Hillas A. M., 1984, ARA&A, 22, 425

Holler M., et al., 2016, PoS, ICRC 2015, 847

Inoue S., Takahara F., 1996, ApJ, 463, 555

Kalberla P. M. W., et al., 2005, A&A, 440, 775

Kapanadze B., 2018, The Astronomer's Telegram, 11538

Kassiola A., Kovner I., Blandford R. D., 1990

Kataoka J., et al., 2008, ApJ, 672, 787

Katarzynski, K. Sol, H. Kus, A. 2001, A&A, 367, 809

Katarzynski K., et al., 2006, A&A, 453, 47

Kellermann K. I., et al., 1989, Astron. J., 98, 1195

Kelner S. R., Aharonian F. A., 2008, Phys. Rev., D78, 034013

Kido E., 2018, PoS, ICRC 2017, 386

Kronberg P. P., 1996, Space Sci. Rev., 75, 387

Kulsrud R. M., Zweibel E. G., 2008, Rept. Prog. Phys., 71, 0046091

Lawrence A., 1987, PASP, 99, 309

Lefa E., Rieger F. M., Aharonian F., 2011, ApJ, 740, 64

Lehto H. J., Valtonen M. J., 1996, ApJ, 460, 207

Li T.-P., Ma Y.-Q., 1983, ApJ, 272, 317

Lister M. L., et al., 2013, A&A

Longair M. S., 2002, Frascati Phys. Series, 24, 3

Lopez-Coto R., 2016, PoS, ICRC 2015, 955

Lv G. J., Shao L., Jin Z. P., Wei D. M., 2011, Acta Astronomica Sinica, 52, 190

MAGIC Collaboration 2019a, arXiv e-prints, p. arXiv:1911.06680

MAGIC Collaboration 2019b, arXiv e-prints, 490, 2284

MAGIC Collaboration 2019c, Nature, 575, 455

MAGIC Collaboration 2019d, Studies on 1ES 2344+514, in preparation

Madau P., Dickinson M., 2014, Ann. Rev. Astron. Astrophys., 52, 415

Majumdar P., et al., 2005, in Proceedings, 29th ICRC 2005. pp 203–206

Mannheim K., 1993, A&A, 269, 67

Maraschi L., Ghisellini G., Celotti A., 1992, ApJ, 397, L5

Markov M. A., 1960, in Proceedings, ICHEP 60. pp 578–581

Massaro E., Maselli A., Leto C., et al., 2015, Ap&SS, 357, 75

Mattox J. R., et al., 1996, ApJ, 461, 396

Mazin D., et al., 2007, in Proceedings ICRC 2007. pp 1253–1256

Millikan R. A., Cameron G. H., 1926, Physical Review, 28, 851

Mirzoyan R., 1997, International Cosmic Ray Conference, 7, 265

Mirzoyan R., 2017, The Astronomer's Telegram, 10817

Mirzoyan R., 2018, The Astronomer's Telegram, 11548

Mirzoyan R., 2019a, The Astronomer's Telegram, 12354

Mirzoyan R., 2019b, The Astronomer's Telegram, 12390

Mirzoyan R., et al., 2019, arXiv e-prints, p. arXiv:1903.04989

Mizobuchi S., et al., 2005, in Proceedings, ICRC 2005. pp 323–326

Moderski R., Sikora M., Błażejowski M., 2003, A&A, 406, 855

Morris S. L., et al., 1991, ApJ, 380, 49

Motch C., et al., 1998, Astron. Astrophys. Suppl. Ser., 132, 341

Mucke A., Protheroe R. J., 2001, in 27th ICRC 2001. p. 1153 (arXiv:0105543)

Murase K., Dermer C. D., Takami H., Migliori G., 2012, ApJ, 749, 63

Neronov A., Vovk I., 2010, Science, 328, 73

Nilsson K., et al., 2018, A&A, 620, A185

Oh K., et al., 2018, Astrophys. J. Suppl., 235, 4

Overbeck J. W., 1965, ApJ, 141, 864

Padovani P., 1997, in VHE phenomena in the universe.. pp 7–16 (arXiv:9704002)

Padovani P., Giommi P., 1995, ApJ, 444, 567

Padovani P., Resconi E., Giommi P., Arsioli B., Chang Y. L., 2016, MNRAS, 457, 3582

Padovani P., et al., 2017, Astron. Astrophys. Rev., 25, 2

Paiano S., Falomo R., Treves A., Scarpa R., 2018, ApJ, 854, L32

Pian E., et al., 1998a, ApJ, 492, L17

Pian E., et al., 1998b, ApJ, 492, L17

Pierre Auger Collaboration et al., 2016, p. arXiv:1604.03637

Plotkin R. M., Markoff S., Trager S. C., Anderson S. F., 2011, MNRAS, 413, 805

Poole T. S., et al., 2008, MNRAS, 383, 627

Prandini E., et al., 2009, arXiv e-prints, p. arXiv:0907.0157

Prandini E., Mariotti M., Tavecchio F., 2011, A&A, p. arXiv:1111.0913

Ptuskin V. S., et al., 1993, A&A, 268, 726

Rapidis P. A., NESTOR Coll. 2009, Nuclear Instr. in Physics Research A, 602, 54

Resconi E., Coenders S., Padovani P., Giommi P., Caccianiga L., 2017, MNRAS, 468, 597

Rieger F. M., 2004, eConf, C041213, 1601

Romero G. E., 2000, in Proceedings. pp 65–80 (arXiv:0012243)

Sanchez D. A., Deil C., 2013, preprint, (arXiv:1307.4534)

Sanders D. B., et al., 2009, in *The Starburst-AGN Connection*. p. 3

Saugé L., Henri G., 2004, ApJ, 616, 136

Sbarrato T., Padovani P., Ghisellini G., 2014, MNRAS, 445, 81

Sbarufatti B., Treves A., Falomo R., 2005, ApJ, 635, 173

Schlafly E. F., Finkbeiner D. P., 2011, ApJ, 737, 103

Sikora M., Begelman M. C., Rees M. J., 1994, ApJ, 421, 153

Sironi L., Spitkovsky A., 2014, ApJ, 783, L21

Sitarek J., et al., 2013, Nucl. Instrum. Meth., A723, 109

Smith E. P., et al., 1986, ApJ, 306, 64

Sobacchi E., Sormani M. C., Stamerra A., 2017, MNRAS, 465, 161

Stecker F. W., de Jager O. C., Salamon M. H., 1996, ApJ, 473, L75

Swordy S. P., 2001, Space Sci. Rev., 99, 85

Tavani M., Cavaliere A., Munar-Adrover P., Argan A., 2018, ApJ, 854, 11

Tavecchio F., Ghisellini G., 2015, MNRAS, 451, 1502

Tavecchio F., Maraschi L., Ghisellini G., 1998, ApJ, 509, 608

Tavecchio F., et al., 2009, MNRAS, 399, L59

Tavecchio F., et al., 2010, MNRAS, 401, 1570

Tavecchio F., Ghisellini G., Bonnoli G., Foschini L., 2011, MNRAS, 414, 3566

Tescaro D., et al., 2013, in Proceedings, 33rd ICRC 2013. p. 0122 (arXiv:1310.1565)

Urry C. M., Padovani P., 1995, PASP, 107, 803

Vercellone S., 2011, p. arXiv:1111.0697

Völk H. J., Bernlöhr K., 2009, Experimental Astronomy, 25, 173

Vovk I., Babić A., 2015, A&A, 578, A92

Vovk I., Neronov A., 2013, ApJ, 767, 103

Wagner R. M., 2006, PhD thesis, Munich, Tech. U.

White R. L., Becker R. H., Helfand D. J., Gregg M. D., 1997, ApJ, 475, 479

Wilson A. S., Colbert E. J. M., 1995, ApJ, 438, 62

Zanin R., 2013, Nucl. Phys. Proc. Suppl., 239-240, 55

Zhou H.-Y., et al., 2007, ApJ, 658, L13

La montagna ha il valore dell'uomo che vi si misura,
altrimenti, di per sé, essa
non sarebbe che un grosso cumulo di pietre.
Walter Bonatti